Regulation of Pancreatic Ductal Adenocarcinoma Subtypes by Chromatin Proteins Determines Sensitivity to Inhibitors of Transcriptional Cyclin-dependent Kinases.

Jessica Erin Gianopulos

A dissertation

submitted in partial fulfillment of the

requirements for the degree of

Doctor of Philosophy

University of Washington

2024

Reading Committee:

Sita Kugel, Chair

David Michael Shechner

Eleanor Y Chen

Program Authorized to Offer Degree:

Molecular and Cellular Biology

University of Washington

Abstract

Regulation of Pancreatic Ductal Adenocarcinoma Subtypes by Chromatin Proteins Determines Sensitivity to Inhibitors of Transcriptional Cyclin-dependent Kinases.

Jessica Erin Gianopulos

Chair of the Supervisory Committee

Sita Kugel

Department of Genome Sciences

Pancreatic ductal adenocarcinoma (PDA) subtype classifications were originally defined by transcriptional differences between two groups, known as the basal and classical PDA subtypes. The biological differences between these two subtypes goes beyond just transcriptional differences as the transcriptome is defined by the epigenome, therefore epigenetic changes including chromatin regulation, control transcriptional expression of the gene groups used to define the basal and classical subtypes. In this dissertation, I discuss how different epigenetic regulators contribute to the basal and classical PDA cell states and that disruptions to these cell states can alter cellular plasticity. I then show that regulation of these subtype-specific cell states defines the cells' ability to respond to stressors such as transcriptional inhibitors. Further investigation of transcriptional inhibitors as a therapeutic option for PDA, led us to uncover that

PDA presents with a subtype-specific sensitivity to inhibitors of transcriptional cyclin-dependent kinases (CDKs). Moreover, we define that altering chromatin regulation and disrupting PDA cell state can modify PDA sensitivity to transcriptional CDK inhibitors. This work presents novel insights into the therapeutic potential of transcriptional CDK inhibitors in the treatment of PDA patients and how regulation of chromatin states can be used to adjust sensitivity of PDA tumors to the inhibitors.

Table of Contents

List of Figures

List of Tables

Acknowledgements

I would like to thank my amazing family for all their support over the years. My parents and especially my mom for always encouraging me and believing in my ability to accomplish anything. Thank you to my mom for being such an amazing, strong female role model, I have and always will look up to you. Thanks to my sister and fellow scientist for all our spirited conversations and late-night talks. Thank you to my whole family for always encouraging my curiosity and random excitement over investigating a new subject. Thank you to my grandparents, who's support has helped make my dream of completely my PhD possible.

I would like to thank all my pre-college teachers and mentors who taught me so much and fueled my love of science and math. I would like to thank all my UW biology professors with special shoutouts to Dr. Alison Crowe, Dr. Amanda (Mandy) Schivell, and Dr. Brian Buchwitz who supported my dream of attaining a PhD and pushed me to always dive deep in my pursuit of knowledge. Thank you to my graduate thesis committee members (Dr. David Shechner, Dr. Andrew Hsieh, and Dr. M.K. Raghuraman) for their direction and guidance throughout the whirl wind of projects I navigated during my PhD, as well as each of their individual support outside of the thesis committee. Thank you to the MCB program staff, especially Maia and Denise, for all their logistical support through the rockiness of covid and general stress of graduate school.

A big thank you to Dr. Eleanor Chen who took me on as an undergraduate researcher, who believed in my capability as a researcher and pushed me towards every new challenge, who helped me plan my career and get into graduate school, and who, despite her busy schedule, made time to be on my graduate thesis committee and continue guiding my career as a scientist. I would also like to thank the members of the Chen Lab: Mike, Terra and Thao and all my fellow

undergraduate researchers: Colton, Ernest, Phuong, Shivani, and Texia. A special thank you to Dr. Michael Phelps (Mike) for being my first in lab research mentor and for teaching me everything I know about lab work. Thank you for teaching me to be an independent scientist and preparing me for graduate school, I continue learning from your lessons every day.

An extra special thank you to Dr. Sita Kugel, my graduate thesis mentor, who has been such a supportive mentor through some of the most challenging years of my life. You have taught me more than I could possibly imagine about science but also about life. Thank you for creating such a warm and welcoming space to learn; thank you for your guidance and your support; thank you for helping me navigate the complex progression of my projects; thank you for trusting in my ability to complete the lab's first paper; thank you for being another strong female role model in my life; thank you for everything. I would also like to thank all the past and present members of the Kugel lab; I am so grateful for the collaborative environment of this lab where we are always teaching and learning from each other. I am thankful for the friends that I have made and all my lab mates who have supported me throughout the years.

I would like to thank all my friends who stuck with me through the most stressful years of my life. Thank you, Samantha Schuster, for being such a good friend and for all our lunch time chats and adventures. Thank you to Phuong, Shivani, and Dayla for your friendship and support over the years and for keeping me grounded. Thank you to Zach Schrank, for being a great lab mate and supportive friend. Thank you to all my dance friends and dance communities who provided such a warm and welcoming space for me to release the mental and physical stress of graduate school. Lastly, I would like to thank my incredible partner and best friend, Niguel Barrio for his friendship and support of me and my career for the past 10 years, you have helped make my dreams possible.

CHAPTER 1: INTRODUCTION

1.1 Pancreatic Cancer

1.1.1 The progression and development of pancreatic cancer

The pancreas is composed of both endocrine and exocrine components. The endocrine pancreas is defined by the pancreatic islet which contains alpha and beta cells. Alpha cells secrete glucagon to promote release of glucose from glycogen storages during times of low blood glucose[1]. Beta cells secrete insulin to maintain normal physiological levels of glucose. Insulin antagonizes glucagon and other hyperglycemic hormones to lower blood glucose levels[2]. The exocrine pancreas is defined by the pancreatic ducts which contain acinar and ductal cells. Acinar cells secrete digestive enzymes that are carried through the pancreatic ducts and released into the duodenum of the small intestine[3].

Pancreas cancer can occur in either the endocrine or exocrine pancreas. Endocrine pancreas cancer is called pancreatic neuroendocrine tumors (PNET) which accounts for less than 5% of pancreas cancer cases. PNET has a relative 5-year survival rate of 53% which increases to 95% if the PNET has remained localized to the primary tumor site[4]. Exocrine pancreas cancer is called Pancreatic Ductal Adenocarcinoma (PDA) which accounts for about 90% of pancreas cancer and is therefore the most common pancreas cancer[5]. Unfortunately, PDA is an extremely lethal disease with a 5-year survival rate of only ~12% and is projected to become the second leading cause of cancer related deaths in the US by 2030[6]. This low survival rate and increase in death is due to a lack of clinically validated screening methods and very minimal treatment options. Early detection of PDA is challenging as most early-stage patients are asymptomatic, therefore detection would largely rely on highly specific and sensitive tests for biomarkers of which there are very few[7,8]. Due to the late stage of diagnosis for most patients, only a small

percentage qualify for surgical resection while most patients present with locally advanced or metastatic disease. Therefore, chemotherapy presents as the standard of care for the large majority of patients yet tumor heterogeneity and plasticity often lead to chemoresistant tumors[5,9].

To better understand the complexity of PDA tumors, researchers first turned to understanding the genetics of PDA progression. As indicated by the name it was originally thought that pancreatic ductal adenocarcinoma was derived solely from aberrant changes to pancreatic ductal cells given that the PDA precursor lesions or pancreatic intraepithelial neoplasias (PanINs) contain characteristics of ductal cells and tumor cells[10]. More recent research has uncovered that PanINs may also be derived from acinar cells that have undergone an acinar to ductal metaplasia (ADM). Both acinar and ductal cells are differentiated cell types meaning that an acinar to ductal metaplasia would be considered transdifferentiation[11]. The ability of acinar cells to undergo ADM elucidates the plasticity of these cells and the potential reversibly of ADM if the stress inducer resolves quickly. Prolonged stress, such as acquired genetic mutations, can lead to irreversible ADM and promote PanIN progression[12]. PanINs progress from low grade to high grade through architectural changes and acquisition of genetic alterations[7,13]. Low-grade PanINs are associated with acquisition of oncogenic kras mutations and telomere shortening leading to accelerated growth of the aberrant cells. As PanINs progress, they acquire loss of p16/CDKN2A tumor suppressor gene leading to decreased cell cycle regulation of the growth accelerated ductal cells. Finally, high grade PanINs associate with loss of p53, SMAD4 and BRCA2 leading to further decreased regulation of these abnormal cells and eventual formation of PDA[7,13].

PDA tumors generally retain some duct like structures in the form of a glandular histology however different regions of individual tumors can still vary in their histology, tumor

grade and 'degree of differentiation'[13]. An early method to classify PDA tumors into groups used degree of differentiation as it corresponded to tumor grade and patient prognosis. Studies of patient tumors identified four grades of differentiation: highly differentiated (G1), moderately differentiated (G2), poorly differentiated (G3) and un-differentiation (G4)[14]. It was then identified that patients with more differentiated tumors generally had a more favorable prognosis while poorly differentiated tumors yielded a worse prognosis[15]. Further investigation into the four grades of differentiation showed that gene expression in PDA tumors changes between the different grades, for example tumor differentiation related genes: JUNB, HMGA2 an MCM2 all increased expression as tumor grade increased[14]. This indicated that PDA tumor differentiation grade could provide more insight into development of PDA.

1.1.2 Introduction to mouse models of pancreatic cancer

Genetically engineered mouse models (GEMMs) are a vital model system for studying PDA tumor biology, from initiation to progression of disease and metastasis. An added benefit of this in vivo system is the capacity to study PDA in a 3D environment thereby enabling retention of all other tumor interacting cells in the tumor microenvironment. Through extensive work studying pancreatic development, the field has developed several GEMMs that can recapitulate the genetic and histological characteristics of human PDA[13]. To create GEMMs with tissue specific expression of the genetic changes needed to induce PDA in the pancreas, researchers opted for a model in which the CRE recombinase enzyme would be expressed under a pancreas-specific gene promoter. PDX1 expression was identified as one of the earliest developmental markers of a pancreatic progenitor cell, specifically PDX1 is expressed in a multipotent pancreas progenitor cell population that exists before differentiation into the acinar, ductal, and endocrine

cell type[16]. P48/PTF1 is a pancreas specific transcription factor expressed slightly later in development during which the progenitor cell fully commits to a pancreatic cell fate[17].

The *Pdx1*-Cre system has been widely used to create many PDA GEMMs that can activate oncogenic Kras, these systems use a *Kras* mutation that converts amino acid 12 from a glycine to an aspartic acid (*Kras^{G12D}*). The *Kras^{G12D}* oncogene is placed downstream of a Lox-STOP-Lox cassette (*LSL- Kras^{G12D}*) which prevents expression of *Kras^{G12D}* unless the Cre recombinase in present. The Cre recombinase will excise the stop codon between loxP sites in the *LSL- Kras^{G12D}* allele and enable expression of oncogenic Kras. These *Pdx1-Cre, LSL-Kras^{G12D}* GEMMs have shown that induction of oncogenic Kras alone can drive PanIN and PDA formation but requires an extended period of time. Further studies identified that combining *Pdx1-Cre, LSL- Kras^{G12D}* with mutations in tumor suppressors such as *p53* could accelerate PDA formation in these GEMMs[13]. Additionally, *Pdx1-Cre, LSL- Kras^{G12D}* with *p53* mutant and *Pdx1-Cre, LSL- Kras^{G12D}* with *Ink4a/Arf* deficiency (cyclin-dependent kinase inhibitor 2A, another tumor suppressor in PDA) GEMM models have shown earlier appearance of PanIN lesion, dramatic induction of highly penetrant PDA, and highly invasive, metastatic disease which strongly recapitulates the disease seen in human PDA patients[18,19]. However, no model system is a perfect representation of human disease, therefore they all have flaws. For example, even though the *Pdx1-Cre, LSL- Kras^{G12D}* GEMM is widely used to study PDA, it has been shown that this model systems results in a stochastic pattern of Cre expression in the mouse pancreas whereas the *p48-Cre, LSL- Kras^{G12D}* mouse results in more uniform Cre expression throughout the pancreas. This study also showed that expression of oncogenic Kras was slightly higher in the *p48-Cre, LSL- Kras^{G12D}* mouse than the *Pdx1-Cre, LSL- Kras^{G12D}* mouse[17]. These studies have all shown the importance of GEMMs in understanding and investigating PDA tumor

biology but like any model system they have limitations and can only address specific scientific questions. Therefore, it's important to incorporate many model systems into any PDA study.

1.2 Epigenetic regulation in pancreatic ductal adenocarcinoma

1.2.1 Introduction to epigenetic regulation in PDA

As described in section 1.1, PDA tumors have very low diversity in genetic mutations yet there is a class of genes frequently mutated in PDA that stands out. This class is epigenetic regulators including transcription factors, histone modifying enzymes and chromatin remodeling complexes. SMAD4 is a prominently mutated transcription factor in PDA, as these mutations are acquired during PanIN lesion formation and promote progression of PDA disease. SMAD4 is part of the TGF-β growth factor signaling pathway. TGF-β binds the SMAD family receptors which in turn bind SMAD4 and translocates to the nucleus where SMAD4 activates transcription of many TGF-β regulated signaling pathway genes[20]. SMAD4 mutations and other disruptions to the TGF-β signaling pathways can lead to more aggressive PDA[21].

In addition to SMAD4 and other key mutations mentioned previously, PDA mutations can exist in many genes that come together to form chromatin remodeling complexes[22]. Chromatin remodeling complexes determine accessibility to chromatin and regulation of transcription through histone modifications. Active transcription is facilitated by histone modifications that promote the opening of chromatin which spatially enables transcription and recruits the transcriptional machinery. Repressing transcription is facilitated by histone modifications that promote compaction of chromatin which spatially blocks transcription machinery[23]. These chromatin modifying complexes comprise of a DNA binding protein, a recruitment mediator, and histone modifying proteins. The general classes of histone modifying

proteins are Histone acetyltransferase (HAT), Histone deacetylase (HDAC), Histone methyltransferase (HMT), and Histone demethylase (HDM). Some chromatin modifying complexes also contain DNA modifying proteins such as DNA methyltransferase (DNMT) which deposits methylation marks on DNA and promotes chromatin compaction[24].

One of these complexes is the SWItch/Sucrose NonFermentable (SWI/SNF) chromatin remodeling complex, which contains five components that can be mutated in pancreatic cancer: ARID1A, ARID1B, PBRM1, SMARCA4, and SMARCA2. Grouping these mutations together, the SWI/SNF complex is then ranked fourth in the list of tumor suppressors mutated in PDA[25]. Mutations in other epigenetic regulator genes were also identified by multiple studies, finding that the group of MLL chromatin regulatory genes (MLL, MLL2 and MLL3) was impacted along with KDM6A, a histone demethylase[26–28]. Interestingly, KDM6A functions as part of the MLL regulatory complex to facilitate active transcription, thereby identifying another chromatin regulatory complex with multiple mutated components in PDA tumors. Mutated genes then imply a worse prognosis for patients, yet mutated MLL, MLL2, MLL3 and ARID1A actually confers improved patient survival[26]. This finding highlights the importance of understanding that altered chromatin regulation in pancreas cancer, as well as other cancers, can be very context specific and needs to be acknowledged when studying the impact of these chromatin regulators on cancer progression.

1.2.2 Mouse models of epigenetic regulators

SMAD4 is deleted or mutated in 55% of human PDA, therefore investigating the importance of SMAD4 in development and progression of PDA was vital to the field. The creation of the *Ptf1-Cre, LSL- Kras^{G12D}*, *Smad4$^{lox/lox}$* GEMM enabled assessment of Smad4 loss

in the context of *Kras*^{G12D} driven disease. The addition of Smad4 loss greatly accelerated the formation of PanIN lesions in the *Ptf1-Cre, LSL- Kras*^{G12D}, *Smad4*$^{lox/lox}$ mice compared to *Ptf1-Cre LSL- Kras*^{G12D} (*Kras* alone) mice, however the *Smad4* null PDA tumors retained a more differentiated histology and expression of epithelial markers[21]. Interestingly the combined loss of Smad4 and Cdkn2a in the *Kras*^{G12D} driven GEMM lead to development of well-differentiated PDA with duct-like/glandular structures[21]. Further investigation of how the disruption to SMAD4/TGF-β pathway affects PDA progression and development was completed using a TGF-β receptor 2 (*Tgfbr2*) knockout GEMM model. *Tgfbr2* knockout alone gave no discernable PDA tumor phenotype but combination of oncogenic Kras plus Tgfbr2 loss yielded PanIN progression to PDA formation[29]. Similar to the *Smad4* knockout mouse model, the *Tgfbr2* knockout mouse also presented with a well-differentiated PDA tumor[21,29]. These model systems provide important insight into how disruptions to transcriptional regulation of the TGF-β signaling pathway can promote development and progression of PDA.

ARID1A is one of the most commonly mutated components of the SWI/SNF chromatin remodeling complex and is known to function as a tumor suppressor in PDA[30]. Several studies have used *Arid1a* knockouts in mice to decipher the role of Arid1a in PDA tumor initiation and progression. It was identified that Arid1a has very compartment-specific tumor suppressive effects in PDA. Lineage specific deletion of *Arid1a*, using the duct-compartment specific *Sox9-CreER; Kras*^{G12D}*;Arid1a*$^{f/f}$, showed that loss of Arid1a in pancreas ductal cells lead to enlargement of ducts and some cysts with eventual formation of PDA[31]. Heterozygous loss of *Arid1a* in acinar cells (*Ptf1a*^{CreER}*; Kras*^{G12D}*;Arid1a*$^{f/+}$) lead to rapid PanIN formation and PDA progression with poor survival[31,32]. These studies prove that Arid1a is necessary to restrict *Kras* driven PDA. Interestingly, another study shows that *Arid1a* loss has a growth suppressive effect

on precursor lesions and results in low grade cyst[33]. This study did not use any lineage specific models and instead used the *Ptf1a-Cre; Kras^{G12D}; Arid1a$^{f/f}$* which induces *Arid1a* knockout in the whole pancreas which would explain the cyst formation from the ductal cells as mentioned previously. Additionally, this study discovered that during PDA tumorigenesis, Arid1a loss drives downregulation of p53, upregulation of Myc, and alterations to EMT-associated transcription factors in some precursor cells which can facilitate further PDA progression[33]. This suggests that the absence of Arid1a promotes loss of general chromatin and transcriptional regulation leading to changes in expression of tumor suppressive and tumor promoting factors thereby driving more aggressive PDA.

Brg1, also known as SMARCA4, is an ATPase catalytic subunit of the SWI/SNF complex. Inactivating mutations and deletions of BRG1 have been found in human PDA tumors and PDA cell lines[34]. The role of Brg1 in pancreatic cancer development has been studied using the *Ptf1a-Cre; Kras^{G12D}; Brg1$^{f/f}$* mouse as Brg1 deficiency alone in the pancreas is not enough to drive tumor formation. Brg1 deficiency in addition to oncogenic Kras leads to formation of a different PDA precursor lesion—Intraductal papillary mucinous neoplasia (IPMN)—whereas oncogenic Kras alone leads to PanIN formation and progression to PDA. This study further identified that Brg1 loss inhibits Kras driven formation of PanIN in adult acinar cells[35]. The same research group later continued investigating the roles of Brg1 in PDA ductal cells and found that Brg1 inhibits a dedifferentiation program prior to cell transformation in pancreas ductal cells. In contrast, Brg1 drives tumorigenesis in PDA cells by promoting a more mesenchymal transcriptional landscape[36]. These studies have identified very context-dependent roles of Brg1 in PDA development and progression which highlights the complexity of chromatin regulation in PDA.

KDM6A (also known as UTX) is an X-chromosome encoded histone H3K27me3 demethylase which antagonizes the EZH2 methyltransferase which deposits H3K27me3[37]. Due to its demethylase activity, KDM6A, in conjunction with other histone modifiers, can promote a more accessible chromatin state enabling active transcription and gene expression. KDM6A is a highly mutated chromatin regulator in PDA but how these mutations contribute to oncogenesis was poorly understood. Pancreatic tumors with mutated or deleted KDM6A were found to correlate with high expression of the squamous differentiation marker, TP63, which is also a marker of highly aggressive PDA[38]. To further understand how KDM6A contributes to oncogenesis, the same group made pancreas specific *Kdm6a* knockout mice in conjunction with *Pdx1-Cre; Kras^{G12D}* or *Ptf1α-Cre; Kras^{G12D}*. They found that both cohorts of *Kdm6a* knockout mice presented with aggressive tumors selectively in female mice. *Kdm6a* null male mice and heterozygous female mice showed much slower disease progression with eventual development of well-differentiated tumors. Females with Kdm6a null tumors exhibited more squamous characteristics including increased proliferation and metastatic potential[38]. This study uncovered the role of Kdm6a in safeguarding pancreatic cell identity and preventing malignant transformation suggesting that epigenetic reprogramming is critical to driving tumorigenesis and metastatic disease.

1.2.3 Histone Deacetylase: SIRT6 in PDA

Sirtuin 6 (SIRT6) is a histone 3 lysine 9 and lysine 56 deacetylase from the family of Sirtuin proteins which are highly conserved NAD+-dependent enzymes. SIRT6 enzymatic activity is known to impact a large diversity of biological functions including genomic stability/DNA repair, inflammation, and glucose/lipid metabolism of which all are important for

maintaining normal cellular function and when disrupted can lead to human diseases such as cancer[39]. SIRT6 loss of function mutations have been found in a variety of human cancers and can alter stability, localization, or enzymatic activity of the protein. These mutations affect SIRT6 regulation of HIF1-alpha and MYC transcriptional activity which can drive glycolytic changes and enhance tumor cell growth, thereby validating the important tumor suppressive role of SIRT6[40].

In pancreatic cancer, the absence of *Sirt6* with the addition of oncogenic *Kras* accelerated PDA formation[41]. To further assess the impact of Sirt6 loss on the development of PDA, *Kugel et al* created a *Sirt6* knockout mouse with a pancreas-specific Cre recombinase (*p48-Cre*), a floxed p53 allele (*p53f/+*), and a *LSL-Kras^{G12D}* allele. This GEMM then presents with specific loss of one or both alleles of *Sirt6* and *p53* in addition to oncogenic *Kras* expression in the pancreas. Interestingly, they found that the absences of Sirt6 in the presence of oncogenic Kras dramatically accelerated the development of PDA regardless of p53 status[41]. To investigate the mechanisms behind this finding, they derived cell lines from their *Sirt6* knockout (*Sirt6* KO) and *Sirt6* wildtype (*Sirt6* WT) murine tumors. They used these murine cell lines as well as human PDA cell lines to uncover that SIRT6 suppresses PDA growth through decreasing the levels of global acetylation and the amount of chromatin-bound MYC as well as specific deacetylation at the Lin28b promoter. Lin28b is an onco-fetal protein highly expressed in embryonic tissue but completely silenced in differentiated cells. Dysregulation of SIRT6 drives aberrant expression of Lin28b and its downstream let-7 targets resulting in poor PDA prognosis[41]. This study highlights that chromatin regulators can directly impact tumor growth through epigenetic regulation, leading to transcriptional changes in specific gene targets important to PDA formation.

1.2.4 Chromatin modifying complex: KRAB-ZNF/KAP1/SETDB1

As previously mentioned, histone modifications can regulate transcription by promoting open or closed chromatin. The KRAB-ZNF/KAP1/SETDB1 is a repressive complex which installs H3K9me3 to maintain chromatin compaction and gene silencing[42]. SETDB1 is a histone methyltransferase that deposits H3K9me3 mark. KAP1 is the recruitment mediator which binds the DNA binding protein and recruits the histone modifying protein (ie. SETDB1). The KRAB-ZNF is a DNA binding protein which contains a Krüppel-associated box (KRAB) domain (which recruits KAP1 and repressive histone modifying proteins) and a Zinc Finger (ZNF) DNA binding domain (which coordinates zinc ions to for specific DNA binding patterns). KRAB-ZNF complexes have now been implicated in the regulation of multiple biological processes such as lipid metabolism, cell differentiation, immune response and more[43]. Historically, KRAB-ZNFs were studied through their function of suppressing endogenous retroviruses (ERVs) and other repetitive DNA elements. Through studies of primate genomes it was discovered that infiltration of new ERVs occurred around the same time as novel duplications of KRAB-ZNF[44]. Further studies have continued to elucidate the evolutionary arms race between ERVs and KRAB-ZNFs that drove the duplication and diversification of KRAB-ZNF genes. KRAB-ZNF duplication enabled continued suppression of ERVs as they evolved and tried to evade suppression which forced selection for KRAB-ZNFs with new mutations that were advantageous in suppressing active ERVs[42]. With the decrease in mobile DNA elements in the human genome, KRAB-ZNFs have acquired new functional roles in biology and have been implicated in human diseases and cancer.

Although no previous studies have assessed the role of a KRAB-ZNF in PDA progression, there is one study that identified another zinc finger, ZNF655, as an oncogene which

has a stimulatory effect on PDA. This study found that ZNF655 promotes binding of E2F transcription factor 1 (E2F1) to the promoter of cyclin-dependent kinase 1 (CDK1) and thereby enhances the activity of CDK1 driving malignant behaviors of PDA cells[45]. This study validates that ZNF genes can play important regulatory roles in defining PDA progression.

SETDB1, the histone methyltransferase component of KRAB-ZNF/KAP1/SETDB1 repressive complex, has been implicated in the development of PDA. *Ogawa et al* used the *Ptf1-Cre, Kras^{G12D}* GEMM with a *Setdb1* deficiency and then with or without *p53* loss to investigate how Setdb1 contributes to PDA development. They found *Setdb1* loss in conjunction with oncogenic *Kras* accelerated formation of PanIN lesion but prevented formation of full PDA in the presence of WT *p53*. They uncovered that Setdb1 binds the p53 promoter and suppresses its expression such that the loss of Setdb1 would increase p53 expression and thereby p53 mediated apoptosis of malignant cells preventing PDA formation. Further loss of p53 in addition to loss of Setdb1 enables progression from PanINs to full PDA due to the complete loss of p53 regulated apoptosis[46]. Here Setdb1 has been described as vital for complete PDA formation through its inhibition of p53 mediate apoptosis. SETDB1 has also been implicated in other cancers such as lung[47] and breast[48] but its impact on tumor progression varies dramatically based on the context, therefore SETDB1 may have different functional roles in PDA formation versus PDA progression.

Investigation of another zinc finger transcription factor, ZBED2, has uncovered novel zinc finger regulation of the interferon response and cellular identity in PDA. ZBED2 is part of the ZBED gene family of DNA binding transcriptional regulators. *Somerville et al* identified that ZBED2 is highly expressed in the more aggressive, squamous PDA subtype. High expression of ZBED2 led to loss of pancreatic progenitor cell identity through suppression of GATA6 and

promotion of more squamous PDA tumors by induction of the epithelial to mesenchymal transition (EMT)[49]. Additionally, they found that ZBED2 is a transcriptional repressor of interferon response pathway genes, showing that zinc finger genes can form complex regulator networks that regulate many pathways in tumors such as the interferon response and cellular identity in PDA.

Together all these studies have shown that chromatin and transcriptional regulators are vital to control the specific cell state that the malignant pancreas cells need in order to form, progress and metastasize into the aggressive disease seen in human PDA patients.

1.3 Subtype classifications of pancreatic ductal adenocarcinoma tumors

1.3.1 Epigenome determines transcriptome:

Chromatin regulators determine chromatin states and chromatin states determine the accessibility of DNA to the transcriptional machinery. Transcription and mRNA expression are major readouts for determining changes that occur in a tumor cell, yet those transcriptional changes are inherently controlled by chromatin regulators. Therefore, epigenetic regulation determines the transcriptome.

As described in the previous section PDA has acquired mutations in many chromatin regulatory proteins and complexes which can alter the different characteristics of the PDA tumors. Expression changes and other alteration to chromatin regulatory proteins can also define specific chromatin states found in PDA. *Lomberk et al*. performed a multiparametric integrative analysis study to assess RNA expression, chromatin accessibility and DNA methylation status in order to define the epigenetic landscapes of PDA. From their analysis, they identified different patterns of epigenetic marks which defined their chromatin states and determine significantly

altered pathways that could characterize each group. Diving further into the data, they were able to identify specific transcriptional landscapes for two PDA subtypes: basal and classical[50]. Interestingly, the classical PDA subtype showed a very high level for chromatin regulation through defined super-enhancer and transcription factor regulatory networks. On the other hand, the basal PDA subtype shows a clear lack of this defined regulatory network[50,51]. Disruptions to this well-defined chromatin regulatory network in classical PDA can lead to phenotypic plasticity and potential switching to a more basal chromatin state[51]. These studies have elucidated the importance of understanding the chromatin regulation behind the transcriptional changes that originally defined the PDA subtypes (described more in the next section). The differential states of PDA subtypes are built through the complex interworking's of these epigenetic landscapes.

1.3.2 Transcriptional subtypes of pancreatic cancer

The basal and classical PDA subtypes were identified through over a decade of research into how transcriptional changes could explain the heterogeneity of PDA tumors. A variety of sample types were used to determine transcriptional signatures of PDA including resected tumors, patient-derived xenografts, organoids, and cell lines which led to an initial discovery of two to four PDA subtypes. *Collisson et al* published the first identification of PDA transcriptional subtypes using microarray data from PDA patient samples as well as human and mouse cell lines and identified three subtypes: Exocrine-like, Classical, and Quasi-mesenchymal[52]. A few years later, *Moffitt et al* used virtual microdissection to profile metastatic PDA tumors by microarray and RNA-sequencing to discover two PDA subtypes: Classical and Basal-like[53]. Next, *Bailey et al* used bulk resected tumor tissue and performed RNA-sequencing and array-based expression profiling to identify four PDA subtypes: Squamous, Immunogenic,

Pancreatic Progenitor and ADEX (aberrantly differentiated endocrine exocrine)[54]. Following these initial three studies, *Raphael et al* performed integrative multi-omics profiling on PDA patient samples and compared with the three previous studies. This study also assessed purity of the samples from each study and identified that high purity samples associated with only two subtype classification (basal-like/squamous and classical/progenitor) while low purity samples associated with the other subtypes (immunogenic and ADEX or exocrine-like)[55].

Around this time, a general consensus was beginning to form that there are two predominant PDA tumor subtypes: Classical (which includes progenitor) and Basal (which includes quasi-mesenchymal and squamous). This was reinforced by the next set of subtyping papers which, using different methodologies, all identified similar forms of classical and basal PDA subtypes[56–58]. One study took a step further and speculated that PDA subtypes may be influenced by lineage plasticity where the cancer cell progenitor may be more classical in subtype and as the tumor progressed, the cancer cells could have diverged into the basal and classical tumor cells identified by these transcriptional signatures[58].

Even though the current consensus is that there are two PDA subtypes—basal and classical—this classification could still be an oversimplification of very complex tumor biology. The basal and classical subtype labels could be better used as overarching classifications that may group together smaller subclasses. This is apparent in *Chan-Seng-Yue et al* which identified two basal and two classical subtypes, along with a hybrid type: Basal-like-A, Basal-like-B, Hybrid, Classical-A and Classical-B. They were able to correlate their subtype classification with stage of disease and found that Classical A/B were more prevalent in early-stage disease (Stage I/II), Basal-like B was found in resectable and locally advanced tumors while Basal-like A was predominantly found in late stage/metastatic disease and accounts for almost a quarter of Stage

IV disease[57]. Even though most PDA tumors are heterogeneous in subtype and consist of some basal regions and some classical regions, tumors with Basal-like A classification presented with the worst overall survival likely in conjunction with them being highly chemoresistant[57]. Therefore, it is important to note that even though basal and classical are the generally accepted subtype classifications, not all basal PDA tumors are the same and that stage of tumor could indicate the basal subclass and inform therapeutic options for the patient.

1.4 Therapies and treatments for pancreatic ductal adenocarcinoma patients

1.4.1 Standard of care chemotherapy treatment

As mentioned earlier, very few patients receive surgical intervention as most PDA patients are not diagnosed until the disease has already progressed to the later stages. This results in chemotherapy being the main source of treatment for many PDA patients. Patients with PDA tumors are typically given Gemcitabine sometimes in combination with albumin-bound (Nab) Paclitaxel or the multi-drug regimen FOLFIRINOX (5-Fluorouracil, Leucovorin, Irinotecan, and Oxaliplatin)[9]. Gemcitabine is the most widely used drug for management of PDA as curative cases are rare. It is a nucleoside analog that enters cells through the SLC nucleoside transporters and is metabolized into dFdC triphosphate which incorporates into genomic DNA preventing DNA synthesis and repair thereby driving apoptosis in cancer cells[59]. Unfortunately, Gemcitabine treatment as a monotherapy or in combination with other drugs only has a modest impact on patient survival and almost all tumors will develop some level of Gemcitabine resistance[60].

Although the multi-drug regimen FOLFIRINOX (5-Fluorouracil, Leucovorin, Irinotecan, and Oxaliplatin) has shown improvement in patient survival over Gemcitabine in PDA patients,

it has also been associated with more adverse effects and therefore not all PDA patients can tolerate it[61,62]. 5-Fluorouracil has shown strong anti-neoplastic effects in a variety of cancer types, including pancreatic cancer, leading to its incorporation into the FOLFIRINOX regimen. Additionally, 5-Fluorouracil is metabolized upon cellular entry and can then inhibit multiple cellular complexes including RNA Polymerase[9]. Irinotecan is a topoisomerase inhibitor which primarily inhibits DNA synthesis in the S phase of the cell cycle. Irinotecan alone showed little anti-tumor activity but was further paired with 5-Fluorouracil which improved response rates and lead to its approval for metastatic PDA in 2013[63]. Oxaliplatin is a platinum-based agent that alone showed anti-tumor activity but no survival benefit in solid tumor patients so was not approved until it was studied in combination with 5-Fluorouracil and Irinotecan[64]. Oxaliplatin was eventually approved for treatment of metastatic PDA and is used as part of the FOLFIRINOX regimen.

These standard of care treatment regimens have changed little in the last few decades even though there has been a plethora of research into developing new therapies for PDA.

1.4.2 Subtype specific response to therapies

PDA subtype classification was key to better understanding current and future therapies for PDA patients. Given that patient tumors are genetically very similar, patients responding differently to therapy was an early indicator that determining specific PDA subtypes that could explain intra- and inter tumoral heterogeneity would be necessary for determining better treatment options for patients. Upon identification of the basal and classical PDA subtypes, multiple studies assess the effect of standard of care chemotherapy on patient tumors subtyped by GATA6 expression which has been shown to be high in more classical tumors and lower in

basal tumors. These studies found that different combinations of the chemotherapies: Gemcitabine, Nab-Paclitaxel, FOLFIRINOX, or sub combinations of the FOLFIRINOX regimen, showed better response and more favorable clinical outcomes in patients with high GATA6 tumors (classical) and lower responses and poorer outcomes in patients with low GATA6 tumors (basal)[65,66]. These studies provided early indications that specific markers of the PDA subtype linages could predict therapeutic response. Unfortunately, many candidate markers show mixed expression in tumor tissue and therefore cannot provide a clear-cut subtype classification. So, *Nicolle et al* developed a transcriptome-based molecular signature that uses a gradient system of PDA subtyping to predict therapeutic response. They were able to validate their model with FOLFIRINOX and showed that the more aggressive (basal) tumor responded less to FOLFIRINOX[67].

Not only can PDA subtypes predict response to treatment, but recent studies have also shown that certain treatments may alter PDA subtypes. These studies have used a combination of transcriptomic data from PDA patient tumors as well as PDA cell lines to study the cellular changes that occur upon chemotherapy treatment and how they related to subtype identity. They found that FOLFIRINOX treatment can promote a more phenotypically basal tumor[68,69]. Through assessment of differentially expressed genes in malignant cells with or without treatment of FOLFIRINOX, *Hwang et al* identified enrichment of basal subtype markers including TP63, a known master regulator of the basal subtype, and deenrichment of classical subtype markers including GATA6[68]. *Porter et al* discovered that FOLFIRINOX treatment can promote a shift in EMT for both classical and basal cells meaning the drug regimen drives all tumors cells towards a more basal state[69]. These studies highlight that transcriptional plastically within PDA tumors plays an immense role in how these tumors respond to therapeutic

intervention. Understanding these changes will enable development of new subtype specific therapies and new combination therapies designed to target subtype alterations within a patient tumor.

1.4.3 Transcriptional inhibitors

As described in section 1.3, PDA tumors contain well-defined transcriptional and epigenetic regulatory networks that maintain the specific cell state of each subtype. As mentioned in the previous section, these subtypes can be classified by the expression of specific transcription factors, such as TP63 for basal and GATA6 for classical. Changes to the expression of these subtype specific factors have been correlated with a shift in PDA subtype, indicating that transcriptional regulation and chromatin state is vital for the maintenance of each PDA subtype cell state. Therefore, as part of this thesis, we hypothesize that transcriptional inhibition may lead to lethal disruption of PDA subtype cell states and drive tumor regression potentially in a subtype specific manner. Therefore, we propose inhibition of transcription as new potentially subtype specific therapy for PDA patients.

Transcriptional inhibitors can be broken down into by the RNA polymerase they impact. Here we will focus on inhibitors of RNA polymerase II as RNA Polymerase I predominantly transcribes ribosomal DNA and RNA Polymerase III predominantly transcribes tRNAs. A few types of RNA Polymerase II inhibitors are bromodomain inhibitors and cyclin dependent kinase inhibitors. Bromodomain inhibitors function to block bromodomain proteins ability to “read” acetyl marks and recruit chromatin modifiers that regulate gene transcription[70]. Cyclin dependent kinase inhibitors are the newest class of transcriptional inhibitors and will be the main focus of transcriptional inhibitors in this thesis[71].

1.4.3.1 Background on cyclin-dependent kinase function in transcription

Cyclin-dependent kinases (CDKs) can be classified into two groups: those that regulate cell cycle (CDK1, 2, 4, & 6) and those that regulate transcription (CDK8, 9, 12, 13, 19). Most are selective to one group except for CDK7 which serves as a CDK-activating kinase for cell cycle control but is also a main transcriptional regulating CDK[72]. CDK7 was one of the first CDKs discovered to facilitate RNA Polymerase II (RNA POL II) transcription. CDK7 is a subunit of TFIIH, which is from the transcription factor II (TFII) family of proteins, and identified as the kinase that phosphorylates the C-terminal Domain (CTD) of RNA POL II[73,74]. Later research determined that CDK7 is not the only kinase that phosphorylates the CTD of RNA POL II. CDK7 is the predominant kinase responsible for phosphorylation of Ser7 on the CTD while both CDK7 and CDK9 are responsible for phosphorylation of Ser5 on the CTD and CDK9 phosphorylates Ser2 on the CTD[75,76]. However, CDK12 and CDK13 can also phosphorylate Ser2, 5, and 7 on the CTD increasing the complexity and redundancy of RNA POL II transcriptional control[77,78]. Phosphorylation of the CTD of RNA POL II is not only important for the initiation of transcription but is also important for every step of the transcription cycle from initiation to termination. The stages of the cycle rely predominantly on transcriptional CDKs as follows: Initiation – CDK7 and CDK9; Pausing – CDK7; Elongation – CDK8, 9 & 12; RNA processing – CDK12 and CDK13; Termination – CDK9 and CDK12[72]. CDK7 also plays a minor role in elongation and termination through its regulation and phosphorylation of CDK9[72,79]. Given their prominent roles in regulation of RNA POL II transcription, it is unsurprising that deletion or loss of CDK7 and CDK9 can affect a plethora of cellular processes making them exciting therapeutic targets.

1.4.3.2 Discovery and development of CDK7 inhibitors

Flavopiridol is a clinically approved CDK9 inhibitor used in cancer therapy while CDK7 inhibitors for cancer therapy have been a much more recent development. Nathanael Gray's group has taken on the task of discovering pure and selective inhibitors of CDK7. They identified THZ1 as a candidate CDK7 inhibitor given its disruption of cell proliferation and biochemical CDK7 activity at low doses[80]. THZ1 bonds irreversibly to Cys312 (C312) on CDK7 which is located outside of the kinase domain of CDK7. Because of the location of C312, which traverses the ATP cleft of the kinase domain, THZ1 can covalently bind to C312 and dock in the ATP binding domain of CDK7, thereby blocking CDK7 kinase activity[80]. THZ1 is unlike other CDK inhibitors which are mostly non-covalent ATP competitive inhibitors like flavopiridol. ATP competitive inhibitors bind in place of ATP with the intention of flooding the system with more drugs than ATP so that the drug out-competes binding of ATP to the ATP binding pocket[81]. These types of inhibitors will eventually unbind from the ATP binding pocket enabling ATP to replace it meaning that higher doses of the drug may be necessary to maintain the desired effect. Since THZ1 is covalently bound to CDK7, it does not have this problem and theoretically, could indefinitely inhibit CDK7 or until a new mutation enables resistance to the drug.

Even though treatment of cells with THZ1 predominantly inhibits CDK7, THZ1 can also inhibit CDK12 and CDK13[80]. Since CDK12 and CDK13 are also involved in phosphorylation of the CTD of RNA POLII and therefore necessary for productive transcription[82], THZ1 still has a very strong impact on transcription despite its lack of CDK7 specificity. Additionally, Nathanael Gray's lab developed a selective CDK12 and CDK13 inhibitor (THZ531) which enables a comparison of effects imparted by CDK12 and CDK13 inhibition versus those imparted by the

addition of CDK7 inhibition[83]. THZ531 is also a covalent inhibitor but binds to a different cystine residue (Cys1039) to be specific to CDK12 and CDK13 but does not inhibit CDK7 or CDK9. THZ531 is able to bind to Cys1039 and still block the ATP binding pocket on CDK12 and CDK13 due to their slightly different structures[83]. To compare the impact of THZ1 versus THZ531 on mammalian cells, they treated Jurkat cells (an immortalized human T lymphocyte cell line) with different doses of THZ531 and compared to THZ1. They found that THZ531 selectively reduces phosphorylation of Ser2 on the CTD of RNA POL II versus THZ1 which reduces phosphorylation of Ser 2, 5 and 7 on the CTD of RNA POL II[83]. This indicates that THZ531 treatment inhibits transcriptional elongation over transcriptional initiation.

Further investigation into these inhibitors of transcriptional CDK7 lead to the development of a pure, covalent CDK7 inhibitor, YKL-5-124. This drug is structurally distinct from THZ1 but still binds the same Cys312 residue on CDK7 and blocks the ATP binding pocket, inhibiting CDK7 kinase activity[84]. Given that YKL-5-124 is structured differently than THZ1, it is unsurprising that its effect on cells would be slightly different. Initial studies showed that YKL-5-124 has a more dramatic inhibitory effect on the cell cycle than on transcription through its inhibition of CDK7[84]. This different inhibitory effect could be cell type specific and therefore needs to be further investigated in different contexts.

There are a few CDK7 inhibitors that are now clinically approved though they are a bit different from the inhibitors described above. SY5609 is a highly selective, orally bioavailable CDK7 inhibitor. SY5609 non-covalently binds to CDK7 and interacts with Met94 in the ATP binding pocket of CDK7[85]. Early assessments showed potent inhibition of CDK7 by SY5609 in cells, mice, and cancer patients[85,86]. Samuraciclib (ICEC0942) is also a non-covalent, oral, clinically approved CDK7 inhibitor with high selectivity and affinity for CDK7 over other

CDKs[87]. The first in human, modular study of samuraciclib demonstrated an acceptable safety profile and evidence of antitumor activity in patients with advanced solid tumors[88].

1.4.3.3 Transcriptional inhibitors in cancer treatment

Transcriptional inhibitors have been assessed for therapeutic potential in many different cancers. Early studies of flavopiridol in HeLa cells showed that it potently inhibits CDK9 leading to reduced RNA Pol II transcription[89]. Other studies showed that CDK9 inhibition has potent anti-tumor activity in Leukemia[90,91]. Flavopiridol later became the first CDK inhibitor to enter clinical trials[92]. Over the past few decades, new versions of flavopiridol as well as many other CDK9 inhibitors have been developed and are now entering the clinic[93]. CDK9 inhibitors have shown preclinical efficacy in many different cancer types including breast[94–96], lung[97–99], ovarian[95,100] and colon/colorectal cancers[95,101]. One such study showed that CDK9 inhibition can lead to reactivation of tumor suppressor genes and can be paired with immunotherapy for an enhanced anti-tumor effect[95].

The role of THZ1 anti-tumor activity have been extensively studied from the specifics of how CDK7 inhibition block RNA POL II capping and pausing[102] to CDK7 inhibition disrupting tumor growth of transcriptionally addicted triple-negative breast cancer[103,104]. CDK7 inhibition by THZ1 also showed promise as a therapeutic strategy against glioblastomas[105], small cell lung cancer[106], and MYC-driven cancers through the suppression of oncogene super enhancers[107]. YKL-5-124 treatment in small cell lung cancer has shown that selective CDK7 inhibition dramatically impairs cell cycle progression and DNA replication. They also found that combination of YKL-5-124 and anti-PD1 treatment clearly reduces tumor growth in mouse

models of small cell lung cancer[108]. Despite the clear anti-tumor activity of THZ1 and YKL-5-124, these CDK7 inhibitors never made it to the clinic.

Clinical versions of CDK7 inhibitors were developed and have shown promising potential in preclinical studies and early clinical trials. Samuraciclib has shown potent therapeutic potential in vitro and in vivo models of AML[109], prostate[110], lung[111], and breast[111–113] cancer. Samuraciclib entered Phase 1 dose escalation study and showed both an acceptable safety profile and evidence of clinical activity in advanced metastatic triple negative breast cancer and hormone receptor-positive (HR+) and HER2- breast cancer[88,114]. Preclinical studies for SY5609 were performed in breast[115,116], ovarian[116] and colorectal cancer[117] with all solid tumor malignancies showing an anti-tumor response. SY5609 treatment of advanced ER+/HER2− breast cancer patients showed encouraging activity at low doses and with a variety of dosing schedules in the Phase 1 study[118]. Additionally, the Phase1/1b study of SY5609 in patients with advanced solid tumors, including advanced and metastatic PDA, presented an acceptable safety profile and encouraging clinical activity as a single agent and in combination with chemotherapy[86,119]. Together, these studies and clinical trials validate the strong therapeutic potential of CDK7 inhibitors in cancer treatment.

CHAPTER 1: REFERENCES

1. Wendt, A. & Eliasson, L. Pancreatic α-cells – The unsung heroes in islet function. *Semin. Cell Dev. Biol.* **103**, 41–50 (2020).
2. Marchetti, P., Bugliani, M., De Tata, V., Suleiman, M. & Marselli, L. Pancreatic Beta Cell Identity in Humans and the Role of Type 2 Diabetes. *Front. Cell Dev. Biol.* **5**, 55 (2017).
3. Pandol, S. J. *The Exocrine Pancreas*. (Morgan & Claypool Life Sciences, San Rafael (CA), 2010).
4. Neuroendocrine Tumor of the Pancreas - Statistics. *Cancer.Net* https://www.cancer.net/cancer-types/neuroendocrine-tumor-pancreas/statistics (2012).
5. Adamska, A., Domenichini, A. & Falasca, M. Pancreatic Ductal Adenocarcinoma: Current and Evolving Therapies. *Int. J. Mol. Sci.* **18**, 1338 (2017).
6. Rahib, L. *et al.* Projecting Cancer Incidence and Deaths to 2030: The Unexpected Burden of Thyroid, Liver, and Pancreas Cancers in the United States. *Cancer Res.* **74**, 2913–2921 (2014).
7. Maitra, A. & Hruban, R. H. Pancreatic Cancer. *Annu. Rev. Pathol. Mech. Dis.* **3**, 157–188 (2008).
8. Singhi, A. D., Koay, E. J., Chari, S. T. & Maitra, A. Early Detection of Pancreatic Cancer: Opportunities and Challenges. *Gastroenterology* **156**, 2024–2040 (2019).
9. Principe, D. R. *et al.* The Current Treatment Paradigm for Pancreatic Ductal Adenocarcinoma and Barriers to Therapeutic Efficacy. *Front. Oncol.* **11**, 688377 (2021).
10. Bardeesy, N. & DePinho, R. A. Pancreatic cancer biology and genetics. *Nat. Rev. Cancer* **2**, 897–909 (2002).
11. Wang, L., Xie, D. & Wei, D. Pancreatic Acinar-to-Ductal Metaplasia and Pancreatic Cancer. in *Pancreatic Cancer: Methods and Protocols* (ed. Su, G. H.) 299–308 (Springer, New York, NY, 2019). doi:10.1007/978-1-4939-8879-2_26.
12. Storz, P. Acinar cell plasticity and development of pancreatic ductal adenocarcinoma. *Nat. Rev. Gastroenterol. Hepatol.* **14**, 296–304 (2017).
13. Hezel, A. F., Kimmelman, A. C., Stanger, B. Z., Bardeesy, N. & DePinho, R. A. Genetics and biology of pancreatic ductal adenocarcinoma. *Genes Dev.* **20**, 1218–1249 (2006).
14. Xi, T. & Zhang, G. Integrated analysis of tumor differentiation genes in pancreatic adenocarcinoma. *PLoS ONE* **13**, e0193427 (2018).
15. Garcea, G. *et al.* Survival following curative resection for pancreatic ductal adenocarcinoma. A systematic review of the literature. *JOP J. Pancreas* **9**, 99–132 (2008).
16. Gu, G., Dubauskaite, J. & Melton, D. A. Direct evidence for the pancreatic lineage: NGN3+ cells are islet progenitors and are distinct from duct progenitors. *Dev. Camb. Engl.* **129**, 2447–2457 (2002).
17. Hingorani, S. R. *et al.* Preinvasive and invasive ductal pancreatic cancer and its early detection in the mouse. *Cancer Cell* **4**, 437–450 (2003).
18. Aguirre, A. J. *et al.* Activated Kras and Ink4a/Arf deficiency cooperate to produce metastatic pancreatic ductal adenocarcinoma. *Genes Dev.* **17**, 3112–3126 (2003).
19. Hingorani, S. R. *et al.* Trp53R172H and KrasG12D cooperate to promote chromosomal instability and widely metastatic pancreatic ductal adenocarcinoma in mice. *Cancer Cell* **7**, 469–483 (2005).
20. Bierie, B. & Moses, H. L. TGFβ: the molecular Jekyll and Hyde of cancer. *Nat. Rev. Cancer* **6**, 506–520 (2006).

21. Bardeesy, N. *et al.* Smad4 is dispensable for normal pancreas development yet critical in progression and tumor biology of pancreas cancer. *Genes Dev.* **20**, 3130–3146 (2006).
22. Ying, H. *et al.* Genetics and biology of pancreatic ductal adenocarcinoma. *Genes Dev.* **30**, 355–385 (2016).
23. Rothbart, S. B. & Strahl, B. D. Interpreting the language of histone and DNA modifications. *Biochim. Biophys. Acta BBA - Gene Regul. Mech.* **1839**, 627–643 (2014).
24. DesJarlais, R. & Tummino, P. J. Role of Histone-Modifying Enzymes and Their Complexes in Regulation of Chromatin Biology. *Biochemistry* **55**, 1584–1599 (2016).
25. Shain, A. H. *et al.* Convergent structural alterations define SWItch/Sucrose NonFermentable (SWI/SNF) chromatin remodeler as a central tumor suppressive complex in pancreatic cancer. *Proc. Natl. Acad. Sci.* **109**, E252–E259 (2012).
26. Sausen, M. *et al.* Clinical implications of genomic alterations in the tumour and circulation of pancreatic cancer patients. *Nat. Commun.* **6**, 7686 (2015).
27. Biankin, A. V. *et al.* Pancreatic cancer genomes reveal aberrations in axon guidance pathway genes. *Nature* **491**, 399–405 (2012).
28. Waddell, N. *et al.* Whole genomes redefine the mutational landscape of pancreatic cancer. *Nature* **518**, 495–501 (2015).
29. Ijichi, H. *et al.* Aggressive pancreatic ductal adenocarcinoma in mice caused by pancreas-specific blockade of transforming growth factor-β signaling in cooperation with active Kras expression. *Genes Dev.* **20**, 3147–3160 (2006).
30. Pandey, S., Gupta, V. K. & Lavania, S. P. Role of epigenetics in pancreatic ductal adenocarcinoma. *Epigenomics* **15**, 89–110 (2023).
31. Wang, S. C. *et al.* SWI/SNF component ARID1A restrains pancreatic neoplasia formation. *Gut* **68**, 1259–1270 (2019).
32. Livshits, G. *et al.* Arid1a restrains Kras-dependent changes in acinar cell identity. *eLife* **7**, e35216 (2018).
33. Ferri-Borgogno, S. *et al.* Paradoxical Role of AT-rich Interactive Domain 1A in Restraining Pancreatic Carcinogenesis. *Cancers* **12**, 2695 (2020).
34. Shain, A. H. *et al.* Convergent structural alterations define SWItch/Sucrose NonFermentable (SWI/SNF) chromatin remodeler as a central tumor suppressive complex in pancreatic cancer. *Proc. Natl. Acad. Sci.* **109**, E252–E259 (2012).
35. von Figura, G. *et al.* The chromatin regulator Brg1 suppresses formation of intraductal papillary mucinous neoplasm and pancreatic ductal adenocarcinoma. *Nat. Cell Biol.* **16**, 255–267 (2014).
36. Roy, N. *et al.* Brg1 promotes both tumor-suppressive and oncogenic activities at distinct stages of pancreatic cancer formation. *Genes Dev.* **29**, 658–671 (2015).
37. Lan, F. *et al.* A histone H3 lysine 27 demethylase regulates animal posterior development. *Nature* **449**, 689–694 (2007).
38. Andricovich, J. *et al.* Loss of KDM6A Activates Super-Enhancers to Induce Gender-Specific Squamous-like Pancreatic Cancer and Confers Sensitivity to BET Inhibitors. *Cancer Cell* **33**, 512-526.e8 (2018).
39. Kugel, S. & Mostoslavsky, R. Chromatin and beyond: the multitasking roles for SIRT6. *Trends Biochem. Sci.* **39**, 72–81 (2014).
40. Kugel, S. *et al.* Identification of and Molecular Basis for SIRT6 Loss-of-Function Point Mutations in Cancer. *Cell Rep.* **13**, 479–488 (2015).

41. Kugel, S. *et al.* SIRT6 Suppresses Pancreatic Cancer through Control of Lin28b. *Cell* **165**, 1401–1415 (2016).
42. Ecco, G., Imbeault, M. & Trono, D. KRAB zinc finger proteins. *Development* **144**, 2719–2729 (2017).
43. Li, X. *et al.* Structures and biological functions of zinc finger proteins and their roles in hepatocellular carcinoma. *Biomark. Res.* **10**, 2 (2022).
44. Thomas, J. H. & Schneider, S. Coevolution of retroelements and tandem zinc finger genes. *Genome Res.* **21**, 1800–1812 (2011).
45. Shao, Z. *et al.* ZNF655 accelerates progression of pancreatic cancer by promoting the binding of E2F1 and CDK1. *Oncogenesis* **11**, 1–10 (2022).
46. Ogawa, S. *et al.* SETDB1 Inhibits p53-Mediated Apoptosis and Is Required for Formation of Pancreatic Ductal Adenocarcinomas in Mice. *Gastroenterology* **159**, 682-696.e13 (2020).
47. Wu, P.-C. *et al.* H3K9 Histone Methyltransferase, KMT1E/SETDB1, Cooperates with the SMAD2/3 Pathway to Suppress Lung Cancer Metastasis. *Cancer Res.* **74**, 7333–7343 (2014).
48. Du, D. *et al.* Smad3-mediated recruitment of the methyltransferase SETDB1/ESET controls Snail1 expression and epithelial–mesenchymal transition. *EMBO Rep.* **19**, 135–155 (2018).
49. Somerville, T. D. D. *et al.* ZBED2 is an antagonist of interferon regulatory factor 1 and modifies cell identity in pancreatic cancer. *Proc. Natl. Acad. Sci.* **117**, 11471–11482 (2020).
50. Lomberk, G. *et al.* Distinct epigenetic landscapes underlie the pathobiology of pancreatic cancer subtypes. *Nat. Commun.* **9**, 1978 (2018).
51. Lomberk, G., Dusetti, N., Iovanna, J. & Urrutia, R. Emerging epigenomic landscapes of pancreatic cancer in the era of precision medicine. *Nat. Commun.* **10**, 3875 (2019).
52. Collisson, E. A. *et al.* Subtypes of pancreatic ductal adenocarcinoma and their differing responses to therapy. *Nat. Med.* **17**, 500–503 (2011).
53. Moffitt, R. A. *et al.* Virtual microdissection identifies distinct tumor- and stroma-specific subtypes of pancreatic ductal adenocarcinoma. *Nat. Genet.* **47**, 1168–1178 (2015).
54. Bailey, P. *et al.* Genomic analyses identify molecular subtypes of pancreatic cancer. *Nature* **531**, 47–52 (2016).
55. Raphael, B. J. *et al.* Integrated Genomic Characterization of Pancreatic Ductal Adenocarcinoma. *Cancer Cell* **32**, 185-203.e13 (2017).
56. Puleo, F. *et al.* Stratification of Pancreatic Ductal Adenocarcinomas Based on Tumor and Microenvironment Features. *Gastroenterology* **155**, 1999-2013.e3 (2018).
57. Chan-Seng-Yue, M. *et al.* Transcription phenotypes of pancreatic cancer are driven by genomic events during tumor evolution. *Nat. Genet.* **52**, 231–240 (2020).
58. Hayashi, A. *et al.* A unifying paradigm for transcriptional heterogeneity and squamous features in pancreatic ductal adenocarcinoma. *Nat. Cancer* **1**, 59–74 (2020).
59. Smid, K., Van Moorsel, C. J., Noordhuis, P., Voorn, D. A. & Peters, G. J. Interference of gemcitabine triphosphate with the measurements of deoxynucleotides using an optimized DNA polymerase elongation assay. *Int. J. Oncol.* **19**, 157–162 (2001).
60. Von Hoff, D. D. *et al.* Increased Survival in Pancreatic Cancer with nab-Paclitaxel plus Gemcitabine. *N. Engl. J. Med.* **369**, 1691–1703 (2013).
61. Conroy, T. *et al.* FOLFIRINOX or Gemcitabine as Adjuvant Therapy for Pancreatic Cancer. *N. Engl. J. Med.* **379**, 2395–2406 (2018).

62. Conroy, T. *et al.* FOLFIRINOX versus Gemcitabine for Metastatic Pancreatic Cancer. *N. Engl. J. Med.* **364**, 1817–1825 (2011).
63. Thota, R., Pauff, J. M. & Berlin, J. D. Treatment of metastatic pancreatic adenocarcinoma: a review. *Oncol. Williston Park N* **28**, 70–74 (2014).
64. Graham, J., Muhsin, M. & Kirkpatrick, P. Oxaliplatin. *Nat. Rev. Drug Discov.* **3**, 11–12 (2004).
65. Aung, K. L. *et al.* Genomics-Driven Precision Medicine for Advanced Pancreatic Cancer: Early Results from the COMPASS Trial. *Clin. Cancer Res.* **24**, 1344–1354 (2018).
66. Martinelli, P. *et al.* GATA6 regulates EMT and tumour dissemination, and is a marker of response to adjuvant chemotherapy in pancreatic cancer. *Gut* **66**, 1665–1676 (2017).
67. Nicolle, R. *et al.* Establishment of a pancreatic adenocarcinoma molecular gradient (PAMG) that predicts the clinical outcome of pancreatic cancer. *eBioMedicine* **57**, (2020).
68. Hwang, W. L. *et al.* Single-nucleus and spatial transcriptomics of archival pancreatic cancer reveals multi-compartment reprogramming after neoadjuvant treatment. 2020.08.25.267336 Preprint at https://doi.org/10.1101/2020.08.25.267336 (2020).
69. Porter, R. L. *et al.* Epithelial to mesenchymal plasticity and differential response to therapies in pancreatic ductal adenocarcinoma. *Proc. Natl. Acad. Sci.* **116**, 26835–26845 (2019).
70. Pérez-Salvia, M. & Esteller, M. Bromodomain inhibitors and cancer therapy: From structures to applications. *Epigenetics* **12**, 323–339 (2017).
71. Laham-Karam, N., Pinto, G. P., Poso, A. & Kokkonen, P. Transcription and Translation Inhibitors in Cancer Treatment. *Front. Chem.* **8**, (2020).
72. Galbraith, M. D., Bender, H. & Espinosa, J. M. Therapeutic targeting of transcriptional cyclin-dependent kinases. *Transcription* **10**, 118–136 (2018).
73. Roy, R. *et al.* The MO15 cell cycle kinase is associated with the TFIIH transcription-DNA repair factor. *Cell* **79**, 1093–1101 (1994).
74. Jordan, P., Cunha, C. & Carmo-Fonseca, M. The cdk7-cyclin H-MAT1 complex associated with TFIIH is localized in coiled bodies. *Mol. Biol. Cell* **8**, 1207–1217 (1997).
75. Glover-Cutter, K. *et al.* TFIIH-Associated Cdk7 Kinase Functions in Phosphorylation of C-Terminal Domain Ser7 Residues, Promoter-Proximal Pausing, and Termination by RNA Polymerase II. *Mol. Cell. Biol.* **29**, 5455–5464 (2009).
76. Bowman, E. A. & Kelly, W. G. RNA Polymerase II transcription elongation and Pol II CTD Ser2 phosphorylation. *Nucleus* **5**, 224–236 (2014).
77. Greifenberg, A. K. *et al.* Structural and Functional Analysis of the Cdk13/Cyclin K Complex. *Cell Rep.* **14**, 320–331 (2016).
78. Liang, K. *et al.* Characterization of human cyclin-dependent kinase 12 (CDK12) and CDK13 complexes in C-terminal domain phosphorylation, gene transcription, and RNA processing. *Mol. Cell. Biol.* **35**, 928–938 (2015).
79. Fisher, R. P. Cdk7: a kinase at the core of transcription and in the crosshairs of cancer drug discovery. *Transcription* **10**, 47–56 (2018).
80. Kwiatkowski, N. *et al.* Targeting transcription regulation in cancer with a covalent CDK7 inhibitor. *Nature* **511**, 616–620 (2014).
81. Olivieri, C. *et al.* ATP-competitive inhibitors modulate the substrate binding cooperativity of a kinase by altering its conformational entropy. *Sci. Adv.* **8**, eabo0696 (2022).

82. Constantin, T. A., Greenland, K. K., Varela-Carver, A. & Bevan, C. L. Transcription associated cyclin-dependent kinases as therapeutic targets for prostate cancer. *Oncogene* **41**, 3303–3315 (2022).
83. Zhang, T. *et al.* Covalent targeting of remote cysteine residues to develop CDK12 and CDK13 inhibitors. *Nat. Chem. Biol.* **12**, 876–884 (2016).
84. Olson, C. M. *et al.* Development of a Selective CDK7 Covalent Inhibitor Reveals Predominant Cell-Cycle Phenotype. *Cell Chem. Biol.* **26**, 792-803.e10 (2019).
85. Marineau, J. J. *et al.* Discovery of SY-5609: A Selective, Noncovalent Inhibitor of CDK7. *J. Med. Chem.* **65**, 1458–1480 (2022).
86. Sharma, M. *et al.* 518MO Tolerability and preliminary clinical activity of SY-5609, a highly potent and selective oral CDK7 inhibitor, in patients with advanced solid tumors. *Ann. Oncol.* **32**, S587–S588 (2021).
87. Greber, B. J., Remis, J., Ali, S. & Nogales, E. 2.5 Å-resolution structure of human CDK-activating kinase bound to the clinical inhibitor ICEC0942. *Biophys. J.* **120**, 677–686 (2021).
88. Krebs, M. G. *et al.* 230MO First in human, modular study of samuraciclib (CT7001), a first-in-class, oral, selective inhibitor of CDK7, in patients with advanced solid malignancies. *Ann. Oncol.* **32**, S458 (2021).
89. Chao, S.-H. & Price, D. H. Flavopiridol Inactivates P-TEFb and Blocks Most RNA Polymerase II Transcription in Vivo *. *J. Biol. Chem.* **276**, 31793–31799 (2001).
90. Byrd, J. C. *et al.* Flavopiridol administered using a pharmacologically derived schedule is associated with marked clinical efficacy in refractory, genetically high-risk chronic lymphocytic leukemia. *Blood* **109**, 399–404 (2006).
91. Rahaman, M. H. *et al.* CDKI-73: an orally bioavailable and highly efficacious CDK9 inhibitor against acute myeloid leukemia. *Invest. New Drugs* **37**, 625–635 (2019).
92. Schwartz, G. K. *et al.* Phase II Study of the Cyclin-Dependent Kinase Inhibitor Flavopiridol Administered to Patients With Advanced Gastric Carcinoma. *J. Clin. Oncol.* (2016) doi:10.1200/JCO.2001.19.7.1985.
93. Mandal, R., Link to external site, this link will open in a new tab, Becker, S. & Strebhardt, K. Targeting CDK9 for Anti-Cancer Therapeutics. *Cancers* **13**, 2181 (2021).
94. Brisard, D. *et al.* Antineoplastic effects of selective CDK9 inhibition with atuveciclib on cancer stem-like cells in triple-negative breast cancer. *Oncotarget* **9**, 37305–37318 (2018).
95. Zhang, H. *et al.* Targeting CDK9 Reactivates Epigenetically Silenced Genes in Cancer. *Cell* **175**, 1244-1258.e26 (2018).
96. Mustafa, E. H. *et al.* Selective inhibition of CDK9 in triple negative breast cancer. *Oncogene* **43**, 202–215 (2024).
97. Padmanabhan, J. *et al.* Inhibitors Targeting CDK9 Show High Efficacy against Osimertinib and AMG510 Resistant Lung Adenocarcinoma Cells. *Cancers* **13**, 3906 (2021).
98. McCool, J. K., Ashamalla, H., Graves, L. M. & Graves, P. R. Inhibition of CDK9 Enhances Radiation Sensitivity of Non-Small Cell Lung Cancer Cells, Increases PARP Cleavage, and Reduces the Level of Antiapoptotic Proteins. *Int. J. Radiat. Oncol. Biol. Phys.* **93**, E530 (2015).
99. Wu, T. *et al.* Discovery of Selective and Potent Macrocyclic CDK9 Inhibitors for the Treatment of Osimertinib-Resistant Non-Small-Cell Lung Cancer. *J. Med. Chem.* **66**, 15340–15361 (2023).

100. Wang, J., Dean, D. C., Hornicek, F. J., Shi, H. & Duan, Z. Cyclin-dependent kinase 9 (CDK9) is a novel prognostic marker and therapeutic target in ovarian cancer. *FASEB J.* **33**, 5990–6000 (2019).
101. Rahaman, M. H. *et al.* Targeting CDK9 for treatment of colorectal cancer. *Mol. Oncol.* **13**, 2178–2193 (2019).
102. Nilson, K. A. *et al.* THZ1 Reveals Roles for Cdk7 in Co-transcriptional Capping and Pausing. *Mol. Cell* **59**, 576–587 (2015).
103. Wang, Y. *et al.* CDK7-Dependent Transcriptional Addiction in Triple-Negative Breast Cancer. *Cell* **163**, 174–186 (2015).
104. Li, B. *et al.* Therapeutic Rationale to Target Highly Expressed CDK7 Conferring Poor Outcomes in Triple-Negative Breast Cancer. *Cancer Res.* **77**, 3834–3845 (2017).
105. Meng, W. *et al.* CDK7 inhibition is a novel therapeutic strategy against GBM both in vitro and in vivo. *Cancer Manag. Res.* **10**, 5747–5758 (2018).
106. Christensen, C. L. *et al.* Targeting Transcriptional Addictions in Small Cell Lung Cancer with a Covalent CDK7 Inhibitor. *Cancer Cell* **26**, 909–922 (2014).
107. Chipumuro, E. *et al.* CDK7 Inhibition Suppresses Super-Enhancer-Linked Oncogenic Transcription in MYCN-Driven Cancer. *Cell* **159**, 1126–1139 (2014).
108. Zhang, H. *et al.* CDK7 Inhibition Potentiates Genome Instability Triggering Anti-tumor Immunity in Small Cell Lung Cancer. *Cancer Cell* **37**, 37-54.e9 (2020).
109. Clark, K. *et al.* CT7001, a Novel Orally Bio-Available CDK7 Inhibitor, Is Highly Active in in-Vitro and in-Vivo Models of AML. *Blood* **130**, 2645 (2017).
110. Constantin, T. A. *et al.* The CDK7 inhibitor CT7001 (Samuraciclib) targets proliferation pathways to inhibit advanced prostate cancer. *Br. J. Cancer* **128**, 2326–2337 (2023).
111. Ainscow, E. K. *et al.* Abstract 4834: CT7001: An orally bioavailable CDK7 inhibitor is a potential therapy for breast, small-cell lung and haematological cancers. *Cancer Res.* **78**, 4834 (2018).
112. Patel, H. *et al.* ICEC0942, an Orally Bioavailable Selective Inhibitor of CDK7 for Cancer Treatment. *Mol. Cancer Ther.* **17**, 1156–1166 (2018).
113. Bahl, A. *et al.* Abstract P1-09-04: Activity of CT7001 an orally bio-available cyclin-dependent kinase 7 selective inhibitor in models of triple negative breast cancer. *Cancer Res.* **78**, P1-09–04 (2018).
114. Coombes, R. C. *et al.* Dose escalation and expansion cohorts in patients with advanced breast cancer in a Phase I study of the CDK7-inhibitor samuraciclib. *Nat. Commun.* **14**, 4444 (2023).
115. Johannessen, L. H. *et al.* Abstract C091: Preclinical evaluation of PK, PD, and antitumor activity of the oral, non-covalent, potent and highly selective CDK7 inhibitor, SY-5609, provides rationale for clinical development in multiple solid tumor indications. *Mol. Cancer Ther.* **18**, C091 (2019).
116. Hu, S. *et al.* Abstract 4421: SY-5609, an orally available selective CDK7 inhibitor demonstrates broad anti-tumor activity in vivo. *Cancer Res.* **79**, 4421 (2019).
117. Johannessen, L. *et al.* Activity of SY-5609, an oral, noncovalent, potent, and selective CDK7 inhibitor, in preclinical models of colorectal cancer. *J. Clin. Oncol.* **38**, 3585–3585 (2020).
118. Juric, D. *et al.* Tolerability and preliminary activity of the potent, selective, oral CDK7 inhibitor SY-5609 in combination with fulvestrant in patients with advanced hormone receptor-positive (HR+), HER2- breast cancer (BC). *J. Clin. Oncol.* **41**, 3081–3081 (2023).

119. Bashir, B. *et al.* Phase 1/1b study of SY-5609, a selective and potent CDK7 inhibitor, in advanced solid tumors and in 2L/3L pancreatic ductal adenocarcinoma (PDA) in combination with gemcitabine +/- nab-paclitaxel. *J. Clin. Oncol.* **41**, 3080–3080 (2023).

CHAPTER 2: PREFACE

This chapter presents work from a major collaborative effort in the Kugel lab and is published in *Science Translational Medicine*. This manuscript contains three co-first authors: Nithya Kartha, a post-doctoral fellow who started the project investigating the connection between SIRT6 expression and THZ1 sensitivity in subtypes of PDA (2017-2020); Zachary Schrank, a research technician who discovered the role of the integrated stress response in determining THZ1 sensitivity of PDA subtypes (2019-2021); Jessica Gianopulos, a PhD student who took over this project from Nithya and Zachary and completed the manuscript prior to initial submission, who led all of the manuscript revisions (experimental, writing, etc.) including the discovery of a new mechanism for SIRT6 regulation of ATF4, and who completed all writing, editing and formatting tasks to revise the manuscript into the version accepted for publication (2021-2023).

Chapter 2 is adapted with minimal modifications from

Kartha, N.*, Gianopulos, J.*, Schrank, Z.* *et al.* Sirtuin 6 is required for the integrated stress response and resistance to inhibition of transcriptional cyclin-dependent kinases. *Sci. Transl. Med.* **15**, eabn9674 (2023).

* Authors contributed equally to the manuscript

Title: Sirtuin 6 is required for the integrated stress response and resistance to inhibition of transcriptional cyclin-dependent kinases

Authors: Nithya Kartha*[1], Jessica E. Gianopulos*[1,2], Zachary Schrank*[1], Sarah M. Cavender[1], Stephanie Dobersch[1], Bryan D. Kynnap[3], Adrianne Wallace-Povirk[1], Cynthia L. Wladyka[1], Juan F. Santana[4], Jaeseung C. Kim[5], Angela Yu[1], Caroline M. Bridgwater[1,12], Kathrin Fuchs[6], Sarah Dysinger[7], Aaron E. Lampano[1], Faiyaz Notta[5,8], David H. Price[4], Andrew C. Hsieh[1], Sunil R. Hingorani[9,10,11,13], Sita Kugel[1#]

Affiliations:
[1]Human Biology Division, Fred Hutchinson Cancer Center, Seattle, WA, 98109
[2]Program in Molecular and Cellular Biology, University of Washington, Seattle, WA,98105
[3]Physician Assistant Program, University of Iowa, Iowa City, IA, 52242
[4]Department of Biochemistry, University of Iowa, Iowa City, IA, 52242
[5]Princess Margaret Cancer Centre, University Health Network, Toronto, ON, Canada, M5G 2C1
[6]Department of Experimental Medicine, Friedrich-Alexander University Erlangen-Nuremberg, Nuremberg, Germany, 91054
[7]Department of Cell and Molecular Biology, University of Pennsylvania, Philadelphia, PA, 19104
[8]Department of Medical Biophysics, University of Toronto, Toronto, ON, Canada, M5G 1L7
[9]Clinical Research Division, Fred Hutchinson Cancer Center, Seattle, WA, 98109
[10]Public Health Sciences Division, Fred Hutchinson Cancer Center, Seattle, WA, 98109
[11]Division of Medical Oncology, University of Washington School of Medicine, Seattle, WA, 98109
[12]Present address: Department of Pharmacology and Cancer Biology, Duke University, Durham, NC, 27708
[13]Present address: Nancy Armitage Presidential Chair in Pancreatic Cancer Director, Pancreatic Cancer Center of Excellence Fred and Pamela Buffet Cancer Center Professor of Medicine, Division of Hematology/Oncology University of Nebraska Medical Center Omaha, NE, 68198

*Authors contributed equally to the manuscript

[#]Corresponding author. Email: skugel@fredhutch.org

ABSTRACT

Pancreatic ductal adenocarcinoma (PDA) is classified into two key subtypes, classical and basal, with basal PDA predicting worse survival. Using in vitro drug assays, genetic manipulation experiments, and in vivo drug studies in human patient-derived xenografts (PDXs) of PDA, we found that basal PDAs were uniquely sensitive to transcriptional inhibition by targeting cyclin-dependent kinase 7 (CDK7) and CDK9, and this sensitivity was recapitulated in the basal subtype of breast cancer. We showed in cell lines, PDXs, and publicly available patient datasets that basal PDA was characterized by inactivation of the integrated stress response (ISR), which leads to a higher rate of global mRNA translation. Moreover, we identified the histone deacetylase sirtuin 6 (SIRT6) as a critical regulator of a constitutively active ISR. Using expression analysis, polysome sequencing, immunofluorescence, and cycloheximide chase experiments, we found that SIRT6 regulated protein stability by binding activating transcription factor 4 (ATF4) in nuclear speckles and protecting it from proteasomal degradation. In human PDA cell lines and organoids as well as in murine PDA genetically engineered mouse models where SIRT6 was deleted or down-regulated, we demonstrated that SIRT6 loss both defined the basal PDA subtype and led to reduced ATF4 protein stability and a nonfunctional ISR, causing a marked vulnerability to CDK7 and CDK9 inhibitors. Thus, we have uncovered an important mechanism regulating a stress-induced transcriptional program that may be exploited with targeted therapies in particularly aggressive PDA.

INTRODUCTION

Pancreatic ductal adenocarcinoma (PDA) is an extremely lethal disease with a 5-year survival of 11% and is likely to become the second leading cause of cancer-related deaths within a decade (*1*). PDA pathogenesis is characterized by a gradual progression through increasingly dysplastic precursor lesions toward invasive and lastly metastatic PDA (*2*). This progression is paired with the early acquisition of oncogenic KRAS (Kirsten rat sarcoma virus) mutations and the subsequent loss of tumor suppressor genes CDKN2A (p16INK4a) (cyclin-dependent kinase inhibitor 2A), TP53 (transformation-related protein 53) and components of the transforming growth factor β (TGFβ) pathway such as SMAD4 (SMAD Family Member 4), TGFβR1 (transforming growth factor beta receptor 1), and TGFβR2 (transforming growth factor beta receptor 2), each of which is mutated in more than 50% of patients. The creation of genetically engineered mouse models (GEMMs) with different combinations of these genes has faithfully recapitulated the disease and validated their importance in the initiation and progression of PDA (*3, 4*). The various genetic analyses of PDA have led to the same conclusion that PDAs are genetically very similar—both between patients, and between primary and metastatic tumors within the same patient (*5, 6*). However, clinical experience would suggest that pancreatic cancer is much more diverse, given the heterogeneity of responses to chemotherapy and corresponding range of survivals observed.

To understand differences in clinical behavior, transcriptional signatures have been examined from resected tumors, biopsies, patient-derived xenografts (PDXs), organoids and cell lines (*7, 8*). The consensus across several studies is that there are two predominant subtypes of PDA: classical (includes immunogenic, aberrantly differentiated endocrine exocrine (ADEX), classical A, and classical B) and basal (alternatively named and overlaps with quasi-mesenchymal (QM), Squamous, basal A, and basal B), and that the basal subtype confers a poorer overall

prognosis (*7-11*). Basal PDA tends to be poorly differentiated with some exhibiting squamous features, whereas the classical subtype is well differentiated and maintains epithelial characteristics. Basal PDA is defined by a complete loss of endodermal identity (low HNF4A (hepatocyte nuclear factor 4 alpha) and GATA6 (GATA binding protein 6)); acquired expression programs characteristic of squamous tumors, including TGF-β signaling, hypoxia response, metabolic reprogramming, and epithelial to mesenchymal transition (EMT); a reduced dependence on oncogenic KRAS for growth (*8*), higher frequency for inactivation of TP53, CDKN2A (*11*), and chromatin modifiers, including MLL2 (lysine methyltransferase 2D), MLL3 (lysine methyltransferase 2C), and KDM6A (lysine demethylase 6A); MYC (MYC proto-oncogene, bHLH transcription factor) amplification (*6, 12*); and MYC pathway activation (*8*).

The mechanism by which this highly aggressive basal PDA subtype is established remains poorly understood, although recent analysis of the PDA epigenome suggests that epigenetic dysregulation may be involved (*13*). An unbiased characterization of the PDA epigenome can predict PDA subtype and prognosis, which has not been possible with genetics alone (*13, 14*). Sirtuin 6 (SIRT6) is an NAD^+-dependent histone deacetylase that acts as a repressor of MYC-driven transcription and has been implicated in cellular stress resistance, genomic stability, aging, and energy homeostasis (*15, 16*). It acts as a strong tumor suppressor in both human and murine PDA, where SIRT6 inactivation cooperates with oncogenic KRAS to drive a more aggressive and highly metastatic form of disease (*17, 18*).

We show here that basal PDA cells are highly sensitive to transcriptional cyclin-dependent kinase (CDK) inhibition. We demonstrate that SIRT6 defines the classical subtype and regulates activating transcription factor 4 (ATF4), the master regulator of the integrated stress response (ISR). Inhibition of transcriptional CDKs elevates cellular stress catastrophically in basal PDA

cells, whereas this stress can instead be resolved in classical PDA cells. The vulnerability of basal PDA cells to CDK inhibition lies in their inability to activate ATF4 to mitigate cellular stress in the absence of SIRT6.

RESULTS

Low SIRT6 expression correlates with basal state

To establish whether SIRT6 expression correlates with PDA subtype, we first analyzed data generated from a previous large-scale integrated genomic analysis of human PDAs (*8*), which were classified into classical and basal PDA subtypes (Fig. 1A). Because stromal contamination in human tumors may confound such transcriptional analyses, we also looked at a panel of 12 human PDA cell lines classified as either classical or basal PDA by previous groups. All classical PDA cell lines expressed higher amounts of *SIRT6* than any basal PDA cell line (Fig. 1B). Moreover, ectopic expression of wild-type (WT) SIRT6 but not a catalytically inactive mutant (HY) form of SIRT6 reduced RNA and protein expression of the ΔN isoform of TP63, a key biomarker of the basal subtype, in two independent basal PDA lines (fig. S1, A to C).

Basal and classical PDA have unique therapeutic vulnerabilities

SIRT6 acts as a potent co-repressor for the MYC oncogene. SIRT6^{low}/basal human PDA cell lines and *Sirt6* knockout (*Sirt6* KO) cell lines derived from PDA GEMMs demonstrated elevated amounts of chromatin-bound MYC and a dependency on MYC expression for growth and survival (*17*). Studies have shown that the CDK7 inhibitor THZ1 can selectively target super-enhancer (SE)-regulated genes such as MYC in some cancers. Unlike most kinase inhibitors, THZ1 binds to an allosteric site on CDK7, CDK12 and CDK13 rather than its adenosine triphosphate (ATP)-

binding pocket, thereby affording high specificity with few off-target effects at clinically relevant doses (*19*). It should be noted that inhibition of CDK12 and CDK13 occurred at slightly higher concentrations when compared to CDK7 (*20*). THZ1 has recently been shown to markedly inhibit tumor cell growth in multiple cancer types (*13, 19, 21-24*). In these studies, THZ1 was found to achieve its anti-proliferative effect through selective inhibition of target genes driven by SEs, which normally function to amplify lineage-specific transcription factors in these cancers (*25*). SEs are areas within the genome typically marked by H3K27ac (histone H3 acetylated at lysine-27), H3K9ac (histone H3 acetylated at lysine-9), and H3K4me1 (histone H3 monomethylated at lysine-4) and occupied by paused RNA polymerase II (RNAPII) (*26, 27*). CDK7 functions as a known regulator of RNAPII-mediated initiation, pause establishment, and elongation through the direct phosphorylation of the RNAPII C-terminal domain (CTD) (*19*). Thus, it has been suggested that CDK7 inhibition by THZ1 leads to reduced occupancy of RNAPII within SEs (*28*).

To evaluate the potential efficacy of THZ1 in basal PDA, we treated a panel of seven human basal PDA cell lines with THZ1 and compared their sensitivity to five human classical PDA lines (Fig. 1C). SIRT6^{low}/basal PDA lines were highly sensitive to THZ1, whereas SIRT6^{high}/classical PDA lines were not as sensitive. By contrast, both basal and classical PDA lines were equally sensitive to gemcitabine (Fig. 1D), the standard of care treatment of pancreatic cancer. Moreover, THZ1 sensitivity was inversely correlated with *SIRT6* expression across a broad panel of 22 PDA lines (fig. S1D). Treatment with THZ1 resulted in a similar reduction in phosphorylation of both substrates of CDK7 within the RNAPII CTD, referred to as phospho-serine 5 (PS5) and PS7, as well as the transition to productive elongation marker PS2, in both basal and classical PDA lines (Fig. 1E). MYC protein was greatly reduced in both cell subtypes. However, activation of the apoptotic marker cleaved caspase-3 was observed as early as 16 hours after treatment with THZ1

at 500nM in basal PDA lines, whereas no activation of cleaved caspase-3 was seen in classical PDA lines even at doses 10-fold higher. Consistent with these results, annexin V staining was markedly increased after 24 hours of treatment with 100nM THZ1 in basal but not classical PDA cell lines (Fig. 1F and fig. S1E). Propidium iodide staining revealed an accumulation of basal PDA cells in G2/M phase after 24 hours of treatment with 100nM THZ1, suggesting a G2/M arrest, as previously observed in neuroblastoma (*13*). No effects on cell cycle were observed in classical PDA cell lines (Fig. 1G and fig. S1F). Moreover, inhibition of SIRT6 using short hairpin RNA (shRNA) sensitized SIRT6^{high}/classical PDA to THZ1 treatment (Fig. 1H) without changing expression of CDK proteins (fig. S1G). Last, both two-dimensional (2D) PDA lines (Fig. 1I) and 3D organoids (Fig. 1, J to L) derived from our *Sirt6* KO GEMM demonstrated marked sensitivity to THZ1, similar to that observed in our human basal PDA cell lines. Thus, reduced amounts of SIRT6 correlate with the basal PDA subtype and can predict THZ1 sensitivity in PDA.

Inhibition of CDK7 but not MYC is both necessary and sufficient for THZ1-induced apoptosis in basal PDA

We next sought to define the specificity of CDK7 inhibition by THZ1 and determine whether CDK7 inhibition was necessary or sufficient for the induction of apoptosis in basal PDA cells. We evaluated the efficacy of THZ1-R, a structural analogue of THZ1 that cannot covalently bind to CDK7 (*19*). As expected, neither basal nor classical PDA cell lines were sensitive to THZ1-R (fig. S2, A and B). We then tested whether ectopic expression of a mutant form of CDK7, CDK7 C312S, which cannot covalently bind THZ1 (*19*), could prevent THZ1 from inducing apoptosis in basal PDA cells and found that expression of CDK7 C312S but not WT CDK7 prevented both cleaved caspase-3 activation and MYC suppression in two independent basal PDA lines (fig. S2, C and D).

Lastly, to specifically assess whether CDK7 inhibition is sufficient for the induction of apoptosis in basal PDA cells, we used CRISPR/Cas9-expressing lentivirus to knock out *CDK7* in two basal and two classical PDA lines. Treatment with two independent single-guide RNA (sgRNAs) against *CDK7*, but not a non-targeting control sgRNA, inhibited cell growth and induced apoptosis in basal but not classical PDA cell lines (fig. S2, E to H). Thus, inhibition of CDK7 is both necessary and sufficient for the efficacy of THZ1 in SIRT6^{low}/basal PDA. Enforced ectopic expression of MYC in three independent basal PDA lines using a doxycycline-inducible promoter restored MYC protein but could not rescue the induction THZ1-mediated apoptosis (fig. S2, I and J). We previously showed SIRT6 inactivation promoted PDA progression and metastasis through upregulation of Lin28b, however Lin28b and let-7 target remained constant upon treatment with THZ1 (fig. S2K). Thus, THZ1-induced apoptosis in basal PDA is not due to transcriptional inhibition of MYC or Lin28b.

SE-regulated genes are not preferentially downregulated by THZ1 in basal PDA

The efficacy of THZ1 at inducing apoptosis in cancer may be through the selective inhibition of SE-regulated genes (including *MYC*). MYC was potently and rapidly downregulated in PDA cells following treatment with THZ1, but this did not appear to be unique to basal PDA cell lines, as we also saw a reduction in MYC expression in classical cell lines (Fig. 1E). We therefore performed a combined RNA sequencing (RNA-seq) and H3K27ac chromatin immunoprecipitation sequencing (ChIP-seq) analysis of basal and classical PDA cells after THZ1 treatment to determine whether SE-regulated genes were indeed selectively targeted. More than 2000 genes were downregulated in both BxPC3 and Panc3.27 (basal) cells by THZ1 and, of these, 1437 were commonly downregulated. However, only 87 genes were downregulated in SUIT2 (classical) cells

after 6 hours of THZ1 treatment (Fig. 2A), and most SE-regulated genes were not downregulated by THZ1 in all three cell lines tested (Fig. 2B). The *MYC* SE itself was not more decorated by H3K27ac in basal PDA compared to classical PDA (Fig. 2, C and D) Instead, both gene ontology (GO) and gene set enrichment analysis (GSEA) demonstrated genes related to transcription were potently and specifically repressed in basal PDA cells after THZ1 exposure (Fig. 2E). To determine if the effects of THZ1 and flavopiridol (an ATP-competitive CDK9 inhibitor) on transcription differed in basal compared to classical PDA, we subjected classical and basal cells to increasing doses of each compound (*19, 28, 29*). Nuclei were isolated and nascent transcripts were extended by the addition of radiolabeled cytidine triphosphate in a nuclear walk-on reaction (*30, 31*) followed by denaturing gel analysis of the labeled transcripts. The signals from transcripts generated by paused Pol II (30 to 70 nucleotides) were quantified. THZ1 treatment, which interferes with pausing, led to nearly identical fold reductions of paused transcripts in both cell types, whereas blocking productive elongation with flavopiridol showed the same result (Fig. 2F). Thus, both basal and classical cells responded similarly to THZ1 and flavopiridol. Altogether our results confirmed a specific dependence on transcription in basal PDA; however, whether this specificity was due to the inhibition of a specific gene program remained unclear.

Basal PDA are sensitive to inhibitors of transcriptional CDKs

To further elucidate the mechanism of action of THZ1 in basal PDA, we extended our evaluation of the efficacy of CDK transcriptional inhibitors to include specific inhibitors for CDK4/6, CDK9, CDK7 and CDK12/13 (*20*) in our panel of PDA cell lines. Basal PDA cell lines were 5- to 10-fold more sensitive to both CDK9 (flavopiridol) (Fig. 3, A and B) and CDK7 (YKL-5-124) (Fig. 3, C and D) inhibition than classical PDA whereas basal and classical PDA were equally sensitive to

the CDK4/6, cell cycle inhibitor palbociclib (Fig. 3E). Basal PDA exhibited only minimal sensitivity to inhibition of CDK12/13 (THZ531) (fig. S3A). Treatment with CDK7, CDK9, and CDK12/13 inhibitors led to reductions in RNAPII phosphorylation marks in both basal and classical lines as well as specific induction of apoptosis as measured by cleaved caspase-3 only in basal PDA lines. MYC protein was reduced similarly between basal and classical PDA lines (Fig. 3, B and D, S3B). To determine if basal PDA was more sensitive to transcriptional inhibitors in general, we assessed the efficacy of bromodomain inhibitors, a class of non-CDK-targeting transcriptional inhibitors. Our panel of PDA cell lines showed equivalent sensitivity to bromodomain inhibition with JQ1, I-BET151, and I-BET762 (fig. S3C). These data indicated the differential sensitivity between PDA subtypes is selective for inhibitors of transcriptional CDKs. To further investigate this, we utilized CRISPR/Cas9-expressing lentivirus to knockout *CDK9*, *CDK12* or *CDK13* in two basal and two classical PDA lines. Treatment with two independent sgRNAs against *CDK9*, but not a non-targeting control sgRNA, inhibited cell growth significantly more in basal PDA cell lines (p-value = 0.0025 and 0.00013) compared to classical (p-value = 0.118 and 0.036) (fig. S3, D to F). KO of *CDK12* only minimally reduced growth in basal lines compared to classical, whereas *CDK13* KO induced no change in growth in both basal and classical PDA cell lines (fig. S3, G to L). Together, these data support that basal PDA is selectively more vulnerable to loss of CDK7 and CDK9 function rather than loss of CDK12 and CDK13 function. Considering the structural and functional differences between CDK7 and CDK9, our data demonstrates a multifaceted dependency on CDK-regulated transcription in basal PDA that is not due to a specific CDK7-regulated pathway or gene program. Instead, our results uncovered a therapeutic vulnerability specifically in the basal but not the classical PDA subtype and prompted us to further explore the mechanistic basis for this 'transcriptional CDK addiction.'

SIRT6 regulates the ISR in PDA

We next examined whether mRNA translation rates were different between basal and classical PDA. Global de novo protein synthesis was markedly different as measured by puromycin incorporation (Fig. 4A) (*32*). We observed that basal PDA cells had increased translation compared to classical PDA cells. Furthermore, treatment with THZ1 markedly inhibited translation in basal PDA but had no impact in classical PDA (Fig. 4B). Lastly, basal cells were more sensitive to the translation inhibitor puromycin and homoharringtonine (HHT), confirming their greater reliance on mRNA translation (fig. S4A).

A variety of inputs regulate global translation in both healthy and cancer cells, many of which converge upon the integrated stress response (ISR). Activation of the ISR occurs when eukaryotic translation initiation factor 2 (eIF2α) is phosphorylated at serine-51. EIF2α phosphorylation causes transient but marked attenuation of global protein synthesis, with the exception of select transcription factors, such as ATF4. Serving as an integration point for the ISR, ATF4 helps to orchestrate the cell's response to the perturbing stress by activating transcription of genes necessary for either stress reduction or apoptosis. In turn, the ISR can be rapidly deactivated through the dephosphorylation of eIF2α by a complex of growth arrest and DNA damage-inducible protein (GADD34) and protein phosphatase 1 (PP1). Thus, the ISR is a reversible mechanism through which cells can markedly reduce global translation to survive a wide variety of stresses.

We interrogated the ISR in a panel of basal and classical PDA cell lines. Virtually all classical PDA lines had high baseline activation of the ISR, as measured by high ATF4 expression and phosphorylation of eIF2α, which correlated with low overall translation rates. Conversely, all

basal PDA lines had low baseline activation of the ISR coupled with relatively high translation rates (Fig. 4, A and C). We further sought to validate these finding using publicly available data from human PDA tumors. Given that ATF4 is principally translationally regulated, and publicly available *ATF4* expression data shows no differential expression between subtypes in PDA, we opted to examine expression of ATF4 target genes within the publicly available data sets as a proxy for ISR activation. We found that genes activated by ATF4 were significantly upregulated (p-values $< 2.7x10^{-8}$) in classical PDA compared to basal PDA according to four published PDA transcriptional subtyping classifications. The inverse was also found to be true; genes repressed by ATF4 were significantly upregulated (p-values $< 1.5x10^{-5}$) in basal PDA compared to classical PDA by the same classifications (Fig. 4, D and E). We next sought to understand how classical lines maintained activation of the ISR, whereas it remained silent in basal lines. As noted, SIRT6 has been implicated, albeit indirectly, in distinct cellular responses to other stressors such as hypoxia and oxidative stress (*33*). SIRT6 has also been shown to bind ATF4, which prompted us to investigate its role in regulating ATF4 and/or function in PDA cells (*34*). We discovered that in classical PDA cells, loss of SIRT6 led to a decrease in overall ATF4 protein abundance (Fig. 4F and S4B), and a decrease in amount of ATF4 bound to chromatin (fig. S4C). In addition, loss of SIRT6 in classical PDA cells reduced expression of ATF4 target gene transcripts and proteins, including *GADD34* (protein phosphatase 1 regulatory subunit 15A), *CHOP* (DNA damage inducible transcript 3), *ASNS* (asparagine synthetase), *Sestrin 2* (SESN2) and the amino acid transporters *SLC7A11* (solute carrier family 7 member 11), *SLC6A9* (solute carrier family 6 member 9), and *CD98hc* (CD98 heavy chain) (Fig. 4, F and G). *SIRT6* KO cells from our PDA GEMMs also demonstrated the same effect (fig. S4, D and E). These targets suggested that SIRT6 regulates ATF4 target genes specifically involved in amino acid deprivation and not oxidative

stress or autophagy (fig. S4F). Conversely, ectopic expression of WT SIRT6, but not the catalytic mutant SIRT6 HY, in basal PDA cells robustly increased ATF4 target gene expression, suggesting that SIRT6 deacetylase activity was necessary for its regulation of ATF4-mediated transcription (fig. S4G). The essential role for SIRT6 in increasing ATF4, and as an adaptive response, became apparent in basal cells that are prevented from increasing SIRT6 in response to stress. In both KP4 and 8988T cells, tunicamycin treatment of the siCTRL causes an increase in expression of *SIRT6*, *ATF4*, and ATF4 target genes. Tunicamycin is a known inducer of ATF4 (*35*) which in our basal model also increased *SIRT6* thereby enabling *ATF4* induction. Knockdown of SIRT6 renders basal PDA cells incapable of fully inducing *ATF4* and ATF4 target genes in response to tunicamycin [which elevates endoplasmic reticulum (ER) stress by inhibiting N-linked glycosylation] (*36*). In addition, the already low amounts of *ATF4* in basal cells are further reduced by knockdown of residual *SIRT6* (Fig. 4H). Together, these data validate the necessity of SIRT6 for complete induction of ATF4.

SIRT6 regulates ATF4 stability

To investigate the principal mechanism by which SIRT6 regulates ATF4, we performed a time course of ATF4 expression dynamics by measuring mRNA and protein abundance upon SIRT6 knockdown. We found that ATF4 protein was reduced after 48 hours of SIRT6 knockdown, but changes in *ATF4* mRNA did not occur until 72 hours (Fig. 5, A and B). Because ATF4 is predominantly translationally regulated and our data showed that ATF4 protein changes occur before mRNA changes with SIRT6 knockdown, we decided to investigate if SIRT6 regulates ATF4 protein translation. To do this, we performed polysome profiling on classical cells with and without SIRT6 knockdown. Polysome profiling uses cycloheximide to block protein synthesis and freeze

the ribosomes on the mRNA transcripts, enabling assessment of a transcript bound at different stages of ribosome assembly and translation. A sucrose gradient and ultracentrifugation are used to separate the monosomes from polysomes and abundance is measured by absorption. We discovered no change in global translation as indicated by similar polysome traces between control and SIRT6 knockdown even with reduction in *SIRT6* mRNA abundance verified by quantitative reverse transcription polymerase chain reaction (qRT-PCR) (fig. S5, A and B). *ATF4* mRNA abundance showed no difference in amount of transcript bound to ribosomes in each fraction (fig. S5C), as well as no change in amount of cumulative *ATF4* mRNA in monosomes or polysomes (fig. S5D) with SIRT6 knockdown as measured by qRT-PCR. Lastly, SIRT6 knockdown and ATF4 protein reduction were verified in our classical cells through paired Western blots (fig. S5E). Therefore, we concluded from these data that ATF4 protein translation is not substantially affected by SIRT6.

mTOR (mammalian target of rapamycin) is known to activate ATF4 through a mechanism distinct from its canonical induction by the ISR, which prompted us to examine this in the context of SIRT6 (*35*). We performed SIRT6 knockdown in two classical PDA cell lines and accessed mTOR pathway components. Loss of SIRT6 resulted in clear ATF4 reduction but no change in expression or phosphorylation of mTOR and its pathway components (fig. S5F). Therefore, we concluded the mTOR pathway is not integral to SIRT6 regulation of ATF4.

To determine if SIRT6 regulated ATF4 protein degradation, we treated classical cells with a proteosome inhibitor (MG132) and observed accumulation of ATF4 protein to be comparable regardless of SIRT6 status (Fig. 5C), indicating that the proteosome is involved in SIRT6 regulation of ATF4. In addition, treating classical cells with cycloheximide to block protein synthesis caused ATF4 protein abundance to decline at a significantly faster rate (p-values <0.05)

with SIRT6 knockdown (Fig. 5D). Conversely, restoration of SIRT6 in basal cells and treating with cycloheximide caused ATF4 protein abundance to decline at a slower rate as compared to the empty vector control (Fig. 5E), confirming that SIRT6 stabilizes ATF4 protein.

To determine if ATF4 instability is a general feature of basal PDA given its low SIRT6 status, we treated four basal and classical PDA cell lines with cycloheximide to observe ATF4 protein stability at baseline. We found that ATF4 protein degraded at a significantly faster rate (p-value < 0.05) in the basal cell lines than in the classical cell lines (Fig. 5F), validating that SIRT6 protein expression dictates ATF4 protein stability. Moreover, we sought to determine if ATF4 was targeted for degradation by β-TRCP (beta-transducin repeat containing E3 ubiquitin protein ligase), the receptor component of the E3 ubiquitin ligase previously shown to bind and target ATF4 for proteosome degradation (*37*). We knocked down β-TRCP in the absence of SIRT6 and achieved a partial rescue of ATF4 protein abundance (Fig. 5G). Therefore, we concluded that SIRT6 control of ATF4 protein stability is protective against β-TRCP mediated proteasome degradation and explains the differential ATF4 protein amounts in basal and classical PDA.

To further investigate how SIRT6 stabilizes ATF4, we performed co-immunoprecipitation to assess direct binding of SIRT6 and ATF4. ATF4 was pulled down in either a basal cell line expressing SIRT6 or an empty vector control. SIRT6 was shown to specifically bind to ATF4 with no non-specific binding in the empty vector or isotope control (Fig. 5H). Next, immunofluorescence was performed to determine if ATF4 localization changed upon stabilization by SIRT6. Individual overexpression of only *SIRT6* or only *ATF4* in a basal line showed diffuse localization of each protein throughout the nucleus (Fig. 5I). However, when SIRT6 and *ATF4* were both overexpressed in the same cell we saw a marked change in ATF4 localization to a distinct speckling pattern within the nucleus (Fig. 5J). To identify if this speckling pattern was protective

against degradation of ATF4, we overexpressed *ATF4* plus an empty vector control or *ATF4* plus *SIRT6* in the same basal line and treated with cycloheximide. As expected, ATF4 staining showed rapid degradation with cycloheximide treatment in the absence of SIRT6. Conversely, in the presence of SIRT6 we saw stabilization of ATF4 as well as maintenance of the speckling pattern throughout cycloheximide treatment (Fig. 5K).

Previous work has identified that stabilization of ATF4 occurs when ATF4 is localized to nuclear speckles (*38*). To determine if SIRT6 induced ATF4 localization to nuclear speckles in PDA, we performed the same overexpression experiment as in Figure 5K and stained for nuclear speckles with the SC35 antibody. In the absence of SIRT6, there was no colocalization of ATF4 and the SC35 nuclear speckles marker; however, the addition of SIRT6 induced colocalization of ATF4 and SC35 as well as maintained this colocalization with cycloheximide treatment (fig. S5G). Moreover, SIRT6 co-localized to these speckles with ATF4 while maintaining localization in other regions of the nucleus (fig. S5H). Lastly, endogenous staining of ATF4 in SIRT6^{high}/classical lines showed a similar speckling pattern to the *ATF4* and *SIRT6* overexpression in a SIRT6^{low} line (Fig. 5L). For comparison, the SIRT6^{low}/basal line showed no endogenous ATF4 staining (Fig. 5L). Together, these data indicated that SIRT6 stabilizes ATF4 through binding and directing ATF4 to nuclear speckles, which protects ATF4 from degradation by the proteosome. This protection of ATF4 by SIRT6 thereby enables transcriptional activation of ATF4-target genes and control of the ISR.

Inability to induce ISR confers sensitivity to transcriptional inhibition

To determine whether ISR activation could protect basal cells from transcriptional CDK inhibition, we altered GADD34 expression in both basal and classical PDA cell lines. Knockdown of

GADD34 was used to induce activation of the ISR by keeping eIF2a phosphorylated. GADD34 knockdown both increased p-eIF2α between DMSO (Dimethyl sulfoxide) siCNTL and DMSO siGADD34 and significantly reduced sensitivity to THZ1 (p-values < 0.04) as shown by loss of cleaved caspase-3 activation and reduced annexin/propidium iodide staining in two independent basal PDA cell lines (Fig. 6A, fig.S6A). Conversely, preventing activation of the ISR in classical PDA cells by overexpression of GADD34 resulted in both reduced p-eIF2α and significantly higher amounts of apoptosis in response to THZ1 (p-values < 0.03) (Fig. 6B and fig. S6B). Similarly, knockdown of ATF4 sensitized classical PDA cells to THZ1 (Fig. 6C). Thus, our results suggested that the inability to launch the ISR in basal PDA cells renders them sensitive to transcriptional inhibition, whereas a constitutively active ISR in classical PDA lines confers resistance.

To test this hypothesis, we treated a panel of three classical and three basal PDA cell lines with increasing doses of either THZ1 or flavopiridol and monitored for the expression of ISR markers, ATF4 and p-eIF2α, as well as the induction of apoptosis (Fig. 6, D and E). All six cell lines were able to induce phosphorylation of eIF2α whereas only the basal lines suppressed global mRNA translation upon drug treatment (Figs. 6F and 4B). However, induction of the ISR remained incomplete in the SIRT6^{low}/basal PDA lines because none were able to express ATF4 (Fig. 6, D to F). In contrast, tunicamycin was able to induce the expression of both *ATF4* and its target gene *CHOP* in all basal PDA lines tested (Fig. 6G and Fig. 4, I and J), a response not seen when these cells were treated with either THZ1 or flavopiridol (Fig. 6G). Moreover, silencing of SIRT6 in SIRT6^{high}/classical PDA reduced baseline expression of ATF4 to basal PDA amounts. These cells behaved similarly to basal PDA cells in the presence of THZ1, where p-eIF2α was increased but

ATF4 and many ATF4-target genes were not able to be induced thus sensitizing classical lines to THZ1 treatment (Fig. 6H).

Lastly, we asked whether the key biological differences in stress response between the more aggressive, mesenchymal-like basal subtype and the less aggressive, epithelial-like classical subtype may extrapolate to other cancers with similar subtype classifications. The basal subtype of PDA was classified as such because of overlap in transcriptional signatures with basal tumors of the bladder and breast (*9*). In addition, basal breast cancers, including triple negative breast cancers, were recently shown to be sensitive to THZ1 when compared to the ER^+ Luminal subtype (*24*). We found that, similar to basal PDA, basal breast cancer cell lines (BT549 and MDA-MB-231) failed to activate a complete ISR program and were more sensitive to THZ1 than their luminal counterparts (Fig. 6I). Thus, although the upstream apparatus of the ISR remained intact in basal PDA and basal breast cancer cell lines, they were unable to activate downstream regulators in the presence of transcriptional inhibitors such as THZ1 or flavopiridol, rendering them vulnerable to this class of compounds.

To show that the ISR confers differential sensitivity to transcriptional inhibition in vivo, we implanted *Sirt6* KO and *Sirt6* WT GEMM-derived PDA organoids subcutaneously in immunocompetent syngeneic C57BL/6 mice and treated daily with flavopiridol for 3 weeks. Flavopiridol inhibited the growth of the *Sirt6* KO but not the *Sirt6* WT organoid-derived tumors (Fig. 7A). The histology of the implanted PDA organoid tumors was independently verified by a pathologist to be indistinguishable from the original GEMM tumors for both *Sirt6* KO and *Sirt6* WT models (Fig. 7B).

We next used two different patient-derived xenograft (PDX) models, subtyped as classical and basal, respectively, based on publicly available RNA-seq data from the NCI patient-derived

model repository (PDMR), and confirmed the designations based on abundance of *SIRT6* expression (Fig. 7C). The models were treated with flavopiridol for 3 weeks and growth of basal PDXs was inhibited (Fig. 7D). In comparison, classical PDXs were not sensitive (Fig. 7E). Flavopiridol also did not cause substantial toxicity as assessed by maintenance of animal weight throughout treatment (Fig. 7F). Together, these results suggested that transcriptional inhibition of the basal subtype of PDA, defined by *SIRT6* expression, is a specific and potent treatment strategy for this deadly disease.

DISCUSSION

Here we have found that SIRT6, an NAD^+ dependent histone deacetylase, can regulate ATF4 stability in response to cellular stresses and is highly expressed in the classical PDA subtype, whereas it is lost in the basal PDA subtype. As a result, basal PDA has a suppressed ISR at baseline whereas classical PDA has an elevated ISR at baseline. We further found that SIRT6 is required for ISR activation through its regulation of ATF4 stability which enables the classical PDA subtype to survive stressors such as inhibition of transcriptional CDKs. Normally, basal PDA cells would induce SIRT6 in response to an applied stressor, with a subsequent increase in ATF4 and an adaptive response to that stress. However, when the applied stress is transcriptional CDK inhibition, SIRT6 cannot be induced and is therefore not present to stabilize ATF4 which prevents the ISR from becoming active. This reduced or inactive ISR prevents the cell from adequately responding to the stress of transcriptional CDK inhibition which drives the basal PDA cells towards cells death. Genetic manipulation of key regulators of the ISR, including *ATF4* and *GADD34*, was sufficient to alter sensitivity to these inhibitors of transcriptional CDKs in both subtypes.

PDA regulation of ATF4 through stability and degradation has not been studied as in-depth as regulation of ATF4 through translational control. However, some insightful work has discovered that ATF4 has a targeted E3 ligase receptor (β-TRCP which directly interacts with and guides ATF4 to the proteasome for degradation. This interaction is mediated by ATF4 phosphorylation at serine 219, which is within a similar motif to other β-TRCP substrates (*37*). We found that β-TRCP is important for ATF4 degradation by the proteasome in PDA, and loss of β-TRCP in the absence of SIRT6 enables a partial rescue of ATF4 protein abundance. However, because this rescue is partial and not complete, β-TRCP may not be the only E3 ligase receptor component that binds ATF4. Considering that loss of SIRT6 enables ATF4 to escape the protection of nuclear speckles, this would increase ATF4 abundance outside of the speckles and increase potential to bind with other E3 ligase receptor components. In addition, it has been identified that epigenetic modifiers such as histone acetyltransferases are able to stabilize ATF4 through mechanisms independent of their catalytic activity. The histone acetyltransferase p300 can stabilize and localize ATF4 to nuclear speckles thereby increasing its transcriptional activity (*38*). Our data identifies that this model of epigenetic modifiers, such as p300 and SIRT6, stabilizing and localizing ATF4 to nuclear speckles holds true in PDA. This model illustrates how protein stability encompasses another layer of post-translational regulation of the ATF4 signaling pathway. Further work will be needed to determine whether the catalytic activity of SIRT6 is necessary for its ability to stabilize ATF4.

Reprogramming of protein synthesis can collaborate with epigenetic and metabolic programs to determine cell state. Global translation is frequently dysregulated in cancer, and it remains an open question whether translation drives or merely reflects cellular identity. The ISR and control of global translation through phosphorylated eIF2α may have an evolutionarily conserved role in cell plasticity in response to stress (*39*). Studies of stem cells in murine models

and human cancers have linked p-eIF2α and the ISR to cancer cell plasticity and maintenance of stem cell populations (*40, 41*). Protein synthesis rates may dictate cell lineage in epithelial populations as well. For example, progenitor basal cells exhibit higher amounts of protein synthesis compared to luminal cells within the murine prostate. This observation is maintained in the context of prostate cancer (*42*). Similarly, in transdifferentiated (EMT) breast cancer cells, overproduction of extracellular matrix components leads to ER stress and activation of the PERK (eukaryotic translation initiation factor 2 alpha kinase 3)/eIF2α axis, which is paralleled by invasion and metastasis (*43*). Breast cancer cells can also increase plasticity in response to mTOR inhibitors and chemotherapeutics that induce translational activation of stemness factors NANOG (Nanog homeobox), SNAIL (snail family transcriptional repressor 1), and NODAL (nodal growth differentiation factor). These effects are overcome with drugs that antagonize the translational reprogramming caused by p-eIF2α, suggesting that the ISR drives breast cancer plasticity (*44*). In the epidermis, an eIF2B5-mediated translational program leads to loss of progenitor self-renewal, which limits tumor initiation and growth (*45*). Collectively, these observations suggest a multifaceted role for the ISR in cancer cell phenotypic switching.

Our study is limited by several factors. First, we recognize that patient tumors can be heterogenous in their subtypes but the more we understand about the individual subtypes, the better we can develop targeted therapies that can convert cell state, constrain plasticity, and kill the resulting tumor population. In addition, we recognize that knockdown of SIRT6 in classical PDA does not reduce ATF4 abundance as low as seen in basal PDA. Considering the complexity of ATF4 regulation, other mechanisms in addition to SIRT6 may control ATF4 abundance in PDA. Specifically, there could be additional modes of regulation keeping ATF4 low in basal PDA other than lack of SIRT6. Although we observe marked sensitivity of basal PDA to inhibitors of

transcriptional CDKs in mouse models, this may not always predict response rates in human patients. However, we made our preclinical studies as relevant as possible by implanting murine PDA organoids into immunocompetent syngeneic C57BL/6 mice to preserve the effects of the immune system on treatment. In addition, we treated PDX models in immunocompromised mice to account for differential response between human and murine tumors.

Lastly, examining the ability for subtype switching through epigenetic adaptation and inhibition of key drivers of the basal/ classical state would be an important future extension of this study to see how this could alter therapeutic response and potential acquired resistance to therapy over time. An understanding of this regulation may allow us to potentially convert classical tumors to basal tumors to reduce intratumoral heterogeneity and constrain plasticity before applying subtype-specific therapies like transcriptional CDK inhibition.

Treatment of patients with cancer with a highly selective and potent oral CDK7 inhibitor has already shown promising results in a Phase I clinical trial across multiple tumor types (*46*). Clinical activity was most notable in pancreatic cancer where stable disease was noted in 38% of patients. Most adverse events were low-grade and reversible. These results have led to expansion of this trial in PDA (*46*). Our study provides an understanding of the biology that determines sensitivity to CDK7 inhibitors, which will aid the clinical development of these inhibitors in PDA. Investigations of resistance mechanisms and combination therapies with transcriptional CDK inhibitors are important next steps in providing successful therapeutic options to patients with PDA.

MATERIALS AND METHODS

Study design. The goals of this study were to uncover a functional relationship between PDA subtypes and SIRT6 expression as well as define the mechanism of subtype-specific sensitivity to inhibition of transcriptional CDKs in PDA. This objective was accomplished by (i) characterizing SIRT6 regulation of the ISR as a defining feature of PDA subtypes, (ii) dissecting the mechanism by which SIRT6 controls ATF4 and thereby influences cellular responses to stress in PDA, (iii) identifying the role of the ISR in sensitivity and resistance to inhibitors of transcriptional CDKs, and (iv) conducting a series of in vitro and in vivo studies to delineate the therapeutic potential of transcriptional CDK inhibitors in basal PDA. For all experiments, our sample size was determined based on experience and published literature. We used the maximum number of mice available for a given experiment based on the following criteria: the number of mice available within the correct age range per strain and tumor availability after implantation of human PDX tissue or organoids. For all studies, mice were randomly assigned to each treatment group. A blinded pathologist performed all histological analyses for murine studies. The number of replicates is specified in each figure legend.

Organoid xenograft. All mouse procedures were conducted in accordance with the Fred Hutchinson Cancer Research Center (FHCRC) IACUC guidelines and the ARRIVE guidelines. C57BL/6J (BL/6J) mice (000664, JAX) were purchased from The Jackson Laboratory. Injections of organoid cultures for the generation of subcutaneously grafted organoid tumors were conducted as described previously (*47*). Typically, 1-2 x 10^6 cells in 100 µL suspension of 50% Matrigel (Corning) in phosphate buffered saline (PBS) and injected into each flank of the mouse. When average tumor diameters of 3-5 mm^3 were reached, mice were treated with a once daily

intraperitoneal injection of vehicle or 5 mg/kg flavopiridol (S1230, Selleck) diluted with dextrose 5% in water solution (600063; Bound Tree Medical) for 21-days. Caliper measurements of tumors and bodyweights were recorded 3-times per week.

Patient derived xenograft. PDX models were acquired from the NCI patient-derived model repository (PDMR). 8333975-119-r (Lot# CD1183), 463931-005-r (Lot# LS2265), 466636-057-r (Lot# MD0903) and 885724-159-r (Lot# AM1179). Vials of cryopreserved PDX tissue fragments were revived, and subsequently repassaged as fresh whole tissue, into both NSG (NOD scid gamma) and nude mice. Freshly repassaged tissue was then used for implantation of study cohorts of nude mice (002019, JAX). All work in mice was approved by the Institutional Animal Care and Use Committee (FHCRC IACUC protocol 50935-200016). Every PDX model tested negative for human pathogens (IDEXX h-IMPACT panel). An aseptic standardized procedure was used uniformly: PDX whole tissue (37degrees C) was rinsed in RPMI, suspended in Matrigel (Corning) and implanted subcutaneously into the right flank of 6 to 8 week-old female mice (see strain notes above) under isoflurane anesthesia. Preemptive analgesia was provided using Buprenorphine SR 0.05 mg/kg. Tumor growth and body condition were monitored, and tumors were measured with electronic calipers. When average tumor diameters of 3-5 mm^3 were reached, mice were treated with a once daily intraperitoneal injection of vehicle or 5 mg/kg flavopiridol (S1230, Selleck) diluted with dextrose 5% in water solution (600063; Bound Tree Medical) for 21-days. Caliper measurements of tumors and bodyweights were recorded 3-times per week.

Statistical Analyses. Statistical significance was determined by specific tests and presented as means ± SEM as indicated in the figure legends. Experimental raw values were depicted when

possible or normalized to internal controls. When comparing data from two groups paired or unpaired Student's two-tailed t test was used to determine significance, which was set at a P value of <0.05. Statistical analyses were performed using GraphPad Prism and R or Python packages. RNA-seq data was analyzed using Python package HTSeq, and Bioconductor packages edgeR and goseq. ChIP-seq data was analyzed using Python packages MACS2 and ROSE. Both RNA-seq and ChIP-seq data used R package VennDiagram and false discovery rates (FDRs) were calculated using the Benjamini-Hochberg method and cut off at 5%. Pearson's correlation coefficient and corresponding P value were used to measure the extent of correlation between SIRT6 expression and THZ1 sensitivity. Additional information can be found in the supplemental materials and methods.

FIGURES

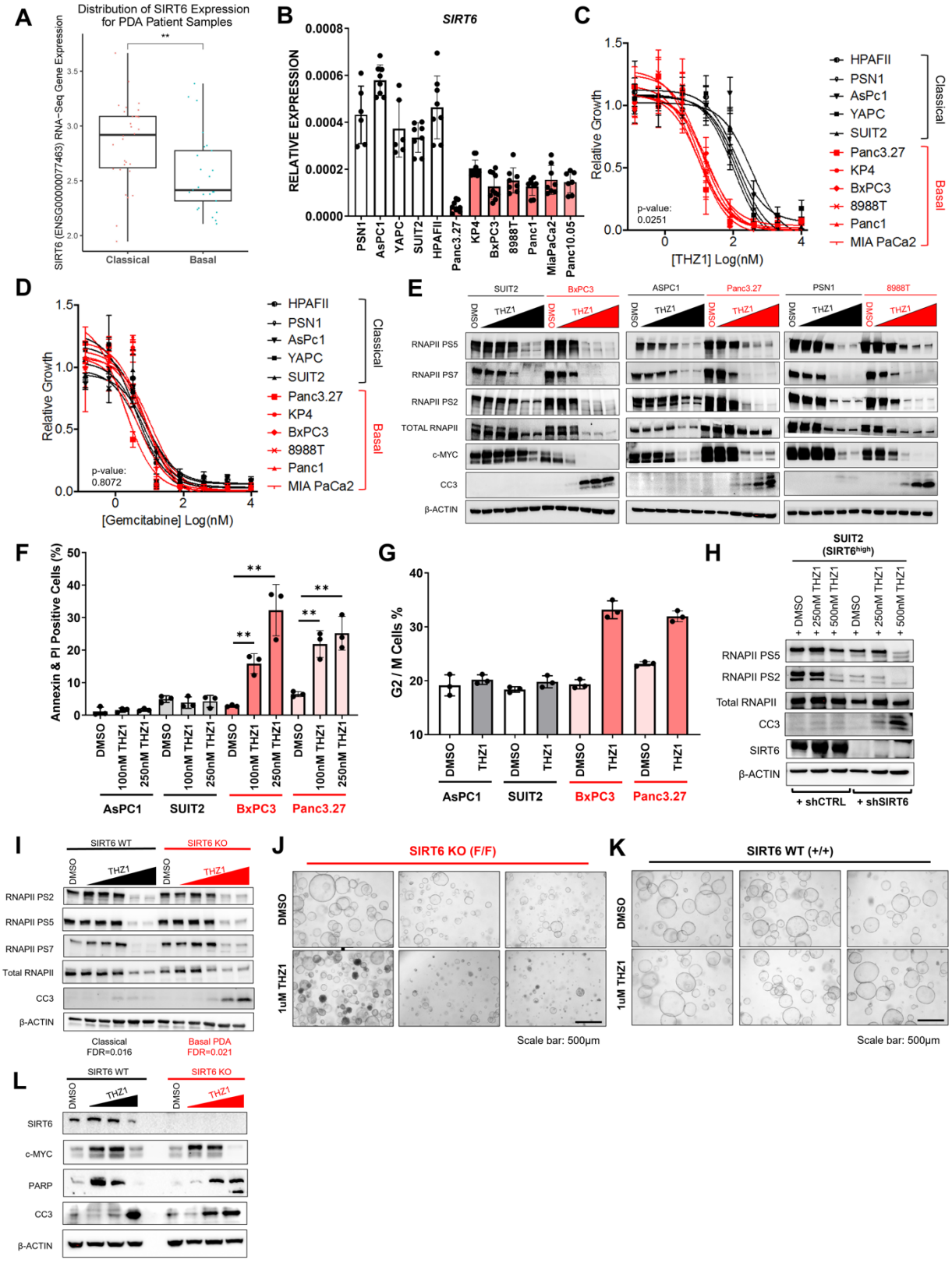
A
Distribution of SIRT6 Expression for PDA Patient Samples
SIRT6 (ENSG00000077463) RNA-Seq Gene Expression
Classical
Basal
B
SIRT6
RELATIVE EXPRESSION
PSN1
AsPC1
YAPC
SUIT2
HPAFII
Panc3.27
KP4
BxPC3
8988T
Panc1
MiaPaCa2
Panc10.05
C
Relative Growth
[THZ1] Log(nM)
p-value: 0.0251
HPAFII
PSN1
AsPc1
YAPC
SUIT2
Panc3.27
KP4
BxPC3
8988T
Panc1
MIA PaCa2
Classical
Basal
D
Relative Growth
[Gemcitabine] Log(nM)
p-value: 0.8072
E
SUIT2
BxPC3
ASPC1
Panc3.27
PSN1
8988T
DMSO
THZ1
RNAPII PS5
RNAPII PS7
RNAPII PS2
TOTAL RNAPII
c-MYC
CC3
β-ACTIN
F
Annexin & PI Positive Cells (%)
DMSO
100nM THZ1
250nM THZ1
AsPC1
SUIT2
BxPC3
Panc3.27
G
G2 / M Cells %
DMSO
THZ1
AsPC1
SUIT2
BxPC3
Panc3.27
H
SUIT2 (SIRT6high)
+ DMSO
+ 250nM THZ1
+ 500nM THZ1
RNAPII PS5
RNAPII PS2
Total RNAPII
CC3
SIRT6
β-ACTIN
+ shCTRL
+ shSIRT6
I
SIRT6 WT
SIRT6 KO
DMSO
THZ1
RNAPII PS2
RNAPII PS5
RNAPII PS7
Total RNAPII
CC3
β-ACTIN
Classical FDR=0.016
Basal PDA FDR=0.021
J
SIRT6 KO (F/F)
DMSO
1uM THZ1
Scale bar: 500μm
K
SIRT6 WT (+/+)
DMSO
1uM THZ1
Scale bar: 500μm
L
SIRT6 WT
SIRT6 KO
DMSO
THZ1
SIRT6
c-MYC
PARP
CC3
β-ACTIN

Figure 1. THZ1 specifically induces apoptosis in basal but not classical PDA. A, *SIRT6* expression from RNA-seq data of human PDA samples classified as belonging to either basal or classical subtypes. **B,** qRT-PCR for *SIRT6* in panel of human PDA cell lines. **C and D,** Proliferation curves for basal PDA (red), compared with classical (black) PDA cell lines treated with increasing doses of THZ1 (**C**) and gemcitabine (**D**). Significant difference in IC50 values for basal versus classical indicated by p-value ≤ 0.05 (two-tailed unpaired Student's t-test). **E,** Western blot for RNA polymerase II (RNAPII) phosphorylation of serine 5 (PS5), serine 7 (PS7), serine 2 (PS2), MYC, cleaved caspase 3 (CC3) and ACTIN in basal (red), compared with classical (black) PDA cell lines treated with increasing doses of THZ1 (20nM – 5uM) for 16 hours. **F**, Quantification of Annexin + Propidium iodide positive cells in classical (grey) versus basal (red) PDA lines after THZ1 treatment. **G,** Quantification of G2/M cell populations in classical (grey) versus basal (red) PDA lines after THZ1 treatment. **H,** Western blots for PS5, PS2, RNAPII, CC3, SIRT6 and ACTIN in classical cell line expressing either short hairpins targeting *SIRT6* (shSIRT6) or control hairpins (shCNTL), treated with increasing doses of THZ1 (250nM and 500nM). **I**, Western blots for PS2, PS5, PS7, RNAPII, CC3 and ACTIN in 2D cell lines derived from GEMM pancreatic tumors with (+/+) and without (F/F) SIRT6 expression treated with increasing concentrations of THZ1 for 16 hours. **J and K,** Bright field imaging of organoids derived from GEMM pancreatic tumors with (+/+) and without (F/F) SIRT6 expression treated with either DMSO or 1uM THZ1 for 24 hours. All bright field images have a scale bar of 500um. **L,** Western blots of SIRT6, cMYC, PARP, CC3 and ACTIN in organoids derived from GEMM pancreatic tumors with and without *SIRT6* expression treated with incremental doses of THZ1 (500nM – 2.5uM) for 16 hours. Error bars represent +/- SEM between technical duplicates. Data are representative of at least 2 independent experiments. *p-value ≤ 0.05; **p-value ≤ 0.01 (two-tailed unpaired Student's *t*-test).

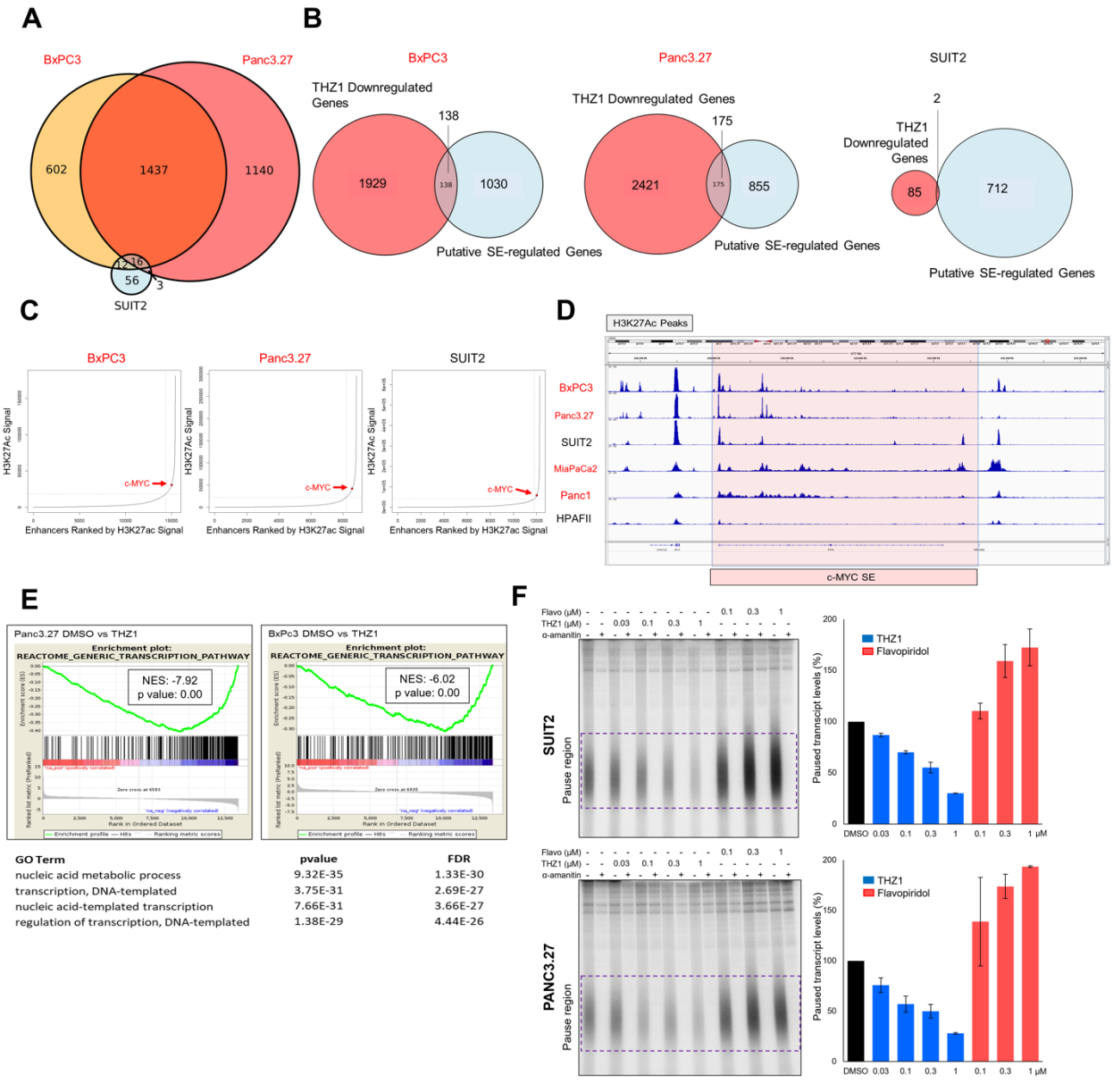

GO Term	pvalue	FDR
nucleic acid metabolic process	9.32E-35	1.33E-30
transcription, DNA-templated	3.75E-31	2.69E-27
nucleic acid-templated transcription	7.66E-31	3.66E-27
regulation of transcription, DNA-templated	1.38E-29	4.44E-26

Figure 2. THZ1 inhibits a broad transcriptional program in basal but not classical PDA. A, Venn diagram showing overlap of downregulated genes between basal lines BxPC3 and Panc3.27 and the classical PDA line SUIT2 after THZ1 treatment. **B,** Venn diagram showing overlap between downregulated genes from RNA-seq experiment and putative super enhancer (SE)-regulated genes in the indicated PDA cell lines. **C,** Enhancer regions plotted in order of increasing input-normalized H3K27ac ChIP-seq signal, comparing basal (red) and classical (black) lines. Super-enhancers are defined as being to the right of the curve inflection point, indicated by a dashed vertical line and c-MYC is highlighted by a red point. **D,** H3K27Ac peaks at a putative c-MYC enhancer in PDA, comparing basal (red) and classical (black) lines. **E,** Gene set enrichment analyses (GSEA) of DE genes and significant gene ontology (GO) pathways suppressed in basal PDA lines after THZ1 treatment. **F,** Nuclear walk on assays of SUIT2 and Panc3.27 cells treated with the indicated amounts of THZ1 and flavopiridol. Autoradiographs of denaturing gels of transcripts generated (left) and quantification of the paused transcripts contained within the purple box (right) are shown. Error bars represent standard deviation from two biological replicates.

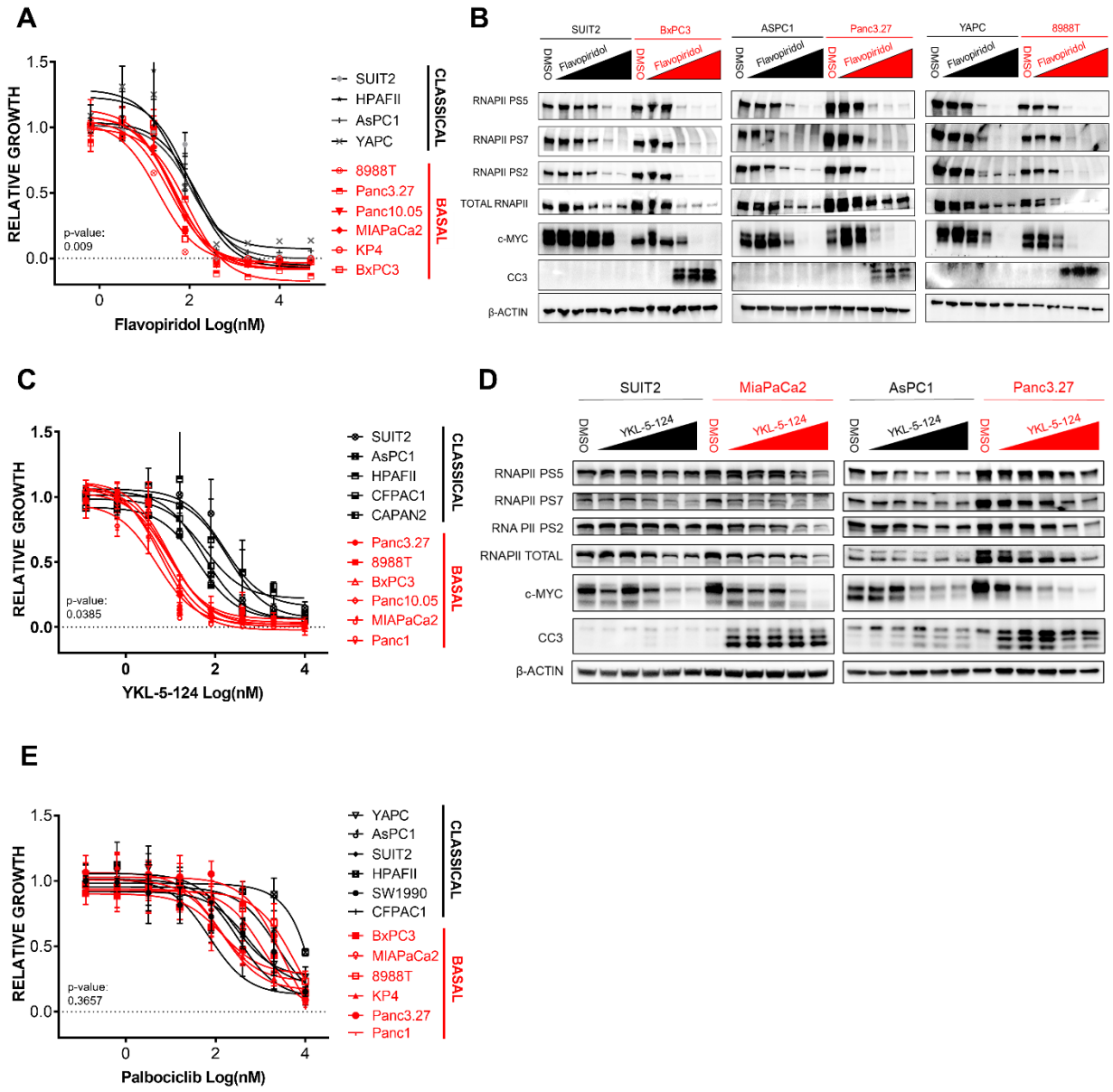

Figure 3. Basal PDA lines are differentially sensitive to inhibitors of transcriptional CDKs. **A,** Proliferation curves for basal PDA (red), compared with classical (black) PDA cell lines treated with increasing doses of flavopiridol **B,** Western blots for RNAPII, PS5, PS7, PS2, MYC, CC3 and ACTIN in basal (red), compared with classical (black) PDA cell lines treated with increasing doses of flavopiridol (20nM – 5uM) **C,** Proliferation curves for basal PDA (red), compared with classical (black) PDA cell lines treated with increasing doses of YKL-5-124 **D,** Western blots for RNAPII, PS5, PS7, PS2, MYC, CC3 and ACTIN in basal (red), compared with classical (black) PDA cell lines treated with increasing doses of YKL-5-124 (20nM – 5uM). **E,** Proliferation curves for basal-PDA (red), compared with classical (black) PDA cell lines treated with increasing doses of palbociclib. Proliferation curves were performed in duplicate, and data are represented as mean ± SEM among three independent experiments. Significant differences in IC50 values for basal versus classical indicated by p-value ≤ 0.05 (two-tailed unpaired Student's t-test with Welch's correction for those with unequal variances).

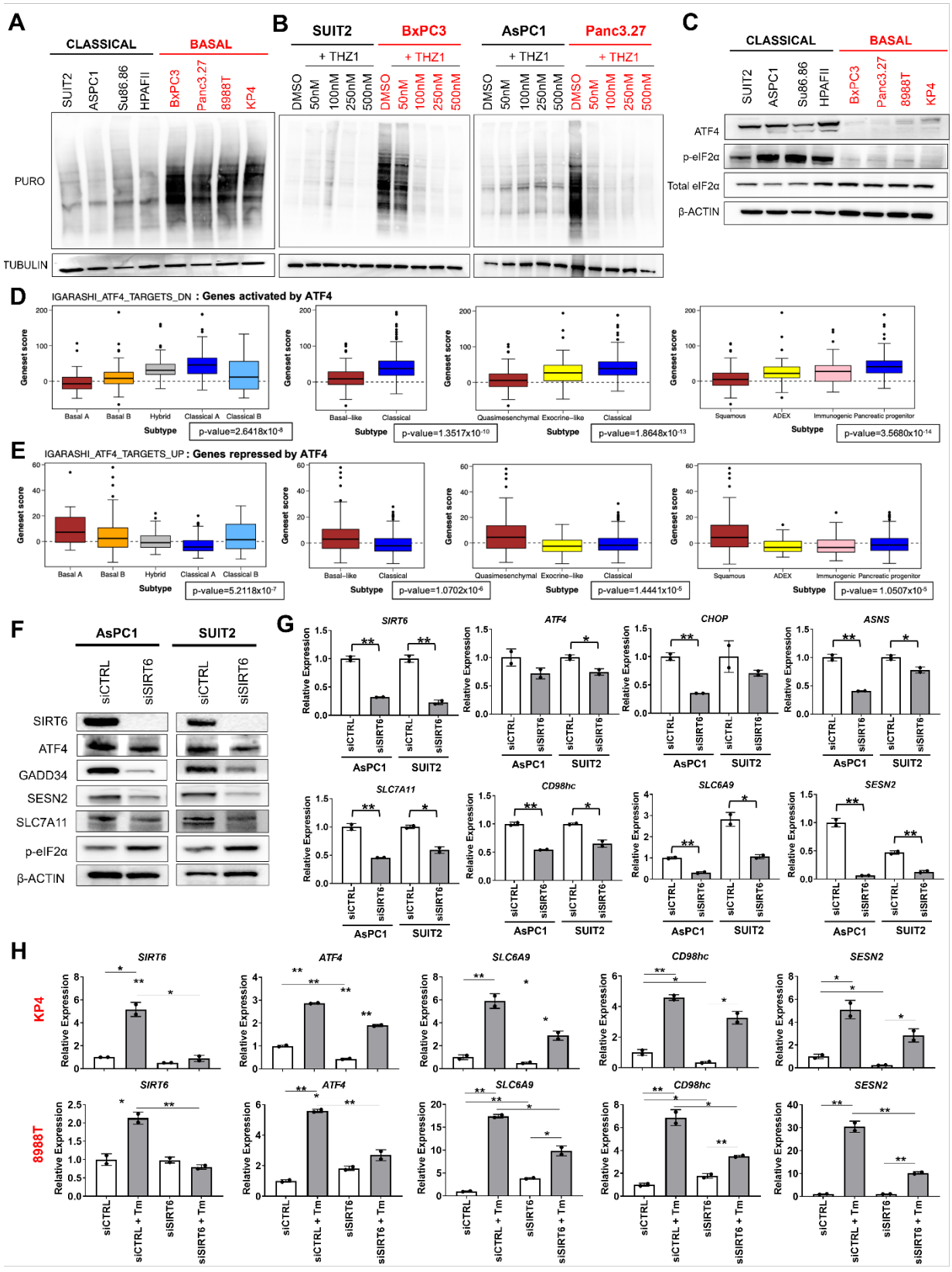
A
CLASSICAL
BASAL
SUIT2
ASPC1
Su86.86
HPAFII
BxPC3
Panc3.27
8988T
KP4
PURO
TUBULIN
B
SUIT2
BxPC3
AsPC1
Panc3.27
+ THZ1
DMSO
50nM
100nM
250nM
500nM
C
CLASSICAL
BASAL
ATF4
p-eIF2α
Total eIF2α
β-ACTIN
D
IGARASHI_ATF4_TARGETS_DN : Genes activated by ATF4
Geneset score
Basal A
Basal B
Hybrid
Classical A
Classical B
Subtype
p-value=2.6418x10-8
Basal-like
Classical
p-value=1.3517x10-10
Quasimesenchymal
Exocrine-like
p-value=1.8648x10-13
Squamous
ADEX
Immunogenic
Pancreatic progenitor
p-value=3.5680x10-14
E
IGARASHI_ATF4_TARGETS_UP : Genes repressed by ATF4
p-value=5.2118x10-7
p-value=1.0702x10-6
p-value=1.4441x10-5
p-value= 1.0507x10-5
F
AsPC1
SUIT2
siCTRL
siSIRT6
SIRT6
ATF4
GADD34
SESN2
SLC7A11
p-eIF2α
β-ACTIN
G
SIRT6
ATF4
CHOP
ASNS
SLC7A11
CD98hc
SLC6A9
SESN2
Relative Expression
H
KP4
8988T
siCTRL + Tm
siSIRT6 + Tm

Figure 4. SIRT6 regulates the ISR in PDA. A, Western blots for puromycin incorporation and TUBULIN in classical (black) and basal (red) PDA lines. **B,** Western blots for puromycin incorporation and TUBULIN in two classical (black) and two basal (red) PDA lines treated with incremental doses of THZ1. **C,** Western blots for ISR markers ATF4, phosphorylated eIF2α (p-eIF2α), total eIF2α and ACTIN in basal (red) and classical (black) PDA lines. **D and E,** Bioinformatic analysis of publicly available data comparing expression of ATF4 target genes according to four published PDA transcriptional subtyping classifications. Wilcoxon rank-sum test was performed comparing basal versus classical (or subtype equivalent) to give an FDR-adjusted p-value. **F,** Western blots for SIRT6, ISR markers ATF4, GADD34 and p-eIF2α, ATF4 target genes SESN2, ASNS, SLC7A11 and ACTIN in classical lines treated with non-specific and SIRT6-specific siRNAs. **G,** qRT-PCRs for *SIRT6*, ISR markers and ATF4 target genes in classical lines treated with non-specific and SIRT6-specific siRNAs. **H,** qRT-PCRs for *SIRT6*, *ATF4* and ATF4 target genes in two basal lines treated with 10uM tunicamycin (Tm) for 5 hours in the presence of non-specific and *SIRT6*-specific siRNAs. Error bars represent +/- SEM between technical duplicates. Data are representative of at least 2 independent experiments. *p-value $\leq$ 0.05; **p-value $\leq$ 0.01 (two-tailed unpaired Student's *t*-test).

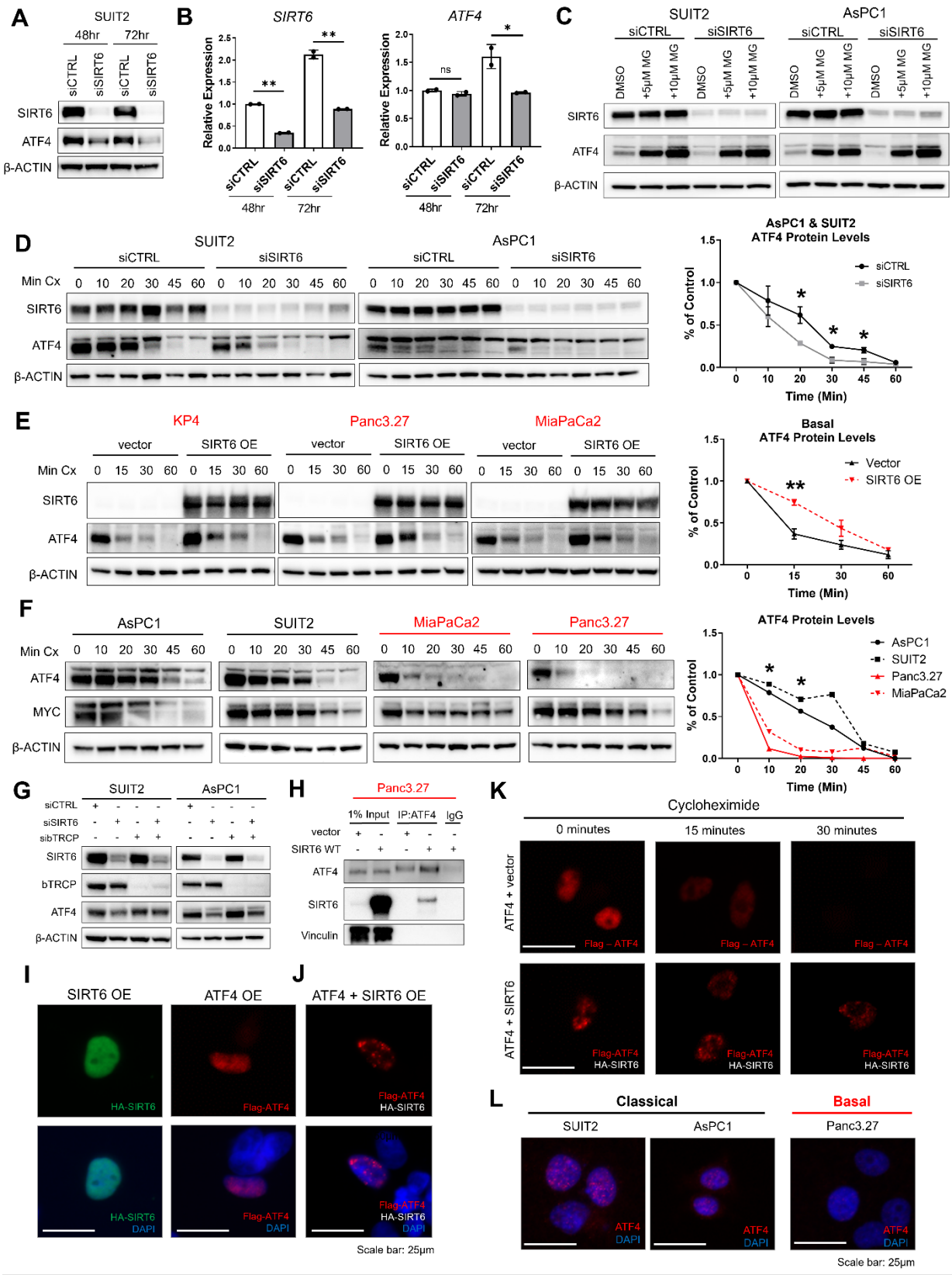
A
SUIT2
48hr
72hr
siCTRL
siSIRT6
siCTRL
siSIRT6
SIRT6
ATF4
β-ACTIN
B
SIRT6
ATF4
Relative Expression
siCTRL
siSIRT6
siCTRL
siSIRT6
48hr
72hr
C
SUIT2
AsPC1
siCTRL
siSIRT6
DMSO
+5μM MG
+10μM MG
SIRT6
ATF4
β-ACTIN
D
SUIT2
AsPC1
siCTRL
siSIRT6
Min Cx
0 10 20 30 45 60
SIRT6
ATF4
β-ACTIN
AsPC1 & SUIT2
ATF4 Protein Levels
% of Control
Time (Min)
siCTRL
siSIRT6
E
KP4
Panc3.27
MiaPaCa2
vector
SIRT6 OE
Min Cx
0 15 30 60
SIRT6
ATF4
β-ACTIN
Basal
ATF4 Protein Levels
Vector
SIRT6 OE
F
AsPC1
SUIT2
MiaPaCa2
Panc3.27
Min Cx
0 10 20 30 45 60
ATF4
MYC
β-ACTIN
ATF4 Protein Levels
AsPC1
SUIT2
Panc3.27
MiaPaCa2
G
SUIT2
AsPC1
siCTRL
siSIRT6
sibTRCP
SIRT6
bTRCP
ATF4
β-ACTIN
H
Panc3.27
1% Input
IP:ATF4
IgG
vector
SIRT6 WT
ATF4
SIRT6
Vinculin
K
Cycloheximide
0 minutes
15 minutes
30 minutes
ATF4 + vector
ATF4 + SIRT6
Flag – ATF4
Flag-ATF4
HA-SIRT6
I
SIRT6 OE
HA-SIRT6
DAPI
J
ATF4 OE
ATF4 + SIRT6 OE
Flag-ATF4
HA-SIRT6
DAPI
Scale bar: 25μm
L
Classical
Basal
SUIT2
AsPC1
Panc3.27
ATF4
DAPI
Scale bar: 25μm

Figure 5. SIRT6 regulates stability of ATF4 protein. A and B, Western blots (A) for SIRT6, ATF4, and ACTIN and qRT-PCR (B) for *SIRT6* and *ATF4* mRNA abundance in SUIT2 cells transfected with non-specific or *SIRT6*-specific siRNAs for 48 or 72 hours. **C,** Western blots for SIRT6, ATF4, and ACTIN in classical PDA cell lines transfected with non-specific or *SIRT6*-specific siRNAs and treated with 5μM or 10μM MG-132 (MG) for 6 hours. **D,** Western blots for SIRT6, ATF4, and ACTIN and quantification of relative ATF4 abundance in classical PDA cell lines transfected with non-specific or *SIRT6*-specific siRNAs and treated with 150μg/mL cycloheximide for 10, 20, 30, 45, or 60 minutes. **E,** Western blots for SIRT6, ATF4, and ACTIN and quantification of relative ATF4 abundance in basal PDA cell lines transfected with empty vector, *SIRT6* WT overexpression, or *SIRT6* HY overexpression plasmids and treated with 150μg/mL cycloheximide for 15, 30, or 60 minutes. **F,** Western blots for ATF4, MYC, and ACTIN and quantification of relative ATF4 abundance in classical and basal PDA cell lines and treated with 150μg/mL cycloheximide for 10, 20, 30, 45, or 60 minutes. Significance indicates basal versus classical comparison. **G,** Western blots for SIRT6, β-TRCP, ATF4, and ACTIN in classical lines treated with non-specific (siCTRL), SIRT6-specific (siSIRT6), β-TRCP-specific (sibTRCP) siRNAs. **H,** Immunoprecipitation of ATF4 followed by Western blotting for ATF4, SIRT6, and Vinculin in Panc3.27 cells transfected with empty vector or *SIRT6* overexpression plasmids. **I,** Immunofluorescence for single transfection of *SIRT6* overexpression (OE) with an HA-tag (green) or *ATF4* overexpression (OE) with a Flag-tag (red) in Panc3.27 cells. **J,** Immunofluorescence for co-transfection of *SIRT6* and *ATF4* overexpression in Panc3.27 cells stained for Flag-ATF4 (red). K, Immunofluorescence for co-transfection of *ATF4* plus empty vector overexpression, and *ATF4* plus *SIRT6* overexpression in Panc3.27 cells with a cycloheximide treatment of 0, 15, and 30 minutes stained for Flag-ATF4 (red). **L,** Immunofluorescence for endogenous ATF4 (red) in two classical and one basal cell lines. All immunofluorescence images have a scale bar of 25μm. Data are representative of at least 2 independent experiments. *p-value ≤ 0.05; **p-value ≤ 0.01 (two-tailed unpaired Student's *t*-test).

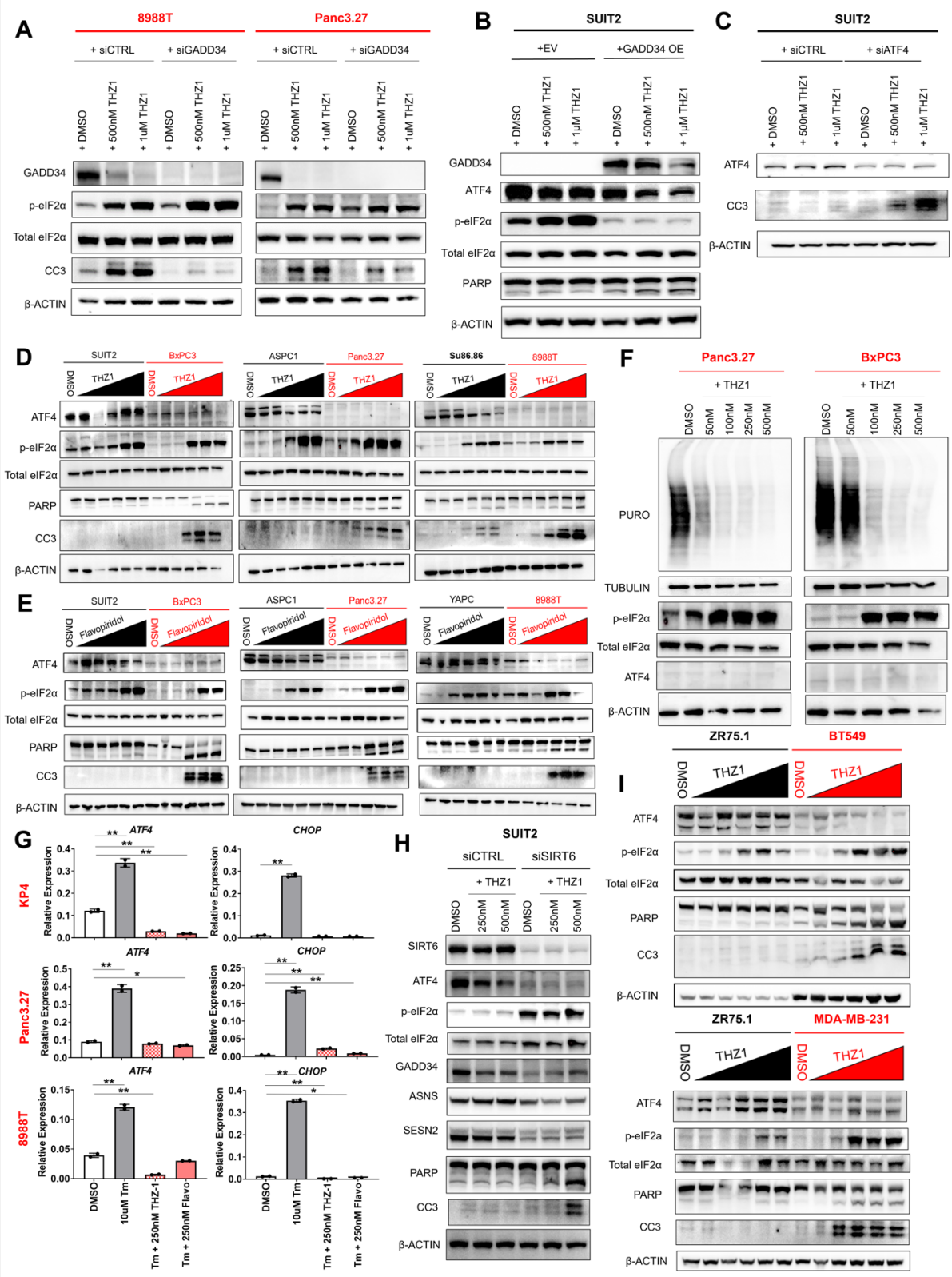
A
8988T
Panc3.27
+ siCTRL
+ siGADD34
+ DMSO
+ 500nM THZ1
+ 1uM THZ1
GADD34
p-eIF2α
Total eIF2α
CC3
β-ACTIN
B
SUIT2
+EV
+GADD34 OE
+ 1μM THZ1
ATF4
PARP
C
+ siATF4
D
SUIT2
BxPC3
ASPC1
Panc3.27
Su86.86
8988T
DMSO
THZ1
E
Flavopiridol
YAPC
F
+ THZ1
50nM
100nM
250nM
500nM
PURO
TUBULIN
ZR75.1
BT549
G
KP4
Panc3.27
8988T
Relative Expression
ATF4
CHOP
DMSO
10uM Tm
Tm + 250nM THZ-1
Tm + 250nM Flavo
H
siCTRL
siSIRT6
SIRT6
GADD34
ASNS
SESN2
I
MDA-MB-231
p-eIF2a

Figure 6. The ISR confers sensitivity or resistance to transcriptional inhibitors. A, Western blots for GADD34, p-eIF2α, total eIF2α, CC3 and ACTIN in two basal PDA lines transfected with control or *GADD34*-specific siRNAs and treated with increasing doses of THZ1. **B,** Western blots for GADD34, ATF4, p-eIF2α, total eIF2α, PARP and ACTIN in a classical PDA line transduced with either an empty vector or *GADD34* and treated with increasing doses of THZ1. **C,** Western blots for ATF4, CC3 and ACTIN in a classical PDA line transfected with either control or *ATF4*-specific siRNAs and treated with increasing doses of THZ1. **D,** Western blots for ATF4, p-eIF2α, total eIF2α, PARP, CC3 and ACTIN in basal (red), compared with classical (black) PDA cell lines treated with increasing doses of THZ1 (20nM – 5uM). **E,** Western blots for ATF4, p-eIF2α, total eIF2α, PARP, CC3 and ACTIN in basal (red), compared with classical (black) PDA cell lines treated with increasing doses of flavopiridol (20nM – 5uM). **F,** Puromycin incorporation and Western blotting for TUBULIN, p-eIF2α, Total eIF2α, ATF4, and β-ACTIN in basal PDA cell lines treated with increasing doses of THZ1. **G,** qRT-PCRs of *ATF4* and *CHOP* in basal lines treated with Tm only, Tm with THZ1 and Tm with flavopiridol. Total treatment time for Tm was 5 hours, total treatment time for THZ1 and flavopiridol was 16 hours. **H,** Western blots for SIRT6, ATF4, p-eIF2α, total eIF2α, GADD34, ASNS, SESN2, PARP, CC3, and ACTIN in SUIT2 PDA cells transfected with non-specific or *SIRT6*-specific siRNAs and treated with 250nM or 500nM THZ-1 for 20 hours. **I,** Western blots for ATF4, p-eIF2α, total eIF2α, PARP, CC3 and ACTIN in basal BT549 and MDA-MB-231 (red), compared with luminal ZR75.1 (black) breast cancer cell lines treated with increasing doses of THZ1 (20nM – 5uM). Error bars represent +/- SEM between technical duplicates. Data are representative of at least 2 independent experiments. *p-value ≤ 0.05; **p-value ≤ 0.01 (two-tailed unpaired Student's *t*-test).

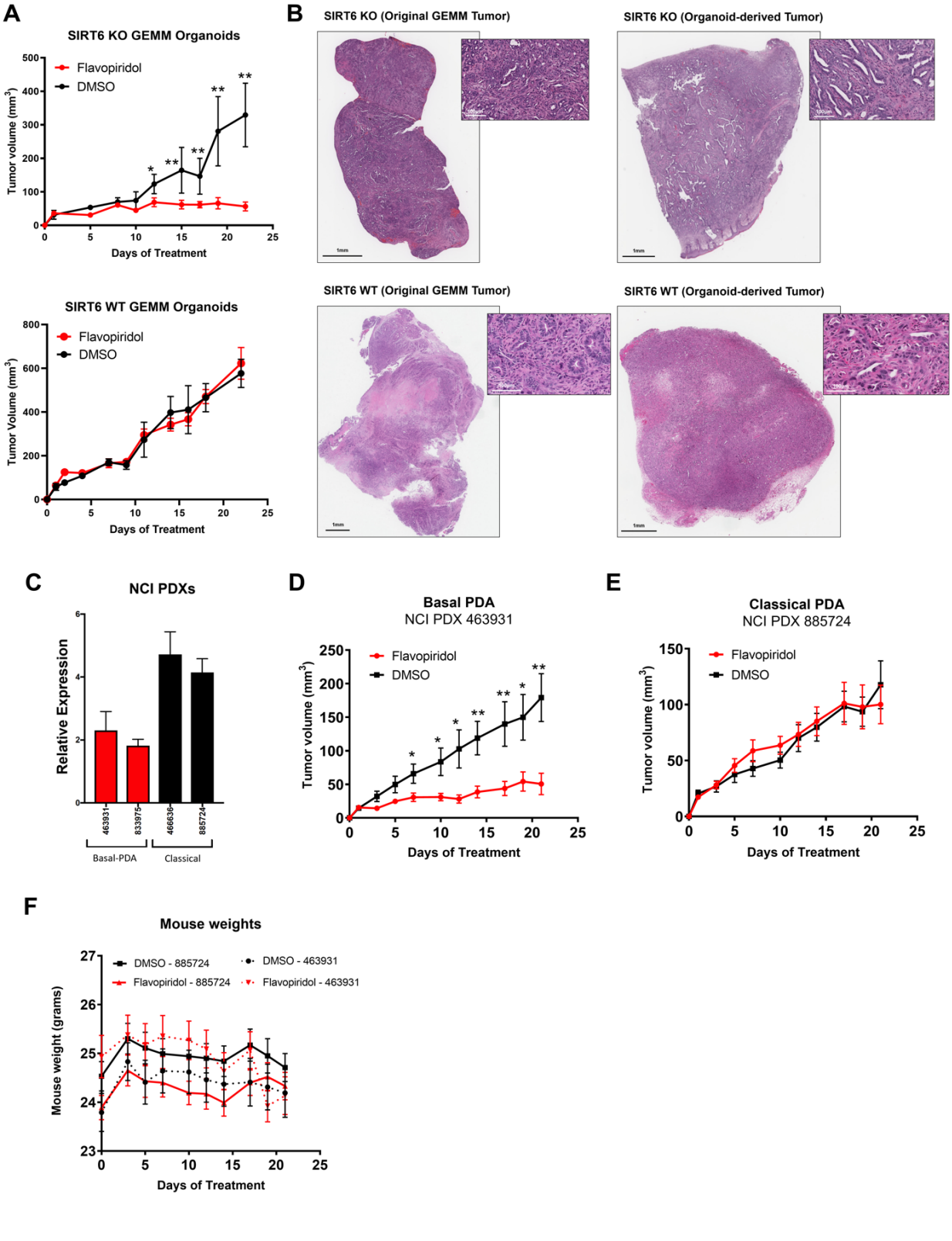
A
SIRT6 KO GEMM Organoids
Flavopiridol
DMSO
Tumor volume (mm3)
Days of Treatment
SIRT6 WT GEMM Organoids
Flavopiridol
DMSO
Tumor Volume (mm3)
Days of Treatment
B
SIRT6 KO (Original GEMM Tumor)
SIRT6 KO (Organoid-derived Tumor)
SIRT6 WT (Original GEMM Tumor)
SIRT6 WT (Organoid-derived Tumor)
C
NCI PDXs
Relative Expression
463931
833975
466636
885724
Basal-PDA
Classical
D
Basal PDA
NCI PDX 463931
Flavopiridol
DMSO
Tumor volume (mm3)
Days of Treatment
E
Classical PDA
NCI PDX 885724
Flavopiridol
DMSO
Tumor volume (mm3)
Days of Treatment
F
Mouse weights
DMSO - 885724
Flavopiridol - 885724
DMSO - 463931
Flavopiridol - 463931
Mouse weight (grams)
Days of Treatment

Figure 7. SIRT6 expression correlates with basal PDA status and flavopiridol sensitivity in vivo. A, Tumor volume of organoid xenografts derived from SIRT6 KO and SIRT6 WT mice after treatment with 5mg/kg once daily flavopiridol (red) compared to DMSO control (black) for 21 days (DMSO n=3, flavopiridol n=3). **B,** H&E staining showing comparison between original tumor and organoid-derived tumor from the same source for SIRT6 KO and SIRT6 WT. **C**, PDA subtype-specific expression of *SIRT6* in patient derived xenografts (PDXs) from the NCI. **D and E**, Tumor volume of NCI PDX 463931 (basal) (**D**) and NCI PDX 885724 (classical) (**E**) xenografts after treatment with 5mg/kg once daily flavopiridol (red) compared to DMSO control (black) for 21 days (DMSO n=10, flavopiridol n=10). **F**, Whole body weights of mice implanted with NCI PDX 885724 (classical) and NCI PDX 463931 (basal) xenografts after treatment with 5mg/kg once daily flavopiridol (red) compared to DMSO control (black) for 21 days. *p-value $\leq$ 0.05; **p-value $\leq$ 0.01 (two-tailed unpaired Student's t-test).

CHAPTER2: REFERENCES

1. L. Rahib, B. D. Smith, R. Aizenberg, A. B. Rosenzweig, J. M. Fleshman, L. M. Matrisian, Projecting cancer incidence and deaths to 2030: the unexpected burden of thyroid, liver, and pancreas cancers in the United States. *Cancer Res* **74**, 2913-2921 (2014).
2. D. P. Ryan, T. S. Hong, N. Bardeesy, Pancreatic adenocarcinoma. *The New England journal of medicine* **371**, 1039-1049 (2014).
3. S. R. Hingorani, E. F. Petricoin, A. Maitra, V. Rajapakse, C. King, M. A. Jacobetz, S. Ross, T. P. Conrads, T. D. Veenstra, B. A. Hitt, Y. Kawaguchi, D. Johann, L. A. Liotta, H. C. Crawford, M. E. Putt, T. Jacks, C. V. Wright, R. H. Hruban, A. M. Lowy, D. A. Tuveson, Preinvasive and invasive ductal pancreatic cancer and its early detection in the mouse. *Cancer Cell* **4**, 437-450 (2003).
4. S. R. Hingorani, L. Wang, A. S. Multani, C. Combs, T. B. Deramaudt, R. H. Hruban, A. K. Rustgi, S. Chang, D. A. Tuveson, Trp53R172H and KrasG12D cooperate to promote chromosomal instability and widely metastatic pancreatic ductal adenocarcinoma in mice. *Cancer Cell* **7**, 469-483 (2005).
5. G. Brar, E. M. Blais, R. Joseph Bender, J. R. Brody, D. Sohal, S. Madhavan, V. J. Picozzi, A. E. Hendifar, V. M. Chung, D. Halverson, S. Mikhail, L. M. Matrisian, L. Rahib, E. Petricoin, M. J. Pishvaian, Multi-omic molecular comparison of primary versus metastatic pancreatic tumours. *Br J Cancer* **121**, 264-270 (2019).
6. A. Hayashi, J. Fan, R. Chen, Y.-j. Ho, A. P. Makohon-Moore, N. Lecomte, Y. Zhong, J. Hong, J. Huang, H. Sakamoto, A unifying paradigm for transcriptional heterogeneity and squamous features in pancreatic ductal adenocarcinoma. *Nature Cancer* **1**, 59-74 (2020).
7. E. A. Collisson, A. Sadanandam, P. Olson, W. J. Gibb, M. Truitt, S. Gu, J. Cooc, J. Weinkle, G. E. Kim, L. Jakkula, H. S. Feiler, A. H. Ko, A. B. Olshen, K. L. Danenberg, M. A. Tempero, P. T. Spellman, D. Hanahan, J. W. Gray, Subtypes of pancreatic ductal adenocarcinoma and their differing responses to therapy. *Nat Med* **17**, 500-503 (2011).
8. P. Bailey, D. K. Chang, K. Nones, A. L. Johns, A. M. Patch, M. C. Gingras, D. K. Miller, A. N. Christ, T. J. Bruxner, M. C. Quinn, C. Nourse, L. C. Murtaugh, I. Harliwong, S. Idrisoglu, S. Manning, E. Nourbakhsh, S. Wani, L. Fink, O. Holmes, V. Chin, M. J. Anderson, S. Kazakoff, C. Leonard, F. Newell, N. Waddell, S. Wood, Q. Xu, P. J. Wilson, N. Cloonan, K. S. Kassahn, D. Taylor, K. Quek, A. Robertson, L. Pantano, L. Mincarelli, L. N. Sanchez, L. Evers, J. Wu, M. Pinese, M. J. Cowley, M. D. Jones, E. K. Colvin, A. M. Nagrial, E. S. Humphrey, L. A. Chantrill, A. Mawson, J. Humphris, A. Chou, M. Pajic, C. J. Scarlett, A. V. Pinho, M. Giry-Laterriere, I. Rooman, J. S. Samra, J. G. Kench, J. A. Lovell, N. D. Merrett, C. W. Toon, K. Epari, N. Q. Nguyen, A. Barbour, N. Zeps, K. Moran-Jones, N. B. Jamieson, J. S. Graham, F. Duthie, K. Oien, J. Hair, R. Grutzmann, A. Maitra, C. A. Iacobuzio-Donahue, C. L. Wolfgang, R. A. Morgan, R. T. Lawlor, V. Corbo, C. Bassi, B. Rusev, P. Capelli, R. Salvia, G. Tortora, D. Mukhopadhyay, G. M. Petersen, I. Australian Pancreatic Cancer Genome, D. M. Munzy, W. E. Fisher, S. A. Karim, J. R. Eshleman, R. H. Hruban, C. Pilarsky, J. P. Morton, O. J. Sansom, A. Scarpa, E. A. Musgrove, U. M. Bailey, O. Hofmann, R. L. Sutherland, D. A. Wheeler, A. J. Gill, R. A. Gibbs, J. V. Pearson, N. Waddell, A. V. Biankin, S. M. Grimmond, Genomic analyses identify molecular subtypes of pancreatic cancer. *Nature* **531**, 47-52 (2016).
9. R. A. Moffitt, R. Marayati, E. L. Flate, K. E. Volmar, S. G. Loeza, K. A. Hoadley, N. U. Rashid, L. A. Williams, S. C. Eaton, A. H. Chung, J. K. Smyla, J. M. Anderson, H. J. Kim, D.

J. Bentrem, M. S. Talamonti, C. A. Iacobuzio-Donahue, M. A. Hollingsworth, J. J. Yeh, Virtual microdissection identifies distinct tumor- and stroma-specific subtypes of pancreatic ductal adenocarcinoma. *Nature genetics* **47**, 1168-1178 (2015).
10. F. Puleo, R. Nicolle, Y. Blum, J. Cros, L. Marisa, P. Demetter, E. Quertinmont, M. Svrcek, N. Elarouci, J. Iovanna, D. Franchimont, L. Verset, M. G. Galdon, J. Devière, A. de Reyniès, P. Laurent-Puig, J. L. Van Laethem, J. B. Bachet, R. Maréchal, Stratification of Pancreatic Ductal Adenocarcinomas Based on Tumor and Microenvironment Features. *Gastroenterology* **155**, 1999-2013.e1993 (2018).
11. M. Chan-Seng-Yue, J. C. Kim, G. W. Wilson, K. Ng, E. F. Figueroa, G. M. O'Kane, A. A. Connor, R. E. Denroche, R. C. Grant, J. McLeod, J. M. Wilson, G. H. Jang, A. Zhang, S. B. Liang, A. Borgida, D. Chadwick, S. Kalimuthu, I. Lungu, J. M. S. Bartlett, P. M. Krzyzanowski, V. Sandhu, H. Tiriac, F. E. M. Froeling, J. M. Karasinska, J. T. Topham, D. J. Renouf, D. F. Schaeffer, S. J. M. Jones, M. A. Marra, J. Laskin, R. Chetty, L. D. Stein, G. Zogopoulos, B. Haibe-Kains, P. J. Campbell, D. A. Tuveson, J. J. Knox, S. E. Fischer, S. Gallinger, F. Notta, Author Correction: Transcription phenotypes of pancreatic cancer are driven by genomic events during tumor evolution. *Nat Genet* **52**, 463 (2020).
12. D. Campagna, L. Cope, S. S. Lakkur, C. Henderson, D. Laheru, C. A. Iacobuzio-Donahue, Gene expression profiles associated with advanced pancreatic cancer. *International journal of clinical and experimental pathology* **1**, 32-43 (2008).
13. G. Lomberk, Y. Blum, R. Nicolle, A. Nair, K. S. Gaonkar, L. Marisa, A. Mathison, Z. Sun, H. Yan, N. Elarouci, L. Armenoult, M. Ayadi, T. Ordog, J. H. Lee, G. Oliver, E. Klee, V. Moutardier, O. Gayet, B. Bian, P. Duconseil, M. Gilabert, M. Bigonnet, S. Garcia, O. Turrini, J. R. Delpero, M. Giovannini, P. Grandval, M. Gasmi, V. Secq, A. De Reynies, N. Dusetti, J. Iovanna, R. Urrutia, Distinct epigenetic landscapes underlie the pathobiology of pancreatic cancer subtypes. Nat Commun 9, 1978 (2018).
14. G. R. Diaferia, C. Balestrieri, E. Prosperini, P. Nicoli, P. Spaggiari, A. Zerbi, G. Natoli, Dissection of transcriptional and cis-regulatory control of differentiation in human pancreatic cancer. EMBO J 35, 595-617 (2016).
15. L. Bosch-Presegué, A. Vaquero, Sirtuins in stress response: guardians of the genome. *Oncogene* **33**, 3764-3775 (2014).
16. S. Kugel, R. Mostoslavsky, Chromatin and beyond: the multitasking roles for SIRT6. *Trends Biochem Sci* **39**, 72-81 (2014).
17. S. Kugel, C. Sebastian, J. Fitamant, K. N. Ross, S. K. Saha, E. Jain, A. Gladden, K. S. Arora, Y. Kato, M. N. Rivera, S. Ramaswamy, R. I. Sadreyev, A. Goren, V. Deshpande, N. Bardeesy, R. Mostoslavsky, SIRT6 Suppresses Pancreatic Cancer through Control of Lin28b. *Cell* **165**, 1401-1415 (2016).
18. C. Sebastian, B. M. Zwaans, D. M. Silberman, M. Gymrek, A. Goren, L. Zhong, O. Ram, J. Truelove, A. R. Guimaraes, D. Toiber, C. Cosentino, J. K. Greenson, A. I. MacDonald, L. McGlynn, F. Maxwell, J. Edwards, S. Giacosa, E. Guccione, R. Weissleder, B. E. Bernstein, A. Regev, P. G. Shiels, D. B. Lombard, R. Mostoslavsky, The histone deacetylase SIRT6 is a tumor suppressor that controls cancer metabolism. *Cell* **151**, 1185-1199 (2012).
19. N. Kwiatkowski, T. Zhang, P. B. Rahl, B. J. Abraham, J. Reddy, S. B. Ficarro, A. Dastur, A. Amzallag, S. Ramaswamy, B. Tesar, C. E. Jenkins, N. M. Hannett, D. McMillin, T. Sanda, T. Sim, N. D. Kim, T. Look, C. S. Mitsiades, A. P. Weng, J. R. Brown, C. H. Benes, J. A. Marto, R. A. Young, N. S. Gray, Targeting transcription regulation in cancer with a covalent CDK7 inhibitor. *Nature* **511**, 616-620 (2014).

20. T. Zhang, N. Kwiatkowski, C. M. Olson, S. E. Dixon-Clarke, B. J. Abraham, A. K. Greifenberg, S. B. Ficarro, J. M. Elkins, Y. Liang, N. M. Hannett, T. Manz, M. Hao, B. Bartkowiak, A. L. Greenleaf, J. A. Marto, M. Geyer, A. N. Bullock, R. A. Young, N. S. Gray, Covalent targeting of remote cysteine residues to develop CDK12 and CDK13 inhibitors. *Nat Chem Biol* **12**, 876-884 (2016).
21. S. Nagaraja, N. A. Vitanza, P. J. Woo, K. R. Taylor, F. Liu, L. Zhang, M. Li, W. Meng, A. Ponnuswami, W. Sun, J. Ma, E. Hulleman, T. Swigut, J. Wysocka, Y. Tang, M. Monje, Transcriptional Dependencies in Diffuse Intrinsic Pontine Glioma. *Cancer Cell* **31**, 635-652.e636 (2017).
22. C. L. Christensen, N. Kwiatkowski, B. J. Abraham, J. Carretero, F. Al-Shahrour, T. Zhang, E. Chipumuro, G. S. Herter-Sprie, E. A. Akbay, A. Altabef, J. Zhang, T. Shimamura, M. Capelletti, J. B. Reibel, J. D. Cavanaugh, P. Gao, Y. Liu, S. R. Michaelsen, H. S. Poulsen, A. R. Aref, D. A. Barbie, J. E. Bradner, R. E. George, N. S. Gray, R. A. Young, K. K. Wong, Targeting transcriptional addictions in small cell lung cancer with a covalent CDK7 inhibitor. *Cancer Cell* **26**, 909-922 (2014).
23. Z. Zhang, H. Peng, X. Wang, X. Yin, P. Ma, Y. Jing, M. C. Cai, J. Liu, M. Zhang, S. Zhang, K. Shi, W. Q. Gao, W. Di, G. Zhuang, Preclinical Efficacy and Molecular Mechanism of Targeting CDK7-Dependent Transcriptional Addiction in Ovarian Cancer. *Mol Cancer Ther* **16**, 1739-1750 (2017).
24. Y. Wang, T. Zhang, N. Kwiatkowski, B. J. Abraham, T. I. Lee, S. Xie, H. Yuzugullu, T. Von, H. Li, Z. Lin, D. G. Stover, E. Lim, Z. C. Wang, J. D. Iglehart, R. A. Young, N. S. Gray, J. J. Zhao, CDK7-dependent transcriptional addiction in triple-negative breast cancer. *Cell* **163**, 174-186 (2015).
25. S. Heinz, C. E. Romanoski, C. Benner, C. K. Glass, The selection and function of cell type-specific enhancers. *Nature reviews. Molecular cell biology* **16**, 144-154 (2015).
26. D. Hnisz, B. J. Abraham, T. I. Lee, A. Lau, V. Saint-Andre, A. A. Sigova, H. A. Hoke, R. A. Young, Super-enhancers in the control of cell identity and disease. *Cell* **155**, 934-947 (2013).
27. I. Sur, J. Taipale, The role of enhancers in cancer. *Nat Rev Cancer* **16**, 483-493 (2016).
28. K. A. Nilson, J. Guo, M. E. Turek, J. E. Brogie, E. Delaney, D. S. Luse, D. H. Price, THZ1 Reveals Roles for Cdk7 in Co-transcriptional Capping and Pausing. *Mol Cell* **59**, 576-587 (2015).
29. S. H. Chao, D. H. Price, Flavopiridol inactivates P-TEFb and blocks most RNA polymerase II transcription in vivo. *J Biol Chem* **276**, 31793-31799 (2001).
30. K. A. Nilson, C. K. Lawson, N. J. Mullen, C. B. Ball, B. M. Spector, J. L. Meier, D. H. Price, Oxidative stress rapidly stabilizes promoter-proximal paused Pol II across the human genome. *Nucleic Acids Res* **45**, 11088-11105 (2017).
31. C. B. Ball, K. A. Nilson, D. H. Price, Use of the nuclear walk-on methodology to determine sites of RNA polymerase II initiation and pausing and quantify nascent RNAs in cells. *Methods* **159-160**, 165-176 (2019).
32. S. Jana, R. Deo, R. P. Hough, Y. Liu, J. L. Horn, J. L. Wright, H. M. Lam, K. R. Webster, G. G. Chiang, N. Sonenberg, A. C. Hsieh, mRNA translation is a therapeutic vulnerability necessary for bladder epithelial transformation. *JCI Insight* **6**, (2021).
33. Z. Yang, Y. Huang, L. Zhu, K. Yang, K. Liang, J. Tan, B. Yu, SIRT6 promotes angiogenesis and hemorrhage of carotid plaque via regulating HIF-1alpha and reactive oxygen species. *Cell Death Dis* **12**, 77 (2021).

34. N. Zhang, X. Yang, F. Yuan, L. Zhang, Y. Wang, L. Wang, Z. Mao, J. Luo, H. Zhang, W. G. Zhu, Y. Zhao, Increased Amino Acid Uptake Supports Autophagy-Deficient Cell Survival upon Glutamine Deprivation. *Cell Rep* **23**, 3006-3020 (2018).
35. Y. Park, A. Reyna-Neyra, L. Philippe, C. C. Thoreen, mTORC1 Balances Cellular Amino Acid Supply with Demand for Protein Synthesis through Post-transcriptional Control of ATF4. *Cell Rep* **19**, 1083-1090 (2017).
36. H. P. Harding, Y. Zhang, H. Zeng, I. Novoa, P. D. Lu, M. Calfon, N. Sadri, C. Yun, B. Popko, R. Paules, D. F. Stojdl, J. C. Bell, T. Hettmann, J. M. Leiden, D. Ron, An integrated stress response regulates amino acid metabolism and resistance to oxidative stress. *Mol Cell* **11**, 619-633 (2003).
37. I. Lassot, E. Segeral, C. Berlioz-Torrent, H. Durand, L. Groussin, T. Hai, R. Benarous, F. Margottin-Goguet, ATF4 degradation relies on a phosphorylation-dependent interaction with the SCF(betaTrCP) ubiquitin ligase. *Mol Cell Biol* **21**, 2192-2202 (2001).
38. I. Lassot, E. Estrabaud, S. Emiliani, M. Benkirane, R. Benarous, F. Margottin-Goguet, p300 modulates ATF4 stability and transcriptional activity independently of its acetyltransferase domain. *J Biol Chem* **280**, 41537-41545 (2005).
39. C. Garcia-Jimenez, C. R. Goding, Starvation and Pseudo-Starvation as Drivers of Cancer Metastasis through Translation Reprogramming. *Cell Metab* **29**, 254-267 (2019).
40. K. Friend, H. A. Brooks, N. E. Propson, J. A. Thomson, J. Kimble, Embryonic Stem Cell Growth Factors Regulate eIF2alpha Phosphorylation. *PLoS One* **10**, e0139076 (2015).
41. P. van Galen, N. Mbong, A. Kreso, E. M. Schoof, E. Wagenblast, S. W. K. Ng, G. Krivdova, L. Jin, H. Nakauchi, J. E. Dick, Integrated Stress Response Activity Marks Stem Cells in Normal Hematopoiesis and Leukemia. *Cell Rep* **25**, 1109-1117 e1105 (2018).
42. A. C. Hsieh, H. G. Nguyen, L. Wen, M. P. Edlind, P. R. Carroll, W. Kim, D. Ruggero, Cell type-specific abundance of 4EBP1 primes prostate cancer sensitivity or resistance to PI3K pathway inhibitors. *Sci Signal* **8**, ra116 (2015).
43. Y. X. Feng, E. S. Sokol, C. A. Del Vecchio, S. Sanduja, J. H. Claessen, T. A. Proia, D. X. Jin, F. Reinhardt, H. L. Ploegh, Q. Wang, P. B. Gupta, Epithelial-to-mesenchymal transition activates PERK-eIF2alpha and sensitizes cells to endoplasmic reticulum stress. *Cancer Discov* **4**, 702-715 (2014).
44. M. Jewer, L. Lee, M. Leibovitch, G. Zhang, J. Liu, S. D. Findlay, K. M. Vincent, K. Tandoc, D. Dieters-Castator, D. F. Quail, I. Dutta, M. Coatham, Z. Xu, A. Puri, B. J. Guan, M. Hatzoglou, A. Brumwell, J. Uniacke, C. Patsis, A. Koromilas, J. Schueler, G. M. Siegers, I. Topisirovic, L. M. Postovit, Translational control of breast cancer plasticity. *Nat Commun* **11**, 2498 (2020).
45. E. Y. Cai, M. N. Kufeld, S. Schuster, S. Arora, M. Larkin, A. A. Germanos, A. C. Hsieh, S. Beronja, Selective Translation of Cell Fate Regulators Mediates Tolerance to Broad Oncogenic Stress. *Cell Stem Cell* **27**, 270-283 e277 (2020).
46. M. Sharma, B. Bashir, E. Hamilton, D. Juric, K. Papadopoulos, D. Richardson, G. Shapiro, G. Hodgson, N. Ke, A. D'Ippolito, S. Henry, L. Zhu, M. Rosario, H. Jolin, D. Roth, V. Klimek, C. Madigan, M. Kelly, Tolerability and preliminary clinical activity of SY-5609, a highly potent and selective oral CDK7 inhibitor, in patients with advanced solid tumors. *Ann Oncol* **32**, S587-S588 (2021).
47. G. Biffi, T. E. Oni, B. Spielman, Y. Hao, E. Elyada, Y. Park, J. Preall, D. A. Tuveson, IL1-Induced JAK/STAT Signaling Is Antagonized by TGFbeta to Shape CAF Heterogeneity in Pancreatic Ductal Adenocarcinoma. *Cancer Discov* **9**, 282-301 (2019).

48. S. F. Boj, C. Hwang, L. A. Baker, I. I. Chio, D. D. Engle, V. Corbo, M. Jager, M. Ponz-Sarvise, H. Tiriac, M. S. Spector, A. Gracanin, T. Oni, K. H. Yu, R. van Boxtel, M. Huch, K. D. Rivera, J. P. Wilson, M. E. Feigin, D. Ohlund, A. Handly-Santana, C . M. Ardito-Abraham, M. Ludwig, E. Elyada, B. Alagesan, G. Biffi, G. N. Yordanov, B. Delcuze, B. Creighton, K. Wright, Y. Park, F. H. Morsink, I. Q. Molenaar, I. H. Borel Rinkes, E. Cuppen, Y. Hao, Y. Jin, I. J. Nijman, C. Iacobuzio-Donahue, S. D. Leach, D. J. Pappin, M. Hammell, D. S. Klimstra, O. Basturk, R. H. Hruban, G. J. Offerhaus, R. G. Vries, H. Clevers, D. A. Tuveson, Organoid models of human and mouse ductal pancreatic cancer. *Cell* **160**, 324-338 (2015)
49. N. E. Sanjana, O. Shalem, F. Zhang, Improved vectors and genome-wide libraries for CRISPR screening. *Nat Methods* **11**, 783-784 (2014).
50. O. Shalem, N. E. Sanjana, E. Hartenian, X. Shi, D. A. Scott, T. Mikkelson, D. Heckl, B. L. Ebert, D. E. Root, J. G. Doench, F. Zhang, Genome-scale CRISPR-Cas9 knockout screening in human cells. *Science* **343**, 84-87 (2014).
51. C. Trapnell, L. Pachter, S. L. Salzberg, TopHat: discovering splice junctions with RNA-Seq. *Bioinformatics* **25**, 1105-1111 (2009).
52. S. Anders, P. T. Pyl, W. Huber, HTSeq--a Python framework to work with high-throughput sequencing data. *Bioinformatics* **31**, 166-169 (2015).
53. M. D. Robinson, D. J. McCarthy, G. K. Smyth, edgeR: a Bioconductor package for differential expression analysis of digital gene expression data. *Bioinformatics* **26**, 139-140 (2010).
54. H. Chen, P. C. Boutros, VennDiagram: a package for the generation of highly-customizable Venn and Euler diagrams in R. *BMC Bioinformatics* **12**, 35 (2011).
55. M. D. Young, M. J. Wakefield, G. K. Smyth, A. Oshlack, Gene ontology analysis for RNA-seq: accounting for selection bias. *Genome Biol* **11**, R14 (2010).
56. A. Subramanian, P. Tamayo, V. K. Mootha, S. Mukherjee, B. L. Ebert, M. A. Gillette, A. Paulovich, S. L. Pomeroy, T. R. Golub, E. S. Lander, J. P. Mesirov, Gene set enrichment analysis: a knowledge-based approach for interpreting genome-wide expression profiles. *Proc Natl Acad Sci U S A* **102**, 15545-15550 (2005).
57. A. Liberzon, A. Subramanian, R. Pinchback, H. Thorvaldsdottir, P. Tamayo, J. P. Mesirov, Molecular signatures database (MSigDB) 3.0. *Bioinformatics* **27**, 1739-1740 (2011).
58. B. Langmead, C. Trapnell, M. Pop, S. L. Salzberg, Ultrafast and memory-efficient alignment of short DNA sequences to the human genome. *Genome Biol* **10**, R25 (2009).
59. Y. Zhang, T. Liu, C. A. Meyer, J. Eeckhoute, D. S. Johnson, B. E. Bernstein, C. Nusbaum, R. M. Myers, M. Brown, W. Li, X. S. Liu, Model-based analysis of ChIP-Seq (MACS). *Genome Biol* **9**, R137 (2008).
60. J. Loven, H. A. Hoke, C. Y. Lin, A. Lau, D. A. Orlando, C. R. Vakoc, J. E. Bradner, T. I. Lee, R. A. Young, Selective inhibition of tumor oncogenes by disruption of super-enhancers. *Cell* **153**, 320-334 (2013).
61. W. A. Whyte, D. A. Orlando, D. Hnisz, B. J. Abraham, C. Y. Lin, M. H. Kagey, P. B. Rahl, T. I. Lee, R. A. Young, Master transcription factors and mediator establish super-enhancers at key cell identity genes. *Cell* **153**, 307-319 (2013).
62. C. Y. McLean, D. Bristor, M. Hiller, S. L. Clarke, B. T. Schaar, C. B. Lowe, A. M. Wenger, G. Bejerano, GREAT improves functional interpretation of cis-regulatory regions. *Nat Biotechnol* **28**, 495-501 (2010).
63. F. Ramirez, D. P. Ryan, B. Gruning, V. Bhardwaj, F. Kilpert, A. S. Richter, S. Heyne, F. Dundar, T. Manke, deepTools2: a next generation web server for deep-sequencing data analysis. *Nucleic Acids Res* **44**, W160-165 (2016).

64. G. M. O'Kane, B. T. Grunwald, G. H. Jang, M. Masoomian, S. Picardo, R. C. Grant, R. E. Denroche, A. Zhang, Y. Wang, B. Lam, P. M. Krzyzanowski, I. M. Lungu, J. M. S. Bartlett, M. Peralta, F. Vyas, R. Khokha, J. Biagi, D. Chadwick, S. Ramotar, S. Hutchinson, A. Dodd, J. M. Wilson, F. Notta, G. Zogopoulos, S. Gallinger, J. J. Knox, S. E. Fischer, GATA6 Expression Distinguishes Classical and Basal-like Subtypes in Advanced Pancreatic Cancer. *Clin Cancer Res* **26**, 4901-4910 (2020).
65. T. Stuart, A. Butler, P. Hoffman, C. Hafemeister, E. Papalexi, W. M. Mauck, 3rd, Y. Hao, M. Stoeckius, P. Smibert, R. Satija, Comprehensive Integration of Single-Cell Data. *Cell* **177**, 1888-1902 e1821 (2019).
66. B. Jassal, L. Matthews, G. Viteri, C. Gong, P. Lorente, A. Fabregat, K. Sidiropoulos, J. Cook, M. Gillespie, R. Haw, F. Loney, B. May, M. Milacic, K. Rothfels, C. Sevilla, V. Shamovsky, S. Shorser, T. Varusai, J. Weiser, G. Wu, L. Stein, H. Hermjakob, P. D'Eustachio, The reactome pathway knowledgebase. *Nucleic Acids Res* **48**, D498-D503 (2020).
67. T. Igarashi, H. Izumi, T. Uchiumi, K. Nishio, T. Arao, M. Tanabe, H. Uramoto, K. Sugio, K. Yasumoto, Y. Sasaguri, K. Y. Wang, Y. Otsuji, K. Kohno, Clock and ATF4 transcription system regulates drug resistance in human cancer cell lines. *Oncogene* **26**, 4749-4760 (2007).

Acknowledgments: We thank R. Eisenman, as well as past and present members of the Kugel Laboratory for helpful discussions and specifically L. Boila for his helpful insight with the flow cytometry experiments and N. Yamamoto for her help compiling statistical information.

Funding: This work was supported in part by National Institutes of Health grants 5R37CA241472 to S.K, R01CA223483 to S.R.H, GM126908 to D.H.P, GM135362 to A.C.H, R37CA230617 to A.C.H, a V scholar award (V218-004) from the V Foundation for Cancer Research to S.K, a Swim across America Pancreas Cancer Development Research Award to S.K, a Chromosome Metabolism to N.K, a Cancer training grant 5T32CA009657 to N.K, an American Cancer Society Postdoctoral Fellowship (133107-PF-20-012-01) to N.K, and a Walter Benjamin fellowship from the German Research Foundation to S. Dobersch. This research was supported by the Genomics & Bioinformatics Core and by Elizabeth Cromwell from the Preclinical Modeling Core in Shared Resource of the Fred Hutch/University of Washington Cancer Consortium (P30 CA015704).

Author contributions: NK, JG, ZS, SC, SD, BK, AWP, CW, JS, JK, AY, CB, KF, SD, AL collected data. NK, JG, ZS and SK analyzed the data. NK, JG, ZS, SK, ACH, SRH, FN and DP contributed to the experimental design. NK, JG, ZS, SRH and SK wrote the paper. All authors discussed the results and commented on the manuscript.

Competing Interests: S. Dobersch owns stocks from QIAGEN and Merck**.** All other authors declare no competing interests.

Data and materials availability: All data associated with this study are present in the paper or the supplementary materials. The RNA-seq and ChIP-seq data generated in this study are publicly available in GEO at National Center for Biotechnology Information under the accession number GSE181606.

SUPPLEMENTAL MATERIALS AND METHODS

Cell lines. PDA cell lines were obtained from the American Type Culture Collection (ATCC) and grown in their required growth medium per the ATCC description. SUIT2 was obtained from Japanese Collection of Research Biosources cell bank. To establish 2D mouse pancreatic cancer cell lines, freshly isolated tumor specimens from *Sirt6$^{f/f}$;KrasG12D;p53$^{f/+}$;p48-Cre* (*Sirt6* KO) and *Sirt6$^{+/+}$;KrasG12D;p53$^{f/+}$;p48-Cre* (*Sirt6* WT) mice were minced with sterile razor blades, digested with trypsin for 30 minutes at 37°C, and then resuspended in RPMI and supplemented with 10% fetal bovine serum and 1% penicillin (100 U/ml)/streptomycin (100 Ug/ml) (Invitrogen Gibco) and seeded on plates coated with rat tail collagen (BD Biosciences). Cells were passaged by trypsinization. All studies were done on cells cultivated for less than ten passages. 2D mouse pancreatic cancer cell lines are listed in Table S1.

Organoids. Mouse pancreatic organoids were derived and cultured according to the methods detailed in (*48*). Mouse tissue was minced and digested in digestion media [DMEM + glucose, L-glutamine, sodium pyruvate (GIBCO) with 10% fetal bovine serum and 1% penicillin (100 U/ml)/streptomycin (100 Ug/ml) (Invitrogen GIBCO)] containing dispase (0.125 mg/ml, GIBCO) and collagenase II (0.125 mg/ml, GIBCO) for 2 hours at 37°C and 15rpm. For mouse specimens, the tissue was further dissociated with TrypLE (GIBCO) for 15 minutes.

Cells isolated from mouse tissue were embedded in Matrigel and cultured in Mouse Feeding Medium (AdDMEM/F12 medium supplemented with HEPES [1×, Invitrogen], Glutamax [1×, Invitrogen], penicillin/streptomycin [1×, Invitrogen], B27 [1×, Invitrogen], Primocin [1 mg/ml, InvivoGen], N-acetyl-L-cysteine [1 mM, Sigma], RSPO1-conditioned medium [10% v/v], Noggin [0.1 µg/ml, Peprotech], Mouse EGF, [50 ng/ml, Peprotech], Gastrin [10 nM, Sigma], FGF10, 100 ng/ml, Preprotech], Nicotinamide [10 mM, Sigma-Aldrich], and A83-01 [0.5 µM, Tocris]).

To passage, organoids were dissociated into single cells using TrypLE (GIBCO) and then they were re-seeded into Matrigel (Corning). Mouse pancreatic organoids are listed in Table S1.

Proliferation IC50 assay. Cells were plated in 96-well plates (1,000 cells/well) in culture medium. The following day, increasing doses of either THZ1, gemcitabine, flavopiridol, YKL-5-124, palbociclib, THZ1-R, THZ531, JQ1, I-BET151, I-BET762, or DMSO control (BP231-100; ThermoFisher Scientific) were added, and the cells were allowed to grow until DMSO-treated wells reached confluency (5–7 days). To quantify viable cells, MTT (3-(4,5-Dimethylthiazol-2-yl)-2,5-diphenyltetrazolium bromide) (M-6494; ThermoFisher Scientific) was added to the culture media at a final concentration of 1 mg/mL and incubated for 3 hours at 37°C. Formazan crystals were solubilized with 100 µL/well of DMSO and absorbance was read at 490 nm and normalized to DMSO control. MTT proliferation assays were performed in duplicate, and data are represented as mean ± SEM among three independent experiments unless otherwise indicated in the figure legend.

Real-time quantitative PCR (qRT-PCR). Total RNA was extracted with the RNeasy Mini Kit (Qiagen) as described by the manufacturer. For cDNA synthesis, 1µg of total RNA was reverse-transcribed using the QuantiTect Reverse Transcription Kit (Qiagen). Real-time quantitative PCR was run in duplicate using SYBR green master mix (Roche), following the manufacturer's instructions, with the exception that the final volume was 12.5 µl of SYBR green reaction mix. Real-time monitoring of PCR amplification was performed using the CFX 394 detection system (Biorad). Data were expressed as relative mRNA abundance normalized to the *β-ACTIN* expression level in each sample and are represented as mean ± s.e.m. between two independent

experiments unless otherwise indicated in the figure legend. The primer sequences are listed in Table S2.

Protein isolation and Western blot. Chromatin fractions were prepared by resuspending the cell pellet in lysis buffer containing 10mM HEPES pH 7.4, 10 mM KCl, 0.05% NP-40 supplemented with a protease inhibitor cocktail (Complete EDTA-free, Roche Applied Science), 5μM TSA, 5mM sodium butyrate, 1mM DTT, 1mM PMSF, 50mM NaF, 0.2mM sodium orthovanadate and phosphatase inhibitors (Phosphatase Inhibitor Cocktail Sets I and II, Calbiochem) and incubated on ice for 20 minutes. The lysate was then centrifuged at 14,000 rpm for 10 minutes at 4°C. The supernatant was removed (cytosolic fraction) and the pellet (nuclei) was acid-extracted using 0.2N HCl and incubated on ice for 20 minutes. The lysate was then centrifuged at 14,000 rpm for 10 minutes at 4°C. The supernatant (contains acid soluble proteins) was neutralized using 1M Tris-HCl pH 8.

Whole cell lysate (WCL) was prepared either by direct boiling of cells in sample buffer or by lysis with lysis buffer. For lysis by direct boiling, cells were trypsinized and centrifuged at 5,000 rpm for 2 minutes at 4ºC. Pellets were resuspended in cold PBS and counted using a TC20 Automated Cell Counter (Biorad). Cells were again centrifuged at 5,000 rpm for 2 minutes at 4ºC. PBS was aspirated, and sample buffer (Invitrogen) with 5% β-mercaptoethanol was added directly to the cell pellet at a ratio of 200μL per $1x10^6$ cells. Pellets were boiled for 15 minutes at 95ºC. For lysis with lysis buffer, the cell pellet was resuspended in RIPA buffer supplemented with a protease inhibitor cocktail (Complete EDTA-free, Roche Applied Science), 5μM TSA, 5mM sodium butyrate, 1mM DTT, and phosphatase inhibitors (Phosphatase Inhibitor Cocktail Sets I, II, and III Calbiochem) and incubated on ice for 20 minutes. The lysate was then centrifuged at 14,000

rpm for 10 minutes at 4°C and the supernatant was harvested. Protein concentration was measured by using a BCA protein assay kit (Pierce). 20μg of the cell lysate (from lysis with buffer) or 10uL of cell lysate (from lysis by direct boiling) was electrophoresed on a 4-20% gradient polyacrylamide gel with SDS (Biorad) and electroblotted onto polyvinylidene difluoride membranes (PVDF) (Millipore). Membranes were blocked in TBS with 5% non-fat milk and 0.1% Tween and probed with antibodies. Bound proteins were detected with horseradish-peroxidase-conjugated secondary antibodies (Vector Biolaboratories) and Clarity Max Western ECL Blotting Substrate (Biorad). Antibodies used were anti-RNA polymerase II CTD phospho S2(Abcam, ab5095), anti-RNA polymerase II CTD phospho S5 (ab5131), anti-RNA polymerase II CTD phospho S7 (ab126537), anti-Total RNA polymerase II (sc-55492), anti-Myc (ab32072), anti-CDK7 (sc-7344), anti-CDK9 (sc-13130), anti-CDK12 (CST #11973), anti-CDK13 (CDC2L5, bethyl lab A301-458A), anti-Cleaved Caspase-3 (CST #9664), anti-PARP (CST #9542), anti-phosphorylated eIF2α (CST #3597), anti-Total eIF2α (CST #9722), anti-ATF4 (CST #11815), anti-xCT (SLC7A11) (Novus NB300-318), anti-SESN2 (Proteintech 10795-1-AP), anti-GADD34 (Proteintech 10449-1-AP), anti-SIRT6 (CST #12486), anti-betaTRCP (CST #4394), anti-LIN28b (CST #4196), anti-IMP1 (CST #8482), anti-IMP2 (CST #14672), anti-IMP3 (Proteintech 14642-1-AP), anti-HMGA2 (CST #8179), anti-phosphorylated p70 S6K (CST # 9234), anti-Total p70 S6K (CST #2708), anti-phosphorylated S6 (CST #4858), anti-Total S6 (CST #2217), anti-phosphorylated 4E-BP1 (CST #2855) anti-Total 4E-BP1 (CST #9644), anti-phosphorylated mTOR (CST #2974), anti-Total mTOR (CST #2972), anti-phosphorylated ATK (CST #13038), anti-phosphorylated ULK1 (CST #14202), anti-vinculin (sc-73614) and anti-betaACTIN (Sigma A5316) as a loading control.

For Western blots performed on organoids, organoids were cultured in feeding media containing either 1uM THZ1 or DMSO control for 24 hours. Organoids were pelleted using Cell Recovery Solution (Corning) to dissolve Matrigel, lysed in RIPA buffer, and processed as detailed above.

Constructs and viral infection. Full-length wild-type *SIRT6* cDNA (variant 1; NM_016539.2) was amplified from the HPDE cells using the following primers (CA**GGATCC** TTGTTCCCGTGGGGCAGTCGAGG; bold sequence indicates BamHI site) and (CA**GAATTC**CTACAAAAAGCCCCACCCTCCC; bold sequence indicates EcoRI site). After PCR amplification and subcloning into pGEMT (Promega), *SIRT6* constructs were digested with BamHI and EcoRI, and purified with the QIAquick Gel extraction kit (Qiagen). Digested *SIRT6* was subcloned into pRetroX-TIGHT-Pur plasmid (Clontech) and site-directed mutagenesis of wild-type *SIRT6* used the QuikChange Lightning site-directed mutagenesis kit (Stratagene) to generate the H133Y, catalytic dead mutant. pLVX-Tet-On was obtained from Clontech. Full-length wild-type *CDK7* expression vector (EV) in the pLX304 backbone was obtained from Harvard Medical School (clone ID # 1832). LacZ control vector in pLX304 backbone was obtained from Addgene (Plasmid #42560). Lightning site-directed mutagenesis kit (Stratagene) to generate the C312S mutant from the *CDK7* EV. Viral particles containing the above mentioned plasmids were synthesized using lentiviral (pCMVdR8.91) packaging plasmids with pCMV-VSV-G (Addgene). Cells were infected by incubating with virus and 10 μg/ml polybrene. Twenty-four hours later, cells were selected in 0.5-2.5 μg/ml puromycin for at least two days and the pooled populations were used for various experiments.

CRISPR knockout growth curves. Single guide RNAs (sgRNAs) for *CDK7*, *CDK9*, *CDK12*, & *CDK13* were designed using the CRISPick tool from the Broad Institute and are listed in Table S3. sgRNAs were cloned into the LentiCRISPRv2 backbone plasmid as previously described (*49, 50*). Viral particles containing the above-mentioned plasmids were synthesized as described previously in the Constructs and viral infection section. Infected cells were then plated as paired experiments for growth curve assays and Western blot verification of knockout. Lysates for Western blot analyses were prepared by lysis with lysis buffer as described previously in the Protein isolation and Western blot section.

Cells were plated in 96-well plates (2,000 cells/well) in culture medium for growth curve assays following viral infection, this is termed Day 0. The following day, termed Day 1, quantification of viable cells using MTT (M-6494; ThermoFisher Scientific) at a final concentration of 1 mg/mL in culture media then incubated for 3 hours at 37°C was performed. The same method of MTT addition to form crystals was repeated for Days 1-7. On Day 7, formazan crystals were solubilized with 100 µL/well of DMSO and absorbance was read at 490 nm and normalized to DMSO control. MTT growth curve assays were performed in duplicate, and data are represented as mean ± SEM among three independent experiments unless otherwise indicated in the figure legend.

Plasmid transfection. The following constructs were kindly gifted from A. Marazuela Duque (Bellvitge Biomedical Research Institute): empty vector and *SIRT6* overexpression in the pcDNA_4/TO backbone. pRK5-ATF4 Flag was kindly gifted from the Eisenman laboratory at Fred Hutch (Addgene Plasmid #26114). The above-mentioned plasmids were transfected into cells in 10cm culture dishes (or 12-well plates for immunofluorescence, respectively) by direct additions

of 1 mL (100ul) of OptiMEM low-serum media (Gibco) containing 20µL (2µL) of Lipofectamine 2000 (Invitrogen) and 2µg (0.2µg) of total plasmid DNA. Media was replaced with fresh culture media after incubation for 4 hours at 37°C and cells were cultured for an additional 20 hours (24 hours total).

siRNA transfection. Cells were reverse transfected with siRNAs in 10 cm culture dishes by direct addition of 4 mL of cell-containing culture media to 1 mL of OptiMEM low-serum media (Gibco) containing 20µL of Lipofectamine RNAiMAX (Invitrogen) and either non-targeting (Control) or targeting siRNAs (0.25µM). Media was replaced with fresh culture media after incubation at 16 hours at 37°C and cells were cultured for an additional 56 hours (72 hours total) unless otherwise stated in the figure legend, after which cell pellets were extracted for downstream assays including Western blotting and qRT-PCR. siRNAs were obtained from Dharmacon: *SIRT6* (L-013306-00), *ATF4* (L-005125-00), *GADD34* (L-004442-02), *beta-TRCP* (L-003463-00), *Control* (D-001810-10).

Apoptosis assay. Cells were washed twice with cold PBS and then resuspended in 1X Binding Buffer at a concentration of 1 x 10^6 cells/ml. 1 x 10^5 cells of the solution were transferred to a 5 ml culture tube, and 5 µl of FITC Annexin V and 5 µl Propidium iodide (FITC Annexin V Apoptosis Detection Kit, BD Pharmingen) were added to the cells and incubated for 15 minutes at RT (25°C) in the dark. After this time, 400 µl of 1X Binding Buffer to each tube and Annexin V positive cells and Propidium iodide positive cells were analyzed by flow cytometry. Data are shown as mean ± SEM between triplicates and are representative of three independent experiments.

Cell cycle analysis. Briefly, cells were resuspended in 500 µl of PBS and fixed in ethanol by adding drop-wise 1ml of 70 % ethanol. Fixed cells were incubated at 4°C overnight, washed with PBS and resuspended in 500 µl of PBS-0.1% Triton-X-100 supplemented with 100 µg/ml of RNAse A and 10 µg/ml of propidium iodide. Samples were incubated at RT (25°C) for 30 minutes and then DNA content analyzed by flow cytometry. Cell cycle analysis was performed using the FlowJo software. Data are shown as mean ± SEM between triplicates and are representative of three independent experiments.

Chromatin immunoprecipitation. Cells were cross-linked with 1% paraformaldehyde for 15 minutes at room temperature. The reaction was quenched for 5 minutes at room temperature by adding 0.125 M glycine. After three washes with 1X PBS, cells were lysed with lysis buffer (1% SDS, 10 mM EDTA pH 8, 50 mM Tris-HCl pH 8) supplemented with protease and deacetylase (TSA) inhibitors. Lysates were sonicated on ice using a QSONICA Q800R3 sonicator (10 seconds ON, 20s OFF, 20% AMP; samples in 4ºC water bath throughout sonication cycles). Size of fragments obtained (between 200 and 1,200 bp) was confirmed by electrophoresis. Soluble chromatin was collected after centrifugation at 14,000 rpm at 4°C for 10 minutes and 1 million cells was diluted to 1/5 in dilution buffer (1% Triton X-100, 2 mM EDTA, 150 mM NaCl, 20 mM Tris-HCl pH 8.1) supplemented with protease and deacetylase inhibitors. Soluble chromatin (1%) was kept as input control. Soluble chromatin was precleared with 100 µg/ml of salmon sperm (Amersham Biosciences), 2.5 µg/ml of unspecific IgGs, and protein-ASepharose at 50% overnight at 4°C in rotation. After centrifugation, supernatants were collected and specific antibodies were added. Mixtures were incubated at 4°C for 8 hrs in rotation and then incubated overnight at 4°C in

rotation with protein-A-Sepharose at 50% (Roche). Beads were collected and washed sequentially at 4°C for 10 minutes with TSE I (150 mM NaCl, 0.1% SDS, 1% Triton X-100, 2 mM EDTA, and 20 mM Tris-HCl (pH 8.1)), TSE II (500 mM NaCl, 0.1% SDS, 1% Triton X-100, 2 mM EDTA, and 20 mM Tris-HCl (pH 8.1)), and buffer III (0.25 LiCl, 1% Nonidet P-40, 1% deoxycholate, 1 mM EDTA, and 10 mM Tris-HCl (pH 8.1)). Beads were washed once with 1X PBS by pipetting and immunoprecipitates were eluted two times (20 minutes incubation) with elution buffer (0.1 M NaHCO3 and 1% SDS). Reversion of cross-linking was performed overnight by adding 0.2M NaCl and heating samples and input controls at 65°C. Samples were then treated with 0.2 mg/mL RNAse A (Qiagen) and incubated for 1hr at 37°C followed by addition of 0.01M EDTA, 0.04M Tris-HCl pH 6.5 and 4 U/mL of Proteinase K (Promega) and samples were incubated at 45°C for 1 hr. DNA was then purified using the QIAquick spin kit (Qiagen).

RNA-seq data analysis: RNA-seq libraries were prepared from extracted total RNA using the TruSeq RNA Sample Preparation v2 kit (Illumina). Libraries were barcoded and pooled, with 18 samples in a single pool, and sequenced using 50bp paired-end reads across three Illumina HiSeq 2500 lanes in “Rapid Run” mode. Illumina's on-board RTA v1.18.66.3 software performed real-time image processing and cluster tracking, followed by off-line application of Illumina's bcl2fastq Conversion Software v1.8.4 to demultiplex the pool and generate FASTQ files for each sample. An average of 29.9M 50bp paired-end reads per sample passed Illumina’s default quality filters and were retained for further analysis. Reads were aligned to the human genome reference GRCh38/hg38 using TopHat v2.1.0 (*51*). Counts were generated from TopHat alignments for each gene using the Python package HTSeq v0.6.1 (*52*). Genes with low counts across all samples were removed prior to TMM normalization and identification of differentially expressed genes using the Bioconductor package edgeR v3.18.1 (*53*). Multiple testing correction was applied to control

false discovery rate (FDR) using the Benjamini-Hochberg method. Differentially expressed genes were defined as having $|\log_2(\text{ratio})| \geq 1$ (± 2-fold) at an FDR of 5%. Venn diagrams were generated from significantly downregulated genes in each comparison using the R package VennDiagram (*54*). Gene ontology enrichment analysis was performed on genes that were significantly downregulated in BxPC3 and Panc3.27, but not SUIT2, using the Bioconductor package goseq v1.28.0 (*55*), reporting GO:BP categories that are significantly over represented at an FDR of 5%. Genes from BxPC3 and Panc3.27 significance testing were ranked by logFC and used to perform GSEA Preranked Gene Set Enrichment Analysis (*56*) with all gene sets from MSigDB v6.1 (*57*). Sequencing data have been deposited in GEO at National Center for Biotechnology Information under the accession number GSE181606.

ChIP-seq data analysis: ChIP-seq libraries were prepared with the KAPA HyperPrep kit (Roche). Libraries were barcoded and pooled, with 12 samples in a single pool, and sequenced using 50bp paired-end reads on two Illumina HiSeq 2500 lanes in "Rapid Run" mode. Illumina's on-board RTA v1.18.66.3 software performed real-time image processing and cluster tracking, followed by off-line application of Illumina's bcl2fastq Conversion Software v1.8.4 to demultiplex the pool and generate FASTQ files for each sample. An average of 32.6M read pairs per sample passed Illumuna's default quality filters were retained for further analysis. Reads were aligned to the human genome reference GRCh37/hg19 using Bowtie v1.1.1 (*58*). MACS2 (*59*) was used to call peaks, followed by using ROSE (Rank Ordering of Super Enhancers) (*60, 61*) to stitch together regions of enriched ChIP-seq signal and identify super-enhancers, which were associated with genes using GREAT (Genomic Regions Enrichment of Annotations Tool) v3.0 (*62*). Enhancer signal values produced by ROSE were ranked and plotted, and the inflection point of the curve

was used as a threshold for calling super enhancers. Venn diagrams displaying the overlap between genes that were significantly downregulated in the RNA-seq dataset and super enhancer associated genes from the ChIP-seq dataset were generated using the R package Venn Diagram (*54*).

ChIP-seq data profiling H3K27ac in several additional pancreatic adenocarcinoma cell lines (*14*) were downloaded from the Sequence Read Archive, including H3K27ac.PANC1 (SRR1736436), H3K27ac.HPAF2 (SRR2919438), and H3K27ac.MiaPaca2 (SRR2919439). These samples were aligned as described above. For visualization in IGV, bamCoverage from DeepTools (*63*) was used to generate coverage tracks from the resulting alignments, with CPM normalization and effective genome size set for GRCh37. Sequencing data have been deposited in GEO at National Center for Biotechnology Information under the accession number GSE181606.

Nuclei isolation and nuclear walk-on. Adherent SUIT2 and Panc3.27 cells were grown to 80% confluence in T-150 flasks at 37°C and 5% CO_2 in RPMI 1640 (Gibco 21875034) supplemented with 10% FBS (Gibco 26140079). Nuclei isolations and walk-on reactions were performed as previously described (*30, 31*). Briefly, flavopiridol (NIH AIDS Reagent Program 9925) or THZ1 (a gift from T. Zhang and N.S. Gray) were dissolved in DMSO and the drugs or DMSO only were added to the cells for 1 h prior to harvesting (the final concentration for DMSO was 0.1% and final concentrations of flavopiridol and THZ1 are indicated in the text). Two biological replicates were used for each treatment. Subsequent to the treatments, media was discarded and cells were washed in ice-cold PBS. Fresh lysis buffer (20 mM HEPES pH 7.6, 1% IGEPAL CA-630, 1 mM EDTA, 1 mM spermine, 1 mM spermidine, 1 mM DTT, 0.004 U/µl SUPERase-In [Ambion AM2696], 320 mM sucrose, 0.1% isopropanol-saturated PMSF and cOmplete EDTA-free protease inhibitor cocktail [Roche 11873580001]) was added and cells were quickly scrapped off the flasks before

being layered on top of a sucrose cushion (20 mM HEPES pH 7.6, 1 M sucrose, 1 mM spermine, 1 mM spermidine, 0.1 mM EDTA, 1 mM DTT, 0.004 U/µl SUPERase-In, 0.1% isopropanol-saturated PMSF and cOmplete EDTA-free protease inhibitor cocktail). Cells were spun at 22500 × g for 5 minutes at 4°C. Pelleted nuclei were resuspended in 60 µl storage buffer (20 mM HEPES pH 7.6, 5 mM $MgCl_2$, 5 mM DTT and 25% glycerol) and stored at –80°C.

Isolated nuclei (15 ul) were incubated with nuclear walk-on buffer (20 mM HEPES pH 7.6, 0.5% Sarkosyl, 5 mM $MgCl_2$, 5 mM DTT, 150 mM KCl, 0.25 U/µl SUPERase-In and 0.167 µM α-^{32}P-CTP [PerkinElmer BLU008H001MC]) in the presence or absence of 1.33 ug/ml α-amanitin (Sigma A2263). Incorporation was carried out at 37°C for 10 minutes and stopped with 20 mM EDTA, 0.1M Tris, 1% Sarkosyl and 200 µg/ml Torula Yeast RNA. RNA was isolated with Trizol LS (Ambion 10296028), run in a TBE/urea polyacrylamide gel and stained with ethidium bromide. ImageJ was used to quantify intensities from the same three selected bands on each lane. Correction factors were calculated to account for small differences in loading. Radiolabeled transcripts were visualized with a Fujifilm Typhoon FLA-7000 phosphorimager and counts were generated using the Fujifilm MultiGauge software. These counts were scaled by applying the corrections factors. The plus α-amanitin lanes were subtracted from each corresponding minus α-amanitin lane to obtain the Pol II signal. Error bars represent standard deviation of the fold changes from two biological replicates.

Puromycin incorporation assay. Cells were treated with 1µM puromycin (ThermoFisher Scientific) and incubated at 37ºC for 30 minutes prior to collection and preparation of lysates for western blot analyses as previously described. Antibodies used for this assay were puromycin

(Millipore Sigma, clone 12D10) and β-tubulin as a loading control (Cell Signaling Technologies, 2146S).

Gene set expression scoring of PDA RNA-seq data. A published PDA RNA-seq dataset was used to assess transcriptomic features of PDA subtypes and gene expression was quantified as previously described (*11, 64*). Average expressions of gene sets in each tumor were scored using the AddModuleScore function in Seurat (*65*). Three gene sets from the C2 curated collection in MSigDB v7.2 were scored: IGARASHI ATF4 TARGETS UP (genes up-regulated in A549 cells after knockdown of ATF4 by RNAi), IGARASHI ATF4 TARGETS DN (genes down-regulated in A549 cells after knockdown of ATF4 by RNAi), and REACTOME ATF4 ACTIVATES GENES IN RESPONSE TO ENDOPLASMIC RETICULUM STRESS (*57, 66, 67*). Scores were compared between subtypes by Kruskal-Wallis test or Wilcoxon rank-sum test and resulting p-values were FDR-adjusted.

Polysome fractionations. SUIT2 and AsPc-1 cells were cultured and transfected with either non-targeting or *SIRT6*-targeting siRNA as described above. Cells were harvested by trypsinization, collected in media and centrifuged. The resulting cell pellets were resuspended in 1mL of a 0.10mg/mL stock of cycloheximide in PBS. The cell suspension was incubated on ice for 10 minutes, centrifuged, and the resulting pellet was snap frozen on a dry ice and ethanol slurry before storage at -80C. Frozen cell pellets were lysed in 300 μL of lysis buffer (Tris-HCl, NaCl, $MgCl_2$, 10% NP-40, Triton-X 100, SUPERase-In RNase Inhibitor (Promega), cycloheximide, DTT, DEPC water) for 45 minutes on ice, and vortexed every 10 minutes. Lysates were centrifuged at 9300 x g for 5 minutes at 4°C to pellet cell debris, and the supernatants were transferred into fresh

tubes. A portion of each lysate (30 µL) was reserved as the total RNA input sample and the remaining volume was layered onto 10% to 50% (w/v) linear sucrose gradients for ribosome fractionation (gradients prepared in Seton 7030 ultracentrifuge tubes). The gradients were centrifuged at 37,000 rpm for 2.5 hours at 4°C in a Beckman SW41Ti rotor. Fractions (820 µL each) were collected by upward displacement into collection tubes (Gilson Fraction Collector) through a Bio-Rad EM1 UV monitor (Bio-Rad) for continuous measurement of the absorbance at 254 nm using a Biocomp Gradient Station (Biocomp). Fractions were mixed 1:1 with TRIzol reagent (Ambion) and stored frozen at -80°C until RNA extraction. Extracted RNA from samples Total RNA, and all Fractions were subjected to Tapestation analysis to confirm the presence of the 18S or 28S rRNA. Extracted RNA from samples Total RNA, and all Fractions were used to synthesize cDNA as described above. qRT-PCR was performed as described above, with samples run in triplicate.

Cycloheximide protein stability assay. Cells were treated with 150µg/mL cycloheximide (Sigma-Aldrich) for increasing timepoints and harvested by trypsinization. Lysates for Western blot analyses were prepared by direct boiling in sample buffer as described previously in the Protein isolation and Western blot section.

Immunofluorescence. Cells were plates on 18mm coverslips #1.5 thickness in 12-well plates. Coverslips were washed once with cold 1x PBS and fixed with 2% paraformaldehyde for 10 minutes. Coverslips were then washed 4 times with 1x PBS and permeabilization solution (20 mM HEPES, 10 mM NaCl, 3 mM MgCl2, 0.3M sucrose. 0.5% Triton X-100) was added for 10 minutes on ice. Coverslips were then washed 4 times with 1x PBS and blocking solution (5% BSA in PBS)

was added for 30 minutes at room temperature. Coverslips were washed once with 1x PBS and incubated with primary antibodies overnight at 4ºC. The next day, coverslips were washed 4 times with 1x PBS and incubated with Alexa Flour-conjugated secondary antibodies (Invitrogen, 1:500 dilution) for 60 minutes at room temperature in the dark. Coverslips were washed 4 times with 1x PBS and mounted on slides with Vectashield Anti-fade Mounting Media with DAPI (Vector Biolaboratories). Antibodies used were: anti-HA (ab9110), anti-FLAG mouse (Sigma-Aldrich F1804), anti-FLAG rabbit (Sigma-Aldrich F7425), anti-SC35 (ab11826), and anti-ATF4 (CST #11815).

Co-immunoprecipitation. Cells were washed twice with 1x PBS and lysed with lysis buffer (25 mM Tris HCl pH 7.5, 150 mM NaCl, 1% NP40, 10% glycerol, 2 mM EDTA) supplemented with protease and phosphatase inhibitors. Lysates were sonicated using a QSONICA Q800R3 sonicator for 5 minutes (30 seconds ON, 30s OFF, 20% AMP; samples in 4ºC water bath throughout sonication cycles). Lysates rotated for 20 minutes at 4ºC and then were clarified at 15,000 rpm for 10 minutes at 4ºC. Protein was quantified using the Bradford method and adjusted to 2.5 mg/ml. Input controls were also saved and prepared with 4X Laemmli sample buffer accordingly. 1 µg of primary antibodies (Cell Signaling: ATF-4 (D4B8)) or appropriate isotype control were added to 1 mL of respective samples and incubated overnight on a rotator at 4°C. Lysates were added to 50 uL/sample of pre-washed Protein-A-Agarose beads (Roche) the next day and rotated for 2 hours at 4ºC. At the end of the antibody-bead conjugation, beads were collected and washed five times with lysis buffer supplemented with protease and phosphatase inhibitors and 200mM NaCl. After the final wash, immunoprecipitates were collected by boiling beads in 50µL of sample

buffer at 95°C for 10 minutes. Immunoprecipitates (50µL) were then loaded on a 4-20% gradient polyacrylamide gel with SDS (Biorad) for western blot analysis as described previously.

SUPPLEMENTAL FIGURES

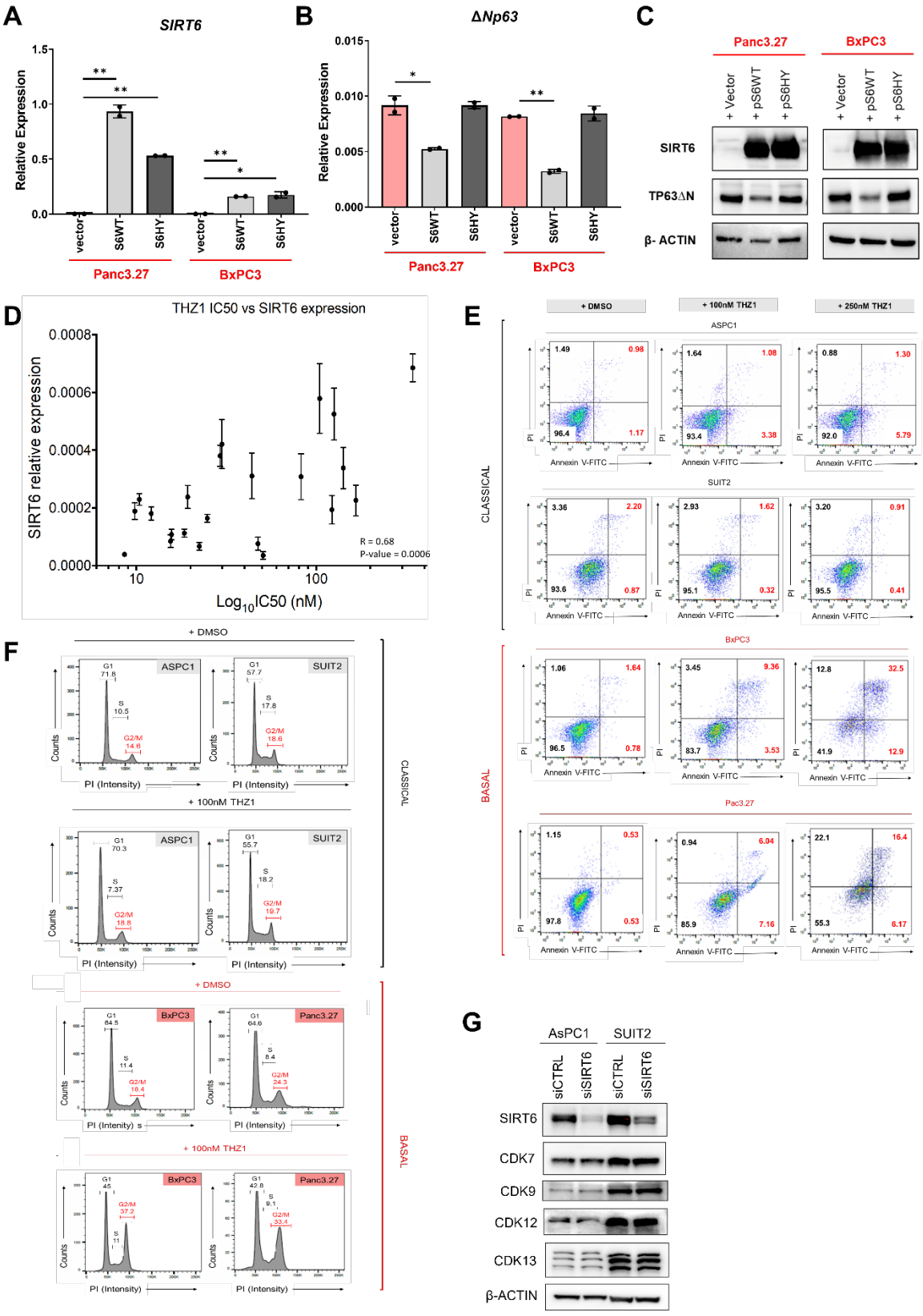

Figure S1. **SIRT6 defines subtype and THZ1 sensitivity in basal and classical PDA**. **A,** qRT-PCR of *SIRT6* in basal PDA lines Panc3.27 and BxPC3 transduced with either empty vector, WT *SIRT6* (pS6WT) or a catalytically inactive point mutant form of *SIRT6* (pS6HY). **B,** qRT-PCR for *TP63* in basal PDA lines from A. **C,** Western blots for SIRT6, TP63 and β-ACTIN in basal PDA lines from A. **D,** Correlation of *SIRT6* expression and THZ1 IC50 in basal and classical PDA cell lines. **E,** Annexin and PI staining of basal (red), compared with classical (black) PDA cell lines after treatment with increasing doses of THZ1 (100nM and 250nM) for 24hrs. **F,** Cell-cycle profiles obtained through PI staining of classical (black) vs basal (red) PDA lines after THZ1 treatment (100nM) for 24hrs. Data are representative of at least 2 independent experiments. **G,** Western blots for SIRT6, CDK7, CDK9, CDK12, CDK13, and β-ACTIN in classical lines treated with non-specific (siCTRL) or *SIRT6*-specific (siSIRT6) siRNAs. Error bars represent +/- SEM between technical duplicates. *p-value ≤ 0.05; **p-value ≤ 0.01 (two-tailed unpaired Student's *t*-test).

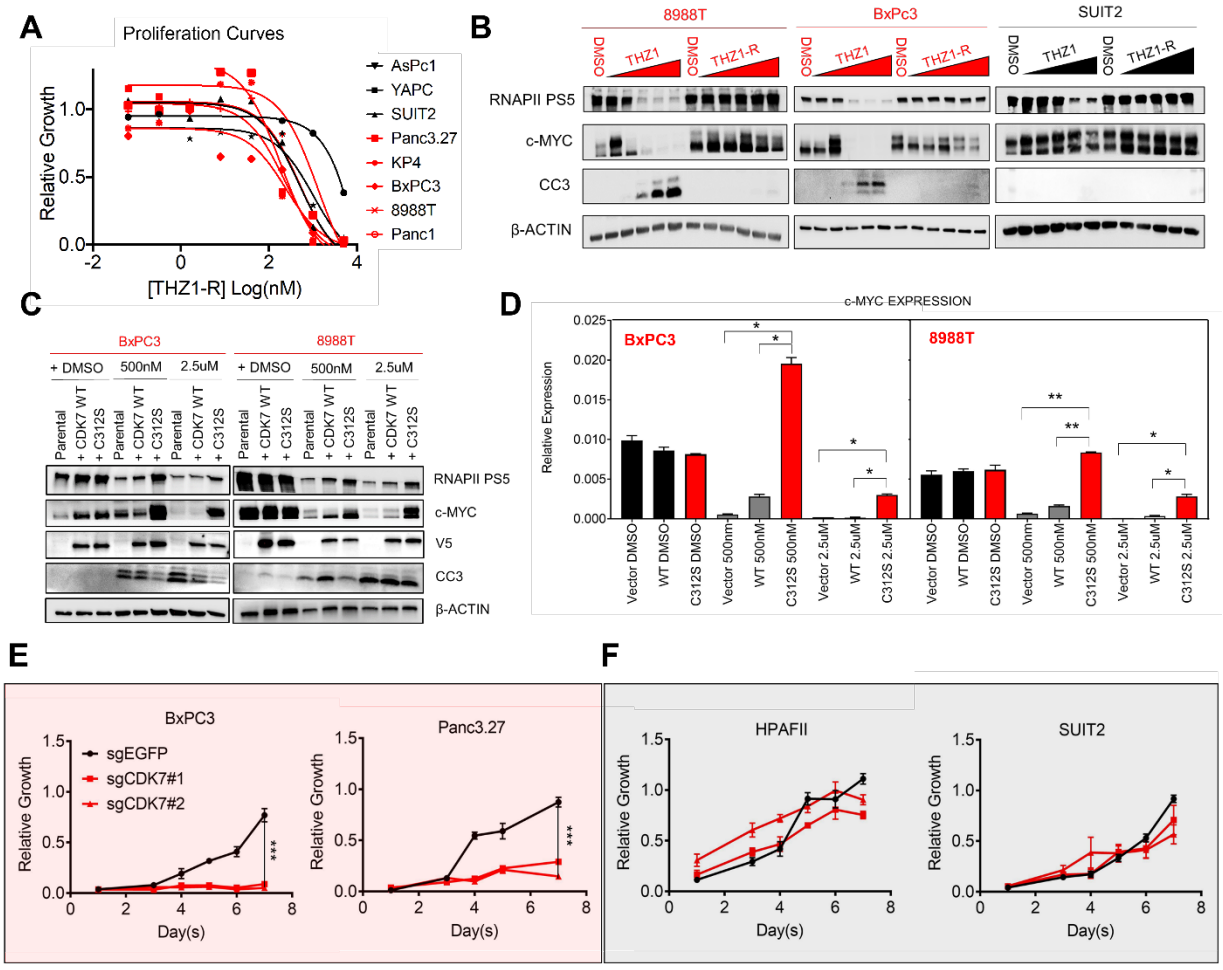

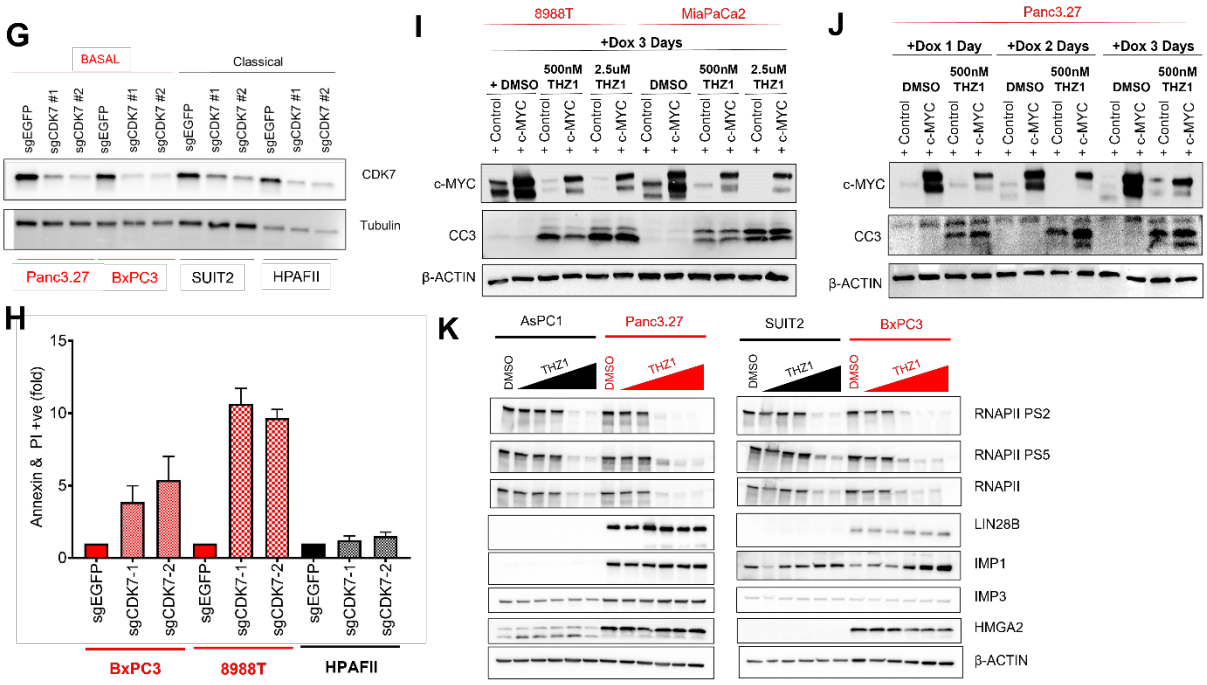

Figure S2. Inhibition of CDK7 is necessary and sufficient for THZ1-induced cytotoxicity in basal PDA. A, Proliferation curves for basal PDA (red), compared with classical (black) PDA cell lines treated with increasing doses of THZ1-R. **B,** Western blots for RNA polymerase II (RNAPII) phosphorylation of serine 5 (PS5), MYC, cleaved caspase 3 (CC3) and β-ACTIN in basal PDA (red), compared with classical (black) PDA cell lines treated with increasing doses of THZ1 or THZ1-R (20nM-5mM). **C,** Basal PDA cell lines were transduced with either wild-type (WT) *CDK7* or the C312S *CDK7* mutant, which is resistant to THZ1 binding. Panels show Western blots for RNAPII PS5, MYC, V5-tag (CDK7), CC3 and β-ACTIN in the above lines treated with 500nM and 2.5□M of THZ1 for 16hrs. **D,** qRT-PCR for *MYC* in transduced basal PDA cell lines treated with 500nM and 2.5□M of THZ1 for 16hrs. Error bars represent +/- 1 SD between technical triplicates. Data are representative of at least 2 independent experiments. **E and F,** Proliferation curves for basal PDA (**E**), compared with classical (**F**) PDA cell lines treated with sgRNAs against *EFGP* (black) or *CDK7* (red). **G,** Western blots for *CDK7* knockout in basal PDA (red), compared with classical PDA cell lines. **H,** Percent apoptosis in basal PDA (red) and classical PDA (black) as measured by Annexin V & PI positive cells treated with sgRNAs against *EFGP* or *CDK7*. **I and J**, Basal PDA cell lines were transduced with either vector control or a tetracycline-inducible *MYC* construct. Cells were treated with 1ug/mL doxycycline for the 3 days (**I**) or 1-3 days (**J**) to induce *MYC* expression before treating with 500nM and 2.5□M of THZ1 for 16hrs. Panels show Western blots for MYC, CC3 and β-ACTIN. **K,** Western blots for RNAPII, PS5, PS2, LIN28b, IMP1, IMP3, HMGA2 and β-ACTIN in basal (red), compared with classical (black) PDA cell lines treated with increasing doses of THZ1 (20nM – 5uM). Assays were performed in duplicate, and data are represented as mean +/- SEM among three independent experiments. *p-value ≤ 0.05; **p-value ≤ 0.01; ***p-value ≤ 0.001 (two-tailed unpaired Student's t-test).

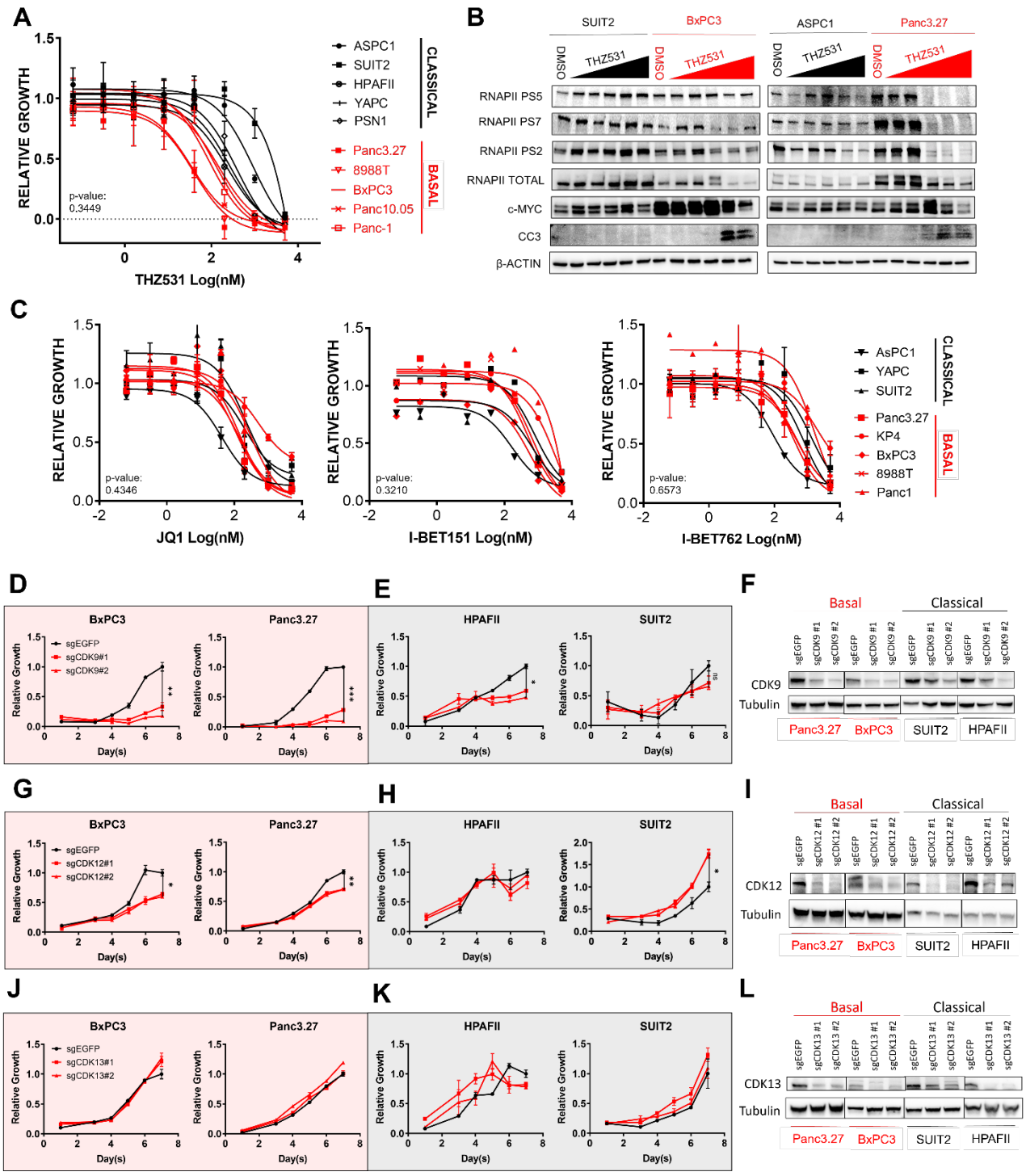
A
RELATIVE GROWTH
THZ531 Log(nM)
p-value:
0.3449
ASPC1
SUIT2
HPAFII
YAPC
PSN1
CLASSICAL
Panc3.27
8988T
BxPC3
Panc10.05
Panc-1
BASAL
B
SUIT2
BxPC3
ASPC1
Panc3.27
DMSO
THZ531
RNAPII PS5
RNAPII PS7
RNAPII PS2
RNAPII TOTAL
c-MYC
CC3
β-ACTIN
C
RELATIVE GROWTH
JQ1 Log(nM)
I-BET151 Log(nM)
I-BET762 Log(nM)
p-value:
0.4346
p-value:
0.3210
p-value:
0.6573
AsPC1
YAPC
SUIT2
CLASSICAL
Panc3.27
KP4
BxPC3
8988T
Panc1
BASAL
D
BxPC3
Panc3.27
sgEGFP
sgCDK9#1
sgCDK9#2
Relative Growth
Day(s)
E
HPAFII
SUIT2
F
Basal
Classical
sgEGFP
sgCDK9 #1
sgCDK9 #2
CDK9
Tubulin
Panc3.27
BxPC3
SUIT2
HPAFII
G
sgCDK12#1
sgCDK12#2
H
I
sgCDK12 #1
sgCDK12 #2
CDK12
J
sgCDK13#1
sgCDK13#2
K
L
sgCDK13 #1
sgCDK13 #2
CDK13

Figure S3. Basal PDA is predominantly sensitive to inhibitors of CDK7 and CDK9. A, Proliferation curves for basal PDA (red), compared with classical (black) PDA cell lines treated with increasing doses of THZ531 **B,** Western blots for RNAPII, PS5, PS7, PS2, MYC, CC3 and β-ACTIN in basal (red), compared with classical (black) PDA cell lines treated with increasing doses of THZ531 (20nM – 5uM). Significant differences in IC50 values for basal versus classical indicated by p-value ≤ 0.05 (two-tailed unpaired Student's t-test with Welch's correction for those with unequal variances) **C,** Proliferation curves for basal PDA (red), compared with classical (black) PDA cell lines treated with increasing doses of bromodomain inhibitors (JQ1, I-BET151, I-BET762). Significant differences in IC50 values for basal versus classical indicated by p-value ≤ 0.05 (two-tailed unpaired Student's t-test with Welch's correction for those with unequal variances). **D and E,** Proliferation curves for basal PDA (**D**), compared with classical (**E**) PDA cell lines treated with sgRNAs against *EFGP* (black) or *CDK9* (red). **F,** Western blots for CDK9 knockout in basal PDA (red), compared with classical PDA cell lines. **G and H,** Proliferation curves for basal PDA (**G**), compared with classical (**H**) PDA cell lines treated with sgRNAs against *EFGP* (black) or *CDK12* (red). **I,** Western blots for CDK12 knockout in basal PDA (red), compared with classical PDA cell lines. **J and K,** Proliferation curves for basal PDA (**J**), compared with classical (**K**) PDA cell lines treated with sgRNAs against *EFGP* (black) or *CDK7* (red). **L,** Western blots for CDK13 knockout in basal PDA (red), compared with classical PDA cell lines. Assays were performed in duplicate, and data are represented as mean +/- SEM among three independent experiments. *p-value ≤ 0.05; **p-value ≤ 0.01; ***p-value ≤ 0.001 (two-tailed unpaired Student's t-test).

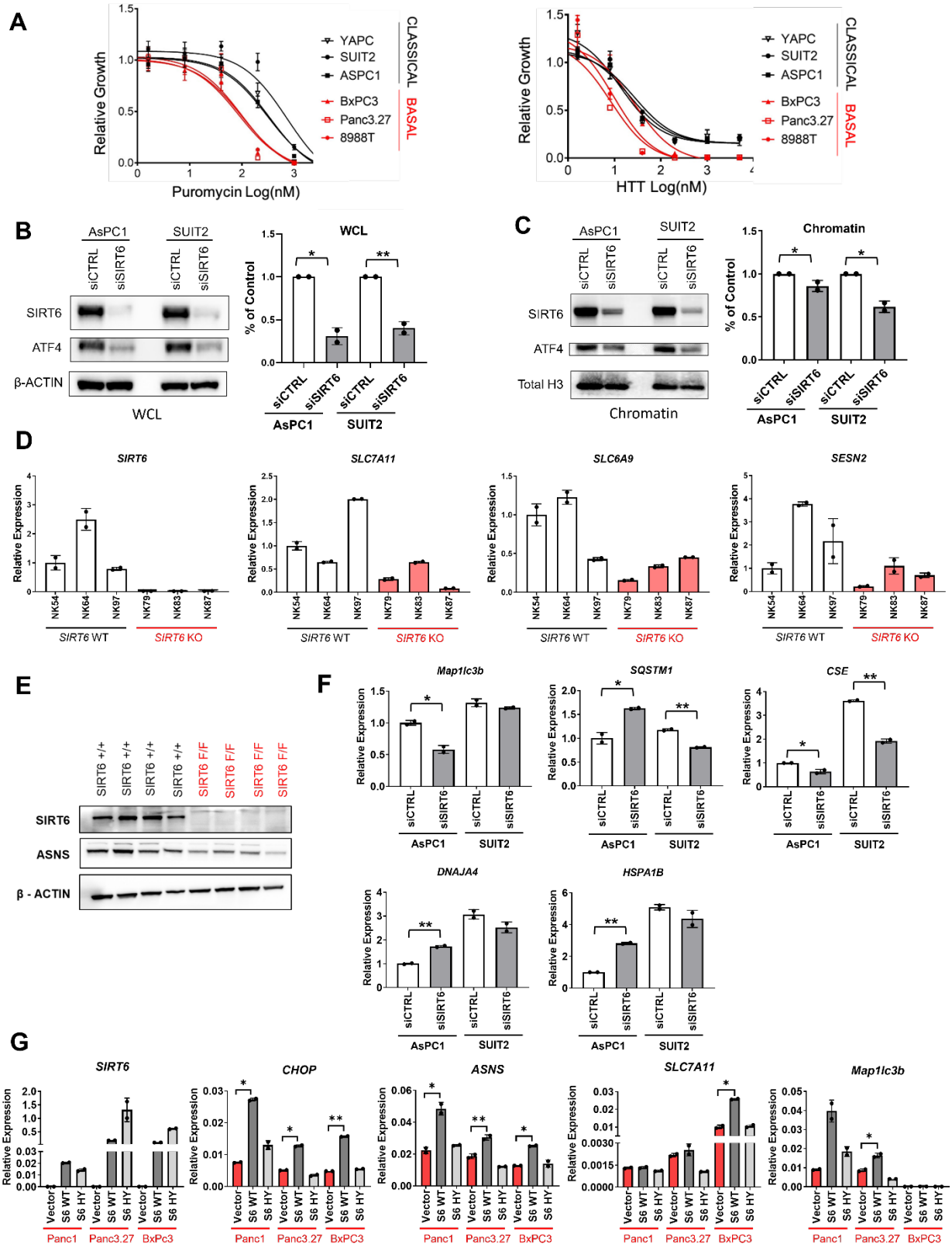
A
Relative Growth
Puromycin Log(nM)
HTT Log(nM)
YAPC
SUIT2
ASPC1
BxPC3
Panc3.27
8988T
CLASSICAL
BASAL
B
AsPC1
SUIT2
siCTRL
siSIRT6
SIRT6
ATF4
β-ACTIN
WCL
% of Control
C
Total H3
Chromatin
D
SIRT6
SLC7A11
SLC6A9
SESN2
Relative Expression
NK54
NK64
NK97
NK79
NK83
NK87
SIRT6 WT
SIRT6 KO
E
SIRT6 +/+
SIRT6 F/F
ASNS
β - ACTIN
F
Map1lc3b
SQSTM1
CSE
DNAJA4
HSPA1B
G
CHOP
ASNS
Vector
S6 WT
S6 HY
Panc1
Panc3.27
BxPc3
BxPC3

Figure S4. SIRT6 influences ATF4 target gene expression. A, Proliferation curves for basal (red), compared with classical (black) PDA cell lines treated with increasing doses of puromycin (top) and homoharringtonine (bottom). **B and C,** Western blots for WCL (B) and chromatin-bound (C) SIRT6, ATF4, β-ACTIN, and H3 with quantification of relative ATF4 levels in classical PDA cells lines treated with non-specific or *SIRT6*-specific siRNAs. **D,** qRT-PCR of *SIRT6*, *SLC7A11*, *SLC6A9*, and *SESN2* in 2D cell lines derived from GEMM pancreatic tumors with (+/+ *SIRT6* WT) and without (F/F *SIRT6* KO) *SIRT6* expression. **E**, Western blots for SIRT6, ASNS and β-ACTIN in 2D cell lines derived from GEMM pancreatic tumors with (+/+ *SIRT6* WT) and without (F/F *SIRT6* KO) *SIRT6* expression. **F**, qRT-PCRs for *SIRT6* and ATF4 target genes involved in autophagy, oxidative stress, and protein folding in classical lines treated with non-specific and *SIRT6*-specific siRNAs. **G,** qRT-PCRs for *SIRT6* and ATF4 target genes in basal lines overexpressing empty vector (vector), wildtype *SIRT6* (S6WT) and a catalytically inactive mutant *SIRT6* (S6HY). Error bars represent +/- SEM between technical duplicates. Data are representative of at least 2 independent experiments. *p-value ≤ 0.05; **p-value ≤ 0.01 (two-tailed unpaired Student's *t*-test).

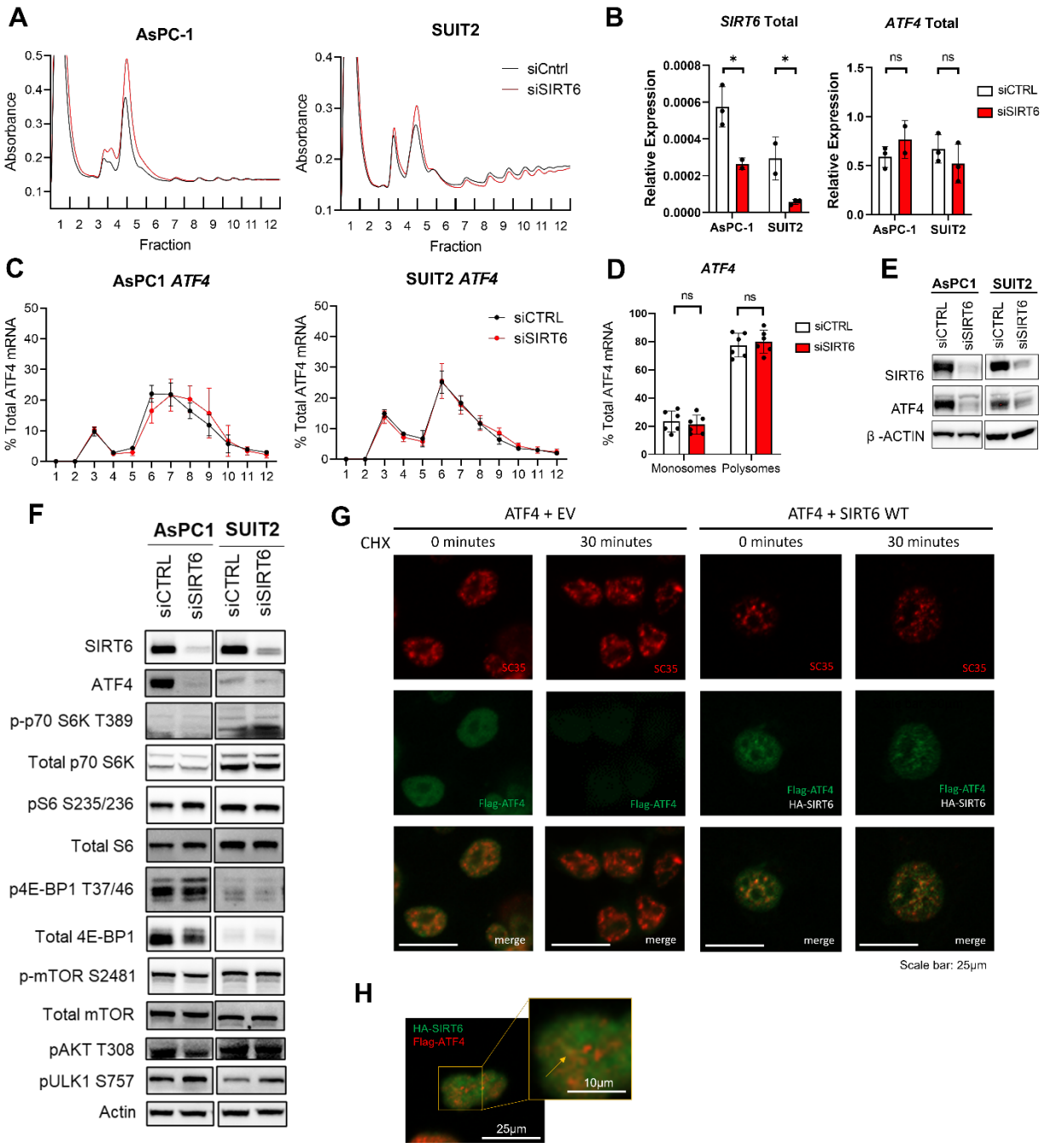
A
AsPC-1
SUIT2
siCntrl
siSIRT6
Absorbance
Fraction
B
SIRT6 Total
ATF4 Total
Relative Expression
siCTRL
siSIRT6
AsPC-1
SUIT2
C
AsPC1 ATF4
SUIT2 ATF4
% Total ATF4 mRNA
D
ATF4
Monosomes
Polysomes
E
AsPC1
SUIT2
SIRT6
ATF4
β -ACTIN
F
AsPC1
SUIT2
siCTRL
siSIRT6
SIRT6
ATF4
p-p70 S6K T389
Total p70 S6K
pS6 S235/236
Total S6
p4E-BP1 T37/46
Total 4E-BP1
p-mTOR S2481
Total mTOR
pAKT T308
pULK1 S757
Actin
G
ATF4 + EV
ATF4 + SIRT6 WT
CHX
0 minutes
30 minutes
SC35
Flag-ATF4
HA-SIRT6
merge
Scale bar: 25μm
H
HA-SIRT6
Flag-ATF4
10μm
25μm

Figure S5. Control of ATF4 by SIRT6 is not mediated by translational regulation or mTOR signaling. A, Full polysome profiling traces for two classical PDA cell lines treated with non-specific (siCTRL) or *SIRT6*-specific (siSIRT6) siRNAs from experiments repeated in triplicates. **B,** qRT-PCR for *SIRT6* and *ATF4* from total RNA extracted from siCTRL (white) and siSIRT6 (red) samples prior to addition of the sample to sucrose gradient for polysome profiling. **C,** qRT-PCR for *ATF4* from all fractions following polysome profiling in the two classical PDA cell lines treated with siCTRL (black) and siSIRT6 (red). **D,** Comparison of amount of *ATF4* mRNA present in monosome versus polysome fractions in siCTRL (white) and siSIRT6 (red) for both classical lines. **E,** Western blots for SIRT6, ATF4, and β-ACTIN for the two classical PDA cell lines treated with non-specific (siCTRL) or SIRT6-specific (siSIRT6) siRNAs. **F,** Western blots for SIRT6, ATF4, mTOR (phospho- and total), mTOR pathway components and β-ACTIN in classical lines treated with non-specific (siCTRL) or SIRT6-specific (siSIRT6) siRNAs. **G,** Immunofluorescence for co-transfection of *ATF4* plus empty vector overexpression, and *ATF4* plus *SIRT6* overexpression in Panc3.27 cells with a cycloheximide treatment of 0 and 30 minutes stained for Flag-ATF4 (green) and nuclear speckles marker SC35 (red). **H,** Immunofluorescence for co-transfection of *SIRT6* and *ATF4* overexpression in Panc3.27 cells stained for Flag-ATF4 (red) and HA-SIRT6 (green). Error bars represent +/- SEM between technical duplicates. Data are representative of at least 2 independent experiments. *p-value ≤ 0.05; **p-value ≤ 0.01 (two-tailed unpaired Student's *t*-test).

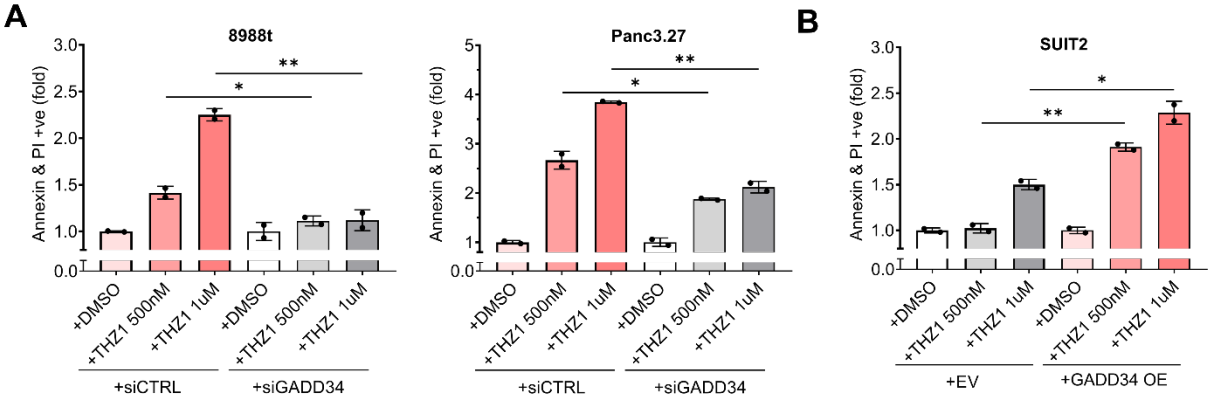

Figure S6. Activation of ISR in basal PDA reverses sensitivity to transcriptional inhibition. A, Quantification of Annexin + PI positive cells in two basal PDA lines transfected with control or *GADD34*-specific siRNAs and treated with increasing doses of THZ1. **B,** Quantification of Annexin + PI positive cells in a classical PDA line transduced with either an empty vector or *GADD34* overexpression and treated with incremental doses of THZ1. Error bars represent +/- SEM between technical duplicates. Data are representative of at least 2 independent experiments. *p-value ≤ 0.05; **p-value ≤ 0.01 (two-tailed unpaired Student's *t*-test).

SUPPLEMENTAL TABLES

Table S1. Primary mouse cultures

Tumor ID	Cell Line	Organoid	Species	Strain	Sex	Genetic modification status
NK54	yes		Mouse	C57B6	M	SIRT6+/+; p53F/+; p48-cre; KrasG12D
NK64	yes		Mouse	C57B6	F	SIRT6+/+; p53F/+; p48-cre; KrasG12D
NK79	yes		Mouse	C57B6	F	SIRT6F/F; p53F/+; p48-cre; KrasG12D
NK83	yes		Mouse	C57B6	M	SIRT6F/F; p53F/+; p48-cre; KrasG12D
NK87	yes	yes	Mouse	C57B6	M	SIRT6F/F; p53F/+; p48-cre; KrasG12D
NK88	yes	yes	Mouse	C57B6	F	SIRT6+/+; p53F/+; p48-cre; KrasG12D
NK89	yes	yes	Mouse	C57B6	M	SIRT6F/F; p53F/+; p48-cre; KrasG12D
NK93		yes	Mouse	C57B6	F	SIRT6+/+; p53F/+; p48-cre; KrasG12D
NK94		yes	Mouse	C57B6	F	SIRT6F/F; p53F/+; p48-cre; KrasG12D
NK97	yes	yes	Mouse	C57B6	F	SIRT6+/+; p53F/+; p48-cre; KrasG12D
NK100	yes	yes	Mouse	C57B7	F	SIRT6+/+; p53F/+; p48-cre; KrasG12D

Table S2. Primers used in this study

Gene	Forward (5' - 3′)	Reverse (5' - 3′)
ASNS	GGAAGACAGCCCCGATTTACT	AGCACGAACTGTTGTAATGTCA
GADD34	GAGGAGGCTGAAGACAGTGG	AATTGACTTCCCTGCCCTCT
ATF4	ATGACCGAAATGAGCTTCCTG	GCTGGAGAACCCATGAGGT
CD98hc	CTGGTGCCGTGGTCATAATC	GCTCAGGTAATCGAGACGCC
SLC6A9	CAGATCGAGTTTGTACTGACGAG	GCGATAGCAGAGGTATGGGAAG
Map1lc3b	CATCACAGTTGGCACAAACG	GACTTTGGGTGTGGTTCTCTTA
SQSTM1	GCACCCCAATGTGATCTGC	CGCTACACAAGTCGTAGTCTGG
CHOP	GGAAACAGAGTGGTCATTCCC	CTGCTTGAGCCGTTCATTCTC
CSE	ACACTTTTATGTCACCATATTTCCAG	TGTTGCAGAATACATAGAAATATCAGC
NRF2	GAGAGCCCAGTCTTCATTGC	TTGGCTTCTGGACTTGGAAC
SLC7A11	GGGCATCTCTCTGACCATCT	TCCCAATTCAGCATAAGACAAA

SESN2	TCCGCCACTCAGAGAAGG	GGAGGGCGTACAGCAGAG
DNAJA4	GGGATGTTTATGACCAAGGCG	GCCAATTTCTTCGTGACTCCA
HSPA1B	CTACCATTGAGGAGGTGGATTAG	CAAAGAAGTGAAGCAGCAAAGA
SIRT6	AGGATGTCGGTGAATTACGC	CCAGTTCCCACACCTTCC
mSIRT6	GCTAATGGGAACGAGACCAA	CCCACACTCAGGATCCATCT
c-MYC	GGCTCCTGGCAAAAGGTCA	CTGCGTAGTTGTGCTGATGT
ΔNp63	GGGGTGGGGGGGTTGGCAAAATCCTGG	CGTCCAGGTGGCCGACTTGGCGGTGCTC
β-ACTIN	CATGTACGTTGCTATCCAGGC	CTCCTTAATGTCACGCACGAT

Table S3. sgRNA target sequences used in this study

Gene	**Target Sequence**
CDK7 #1	AGCTCCAAATAGTAACTCGG
CDK7 #2	ATCTCTGGCCTTGTAAACGG
CDK9 #1	CCAGAGTGTCACCACACGGT
CDK9 #2	GCTTCTAAAACACGAGAATG
CDK12 #1	AAGTTCAAAGCGTTCGAATG
CDK12 #2	CCAGTCCCTATGGTCGAAGG
CDK13 #1	GGTTCCTTGTAGGCCGAAGG
CDK13 #2	CACAGTTACATAGTAAAAGG

APPENDIX 1:

This section is an extension of data related to the STM paper but is all unpublished.

Jessica Gianopulos performed all ISR experiments. Murine drug trials were performed by Jessica Gianopulos, Adrianne Wallace-Povirk, and Naomi Yamamoto. SY5609 drug characterization experiments in PDA subtypes were performed by Jessica Gianopulos. Samuraciclib drug characterization experiments in PDA subtypes were performed by Jessica Gianopulos and Aidan Schutter.

RESULTS

Extension of ISR regulation and THZ1 treatment

The following work is beyond the scope of the publication in chapter 1 but is a side project I worked on to investigate how THZ1 induces p-eIF2α in both basal and classical PDA cell lines. First, we looked to the ISR upstream kinases which are a group of 4 kinase proteins that can facilitate the addition of a phosphorylation onto eIF2α. All 4 ISR upstream kinases dimerize and autophosphorylate to become fully active[1]. Therefore, we sought to assess phosphorylation of these ISR upstream kinases as a way of measuring their activation status. Unfortunately, only three of the four ISR upstream kinases had commercially available antibodies for their phosphorylated forms. So, we were able to assess activation status of PERK, GCN2, and PKR but not HRI. PERK (PKR-like ER kinase) is activated by ER stress; GCN2 (general control nonderepressible 2) is activated by amino acid deprivation; PKR (double-stranded RNA-dependent protein kinase) is mainly activated by double-stranded RNA (dsRNA) during viral infection; HRI (heme-regulated eIF2α kinase) is expressed mostly in the developmental context of erythrocyte differentiation during erythropoiesis and therefore is fairly specific to erythroid cells[1]. Because of the specific function of HRI in erythroid cells, it is unlikely the HRI would be impacting our ISR phenotype in pancreas tumor cells. Therefore, we proceeded with investigating activation of PERK, GCN2 and PKR. We observed slight changes in phosphorylation status of all three ISR kinases, but none showed the dramatic increase in activation status necessary to induce the high levels of p- eIF2α we normally see with THZ1 treatment (Figure A1A). To further validate that the slight increases in PKR and GCN2 activation were not affecting phosphorylation of eIF2α, we performed siRNA knockdown of PKR or GCN2. No changes were observed in p- eIF2α status between either PKR or GCN2 knockdown

when compared to the control, all subject to THZ1 treatment (data not shown). This evidence suggests that the ISR upstream kinases are not responsible for the increase in p- eIF2α seen with THZ1 treatment in PDA cell lines.

Further investigation uncovered that we see a transcriptionally dependent induction of the ISR through GADD34 upon treatment of PDA cell lines with THZ1. GADD34 is the phosphatase that dephosphorylates eIF2α deactivating the ISR[1]. Upon CDK inhibition, we see dramatic reduction of GADD34 protein in all PDA lines which coincides with p- eIF2α induction (Figure A1A). Dephosphorylation of eIF2α is therefore greatly reduced when GADD34 is lost which enables the accumulation of p- eIF2α. We also see rapid reduction of GADD34 mRNA with a low dose THZ1 time course (Figure A1B) indicating that GADD34 is lost in a transcriptionally dependent manner upon CDK inhibition. Therefore, we uncovered the specific regulation of eIF2α phosphorylation under transcription inhibition in PDA cell lines.

Characterization of CDK7 inhibitors in PDA subtypes

The following work was completed after publication of the STM manuscript. YKL-5-124 is the pure CDK7 inhibitor development by Nathanael Gray's lab and covalently bindings to the C312 residue located outside of the catalytic domain of CDK7 (the same covalent binding site as THZ1)[2,3]. In vitro characterization of PDA subtype sensitivity to YKL-5-124 was performed and published in our previous work[4]. In vivo validation of PDA subtype sensitivity was performed using subtyped PDA patient-derived xenografts (PDXs) implanted subcutaneously into nude mice (2 basal and 2 classical). Mice were treated with 2.5mg/kg of YKL-5-124 or DMSO both diluted with 5% dextrose in water solution and administered once daily by intraperitoneal injection to nude mice for 3 weeks. Basal PDA PDX mice showed clear sensitivity to YKL-5-

124 treatment through dramatic reduction of tumor growth (Figure A2A, red) while the classical PDA PDX mice showed no changed in tumor growth with YKL-5-124 treatment (Figure A2A, black). This data provides clear validation that PDA basal and classical tumors are differentially sensitive to CDK7 inhibition in vivo and highlights the increasing potential of CDK7 inhibitors as a new treatment option for PDA patient tumors.

There are now two promising clinically approved CDK7 inhibitors, SY5609 develop by Syros therapeutics and Samuraciclib developed by Carrick therapeutics. We acquired both drugs and characterized the sensitivity of PDA subtypes to each of these drugs in vitro. Basal PDA cell lines are dramatically more sensitive to SY5609 than classical PDA cell lines as shown by a clear increase in cleaved PARP and lower IC50 dose values with increasing doses of SY5609 (Figure A2B&C). Basal PDA cell lines showed increased sensitivity to Samuraciclib compared to classical PDA cell lines (Figure A2D) even though the SY5609 is generally more potent then Samuraciclib as indicated by its lower IC50 doses (Figure A2C&D). Samuraciclib also induces an increase in cleaved PARP and cleaved caspase-3 in basal PDA cell lines as compared to classical PDA cells lines (Figure A2E). Treatment with SY5609 and Samuraciclib lead to reduction in RNAPII phosphorylation marks in both basal and classical lines validating the effectiveness of the drugs at inhibiting transcription in all PDA subtypes (Figure A2B&E). Together, this data proves that both SY5609 and Samuraciclib can induce apoptosis in basal PDA cell lines through CDK7 inhibition of transcription.

MATERIALS AND METHODS

Protein isolation and Western blot. Protein lysates were prepared by resuspending the cell pellets in RIPA lysis buffer supplemented with a protease inhibitor cocktail (Complete EDTA-free, Roche Applied Science), 5μM TSA, 5mM sodium butyrate, 1mM DTT, and phosphatase inhibitors (Phosphatase Inhibitor Cocktail Sets I, II, and III Calbiochem) and incubated on ice for 20 minutes. The lysate was then centrifuged at 14,000 rpm for 10 minutes at 4°C and the supernatant was harvested. Protein concentration was measured by using a BCA protein assay kit (Pierce). 20μg of the cell lysate (from lysis with buffer) electrophoresed on a 4-20% gradient polyacrylamide gel with SDS (Genscript) and electroblotted onto polyvinylidene difluoride membranes (PVDF) (Millipore). Membranes were blocked in TBS with 5% non-fat milk and 0.1% Tween and probed with antibodies. Bound proteins were detected with horseradish-peroxidase-conjugated secondary antibodies (Vector Biolaboratories) and Clarity Max Western ECL Blotting Substrate (Biorad). Antibodies used were anti-phosphorylated PERK (Invitrogen PA5-102853), anti-Total PERK (CST #3192S), anti-phosphorylated GCN2 (abcam # ab75836), anti-Total GCN2 (CST #3302S), anti-phosphorylated PKR (abcam #ab32036), anti-Total PKR (CST #D7F7), anti-GADD34 (Proteintech 10449-1-AP), anti-phosphorylated eIF2α (CST #3597), anti-Total eIF2α (CST #9722), anti-ATF4 (CST #11815), anti-Cleaved Caspase-3 (CST #9664), anti-PARP (CST #9542), anti-RNA polymerase II CTD phospho S7 (abcam #ab126537), anti-RNA polymerase II CTD phospho S2(abcam #ab5095), and anti-betaACTIN (Sigma A5316) as a loading control.

Real-time quantitative PCR (q-PCR). Total RNA extraction, cDNA synthesis and real-time quantitative PCR were performed as previously described[4]. Data were expressed as relative mRNA abundance normalized to the β-ACTIN expression level in each sample or as fold change over control and error bars are represented as mean ± s.e.m. between two independent experiments unless otherwise indicated in the figure legend. GADD34 primer sequences are forward (5'-3'): GAGGAGGCTGAAGACAGTGG and reverse (5'-3'): AATTGACTTCCCTGCCCTCT.

Patient-derived Xenograft. PDX models were acquired from the NIC PDMR and JAX (PAAD154b - NCI 885724; PAAD141b - NCI 463931; PAAD169b - JAX TM 00176; PAAD200 - JAX TM01212). PDX implantations were administered as previously described[4] and followed by post-surgical monitoring. Tumors were measure with electronic calipers and upon reaching an average tumor diameter of 3 to 5 mm^3, mice were treated with a once daily intraperitoneal injections of YKL-5-124 (2.5 mg/kg) or DMSO both diluted with 5% dextrose in water solution (600063, Bound Tree Medical) for 22 days. Caliper measurements of tumors and body weights were recorded three times a week.

Proliferation IC50 assay. IC50 proliferation assays were performed as previously described[4] with the following modifications. Cells were plated in 96-well plates (2,000 cells/well) in culture medium and the following drugs were used: SY5609, Samuraciclib, or DMSO control (BP231-100; ThermoFisher Scientific).

APPENDIX FIGURES

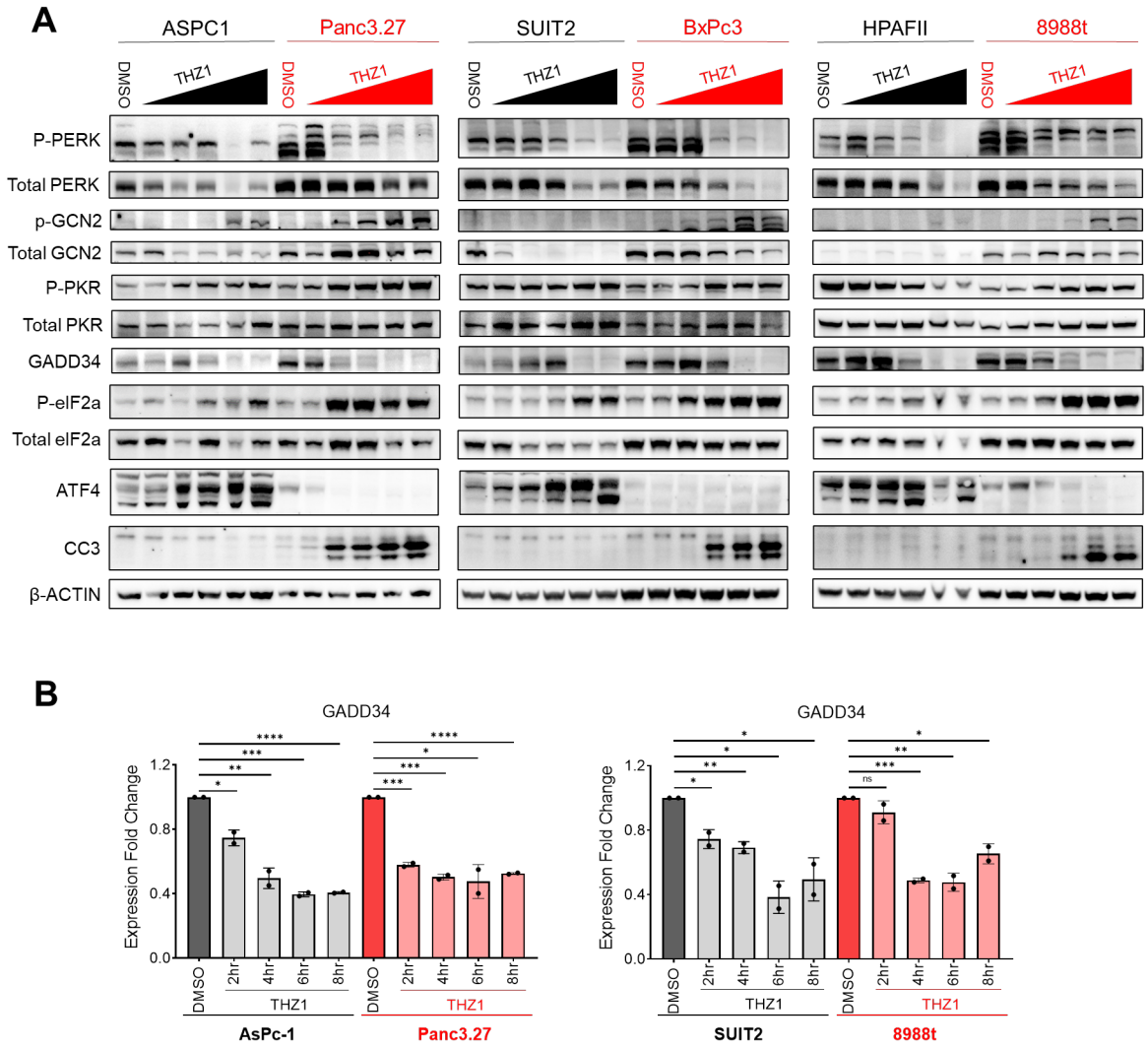

Figure A1: THZ1 induced GADD34 regulation of p-eIF2α. **A,** Western blot for p-PERK, Total PERK, p-GCN2, Total GCN2, p-PRK, Total PRK, GADD34, p-eIF2α, total eIF2α, ATF4, cleaved-caspase 3 (CC3), and ACTIN in basal (red), compared with classical (black) PDA cell lines treated with increasing doses of THZ1 (20nM – 5uM). **B,** qRT-PCR for GADD34 in basal (red), compared with classical (black) PDA cell lines treated with 100nM THZ1 for 0-8hrs in 2hr increments. *p-value ≤ 0.05; **p-value ≤ 0.01; ***p-value ≤ 0.001; ****p-value ≤ 0.0001 (two-tailed paired Student's t-test).

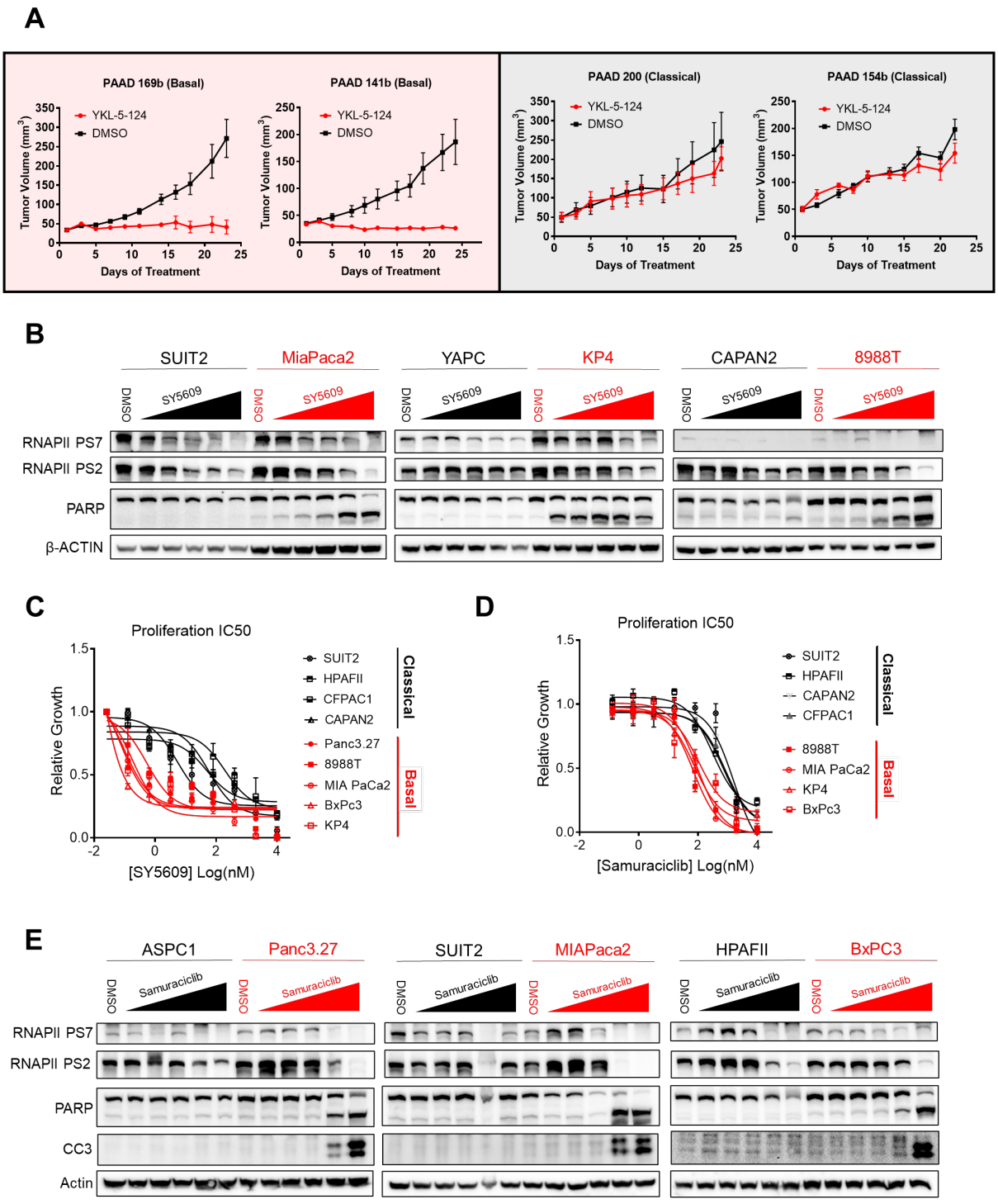

Figure A2: Characterization of pure CDK7 inhibitors. A, Tumor volume of basal and classical PDA xenografts after treatment with once daily intraperitoneal injections of YKL-5-124 (2.5 mg/kg) (red) or DMSO (black) both diluted with 5% dextrose in water solution (600063, Bound Tree Medical) for 21 days (DMSO n = 8, SY-5609 n = 8). **B,** Western blots for RNAPII PS7, RNAPII PS2, PARP, and β-ACTIN in basal (red) compared with classical (black) PDA cell lines treated with increasing doses of SY5609 (20 nM to 5 μM) for 48 hours. **C-D,** Proliferation

curves for basal PDA (red) compared with classical (black) PDA cell lines treated with increasing doses of SY5609 (C) and Samuraciclib (D). **E,** Western blots for RNAPII PS7, RNAPII PS2, PARP, cleaved-caspase 3 (CC3) and β-ACTIN in basal (red) compared with classical (black) PDA cell lines treated with increasing doses of Samuraciclib (20 nM to 5 μM) for 24 hours. Proliferation curves were performed in duplicate, and data are represented as mean ± SEM among three independent experiments.

APPENDIX REFERENCES

1. Pakos-Zebrucka, K. *et al.* The integrated stress response. *EMBO Rep.* **17**, 1374–1395 (2016).
2. Kwiatkowski, N. *et al.* Targeting transcription regulation in cancer with a covalent CDK7 inhibitor. *Nature* **511**, 616–620 (2014).
3. Olson, C. M. *et al.* Development of a Selective CDK7 Covalent Inhibitor Reveals Predominant Cell-Cycle Phenotype. *Cell Chem. Biol.* **26**, 792-803.e10 (2019).
4. Kartha, N., Gianopulos, J., Schrank, Z. *et al.* Sirtuin 6 is required for the integrated stress response and resistance to inhibition of transcriptional cyclin-dependent kinases. *Sci. Transl. Med.* **15**, eabn9674 (2023).

CHAPTER 3:

This chapter presents unpublished work, manuscript in preparation.

TITLE: The ZNF274 chromatin modifying complex controls cellular plasticity and sensitivity to CDK7 inhibitors

Authors: Jessica E. Gianopulos[1,2], Adrianne Wallace-Povirk[1], Aidan Schutter[1], Naomi Yamamoto[1], Andrea Doak[2,3], Stephanie Dobersch[1], Kevin Cheung[3], Sita Kugel[1#]

Affiliations:
[1]Human Biology Division, Fred Hutchinson Cancer Center, Seattle, WA, 98109
[2]Program in Molecular and Cellular Biology, University of Washington, Seattle, WA,98105
[3]Public Health Sciences Division, Fred Hutchinson Cancer Center, Seattle, WA, 98109

[#]Corresponding author. Email: skugel@fredhutch.org

ABSTRACT

Pancreatic Ductal Adenocarcinoma (PDA) can be characterized by two distinct transcriptional subtypes: classical and basal. The basal and classical PDA subtypes also correlate with specific DNA methylation and chromatin states. These DNA methylation states resulted in differential expression of repetitive elements between the two PDA subtypes. Repetitive elements are regulated by the KRAB-ZNF repressive complex which functions to maintain heterochromatin at repetitive elements and other genomic loci by removing marks of open chromatin and installing marks of repressive chromatin (i.e. H3K9me3) with histone methyltransferase, SETDB1 and DNA methyltransferase, DNMT1. The KRAB-ZNF protein binds DNA and directs the complex to specific regions of the genome in need of heterochromatin maintenance and gene suppression. ZNF274 is the most well-defined KRAB-ZNF which has been proven to bind/colocalize with SETDB1 and H3K9me3 at genomic loci. Given that DNA methylation and expression of repetitive elements correlates with PDA subtype, we hypothesize that the ZNF274/SETDB1 complex, which regulates repetitive element expression, may be an important epigenetic regulator of PDA cell state. We identified that high ZNF274 expression corresponds to the classical PDA subtype and that loss of ZNF274 can induce the epithelial to mesenchymal transition (EMT) and drive a subtype switch in PDA cells. We defined the mechanism of EMT induction by showing that ZNF274 directly binds to the ZEB1 gene, recruiting SETDB1 which deposits H3K9me3 thereby suppressing ZEB1 whereas loss of ZNF274 prevents SETDB1 recruitment decreasing H3K9me3 and enabling expression of ZEB1 and driving EMT. To determine if this mechanism could sensitize classical PDA to CDK7 inhibition, we performed ZNF274 knockdown in cell lines, organoids, and cell line-derived xenografts in mice followed by treatment with a CDK7 inhibitor. The absence of ZNF274 led to a dramatic increase in the

sensitivity of classical PDA to CDK7 inhibition. Therefore, we identified the importance of the ZNF274/SETDB1 repressive complex in regulating PDA cell state and sensitivity to CDK7 inhibition which can be employed to improve patient responses to CDK7 inhibition therapy.

INTRODUCTION

Pancreatic ductal adenocarcinoma (PDA) presents with an extremely poor prognosis as well as a rising incidence rate driving it to become the 2nd-leading cause of cancer-related deaths in the US by 2030 with a current 5-year survival rate of about 12%[1]. The progression of PDA tumors through acquisition of genetic mutations is well understood with early acquisition of oncogenic KRAS mutations followed by subsequent loss of tumor suppressor genes, p53, CDKN2A, SMAD4, etc[2,3]. However, this investigation led to the same conclusion: PDA tumors are genetically very similar, both between patients as well as between primary and metastatic tumors within the same patient, yet patients respond differently to standard of care chemotherapy treatment[4]. PDA tumors are intrinsically heterogeneous which may explain this differential patient response to treatment and promoted the discovery of transcriptional PDA subtypes. After almost a decade of research into PDA subtypes, the consensus in the field is that PDA is characterized by two major transcriptional subtypes: classical and basal[5–11]. The basal subtype (~25%) has the worst overall survival, acts as an independent poor prognostic factor, and presents a unique and outsized clinical challenge.

The PDA transcriptional subtypes are determined by specific chromatin states given that the epigenome determines the transcriptome. Lomberk et al. performed a multiparametric integrative analysis of histone modifications on chromatin, RNA expression, and DNA methylation to define epigenomic landscapes for PDA subtypes[12]. They discovered that PDA tumors present two distinct epigenomic landscapes that align well with the predefined classical and basal transcriptional PDA subtypes. They defined a complex regulatory network of super-enhancers and transcription factors that control cellular pathways and functions in the classical tumors, but which are lost in the basal tumors[12,13]. Another group identified that PDA subtypes

can be characterized by the DNA methylome. They found that the more aggressive PDA subtype (basal) presents with hypomethylation of repetitive elements which they termed the methylation low subset while the methylation high subset retains characteristics of the pancreatic cell lineage (classical)[14]. The lack of methylation in the methylation low subset enables expression of the repetitive elements including endogenous retroviruses (ERVs) which activates a cell-intrinsic interferon response[14]. This methylation low subset is in concordance with basal PDA lacking the amount of epigenetic regulation present in the classical subtype.

Epigenetic regulation of repetitive elements is vital to maintaining suppression of these elements and genomic integrity. Specific epigenetic regulators evolved in conjunction with ERVs to combat the mobile ability of ERVs and other repetitive elements, keep these elements suppressed, and protect the genome. These regulators are the Krüppel-associated box (KRAB) zinc finger (ZNF) proteins which are a subclass of the ZNF family, the largest class of sequence-specific DNA binding proteins in the human genome[15,16]. KRAB-ZNF genes engaged in an evolutionary arms race with these repetitive elements which drove KRAB-ZNF gene duplication and divergence[17–21]. However, this arms race did not occur randomly throughout the genome but maintained stringent localization to chromosome 19 in humans leading to large clusters of ZNF genes on chromosome 19[22]. These large clusters of KRAB-ZNF genes are pristinely localized to facilitate suppression of the repetitive elements[23]. For adequate suppression to occur, the KRAB-ZNF proteins must bind DNA and recruit chromatin modifiers to form a chromatin modifying complex. The KRAB-ZNF proteins form a complex with KAP1 (a scaffold or co-factor), SETDB1 (histone methyltransferase), HDACs (histone deacetylases), DNMTs (DNA methyltransferases), and HP1 (heterochromatin protein 1)[24]. This KRAB-ZNF complex facilitates silencing of repetitive elements and genes through heterochromatin maintenance by

removing marks of active chromatin and installing marks of repressive chromatin including H3K9me3[24,25].

SETDB1 has been identified as a specific component of the KRAB-ZNF complex that can promote silencing of genes and repetitive elements though its histone methyltransferase activity[26]. SETDB1 repression of repetitive elements has also been uncovered to regulate suppression tumor-intrinsic immunogenicity[27]. This group discovered that loss of SETDB1 derepresses repetitive elements and immunostimulatory genes leading to a repetitive RNA specific cytotoxic T cell response. They then identified that SETDB1 loss sensitizes mouse melanoma and lung carcinoma cell lines to immune checkpoint inhibitors, uncovering a new role for SETDB1 in cancer therapy[27]. Additionally, the role of SETDB1 in the development of PDA tumors has been investigated in mice. They found that p53-mediated apoptosis can only occur in the absence of SETDB1 resulting in no PDA formation. In contrast, when SETDB1 is present, it binds the p53 promoter and inhibits p53 function which drives PDA formation[28]. These studies highlight the importance of investigating how the components of the KRAB-ZNF complex can influence genes and pathways in addition to regulation of repetitive elements.

Even though the KRAB-ZNF component of the complex does not have chromatin modifying abilities, its role as the DNA binding component controls where in the genome the complex functions. Therefore, a better understanding of these KRAB-ZNFs in necessary to further interrogate how the complex functions to regulate gene expression. The most well-defined KRAB-ZNF of the complex is ZNF274 which has been found to bind and/or colocalize with KAP1, SETDB1 and H3K9me3 on the genome[29,30]. KAP1 binding to the KRAB domain of KRAB-ZNF proteins has been generally described but ZNF274 was the first KRAB-ZNF to be shown to directly bind to SETDB1 and KAP1 in the KRAB-ZNF complex[31,32]. Lastly, the

ZNF274/KAP1/SETDB1 complex has been identified as necessary for the maintenance of genomic stability[30]. Additionally, more research into ZNF genes has discovered new functions for ZNFs in the regulation of tumorigenesis in multiple cancers[33–38].

Given that DNA methylation and expression of repetitive elements were found to be important characterizations of PDA subtypes, we sought to investigate whether regulators of repetitive element silencing such as the ZNF274/SETDB1 complex are important epigenetic regulators of PDA cell state. A better understanding of these regulators and their epigenetic impact on PDA progression could enhance development of subtype-specific therapies in PDA.

RESULTS

Identification of ZNF274 and SETDB1 in PDA subtypes

To identify whether expression of ZNF274 or SETDB1 correlates with PDA subtypes, we interrogated publicly available PDA data sets. SETDB1 showed little difference in expression between PDA subtypes while ZNF274 showed a small difference with slightly higher expression in classical PDA than basal PDA (Figure 1A). To identify if the slight differential expression of ZNF274 in patient data is worth further investigation, we performed qPCR on an expanded panel of PDA cell lines classified as either classical or basal by previous groups to assess their ZNF274 expression. We observed a clear differential in mRNA expression for ZNF274 in PDA subtyped cell lines, with higher expression in the classical lines and lower expression in the basal lines (Figure 1B). Additionally, SETDB1 did not show differential mRNA expression in PDA cell lines which match the patient data (Figure 1B). Therefore, we opted to further investigate this differential ZNF274 expression with patient survival data. We accessed the TCGA dataset containing mRNA expression data from cBioPortal and grouped patients by high (up-regulated)

or low (down-regulated) ZNF274 expression. Low ZNF274 expression corresponds to worse overall survival in patients while high ZNF274 expression indicates better survival (Figure 1C). Lastly, we validated ZNF274 protein expression in our basal and classical PDA cell lines and organoids by western blots and immunofluorescence. ZNF274 protein expression matched our mRNA expression data showing high ZNF274 in classical cell lines and organoids and low ZNF274 in basal cell lines and organoids (Figure 1D&E). Therefore, we can conclude that ZNF274-high models correlate with the classical PDA subtype.

Loss of ZNF274 drives the epithelial to mesenchymal transition (EMT)

Given that ZNF274 is known to complex with KAP1 and SETDB1 to deposit the H3K9me3 mark on chromatin, we first assessed whether global H3K9 trimethylation changes with ZNF274 knockdown (KD). We found that in classical PDA cell lines, loss of ZNF274 did not impact the global level of H3K9me3 (Figure S1A). However, we did notice a dramatic morphological change in the classical PDA cell lines with ZNF274 knockdown. Classical PDA cell lines tend to be more epithelial in phenotype and grow in colonies rather than as individual cells. Basal PDA tends to be more mesenchymal in nature and therefore presents with more spindle shaped cells that grow spread out and with more individual cells rather than forming colonies[39]. Interestingly, we saw classical PDA cell lines lose their epithelial phenotype and became more spindle shaped, growing more diffuse throughout the plate upon ZNF274 loss (Figure 2A). Next, we sought to determine what might be changing within these cells enabling them to present with a more mesenchymal morphology. We assessed both protein and RNA expression of different markers of the epithelial to mesenchymal transition (EMT) to identify changes upon ZNF274 knockdown in a panel of classical PDA cell lines. ZEB1, a transcriptional

driver of EMT and master regulator of the mesenchymal state, showed a dramatic increase in both chromatin-bound protein and global protein expression when ZNF274 is lost (Figure 2B& S1B). In contrast, chromatin-bound EpCAM, an epithelial cell marker, was substantially decreased upon ZNF274 loss (Figure 2B) and both EpCAM and another marker of epithelial cell state, E-cadherin, showed decreased protein expression in the absence of ZNF274 compared to control (Figure 2B& S1B). We then assessed mRNA expression in our ZNF274 KD and control cells and observed the same pattern in an expanded panel of EMT markers where those characterizing the mesenchymal state (ZEB1, SNAIL1, SNAIL2) were upregulated and those characterizing the epithelial state (EpCAM and E-cadherin) were downregulated in the absence of ZNF274 (Figure 2C). ZEB1 shows the most dramatic change of all the EMT markers upon ZNF274 KD. Therefore, we hypotheses that ZNF274 may be directly regulating ZEB1 and then ZEB1 regulates the rest of the EMT pathway, given that ZEB1 is a known regulator of many EMT pathway genes.

Given that ZEB1 has previously been identified as a regulator of the mesenchymal cell state in high-grade (basal) PDA[40], we opted to determine if the induction of ZEB1 by ZNF274 KD could convert classical into more basal PDA. The deltaN form of TP63 (TP63ΔN), Keratin17 (KRT17) and Keratin5 (KRT5) are all well-known markers of the squamous subtype which is the most aggressive form of basal PDA[41–43]. Therefore, we assessed protein expression of all three basal markers for any changes induced upon ZNF274 KD. We observed an increase in KRT5 in one classical PDA cell line with ZNF274 KD compared to control while TP63ΔN and KRT17 protein expression increased in both classical PDA cell lines with ZNF274 KD compared to control (Figure S1C). This data verifies that the EMT phenotype induced upon ZNF274 loss is initiating a subtype switch from classical to more squamous basal PDA.

To identify if DNMT1 cooperates with ZNF274 to induce the observed EMT phenotype, we assessed DNMT1 expression in ZNF274 KD cells and observed a slight decrease in DNMT1 expression and chromatin binding in ZNF274 KD cells compared to control (Figure S1D). This suggests that DNMT1 could be bound to the ZNF274/SETDB1 complex and that loss of ZNF274 prevents the complex from binding DNA and results in decreased complex-dependent chromatin binding of DNMT1. The loss of the ZNF274/SETDB1 complex could also increase the accessibility of DNMT1 to proteasomal degradation thereby resulting in decreased protein expression. Next, we performed DNMT1 KD in a classical PDA cell line to determine if loss of DNMT1 could also induce EMT. We observed no change in ZNF274 protein expression or global H3K9 trimethylation with DNMT1 KD (Figure S1E&F). Additionally, we observed a slight increase in ZEB1, a slight decrease in E-cadherin, and a clear decrease in EpCAM protein expression in DNMT1 KD cells compared to control (Figure S1E). This data indicates that DNMT1 loss can induce changes in EMT genes but may not be enough to drive full EMT given the small increase in ZEB1. It is likely DNMT1 could play a more prominent role in the suppression of EpCAM, given that decreased EpCAM expression was the most dramatic change upon DNMT1 loss. Therefore, DNMT1 functions to help promote the ZNF274 driven EMT phenotype but is not the main regulator of the EMT induction.

To determine how ZNF274 is regulating ZEB1 expression and thereby controlling EMT, we assessed changes in H3K9me3 as well as binding of ZNF274, SETDB1, and DNMT1 at the ZEB1 locus by using ChIP-qPCR on ZNF274 KD and control cells. We utilized doxycycline (dox) inducible shRNA cell lines with either a control, non-targeting shRNA, (shCTRL) or a ZNF274 targeting shRNA (shZNF274) to prolong the knockdown and obtain enough material for ChIP. Phenotype validation of the stable, dox-inducible shZNF274 PDA cell lines showed the

same induction of EMT with increased expression of mesenchymal genes such as ZEB1 and decreased expression of epithelial genes (Figure S1G&H). Since ZNF274 has been shown to bind the 3' exons of other ZNF genes[29], we designed ChIP primers to both the promoter and 3' exons of ZEB1. ChIP pulldown with ZNF274 showed clear reduction in ZNF274 binding at the ZEB1 locus as well as positive control, known ZNF274 bound, genes and no binding of the negative control, not bound by ZNF274, genes in ZNF274 KD cells compared to control cells (Figure 2D). H3K9me3 ChIP showed a clear decrease in H3K9me3 at positive control genes and a slight decrease in H3K9me3 at the ZEB1 locus, with no change in H3K9me3 at negative control genes upon loss of ZNF274 (Figure 2E). ChIP pulldown with SETDB1 showed a clear reduction in SETDB1 binding at the ZEB1 locus and positive control genes, and no change at the negative control genes in ZNF274 KD cells compared to control (Figure 2F). ChIP pulldown with DNMT1 also showed a reduction in DNMT1 binding at the ZEB1 locus and positive control genes (Figure S1I) but the overall signal was much weaker compared to SETDB1 indicating that DNMT1 is likely bound to the ZNF274 complex regulating the ZEB1 locus but in a much lower capacity than SETDB1. Together, this data shows that ZNF274 can bind the ZEB1 gene and facilitate direct transcriptional regulation of ZEB1. Since ZNF274 is known to recruit SETDB1 which then deposits the H3K9me3 mark to repress transcription, we expected that loss of ZNF274 would lead to reduced SETDB1 binding/recruitment which in turn would decrease the prevalence of the H3K9me3 mark. Our data showed significant reductions in H3K9 trimethylation and SETDB1 binding at ZEB1 loci and positive control genes. Therefore, we will further investigate the role of SETDB1 in regulating ZEB1 control of our EMT phenotype in classical PDA.

SETDB1 regulation of EMT in classical PDA

Even though ZNF274 had no previously documented connection to EMT, there is extensive literature connecting SETDB1 to EMT. One study found SETDB1 to have increased expression in pediatric high-grade gliomas compared to normal brain. In this study loss of SETDB1 reduces cell proliferation and migration as well as decreases expression of mesenchymal markers such as vimentin, N-cadherin, and SNAIL1 identifying a potential oncogenic role for SETDB1 in pediatric high-grade gliomas[44]. Another study found that SETDB1 suppresses SNAIL1 expression by binding its promoter with SMAD3/4 and blocking SNAIL1 expression in breast cancer and that loss of SETDB1 in this context increases invasion of breast cancer cells[45]. There is no clear consensus in the literature if SETDB1 drives or inhibits EMT. Regulation of SNAIL1 seems to be a reoccurring player but other papers have found TGF-β and mircoRNAs to be involved as well in different model systems. Therefore, we sought to further investigate the role of SETDB1 in our ZNF274 regulated EMT phenotype in PDA. If ZNF274 recruitment of SETDB1 and deposition of H3K9me3 is the mechanism by which ZNF274 is controlling ZEB1 transcription, then SETDB1 KD should induce a similar change in ZEB1 expression and downstream EMT targets. Therefore, we knocked down SETDB1 in our classical PDA cell lines and, surprisingly, observed no changes in ZEB1 expression. However, SETDB1 KD did cause a clear increase in expression of the epithelial genes, EpCAM and E-cadherin (Figure S2A). This was unexpected given that ZNF274 KD increases ZEB1 expression and decreases EpCAM expression. SETDB1 has previously been shown to regulate expression of endogenous retroviruses (ERVs) and genes that contain intronic ERVs such as EpCAM. In that study, loss of SETDB1 reduced H3K9me3 at the EpCAM promoter identifying EpCAM as a direct target of SETDB1[46]. This unexpected data prompted us to hypothesize that SETDB1 may

function to regulate epithelial genes independent of ZNF274 binding. We proposed that ZNF274 may sequester SETDB1 at ZNF274 bound genes, while loss of ZNF274 would release SETDB1 to go increase suppression of epithelial genes independent of ZNF274 binding. Under normal conditions, SETDB1 could be bound to chromatin both dependent and independent of ZNF274. SETDB1 KD may predominantly impact expression of genes bound by SETDB1 independent of ZNF274 and therefore have little or no impact on ZNF274 dependent SETDB1 bound genes. To test this hypothesis, we performed ChIP on ZNF274 KD and control cells for H3K9me3, SETDB1, and H3K4me3. H3K4me3 marks transcriptional start sites and is positively correlated with active transcription[47]. We observed slight increases in H3K9me3 and SETDB1 binding at epithelial genes, E-cadherin (CDH1) and EpCAM, with ZNF274 KD as compared to control (Figure S2B&C). Additionally, we observed a significant decrease in H3K4me3 at E-cadherin (CDH1) and EpCAM which indicates a decrease in active transcription at those loci (Figure S2D). This data validates our previous finding that ZNF274 KD decreases expression of epithelial genes in the EMT pathway and confirms the role of SETDB1 in this regulation.

Altogether, this data has uncovered that SETDB1 is involved in ZNF274 control of ZEB1 expression and downstream EMT targets. Additionally, we have proven that SETDB1 regulation of epithelial genes is independent of ZNF274 in classical PDA. Therefore, we have presented the novel finding that SETDB1 functions both independent and dependent of ZNF274 in PDA.

ZNF274 is necessary to prevent invasion and metastatic capacity of classical PDA cells.

To examine if the morphological change undergone by ZNF274 KD cells, through the induction of EMT, can increase their mobility and migration, we performed a scratch assay and measured the quantity of cells migrating into the scratch by percent wound confluence. ZNF274

KD cells showed a dramatic increase in wound confluence over time compared to the control cells (Figure 3A). This data indicates that loss of ZNF274 induces an increase in migratory capacity of classical PDA cells. To understand this further, we moved to a 3D organoid model system in which we created stable, dox-inducible shZNF274 classical PDA organoids. We validated dox-inducible ZNF274 KD in these organoids by immunofluorescence and observed a clear reduction in ZNF274 signal in the shZNF274 organoids compared to the shCTRL organoids (Figure S2E). Interestingly, loss of ZNF274 in our classical PDA organoids induces a thickening of the cellular layer that forms the organoid structure. Quantification of this thickening showed a statistically significant difference between control and ZNF274 KD organoids (Figure 3B). This thickening phenotype may be the result of a process called delamination which refers to the formation of multiple layers. The delamination process can also involve a partial or complete EMT as seen in neural crest cells which enables them to migrate and colonize different organs and tissues[48,49]. This morphological change upon ZNF274 loss and induction of EMT would be consistent with our cell line data. Additionally, it has been identified that PDA organoids can form these glandular cysts, and a glandular histology has been shown to correlate with the classical PDA subtype[50,51]. It appears that ZNF274 KD is causing a loss in glandular identity of the classical PDA organoids through this process of delamination and driving them towards a more basal morphology. Quantification of basal versus classical organoid cell thickness shows that basal PDA organoids have a significantly thicker cellular layer than classical organoids (Figure 3C) validating this subtype switch is induced by ZNF274 loss. Next, we used these organoids to assess migration and invasion using a 3D collagen matrix assay to mimic the invasion requirements of a cell squeezing through the extracellular matrix surrounding a tumor. For this assay, invasion is quantified as an increase in spine formation and protrusion

out of the organoid. Very strikingly, we observed a clear presence of spine formation in the ZNF274 knockdown organoids as compared to an absence of spine formation in the control organoids (Figure 3D). Spine counts show a statistically significant increase in spine formation and protrusions with ZNF274 loss which confirms that ZNF274 is necessary to prevent invasion in classical PDA tumor cells.

ZNF274 promotes resistance to CDK7 inhibition in classical PDA.

In our previous work, we discovered basal PDA is exquisitely sensitive to transcriptional inhibitors, most notably cyclin-dependent kinase 7 inhibition (CDK7i). This sensitivity was typified by THZ1 (a covalent inhibitor of CDK7/12/13) and YKL-5-124 (a covalent inhibitor of CDK7 alone), but not to the non-transcriptional inhibitor's gemcitabine or the CDK4/6 inhibitor Palbociclib[52]. CDK7 is a component of the TFIIH subunit of RNA Polymerase II (RNA POL II) and facilitates phosphorylation of Ser5, Ser7, and indirectly regulates phosphorylation of Ser2 on the C-terminal domain (CTD) of RNA Pol II[53]. Phosphorylation of the CTD of RNA POL II enables transcription initiation and productive elongation[54]. Inhibition of CDK7 blocks phosphorylation of the CTD of RNA Pol II and prevents transcription[55,56]. In many different cancer types, inhibition of CDK7 by THZ1 or YKL-5-124 disrupts transcription and leads to decreased cell growth[57–60]. Therefore, clinical versions of these compounds were developed to test the effectiveness of CDK7 inhibition in cancer patients. SY5609 is a clinically approved, non-covalent inhibitor of CDK7 which has cleared phase I clinical trials and shows exciting promising in PDA patients[61–63].

To elucidate the impact of ZNF274 on regulation of sensitivity to CDK7 inhibitors, we performed knockdown of ZNF274 by siRNA and shRNA followed by treatment with increasing

doses of THZ1 (Figure 4A) or YKL-5-124 (Figure 4B and S3A). ZNF274 knockdown increased ZEB1 expression between the siCTRL DMSO (dimethyl sulfoxide) and the siZNF274 DMSO validating induction of EMT. Additionally, ZNF274 knockdown increased sensitivity to both CDK7 inhibitors, THZ1 and YKL-5-124, through an increase in cleaved caspase-3 activation in multiple independent classical PDA cell lines (Figure 4A-B & S3A). To validate this phenotype in a 3D model system, we treated our dox-inducible control and ZNF274 knockdown classical PDA organoids with increasing doses of YKL-5-124. Upon completion of treatment, the organoids were fixed and embedded in a cone of agarose, paraffin processed and embedded, and then stained for H&E. The shCTRL organoids show intact organoid structure as indicated by their round and cystic morphology. This intact structure is then maintained throughout treatment with increasing doses of YKL-5-124. In contrast, shZNF274 organoids show intact organoid structure by their thick, multicellular-layer morphology prior to treatment, and then upon treatment, increasing doses of YKL-5-124 causes disintegration and loss of an intact organoid structure in the shZNF274 organoids (Figure 4C). This loss of integrity of the shZNF274 organoid structure indicates increased sensitivity to CDK7 inhibition upon loss of ZNF274 in classical PDA organoids.

To investigate if ZNF274 is sufficient to promote resistance to CDK7 inhibition, we overexpressed ZNF274 in basal (CDK7i sensitive) PDA cell lines and treated with increasing doses of CDK7 inhibitors. ZNF274 overexpression (OE) in basal PDA cell lines leads to a significant decrease in ZEB1 mRNA expression compared to the control as well as a substantial decrease in an additional marker of the mesenchymal state, SNAIL2. Markers of the epithelial cell state are not significantly altered, indicating that in this rescue experiment, increasing ZNF274 expression is predominantly impacting ZEB1 (Figure 4D & S3B). ZNF274 OE cells

treated with increasing doses of CDK7 inhibition show a substantial reduction in sensitivity to THZ1 and YKL-5-124 as indicated by reduced activation of cleaved caspase-3 compared to the empty vector control (Figure 4E&F). Thus, our results suggest that ZNF274 constrains ZEB1 thereby promoting resistance to CDK7 inhibition while disinhibition of ZEB1, in the absence of ZNF274, enables sensitivity to CDK7 inhibition. To further confirm the hypothesis that the change in CDK7i sensitivity is through altered expression of ZEB1, we overexpressed ZEB1 in a classical PDA cell line that has low baseline expression of ZEB1 and high baseline expression of ZNF274. We found that ZEB1 OE does increase sensitivity of a classical PDA cell line to THZ1 as shown by an increase in cleaved PARP (Figure S3C). Together this data indicates that sensitivity to CDK7 inhibition is regulated by ZNF274 control of ZEB1 expression and that modulations to either ZNF274 or ZEB1 is sufficient to alter sensitivity to CDK7i in either subtype of PDA.

Finally, to show that the absence of ZNF274 confers sensitivity to CDK7 inhibition in vivo, we implanted the dox-inducible shCTRL and shZNF274 classical PDA cell lines subcutaneously into immune-compromised nude mice and treated them daily with SY-5609 (a clinically approved oral CDK7 inhibitor) for 3 weeks. SY-5609 significantly reduced growth of the ZNF274 knockdown tumors but not the control tumors (Figure 4G). Mice did not experience any toxicity from the drug as indicated by stable mouse weights (Figure 4H). Our results identify the ZNF274 regulation of ZEB1 as a potential therapeutic option for sensitizing classical PDA to CDK7 inhibitors.

DNMT inhibition sensitizes classical PDA to CDK7 inhibition.

Unfortunately, ZNF274 is not targeted by any clinically approved drugs but other components of the KRAB-ZNF complex do have clinically approved inhibitors. Specifically, we hope to identify which drugs have the greatest potential to induce sensitivity of classical PDA to CDK7 inhibition. Clinically approved drugs exist to target the HDAC and DNMT components of the complex. Given that knockdown of DNMT1 recapitulates the increase in ZEB1 expression seen with ZNF274 KD (Figure S1E), we opted to test inhibitors of DNMTs first. The two clinically approved DNMT inhibitors are decitabine (DAC) and azacytidine (AZA)[64,65]. We treated classical PDA with either a DAC or AZA and observed that AZA induced a robust increase in ZEB1 protein expression while we observed no change in ZEB1 expression with DAC treatment (Figure 5A and S4A). We then expanded this observation to three classical PDA cell lines and showed that RNA expression of ZEB1 increased with AZA treatment across all three cell lines and continued to increase with higher doses of AZA (Figure 5B) while RNA expression of epithelial genes did not change with AZA treatment (Figure S4B). This suggests that AZA induces a partial EMT driven solely by ZEB1. Additionally, we observed the same cellular morphological change, from clumped growth pattern to a more spindle shaped and individual growth pattern, with AZA treatment as described previously with ZNF274 KD (Figure 5C), indicating that ZEB1 driven partial EMT is enough to induce a cellular state change. Interestingly, high doses of AZA eventually halted cell growth more prominently in the classical PDA cell lines compared to basal (Figure S4C). This indicates that the classical cells may not be able to recover from the induction of ZEB1 driven EMT leading to growth inhibition suggesting a potential EMT-induced lethality.

Given the clear increase in ZEB1 expression and morphology change with AZA treatment, we hypothesized that AZA induced ZEB1 driven EMT might promote enough of a cell

state change to sensitize classical PDA to CDK7 inhibition. Therefore, we next performed a combination treatment of AZA with the clinical CDK7 inhibitor, SY5609, in classical PDA cell lines. Cells treated with the combination of AZA and SY5609 showed a substantial increase in apoptosis as seen by increased cleaved PARP and cleaved caspase 3 (Figure 5D). This data indicates that AZA treatment can sensitize classical PDA cells to CDK7 inhibition, broadening the therapeutic application of CDK7 inhibitors in PDA.

To further investigate this potential treatment in vivo, we first treated four patient-derived xenograft (PDX) models of PDA (2 basal and 2 classical) with SY5609 dissolved in 5% Captisol and administered once daily by oral gavage to nude mice for 3 weeks. Basal PDA PDX mice showed marked sensitivity to SY5609 treatment through dramatic reduction of tumor growth (Figure 5E, red) while the classical PDA PDX mice showed no change in tumor growth with SY5609 treatment (Figure 5E, black). This data shows clear differential sensitivity of basal and classical PDA tumors to the clinically approved CDK7 inhibitor, SY5609, and potentially efficacy of SY5609 to treat PDA patients with more basal-like tumors. However, since PDA patient tumors are intrinsically heterogeneous, the best treatment course would be able to target both basal and classical PDA cells within the tumor. To determine if a combination treatment of AZA and CDK7 inhibition would be able to treat more classical PDA patient tumors, we utilized one of our PDX mouse models of classical PDA to test the efficacy of the combination treatment. We split the trial into four arms of treatment, vehicle (5% Captisol), SY5609 only, AZA only, and AZA plus SY5609 combination which were administered by oral gavage to nude mice for 3 weeks. The combination treatment of AZA plus SY5609 showed dramatic reduction of tumor growth over all other treatment arms in our classical PDA PDX model (Figure 5F, left). Additionally, the combination treatment, as well as the solo arms, showed no toxicity to the mice

as seen by continued stable weight of the mice throughout the trial (Figure 5F, right). A subset of the combination trial mice were enrolled in an endpoint survival study in which the treatment was stopped after 22 days and the mice were monitored for 80 days post initiation of treatment. Endpoint was called when a tumor reached ~2cm in diameter and that indicated a notch on the survival curve. Interestingly, mice treated with AZA alone showed a slight but significant increase in survival even though no decrease in tumor growth while on treatment was observed (Figure 5F&G). This indicates that AZA alone may have a small impact on tumor growth over an extended period of time suggesting a time-dependent effect of EMT on tumor growth with AZA treatment. Mice from the combination treatment arm (AZA + SY) survived significantly longer than any of the single arm treatments or the vehicle control arm, indicating that the combination treatment has a long-term effect on tumor growth even after removal of the treatment doses (Figure 5G). Together, we have shown that combination treatment of AZA plus the clinical CDK7 inhibitor, SY5609, would be an effective treatment for classical PDA patient tumors as well as any mixed classical and basal tumors thereby dramatically increasing the application of CDK7 inhibition in treatment of PDA patient tumors.

DISCUSSION

Here we have found that ZNF274, a DNA-binding protein that recruits the ZNF274/SETDB1/DNMT1 repressive chromatin modifying complex, constrains the epithelial to mesenchymal transition (EMT) through direct regulation of ZEB1 expression in classical PDA tumor models. As a result, loss of ZNF274 leads to derepression of ZEB1, and increased suppression of epithelial gene expression thereby driving EMT. Tumors with mesenchymal features tend to have an increased ability to migrate and invade nearby tissues. We found that the

presence of ZNF274 is necessary to prevent migration and invasion in classical PDA models. Therefore, we have identified ZNF274 as a novel regulator of the epithelial cell state.

ZEB1 is a well-known master regulator of EMT, and it has been shown that when ZEB1 expression is altered in PDA, a cell state change can occur[40]. Regulation of ZEB1 itself is not as well studied as ZEB1 regulation of other genes, such as EMT regulatory genes. In this study, we determined that ZNF274 is a regulator of ZEB1 thereby controlling ZEB1's influence over EMT. Interestingly, ZNF274 expression is inversely correlated with ZEB1 expression in classical PDA cell lines (Figure 2B). This points to a complex, homeostatic relationship between ZNF274 and ZEB1 in which when one goes up the other goes down and vice versa to maintain a specific cellular balance. This connection between ZNF274 and ZEB1 is one of many connections which builds the complex regulatory network that defines the chromatin landscape of classical PDA.

Furthering the clinical application of this work, we uncovered that the absence of ZNF274 or inhibition of DNMTs sensitizes classical PDA models to inhibitors of CDK7. These manipulations lead to disruption of the complex chromatin landscape that enables classical PDA to maintain its epithelial cell state and resistance to CDK7 inhibition. Specifically, treatment of classical PDA with azacytidine induced a pseudo-basal state through increased ZEB1 expression but maintains expression of epithelial markers and therefore has not completely lost its epithelial identity. Therefore, initial treatment of AZA promotes EMT but upon extended AZA treatment, classical cells struggle to adapt to their loss of chromatin regulation and more mesenchymal identity thereby driving the cells into lethal EMT. This finding is similar to a previous study that found their kras-dependent (classical) PDA models to be more sensitive to another DNMT inhibitor, decitabine, compared to their kras-independent (basal) PDA models[66]. This study did not identify a mechanism that defined why kras-dependent PDA was more sensitive to

decitabine, therefore it could be similar to the lethal EMT we see with AZA or something else entirely. Collectively, these observations suggest a multifaceted role of DNMTs in maintenance of classical PDA cellular integrity.

Treating PDA patients with AZA was attempted in a clinical using an oral azacytidine (CC-486) followed by adjuvant therapy. This trial showed no improvement in patient disease response and no increase in time-to-relapse[67]. This is not surprising given that our study as well as others have shown that AZA treatment alone does not inhibit growth until very high doses are reached, such as 5uM or more in PDA cell lines in culture[68]. The equivalent treatment of these higher doses in humans would likely be too toxic, therefore a better approach is to pair AZA with another drug that can improve its anti-tumor effect and enable lower treatment doses. In our study we show that the psuedo-basal state induced by AZA that drives the lethal EMT is enough to sensitive classical PDA tumors to CDK7 inhibition. The combination treatment of AZA + CDK7i in classical PDA in vivo tumor models thereby accelerates the apoptotic effect compared to treatment with each drug alone. Therefore, this combination treatment presents as a potent but less toxic therapeutic option to treat heterogeneous PDA tumors.

MATERIALS AND METHODS

Cell lines. PDA cell lines were obtained from the American Type Culture Collection (ATCC) and grown in their required growth medium per the ATCC description. SUIT2 was obtained from Japanese Collection of Research Biosources cell bank and grown in RPMI supplemented with 10% FBS. Cells were passaged by trypsinization. All studies were done on cells cultivated for less than ten passages.

Organoids. Basal and classical subtyped human PDA organoids were generously gifted from the Notta Lab at the University of Toronto. Human PDA organoids were grown by embedding in Matrigel (Corning) and cultured in human feeding medium (AdDMEM/F12 medium supplemented with HEPES [1×, Invitrogen], Glutamax [1×, Invitrogen], penicillin/streptomycin [1×, Invitrogen], B27 [1×, Invitrogen], Primocin [1 mg/mL, InvivoGen], N-acetyl-L-cysteine [200 μg/mL, Sigma], Wnt3a-conditioned medium [20% v/v], RSPO1-conditioned medium [30% v/v], Noggin [0.1 μg/mL, Peprotech], Human EGF, [50 ng/mL, Peprotech], Gastrin [0.21 μg/mL, Tocris], Human FGF10 [0.1 μg/mL, Preprotech], Nicotinamide [0.045 mg/mL, Sigma], and A83-01 [0.21 μg/mL, Tocris]). To passage, organoids were dissociated into single cells using TrypLE (GIBCO) and then re-seeded into Matrigel (Corning) and topped with human feeding media. All studies were done on organoids cultivated for less than ten passages.

Real-time quantitative PCR (q-PCR). Total RNA extraction, cDNA synthesis and real-time quantitative PCR were performed as previously described in[52]. Data were expressed as relative mRNA abundance normalized to the β-ACTIN expression level in each sample or as fold change over control and error bars are represented as mean ± s.e.m. between two independent

experiments unless otherwise indicated in the figure legend. The primer sequences are listed in Table S1.

Protein isolation and Western blot. Chromatin fractions were prepared by resuspending the cell pellet in lysis buffer containing 10mM HEPES pH 7.4, 10 mM KCl, 0.05% NP-40 supplemented with a protease inhibitor cocktail (Complete EDTA-free, Roche Applied Science), 5μM TSA, 5mM sodium butyrate, 1mM DTT, and phosphatase inhibitors (Phosphatase Inhibitor Cocktail Sets I, II, and III Calbiochem) and incubated on ice for 20 minutes. The lysate was then centrifuged at 14,000 rpm for 10 minutes at 4°C. The supernatant was removed (cytosolic fraction) and the pellet (nuclei) was acid-extracted using 0.2N HCl and incubated on ice for 20 minutes. The lysate was then centrifuged at 14,000 rpm for 10 minutes at 4°C. The supernatant (contains acid soluble proteins) was neutralized using 1M Tris-HCl pH 8.
Whole cell lysate (WCL) was prepared by resuspending the cell pellets in RIPA lysis buffer supplemented with a protease inhibitor cocktail (Complete EDTA-free, Roche Applied Science), 5μM TSA, 5mM sodium butyrate, 1mM DTT, and phosphatase inhibitors (Phosphatase Inhibitor Cocktail Sets I, II, and III Calbiochem) and incubated on ice for 20 minutes. The lysate was then centrifuged at 14,000 rpm for 10 minutes at 4°C and the supernatant was harvested. Protein concentration was measured by using a BCA protein assay kit (Pierce). 20μg of the cell lysate (from lysis with buffer) electrophoresed on a 4-20% gradient polyacrylamide gel with SDS (Genscript) and electroblotted onto polyvinylidene difluoride membranes (PVDF) (Millipore). Membranes were blocked in TBS with 5% non-fat milk and 0.1% Tween and probed with antibodies. Bound proteins were detected with horseradish-peroxidase-conjugated secondary antibodies (Vector Biolaboratories) and Clarity Max Western ECL Blotting Substrate (Biorad).

Antibodies used were anti-ZNF274 (Novus Biologicals, catalog # H00010782-A01), anti-H3K9me3 (CST #13969), anti-ZEB1 (abcam #ab203829), anti-EpCAM (abcam # ab32392), anti-E-cadherin (CST #3195), anti-SETDB1 (Proteintech Group #11231-1-AP), anti-DNMT1 (abcam #ab13537), anti-p63 (CST #39692), anti-Cytokeratin17 (Invitrogen #MA1-06325), anti-Cytokeratin5 (abcam #ab52635), anti-Cleaved Caspase-3 (CST #9664), anti-PARP (CST #9542), anti-Total Histone H3 (abcam #ab1791), and anti-betaACTIN (Sigma A5316) as a loading control.

For Western blots performed on organoids, organoids were cultured in human feeding media. Organoids were pelleted using Cell Recovery Solution (Corning) to dissolve Matrigel, lysed in RIPA buffer, and processed as detailed above.

Organoid Embedding. Human PDA organoids were cultured as described above and then fixed in their Matrigel domes by removing the culture media and replacing with 4% PFA in PBS, then incubated for 1-2 hours at room temperature. Organoids were collected in a 50ml conical tube and centrifuge at 1300 rpm for 5 minutes at room temperature then the supernatant was removed. Washes were done consecutively by adding ddH2O, followed by centrifugation, then washed with 0.2% BSA in PBS and centrifuged. Organoids are suspended with 2% agarose and centrifuge at 1000 rpm, for 3 minutes, at room temperature and then cooled on ice. The solid gel from the conical tube is transferred to a histology cassette using disposable plastic scoop, stored in 70% ethanol, and submitted to the experimental histology core for FFPE processing and H&E staining.

Immunofluorescence. Following organoid embedding, unstained slides are deparaffinize by placing in the following liquids for the specified amount of time each: xylene for 15 minutes, xylene for 15 minutes, 100% ETOH for 5 minutes, 100% ETOH for 2 minutes, 100% ETOH for 2 minutes, 95% ETOH for 2 minutes, 70% ETOH for 2 minutes, 50% ETOH for 2 minutes, H2O for 2 minutes, H2O for 2 minutes. Slides are then placed in 1x antigen retrieval buffer (BRAND) and heated up using a pressure cooker. Slides are then cooled for 30 minutes to about 50°C and then washed with 1x PBS twice for 2 minutes each, then in PBS for 10 minutes, and then in permeabilization solution (PBS/gelatin/Triton 0.25%) twice for 10 minutes each. Slides are then blocked in 5% BSA in permeabilization solution in a moist chamber for 1 hour at room temperature. Primary antibodies are diluted with 1% BSA in permeabilization solution (ZNF274 1:100), added to the slides and placed in a moist chamber at 4°C overnight. The next day, the slides are washed twice with PBS for 10 minutes each and then placed in permeabilization solution (PBS/gelatin/Triton 0.25%) once for 10 minutes. Secondary antibodies are diluted with 1% BSA in permeabilization solution (Alexa Fluor 555, Invitrogen, 1:400 dilution), added to the slides and incubated for 1 hour at room temperature. Next, perform 3x washes in TBST 0.1% Tween for 5 minutes each. Mount using mounting media containing DAPI (H-1500, Vectashield Vector Laboratories), top with coverslip and seal. Antibodies used were: anti-ZNF274 (Novus Biologicals, catalog # H00010782-A01).

Crystal violet staining. Grow cells in a 6cm or 10cm plate, then place cells on ice and wash twice with cold PBS. Fix for 10 minutes with ice-cold 100% methanol and then aspirate. Move the cells off ice to room temperature and cover them with 0.5% crystal violet solution in 25% methanol. Incubate for 10 minutes and then remove the crystal violet. Wash the cells in water

several times, until the dye stops coming off. Allow the cells to dry at room temperature (possibly overnight) and then store at room temperature.

siRNA transfection. Cells were plated and then forward transfected the next day with siRNAs in a 6cm or 10cm culture dishes by replacing the media with 2mL or 4mL of OptiMEM low-serum media (Gibco) and then adding 500µL or 1mL OptiMEM low-serum media (Gibco) containing 10µL or 20µL of Lipofectamine RNAiMAX (Invitrogen) and either non-targeting (Control) or targeting siRNAs (0.25µM). The plates were supplemented with 2mL or 4mL of complete media after 8 hours of incubation at 37°C and then completely replaced with fresh media 24 hours after transfection. Cells were cultured for an additional 40 hours (72 hours total) unless otherwise stated in the figure legend, after which cell pellets were extracted for downstream assays including Western blotting and q-PCR. siRNAs were obtained from Dharmacon: ZNF274 (L-013359-02), SETDB1 (L-020070-00), DNMT1 (L-004605-00), Control (D-001810-10).

Constructs and viral infection. Plasmids for viral infection: SMART vector shZNF274 and shCTRL, pTRE-ZNF274-3xHA, pSCALP-ZEB1.
SMARTvector Inducible Lentiviral shRNA plasmids containing ZNF274 or control short hairpin RNAs were purchased from Dharmacon. These plasmids are used for dox-inducible knockdown of ZNF274 or control and were used to create stable lines. pTRE-ZNF274-3xHA was kindly gifted from Dr. Martina Begnis in the Trono lab at the Swiss Federal Institute of Technology in Lausanne. This plasmid is a dox-inducible ZNF274 overexpression construct. pSCALP-ZEB1 (ZEB1 overexpression plasmid) was kindly gifted from Dr. Giuseppe Diaferia at Humanitas University in Italy.

Viral particles were synthesized and infected as described in[52]. Cells infected with the SMART vector shZNF274 and shCTRL were then select for single clones by dilution for single cells in a 96 well plate and grown out to form stable cell lines.

Chromatin immunoprecipitation. Cells were cross-linked with 1% paraformaldehyde for 15 minutes at room temperature. The reaction was quenched for 5 minutes at room temperature by adding 0.125 M glycine. After three washes with 1X PBS, cells were lysed with lysis buffer (1% SDS, 10 mM EDTA pH 8, 50 mM Tris-HCl pH 8) supplemented with a protease inhibitor cocktail (Complete EDTA-free, Roche Applied Science), 5µM TSA, 5mM sodium butyrate, 1mM DTT, and phosphatase inhibitors (Phosphatase Inhibitor Cocktail Sets I, II, and III Calbiochem). Lysates were incubated on ice for 20 minutes and then sonicated using a QSONICA Q800R3 sonicator (10 seconds ON, 20s OFF, 30% AMP; samples in 4ºC water bath throughout sonication cycles). Size of fragments obtained (between 200 and 1,200 bp) was confirmed by electrophoresis. Soluble chromatin was collected after centrifugation at 14,000 rpm at 4°C for 10 minutes and diluted to 1/5 in dilution buffer (1% Triton X-100, 2 mM EDTA, 150 mM NaCl, 20 mM Tris-HCl pH 8.1) supplemented with protease, deacetylase, and phosphatase inhibitors. Soluble chromatin (1%) was kept as input control. Soluble chromatin was precleared with 100 µg/ml of salmon sperm (Amersham Biosciences), 2.5 µg/ml of unspecific IgGs, and 20µL of protein-PLUS A/G Sepharose beads overnight at 4°C in continued rotation. The next day samples were centrifuged, supernatants were collected, and specific antibodies were added. Mixtures were incubated at 4°C overnight in rotation. The following day protein-PLUS A/G Sepharose beads (sc-2003) were added to the samples and incubated for 2-4 hours at 4°C in rotation. Beads were collected and washed sequentially at 4°C for 10 minutes with TSE I (150

mM NaCl, 0.1% SDS, 1% Triton X-100, 2 mM EDTA, and 20 mM Tris-HCl (pH 8.1)), TSE II (500 mM NaCl, 0.1% SDS, 1% Triton X-100, 2 mM EDTA, and 20 mM Tris-HCl (pH 8.1)), buffer III (0.25 LiCl, 1% Nonidet P-40, 1% deoxycholate, 1 mM EDTA, and 10 mM Tris-HCl (pH 8.1)) and then 1x PBS. Immunoprecipitates were eluted with 100μL of with elution buffer (0.1 M NaHCO3 and 1% SDS) and rocked for 40 minutes. Reversion of cross-linking was performed overnight by adding 0.2M NaCl and heating and shaking samples and input controls at 65°C. Samples were then treated with 0.2 mg/mL RNAse A (Qiagen) and incubated for 1hr at 37°C followed by addition of 0.01M EDTA, 0.04M Tris-HCl pH 6.5 and 4 U/mL of Proteinase K (Promega) and samples were incubated at 45°C for 1 hr. DNA was then purified using the Monarch DNA Clean up kit (NEB). 1μL of purified DNA was then used in real-time quantitative PCR as described above. The primer sequences are listed in Table S2.

Scratch Assay. Plate 30,000 cells per well in a 96-well plate. The next day preform scratch, wash twice with PBS, and replace each well with 200 μL of media. Place plate in IncuCyte and program to take images every 4 hours for 24 hours. After imaging completes, remove plate, export images, and analyze using Sartorius.

Invasion Assay. Human PDA organoids were cultured as described above and then were recovered from Matrigel by resuspension in cold cell recovery solution and incubated on ice. Organoids were centrifuged at 200 rcf and resuspended in cold DMEM and kept on ice. Organoids were embedded in 1.5 mg/mL collagen gels using protocols previously published, which were prepared from the 4.5 mg/mL rat-tail collagen made by the Cheung lab[69,70]. 4.5

mg/mL collagen was diluted to 1.8 mg/mL in 0.1% acetic acid. This was then mixed with 10X DMEM, 1 N NaOH, and ultrapure water at the following ratio:

1 mL collagen (1.8 mg/mL): 100 µL 10X DMEM: 32 µL NaOH: 66.66 µL H2O

This mixture was allowed to polymerize at 4°C and was then mixed with organoids at a concentration of ~180 organoids/100 µL. Glass-bottom 24 well plates were prepared by plating 40 µL of collagen (without organoids) in the center of each well to be used. The plate was placed at 37°C for 5-10 minutes to allow the collagen disks to polymerize, after which 100 µL of the collagen/organoid mixture was plated on top as a dome. This was allowed to polymerize for an additional 45-60 minutes at 37°C. After complete polymerization, 1 mL of human organoid feeding media was added to each well.

At the end of the experiment, the media was removed and PBS was added for 5-10 minutes. The organoids in collagen were fixed with 4% PFA for 20 minutes at room temperature in the 24 well plate. Wells were washed with PBS and then stored at 4°C. Plates were imaged using an Andor CSU-W confocal spinning disk on a Leica DMi8 inverted microscope. All organoids per well were imaged and counted for spine formation.

Subcutaneous Cell line Xenografts. All mouse procedures were conducted in accordance with the Fred Hutchinson Cancer Center (FHCC) Institutional Animal Care and Use Committee (IACUC) guidelines and the ARRIVE guidelines. Athymic nude (NU/J) mice (002019, JAX) were purchased from the Jackson Laboratory. Injections of cell lines for the generation of subcutaneously grafted cell line tumors were prepared by resuspending 1.5x10^6 cells in a 100

μL suspension of 50% Matrigel (Corning) in phosphate-buffered saline (PBS). Cell suspensions were injected into each flank of the mouse. 5 days after injection the mice were put on water with 200 μg/mL of doxycycline. 3 days after the initiation of doxycycline water, initial tumor volumes were measured, and mice started on once daily oral gavage treatment of vehicle (5% captisol) or SY5609 (0.5 mg/kg, Syros) dissolved in 5% captisol for 22 days. Caliper measurements of tumors and body weights were recorded three times per week. Tumor volumes were normalized to the initial tumor volume for each mouse and plotted as normalized tumor growth.

Patient-derived Xenograft. PDX models were acquired from the NIC PDMR and JAX (PAAD154b - NCI 885724; PAAD141b - NCI 463931; PAAD169b - JAX TM 00176; PAAD200 - JAX TM01212). PDX implantations were administered as previously described in[52] followed by post-surgical monitoring. Tumors were measure with electronic calipers and upon reaching an average tumor diameter of 3 to 5 mm^3, mice were treated with a once daily oral gavage of vehicle (5% captisol), SY5609 alone (0.5 mg/kg, Syros), Azacytidine alone (2.5mg/kg, S1782, Selleck), or combination of SY5609 (0.5mg/kg) plus AZA (2.5mg/kg) for 22 days. Caliper measurements of tumors and body weights were recorded three times a week. A subset of trial mice were taken out to endpoint following termination of treatment at 22 days. Endpoint is called when the tumor diameter reaches ~2cm and this indicates a notch in the survival curve. The survival study concluded at 80 days post initiation of treatment.

FIGURES

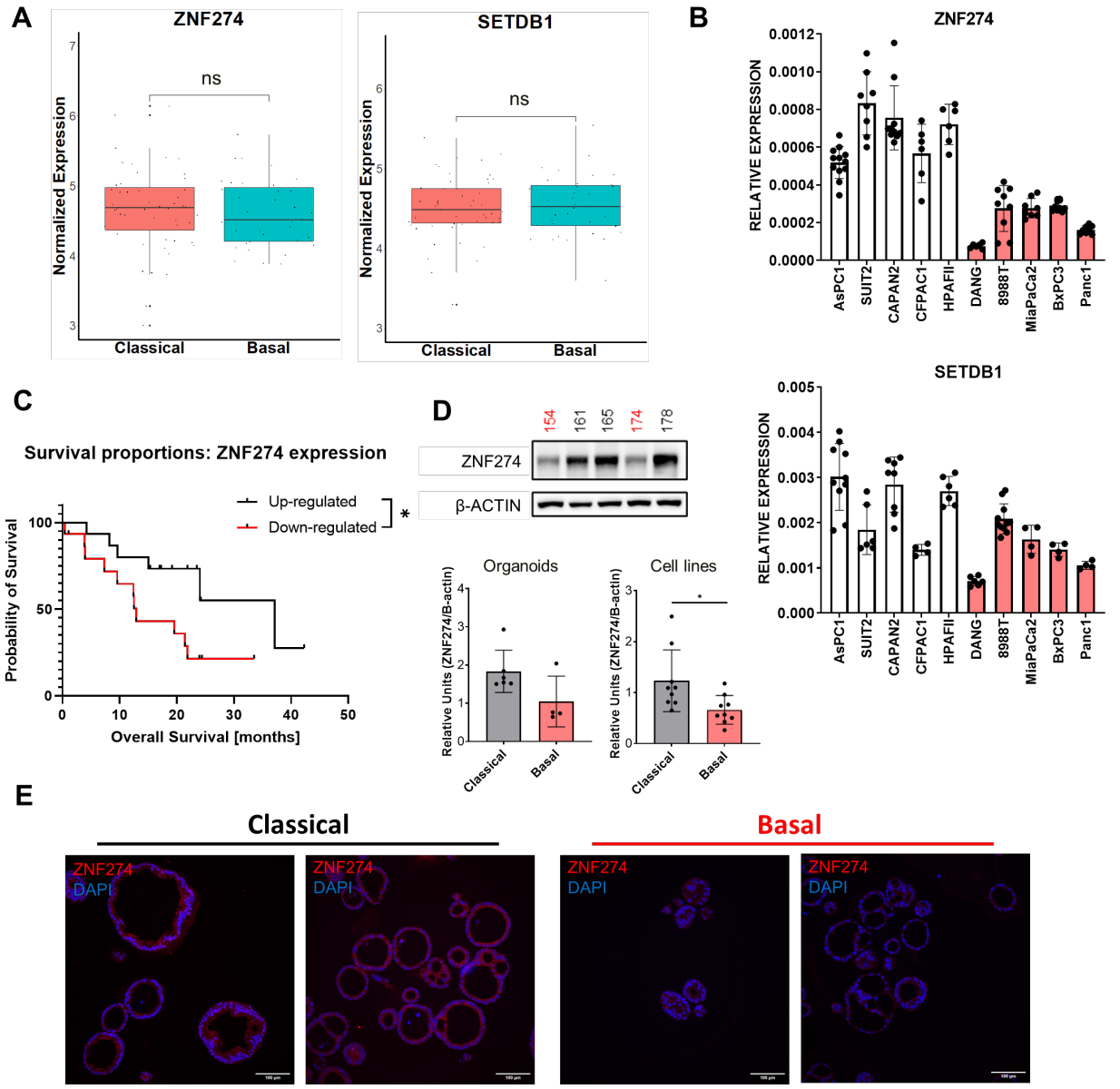

Figure 1. ZNF274 expression characterizes Classical PDA. A, ZNF274 and SETDB1 expression from TCGA-PAAD publicly available dataset from human tumors classified as basal or classical PDA. **B,** RT-PCR for ZNF274 and SETDB1 in a panel of human PDA cell lines. **C,** Survival curves using TCGA patient data classified by ZNF274 mRNA expression using the highest and lowest quartile. A log rank (Mantel-Cox) test was performed to determine significance between up-regulated and down regulated ZNF274 expression. **D,** WB for ZNF274 and ACTIN in basal (red) and classical (black) PDA organoids with WB quantification of relative ZNF274 expression normalized to actin for PDA organoids and cell lines. **E,** Immunofluorescence images of ZNF274 stained embedded classical (black) and basal (red) PDA organoids. Error bars represent +/- SEM between technical triplicates. Data are representative of at least 2 independent experiments. *p-value ≤ 0.05; **p-value ≤ 0.01 (two-tailed unpaired Student's *t*-test).

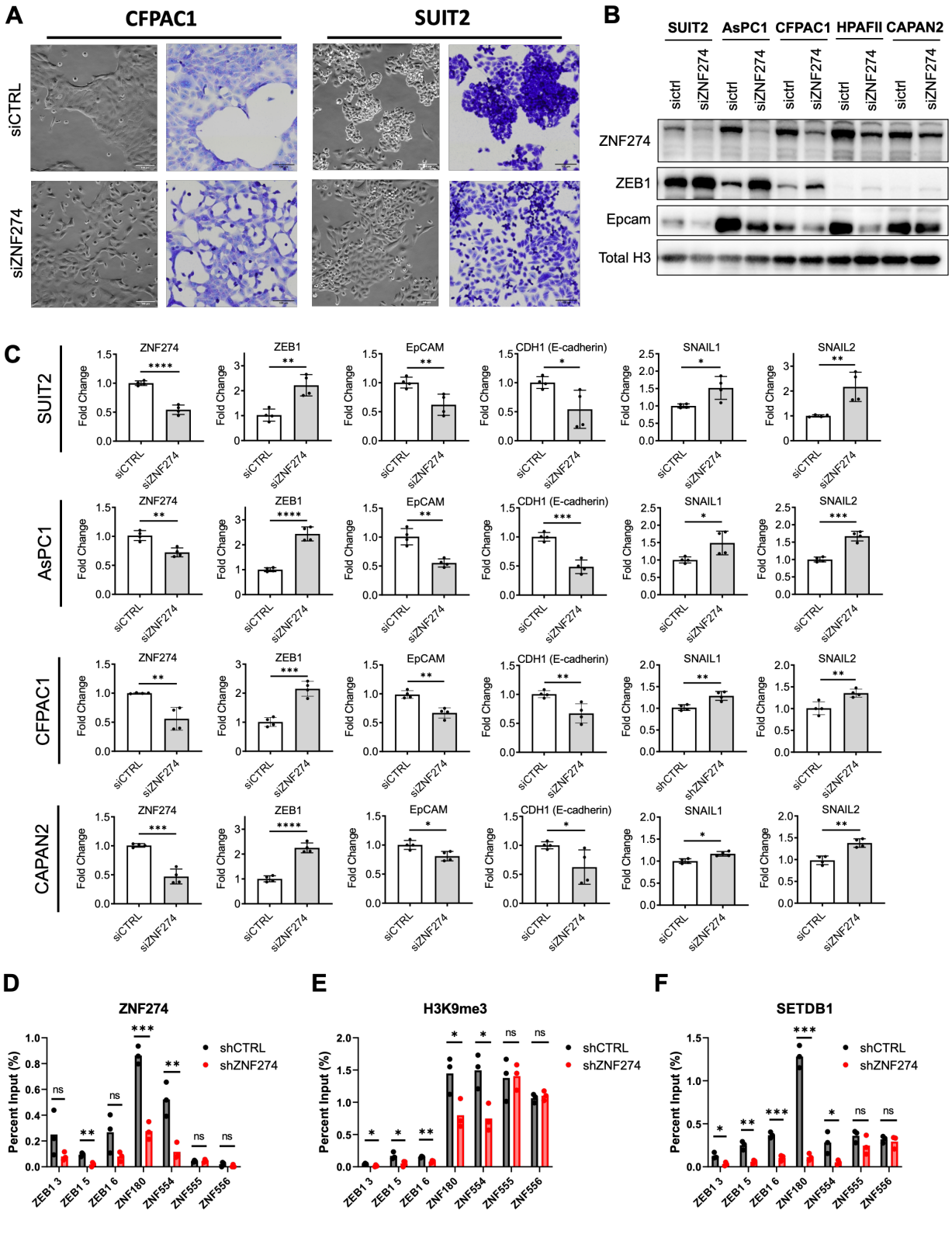
A
CFPAC1
SUIT2
siCTRL
siZNF274
B
SUIT2
AsPC1
CFPAC1
HPAFII
CAPAN2
sictrl
siZNF274
ZNF274
ZEB1
Epcam
Total H3
C
SUIT2
AsPC1
CFPAC1
CAPAN2
ZNF274
ZEB1
EpCAM
CDH1 (E-cadherin)
SNAIL1
SNAIL2
Fold Change
siCTRL
siZNF274
shCTRL
shZNF274
D
ZNF274
E
H3K9me3
F
SETDB1
Percent Input (%)
shCTRL
shZNF274
ZEB1 3
ZEB1 5
ZEB1 6
ZNF180
ZNF554
ZNF555
ZNF556

Figure 2. ZNF274 loss promotes epithelial to mesenchymal transition in Classical PDA. A, Phase contrast images of live classical PDA cells and brightfield color images of crystal violet-stained classical PDA cells treated with non-specific or ZNF274-specific siRNAs. Images were taken on the Nikon Live microscope and have a scale bar of 100um. **B,** WB for chromatin bound ZNF274, ZEB1, EpCAM, and Total H3 in classical PDA cells lines treated with non-specific or ZNF274-specific siRNAs. **C,** RT-PCR for ZNF274, markers of the mesenchymal cell state: ZEB1, SNAIL1 and SNAIL2; and markers of the epithelial cell state: EpCAM and CDH1 (E-cadherin) in classical PDA cells lines treated with non-specific or ZNF274-specific siRNAs. **D-F,** ChIP-qPCR for ZEB1 3 (promoter), ZEB1 5 (3' exon), ZEB1 6 (3' exon), ZNF180 and ZNF554 (ZNF274 bound positive control genes), ZNF555 and ZNF556 (non-ZNF274 bound negative control genes) with pulldown for ZNF274 (D), H3K9me3 (E), and SETDB1 (F) in a classical PDA cell line with doxycycline induced control or ZNF274-specific shRNAs. Error bars represent +/- SEM between technical triplicates. Data are representative of at least 2 independent experiments. *p-value $\leq$ 0.05; **p-value $\leq$ 0.01, ***p-value $\leq$ 0.001, ****p-value $\leq$ 0.0001 (two-tailed unpaired Student's *t*-test).

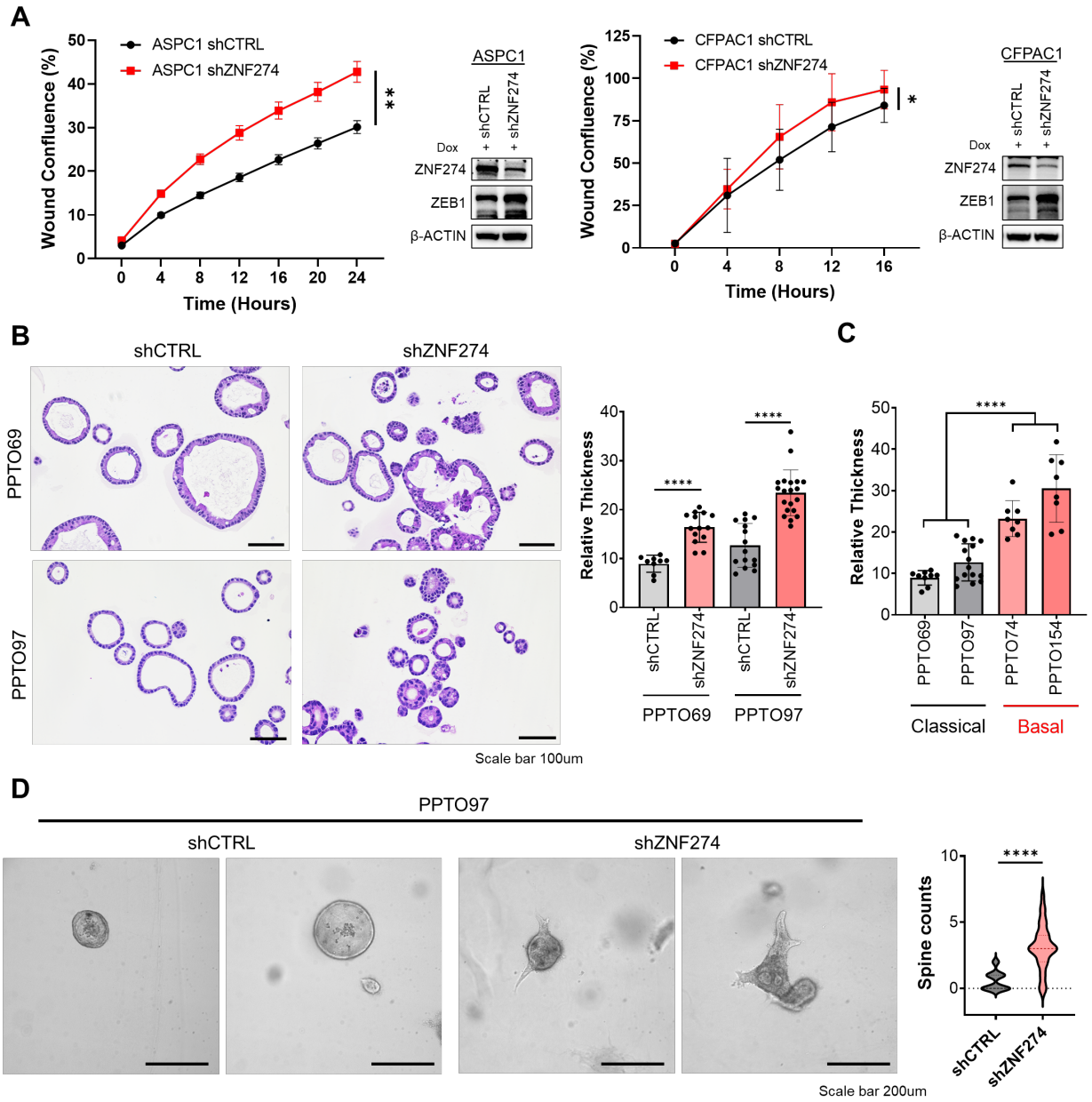

Figure 3. Classical PDA cells acquire increased migration and invasion capacities upon removal of ZNF274. A, Scratch assay plot showing percent of wound confluence over 24 hours following doxycycline induction of control or ZNF274-specific shRNAs in two classical PDA cell lines (left) and paired WB for ZNF274, ZEB1 and ACTIN (right) for each line. **B,** Brightfield color images of H&E slides from embedded classical PDA organoids with doxycycline induced of control or ZNF274-specific shRNAs (left) and quantification of relative thickness by FIJI local thickness plug in (right). All images were taken on the Nikon Live microscope and have a scale bar of 100µm. **C,** Quantification of relative thickness by FIJI local thickness plug in from brightfield color images of H&E slides from embedded classical and basal PDA organoids. **D,** Brightfield images of live classical PDA organoids with doxycycline induced control or ZNF274-specific shRNAs grown in collagen to assess invasion. Images were taken on

the Leica DMi8 inverted microscope and have a scale bar of 200μm. Quantification of number of spines protruding from shCTRL and shZNF274 classical PDA organoids (right). Error bars represent +/- SEM between technical triplicates. Data are representative of at least 2 independent experiments. *p-value ≤ 0.05; **p-value ≤ 0.01, ***p-value ≤ 0.001, ****p-value ≤ 0.0001 (two-tailed unpaired Student's *t*-test).

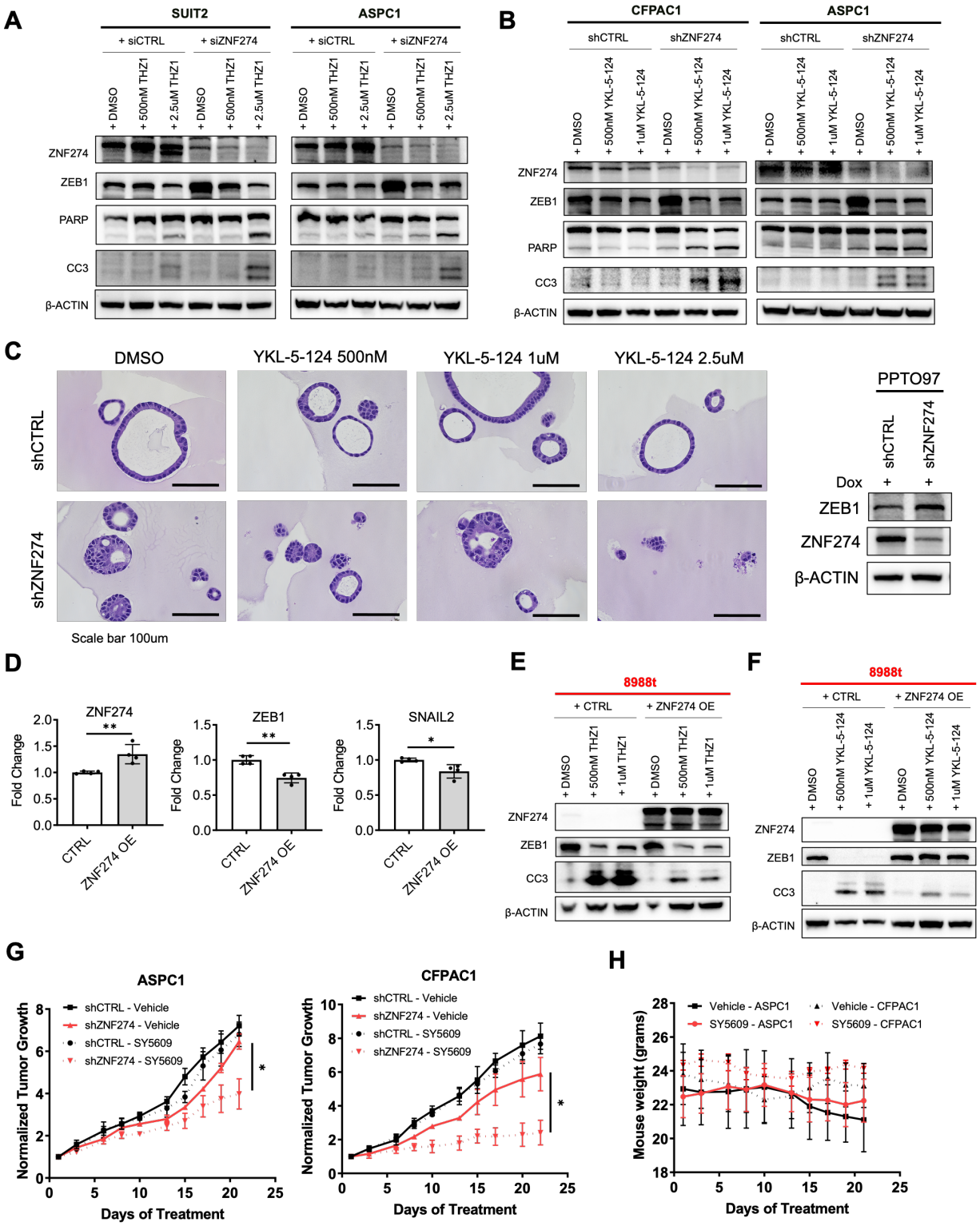

Figure 4. ZNF274 is necessary to maintain resistance to CDK7 inhibitors. A, WB for ZNF274, ZEB1, PARP, CC3 and ACTIN in classical PDA cells lines transfected with non-specific or ZNF274-specific siRNAs and treated with 500nM or 2.5uM THZ1 for 40 hours. **B,**

WB for ZNF274, ZEB1, PARP, CC3 and ACTIN from doxycycline inducible control or ZNF274-specific shRNAs classical PDA cell lines treated with 500nM, 1uM or 2.5uM YKL-5-124 for 72 hours. **C,** Brightfield color images of H&E slides from embedded classical PDA organoids with doxycycline induced of control or ZNF274-specific shRNAs and then treated with 500nM, or 1uM YKL-5-124 for 72 hours (left). Images were taken on the Nikon Live microscope and have a scale bar of 100um. Paired WB for ZNF274, ZEB1 and ACTIN from classical PDA organoids with doxycycline induced of control or ZNF274-specific shRNAs (right). **D,** RT-PCR for ZNF274, ZEB1 and SNAIL2 in a basal PDA cell line infected with an empty vector or ZNF274 overexpression vector. **E-F,** WB for ZNF274, ZEB1, CC3 and ACTIN in a basal PDA cell line infected with an empty vector or ZNF274 overexpression vector and treated with 500nM or 1uM THZ1 for 24 hours (E) and 500nM or 1uM YKL-5-124 for 72 hours (F). **G-H,** Normalized tumor growth (G) and mouse weights (H) of subcutaneously implanted ASPC1 and CFPAC1 dox-inducible shCTRL or shZNF274 cell lines treated with once-daily SY5609 (0.5mg/kg) compared with Vehicle control (5% captisol) for 21 days (each arm n=3). Error bars represent +/- SEM between technical triplicates. Data are representative of at least 2 independent experiments. *p-value ≤ 0.05; **p-value ≤ 0.01 (two-tailed unpaired Student's *t*-test).

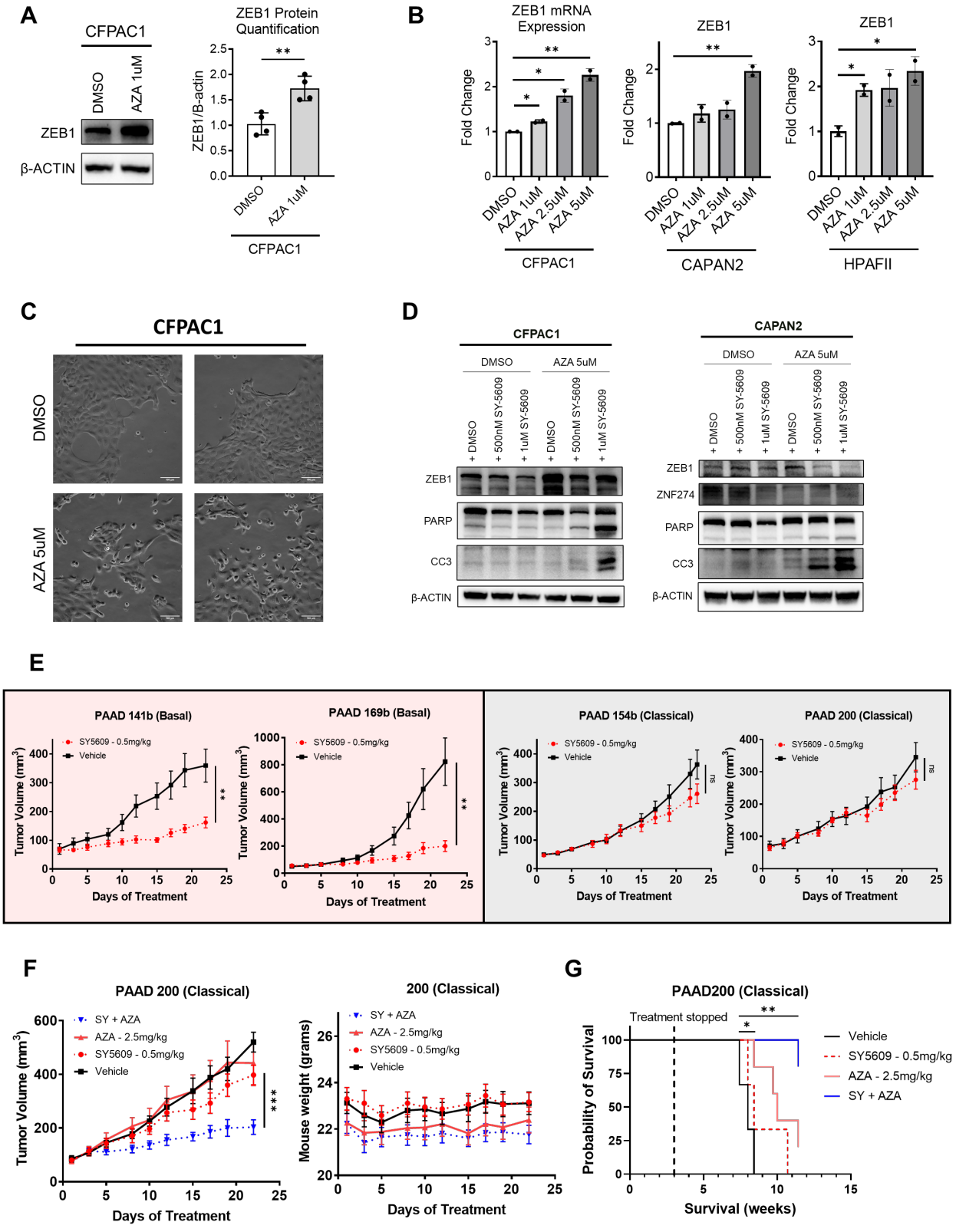
A
CFPAC1
DMSO
AZA 1uM
ZEB1
β-ACTIN
ZEB1 Protein Quantification
ZEB1/B-actin
B
ZEB1 mRNA Expression
Fold Change
DMSO
AZA 1uM
AZA 2.5uM
AZA 5uM
CFPAC1
ZEB1
CAPAN2
HPAFII
C
CFPAC1
DMSO
AZA 5uM
D
CFPAC1
CAPAN2
+ DMSO
+ 500nM SY-5609
+ 1uM SY-5609
ZEB1
ZNF274
PARP
CC3
β-ACTIN
E
PAAD 141b (Basal)
PAAD 169b (Basal)
PAAD 154b (Classical)
PAAD 200 (Classical)
SY5609 - 0.5mg/kg
Vehicle
Tumor Volume (mm3)
Days of Treatment
ns
F
PAAD 200 (Classical)
200 (Classical)
SY + AZA
AZA - 2.5mg/kg
SY5609 - 0.5mg/kg
Vehicle
Tumor Volume (mm3)
Mouse weight (grams)
Days of Treatment
G
PAAD200 (Classical)
Treatment stopped
Probability of Survival
Survival (weeks)
Vehicle
SY5609 - 0.5mg/kg
AZA - 2.5mg/kg
SY + AZA

Figure 5. DNMT inhibition induces ZEB1 and enhances sensitivity to CDK7 inhibition. A, Representative WB for ZEB1 and Actin in a classical PDA cell line treated with 1uM Azacytidine for 48 hours (left). WB quantification of relative ZEB1 expression normalized to ACTIN for classical PDA cells treated with 1uM Azacytidine for 48 hours replicates (right). **B,** RT-PCR for ZEB1 in classical PDA cells lines treated with increasing doses of Azacytidine for 48 hours. **C,** Phase contrast images of live classical PDA cells treated with 5uM Azacytidine for 48 hours. Images were taken on the Nikon Live microscope and have a scale bar of 100um. **D,** WB for ZEB1, PARP, CC3, yH2Ax, and ACTIN in classical PDA cells treated with 5uM Azacytidine plus either 500nM or 1uM SY-5609 for 48 hours. **E,** Tumor volume of basal and classical PDA xenografts after treatment with once-daily SY5609 (0.5 mg/kg) (red) compared with Vehicle control, 5% captisol, (black) for 21 days (Vehicle n = 8, SY-5609 n = 8). **F,** Tumor volume of a classical PDA xenograft after treatment with once-daily combo (SY-5609 0.5mg/kg and azacytidine 2.5mg/kg) (dotted blue), azacytidine alone (2.5mg/kg) (solid red), SY-5609 alone (0.5mg/kg) (dotted red), or Vehicle control (5% captisol) (solid black) for 21 days (n=7 for each treatment group) and mouse weights. **G,** Endpoint survival study for a subset of AZA+SY combination study mice. Treatment was stopped at 22 days and mice were monitored for a total of 80 days post initiation of treatment (Vehicle and SY5609 only n = 3; AZA only and AZA + SY n = 5). A log rank (Mantel-Cox) test was performed to determine significance between the AZA + SY arm or the AZA alone arm and the Vehicle control arm. Error bars represent +/- SEM between technical triplicates. Data are representative of at least 2 independent experiments. *p-value $\leq$ 0.05; **p-value $\leq$ 0.01; ***p-value $\leq$ 0.001 (two-tailed unpaired Student's *t*-test).

CHAPTER 3: REFERENCES

1. Rahib, L. *et al.* Projecting Cancer Incidence and Deaths to 2030: The Unexpected Burden of Thyroid, Liver, and Pancreas Cancers in the United States. *Cancer Res.* **74**, 2913–2921 (2014).
2. Hingorani, S. R. *et al.* Preinvasive and invasive ductal pancreatic cancer and its early detection in the mouse. *Cancer Cell* **4**, 437–450 (2003).
3. Hingorani, S. R. *et al.* Trp53R172H and KrasG12D cooperate to promote chromosomal instability and widely metastatic pancreatic ductal adenocarcinoma in mice. *Cancer Cell* **7**, 469–483 (2005).
4. Brar, G. *et al.* Multi-omic molecular comparison of primary versus metastatic pancreatic tumours. *Br. J. Cancer* **121**, 264–270 (2019).
5. Collisson, E. A. *et al.* Subtypes of pancreatic ductal adenocarcinoma and their differing responses to therapy. *Nat. Med.* **17**, 500–503 (2011).
6. Moffitt, R. A. *et al.* Virtual microdissection identifies distinct tumor- and stroma-specific subtypes of pancreatic ductal adenocarcinoma. *Nat. Genet.* **47**, 1168–1178 (2015).
7. Bailey, P. *et al.* Genomic analyses identify molecular subtypes of pancreatic cancer. *Nature* **531**, 47–52 (2016).
8. Raphael, B. J. *et al.* Integrated Genomic Characterization of Pancreatic Ductal Adenocarcinoma. *Cancer Cell* **32**, 185-203.e13 (2017).
9. Puleo, F. *et al.* Stratification of Pancreatic Ductal Adenocarcinomas Based on Tumor and Microenvironment Features. *Gastroenterology* **155**, 1999-2013.e3 (2018).
10. Hayashi, A. *et al.* A unifying paradigm for transcriptional heterogeneity and squamous features in pancreatic ductal adenocarcinoma. *Nat. Cancer* **1**, 59–74 (2020).
11. Chan-Seng-Yue, M. *et al.* Transcription phenotypes of pancreatic cancer are driven by genomic events during tumor evolution. *Nat. Genet.* **52**, 231–240 (2020).
12. Lomberk, G. *et al.* Distinct epigenetic landscapes underlie the pathobiology of pancreatic cancer subtypes. *Nat. Commun.* **9**, 1978 (2018).
13. Lomberk, G., Dusetti, N., Iovanna, J. & Urrutia, R. Emerging epigenomic landscapes of pancreatic cancer in the era of precision medicine. *Nat. Commun.* **10**, 3875 (2019).
14. Espinet, E. *et al.* Aggressive PDACs Show Hypomethylation of Repetitive Elements and the Execution of an Intrinsic IFN Program Linked to a Ductal Cell of Origin. *Cancer Discov.* **11**, 638–659 (2021).
15. Lander, E. S. *et al.* Initial sequencing and analysis of the human genome. *Nature* **409**, 860–921 (2001).
16. Tupler, R., Perini, G. & Green, M. R. Expressing the human genome. *Nature* **409**, 832–833 (2001).
17. Shannon, M., Hamilton, A. T., Gordon, L., Branscomb, E. & Stubbs, L. Differential Expansion of Zinc-Finger Transcription Factor Loci in Homologous Human and Mouse Gene Clusters. *Genome Res.* **13**, 1097–1110 (2003).
18. Schmidt, D. & Durrett, R. Adaptive Evolution Drives the Diversification of Zinc-Finger Binding Domains. *Mol. Biol. Evol.* **21**, 2326–2339 (2004).
19. Emerson, R. O. & Thomas, J. H. Adaptive Evolution in Zinc Finger Transcription Factors. *PLOS Genet.* **5**, e1000325 (2009).
20. Thomas, J. H. & Schneider, S. Coevolution of retroelements and tandem zinc finger genes. *Genome Res.* **21**, 1800–1812 (2011).

21. Jacobs, F. M. J. *et al.* An evolutionary arms race between KRAB zinc-finger genes ZNF91/93 and SVA/L1 retrotransposons. *Nature* **516**, 242–245 (2014).
22. Grimwood, J. *et al.* The DNA sequence and biology of human chromosome 19. *Nature* **428**, 529–535 (2004).
23. Lukic, S., Nicolas, J.-C. & Levine, A. J. The diversity of zinc-finger genes on human chromosome 19 provides an evolutionary mechanism for defense against inherited endogenous retroviruses. *Cell Death Differ.* **21**, 381–387 (2014).
24. Ecco, G., Imbeault, M. & Trono, D. KRAB zinc finger proteins. *Development* **144**, 2719–2729 (2017).
25. Nishibuchi, G. & Déjardin, J. The molecular basis of the organization of repetitive DNA-containing constitutive heterochromatin in mammals. *Chromosome Res.* **25**, 77–87 (2017).
26. Schultz, D. C., Ayyanathan, K., Negorev, D., Maul, G. G. & Rauscher, F. J. SETDB1: a novel KAP-1-associated histone H3, lysine 9-specific methyltransferase that contributes to HP1-mediated silencing of euchromatic genes by KRAB zinc-finger proteins. *Genes Dev.* **16**, 919–932 (2002).
27. Griffin, G. K. *et al.* Epigenetic silencing by SETDB1 suppresses tumour intrinsic immunogenicity. *Nature* **595**, 309–314 (2021).
28. Ogawa, S. *et al.* SETDB1 Inhibits p53-Mediated Apoptosis and Is Required for Formation of Pancreatic Ductal Adenocarcinomas in Mice. *Gastroenterology* **159**, 682-696.e13 (2020).
29. Frietze, S., O'Geen, H., Blahnik, K. R., Jin, V. X. & Farnham, P. J. ZNF274 Recruits the Histone Methyltransferase SETDB1 to the 3′ Ends of ZNF Genes. *PLOS ONE* **5**, e15082 (2010).
30. Valle-García, D. *et al.* ATRX binds to atypical chromatin domains at the 3′ exons of zinc finger genes to preserve H3K9me3 enrichment. *Epigenetics* **11**, 398–414 (2016).
31. Iyengar, S., Ivanov, A. V., Jin, V. X., Rauscher, F. J. & Farnham, P. J. Functional Analysis of KAP1 Genomic Recruitment. *Mol. Cell. Biol.* **31**, 1833–1847 (2011).
32. Iyengar, S. & Farnham, P. J. KAP1 Protein: An Enigmatic Master Regulator of the Genome*. *J. Biol. Chem.* **286**, 26267–26276 (2011).
33. Jen, J. & Wang, Y.-C. Zinc finger proteins in cancer progression. *J. Biomed. Sci.* **23**, (2016).
34. Zhao, J., Wen, D., Zhang, S., Jiang, H. & Di, X. The role of zinc finger proteins in malignant tumors. *FASEB J.* **37**, e23157 (2023).
35. Iyer, A. S., Shaik, M. R., Raufman, J.-P. & Xie, G. The Roles of Zinc Finger Proteins in Colorectal Cancer. *Int. J. Mol. Sci.* **24**, 10249 (2023).
36. Bhat, S. *et al.* ZNF471 modulates EMT and functions as methylation regulated tumor suppressor with diagnostic and prognostic significance in cervical cancer. *Cell Biol. Toxicol.* **37**, 731–749 (2021).
37. Wang, S. *et al.* Zinc-finger protein 545 is a novel tumour suppressor that acts by inhibiting ribosomal RNA transcription in gastric cancer. *Gut* **62**, 833–841 (2013).
38. Marzbany, M., Bishayee, A. & Rasekhian, M. Increased expression of ZNF 703 in breast cancer tissue: An opportunity for RNAi–NSAID combinatorial therapy. *Biotechnol. Appl. Biochem.* **66**, 808–814 (2019).
39. Sipos, B. *et al.* A comprehensive characterization of pancreatic ductal carcinoma cell lines: towards the establishment of an in vitro research platform. *Virchows Arch.* **442**, 444–452 (2003).
40. Diaferia, G. R. *et al.* Dissection of transcriptional and cis-regulatory control of differentiation in human pancreatic cancer. *EMBO J.* **35**, 595–617 (2016).

41. Somerville, T. D. D. *et al.* TP63-Mediated Enhancer Reprogramming Drives the Squamous Subtype of Pancreatic Ductal Adenocarcinoma. *Cell Rep.* **25**, 1741-1755.e7 (2018).
42. Roa-Peña, L. *et al.* Keratin 17 identifies the most lethal molecular subtype of pancreatic cancer. *Sci. Rep.* **9**, 11239 (2019).
43. Hosein, A. N., Dougan, S. K., Aguirre, A. J. & Maitra, A. Translational advances in pancreatic ductal adenocarcinoma therapy. *Nat. Cancer* **3**, 272–286 (2022).
44. Klonou, A. *et al.* Histone H3K9 methyltransferase SETDB1 overexpression correlates with pediatric high-grade gliomas progression and prognosis. *J. Mol. Med.* **101**, 387–401 (2023).
45. Du, D. *et al.* Smad3-mediated recruitment of the methyltransferase SETDB1/ESET controls Snail1 expression and epithelial–mesenchymal transition. *EMBO Rep.* **19**, 135–155 (2018).
46. Koide, S. *et al.* Setdb1 maintains hematopoietic stem and progenitor cells by restricting the ectopic activation of nonhematopoietic genes. *Blood* **128**, 638–649 (2016).
47. Liang, G. *et al.* Distinct localization of histone H3 acetylation and H3-K4 methylation to the transcription start sites in the human genome. *Proc. Natl. Acad. Sci.* **101**, 7357–7362 (2004).
48. Lee, B. H., Seijo-Barandiaran, I. & Grapin-Botton, A. Epithelial morphogenesis in organoids. *Curr. Opin. Genet. Dev.* **72**, 30–37 (2022).
49. Theveneau, E. & Mayor, R. Neural crest delamination and migration: From epithelium-to-mesenchyme transition to collective cell migration. *Dev. Biol.* **366**, 34–54 (2012).
50. Shi, X. *et al.* Integrated profiling of human pancreatic cancer organoids reveals chromatin accessibility features associated with drug sensitivity. *Nat. Commun.* **13**, 2169 (2022).
51. Thompson, J. K. & Bednar, F. Clinical Utility of Epigenetic Changes in Pancreatic Adenocarcinoma. *Epigenomes* **5**, 20 (2021).
52. Kartha, N. *et al.* Sirtuin 6 is required for the integrated stress response and resistance to inhibition of transcriptional cyclin-dependent kinases. *Sci. Transl. Med.* **15**, eabn9674 (2023).
53. Constantin, T. A., Greenland, K. K., Varela-Carver, A. & Bevan, C. L. Transcription associated cyclin-dependent kinases as therapeutic targets for prostate cancer. *Oncogene* **41**, 3303–3315 (2022).
54. Galbraith, M. D., Bender, H. & Espinosa, J. M. Therapeutic targeting of transcriptional cyclin-dependent kinases. *Transcription* **10**, 118–136 (2018).
55. Kwiatkowski, N. *et al.* Targeting transcription regulation in cancer with a covalent CDK7 inhibitor. *Nature* **511**, 616–620 (2014).
56. Olson, C. M. *et al.* Development of a Selective CDK7 Covalent Inhibitor Reveals Predominant Cell-Cycle Phenotype. *Cell Chem. Biol.* **26**, 792-803.e10 (2019).
57. Wang, Y. *et al.* CDK7-Dependent Transcriptional Addiction in Triple-Negative Breast Cancer. *Cell* **163**, 174–186 (2015).
58. Christensen, C. L. *et al.* Targeting Transcriptional Addictions in Small Cell Lung Cancer with a Covalent CDK7 Inhibitor. *Cancer Cell* **26**, 909–922 (2014).
59. Chipumuro, E. *et al.* CDK7 Inhibition Suppresses Super-Enhancer-Linked Oncogenic Transcription in MYCN-Driven Cancer. *Cell* **159**, 1126–1139 (2014).
60. Zhang, H. *et al.* CDK7 Inhibition Potentiates Genome Instability Triggering Anti-tumor Immunity in Small Cell Lung Cancer. *Cancer Cell* **37**, 37-54.e9 (2020).
61. Marineau, J. J. *et al.* Discovery of SY-5609: A Selective, Noncovalent Inhibitor of CDK7. *J. Med. Chem.* **65**, 1458–1480 (2022).
62. Sharma, M. *et al.* 518MO Tolerability and preliminary clinical activity of SY-5609, a highly potent and selective oral CDK7 inhibitor, in patients with advanced solid tumors. *Ann. Oncol.* **32**, S587–S588 (2021).

63. Bashir, B. *et al.* Phase 1/1b study of SY-5609, a selective and potent CDK7 inhibitor, in advanced solid tumors and in 2L/3L pancreatic ductal adenocarcinoma (PDAC) in combination with gemcitabine +/- nab-paclitaxel. *J. Clin. Oncol.* **41**, 3080–3080 (2023).
64. Giri, A. K. & Aittokallio, T. DNMT Inhibitors Increase Methylation in the Cancer Genome. *Front. Pharmacol.* **10**, (2019).
65. Nepali, K. & Liou, J.-P. Recent developments in epigenetic cancer therapeutics: clinical advancement and emerging trends. *J. Biomed. Sci.* **28**, (2021).
66. Mottini, C. *et al.* Predictive Signatures Inform the Effective Repurposing of Decitabine to Treat KRAS–Dependent Pancreatic Ductal Adenocarcinoma. *Cancer Res.* **79**, 5612–5625 (2019).
67. Heumann, T. R. *et al.* A randomized, phase II trial of oral azacitidine (CC-486) in patients with resected pancreatic adenocarcinoma at high risk for recurrence. *Clin. Epigenetics* **14**, 166 (2022).
68. Gailhouste, L., Liew, L. C., Hatada, I., Nakagama, H. & Ochiya, T. Epigenetic reprogramming using 5-azacytidine promotes an anti-cancer response in pancreatic adenocarcinoma cells. *Cell Death Dis.* **9**, 1–12 (2018).
69. Bayless, K. J., Kwak, H.-I. & Su, S.-C. Investigating endothelial invasion and sprouting behavior in three-dimensional collagen matrices. Nat. Protoc. 4, 1888–1898 (2009).
70. Cheung, K. J., Gabrielson, E., Werb, Z. & Ewald, A. J. Collective Invasion in Breast Cancer Requires a Conserved Basal Epithelial Program. Cell 155, 1639–1651 (2013).

Acknowledgments: We thank A. Hsieh, as well as past and present members of the Kugel Laboratory for helpful discussions and specifically I. Luk for her helpful insight with organoid embedding and tissue immunofluorescence.

Funding: This work was supported in part by National Institutes of Health grants 5R37CA241472 to S.K, R37CA234488 to K.C., a V Foundation grant: Women Scientists Innovation Award for Translational Cancer Research to S.K, a Fred Hutchinson Cancer Center Human Biology Pilot Grant to J.E.G, and a ARCS Foundation Fellowship to J.E.G. This research was supported by the Cellular Imaging Core, the Experimental Histopathology Core, the Genomics & Bioinformatics Core, and the Preclinical Modeling Core for access to PDX models in Shared Resource of the Fred Hutch/University of Washington Cancer Consortium (P30 CA015704).

Author contributions: JEG, AWP, AS, AD collected data. NY and SD performed murine surgical procedures. JEG and SK analyzed the data. JEG, KC and SK contributed to the experimental design. JEG wrote the paper. All authors discussed the results and commented on the manuscript.

Competing Interests: All authors declare no competing interests.

Data and materials availability: All data associated with this study are present in the paper and the supplementary materials or publicly available datasets.

SUPPLEMENTAL FIGURES

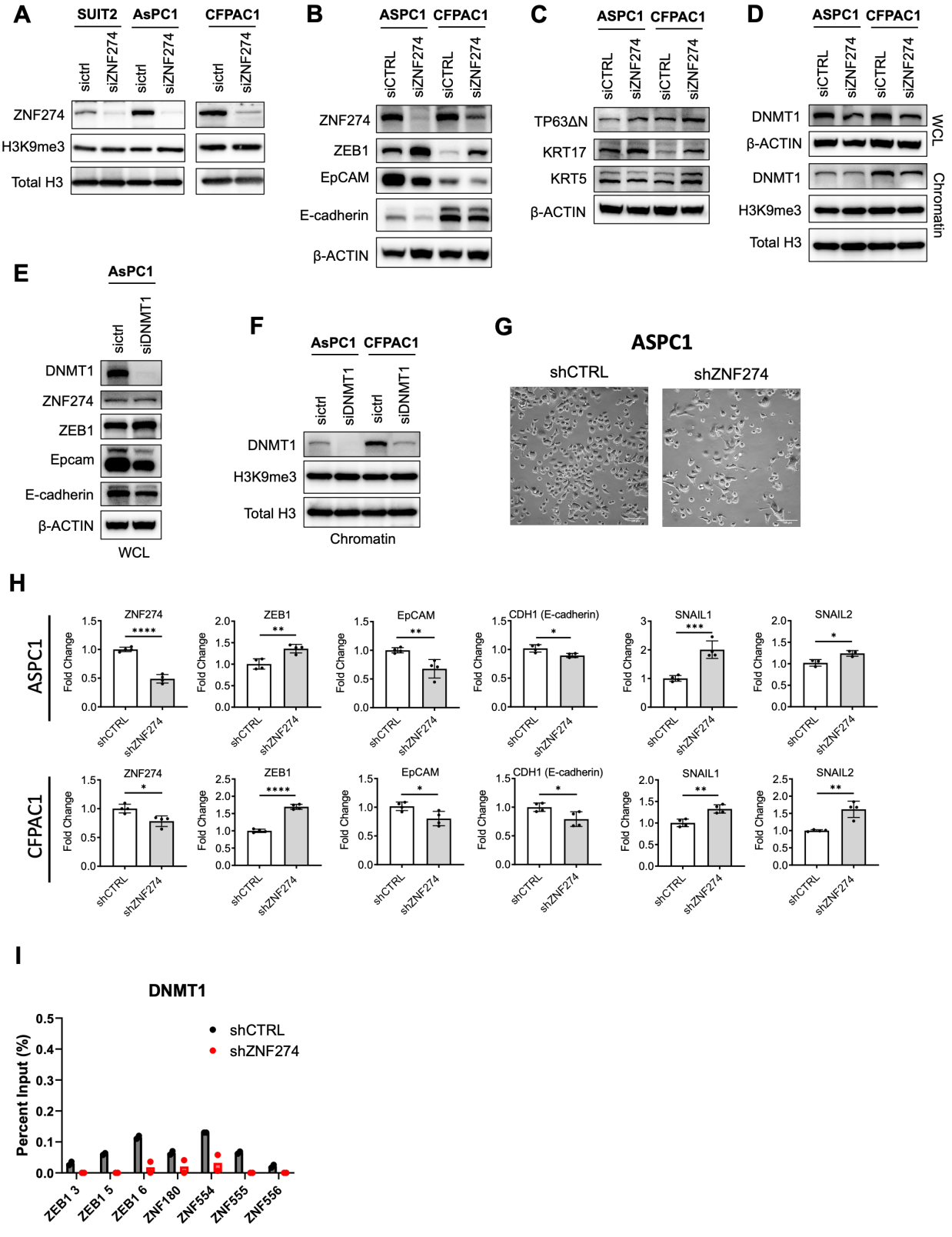

Figure S1. ZNF274 and DNMT1 regulation of EMT in classical PDA. A, WB for chromatin bound ZNF274, H3K9me3, and Total H3 in classical PDA cells lines treated with non-specific or ZNF274-specific siRNAs. **B,** WB for ZNF274, ZEB1, EpCAM, E-cadherin, and ACTIN in classical PDA cells lines treated with non-specific or ZNF274-specific siRNAs. **C,** WB for TP63ΔN, keratin17, keratin5, and ACTIN in classical PDA cells lines treated with non-specific or ZNF274-specific siRNAs. **D,** WB for WCL DNMT1 and ACTIN and chromatin bound DNMT1, H3K9me3, and Total H3 in classical PDA cells lines treated with non-specific or ZNF274-specific siRNAs. **E,** WB for DNMT1, ZNF274, ZEB1, EpCAM, E-cadherin, and ACTIN in classical PDA cells lines treated with non-specific or DNMT1-specific siRNAs. **F,** WB for chromatin bound DNMT1, H3K9me3, and Total H3 in classical PDA cells lines treated with non-specific or DNMT1-specific siRNAs. **G,** Phase contrast images of live classical PDA cells with doxycycline induced control or ZNF274-specific shRNAs . Images were taken on the Nikon Live microscope and have a scale bar of 100um. **H,** RT-PCR for ZNF274, markers of the mesenchymal cell state: ZEB1, SNAIL1 and SNAIL2; and markers of the epithelial cell state: EpCAM and CDH1 (E-cadherin) in classical PDA cells lines with doxycycline induced control or ZNF274-specific shRNAs. **I,** ChIP-qPCR for ZEB1 3 (promoter), ZEB1 5 (3' exon), ZEB1 6 (3' exon), ZNF180 and ZNF554 (ZNF274 bound positive control genes), ZNF555 and ZNF556 (non-ZNF274 bound negative control genes) with pulldown for DNMT1 in a classical PDA cell line with doxycycline induced control or ZNF274-specific shRNAs. Error bars represent +/- SEM between technical triplicates. Data are representative of at least 2 independent experiments. *p-value ≤ 0.05; **p-value ≤ 0.01, ***p-value ≤ 0.001, ****p-value ≤ 0.0001 (two-tailed unpaired Student's *t*-test).

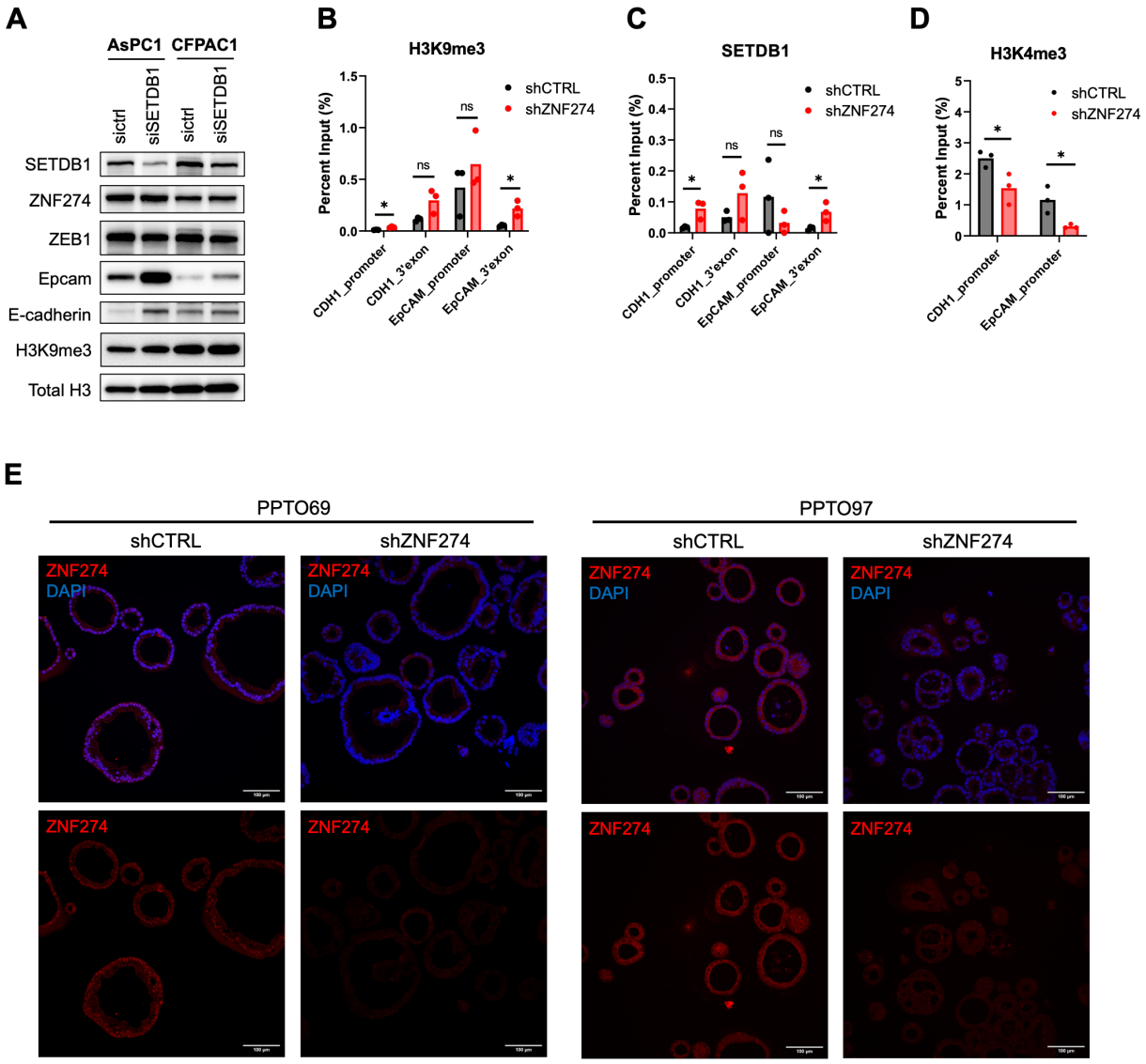

Figure S2. SETDB1 regulation of EMT in classical PDA. A, WB for chromatin bound SETDB1, ZNF274, ZEB1, EpCAM, E-cadherin, H3K9me3, and Total H3 in classical PDA cells lines treated with non-specific or SETDB1-specific siRNAs. **B-C,** ChIP-qPCR for CDH1_promoter, CDH1_3'exon, EpCAM_promoter, EpCAM_3'exon with pulldown for H3K9me3 (E), and SETDB1 (F) in a classical PDA cell line with doxycycline induced control or ZNF274-specific shRNAs. **D,** ChIP-qPCR for CDH1_promoter, and EpCAM_promoter, with pulldown for H3K4me3 in a classical PDA cell line with doxycycline induced control or ZNF274-specific shRNAs. **E,** Immunofluorescence images of ZNF274 stained embedded classical PDA organoids with doxycycline induced control or ZNF274-specific shRNAs. Images were taken on the Nikon Live microscope and have a scale bar of 100um. Error bars represent +/- SEM between technical triplicates. Data are representative of at least 2 independent experiments. *p-value ≤ 0.05; **p-value ≤ 0.01 (two-tailed unpaired Student's *t*-test).

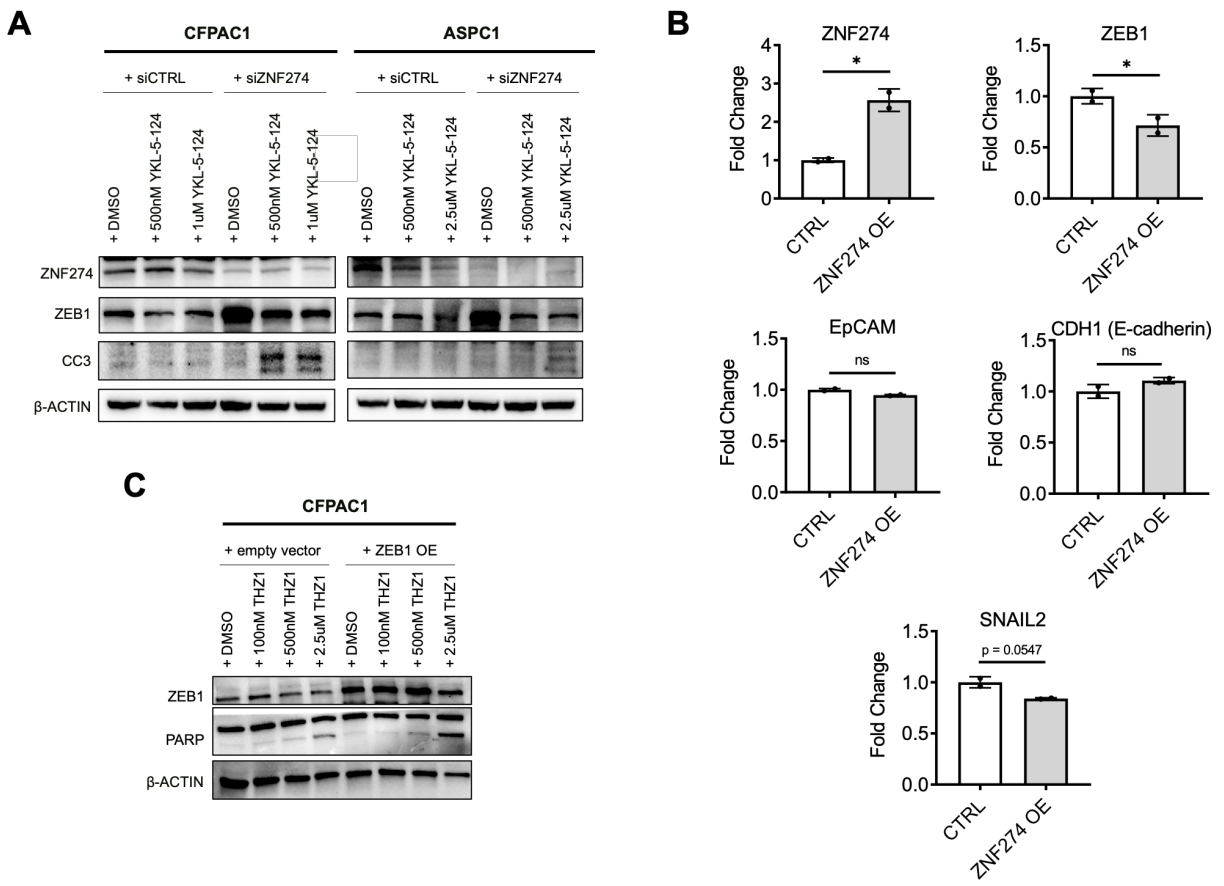

Figure S3. ZNF274 and ZEB1 control of sensitivity to CDK7 inhibition. A, WB for ZNF274, ZEB1, CC3 and ACTIN in classical PDA cells lines transfected with non-specific or ZNF274-specific siRNAs and treated with 500nM, 1uM or 2.5uM YKL-5-124 for 72 hours. **B,** RT-PCR for ZNF274, ZEB1, EpCAM and CDH1 (E-cadherin) in a second basal PDA cell line infected with an empty vector or ZNF274 overexpression vector. **C,** WB for ZEB1, PARP and ACTIN in a classical PDA cell line infected with an empty vector or ZEB1 overexpression vector and treated with 100nM, 500nM or 2.5uM THZ1 for 24 hours. Error bars represent +/- SEM between technical duplicates. Data are representative of at least 2 independent experiments. *p-value ≤ 0.05; **p-value ≤ 0.01 (two-tailed unpaired Student's *t*-test).

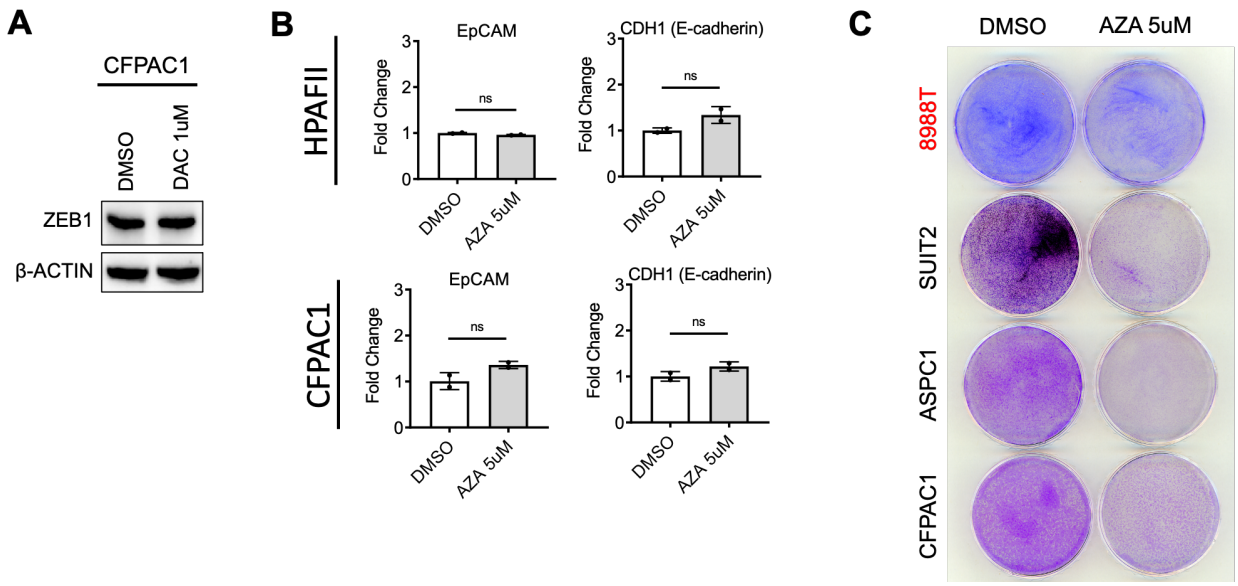

Figure S4. DNMT1 inhibition in basal and classical PDA. A, WB for ZEB1 and ACTIN in a classical PDA cell line treated with DMSO or 1uM Decitabine for 48 hours. **B,** RT-PCR for EpCAM and CDH1 (E-cadherin) in classical PDa cell lines treated with 5uM Azacytidine for 48 hours. **C,** Plate scan of a basal cell line and three classical cell lines treated with DMSO or 5uM Azacytidine for 48 hours and then stained with crystal violet. Error bars represent +/- SEM between technical duplicates. Data are representative of at least 2 independent experiments. *p-value ≤ 0.05; **p-value ≤ 0.01 (two-tailed unpaired Student's *t*-test).

SUPPLEMENTAL TABLES

Table S1. qPCR primers used in this study

Gene	Forward (5' - 3′)	Reverse (5' - 3′)
ZNF274	ATCCAGGCCCTATATGCTGAA	GAGCGTGCCTTAGGCTGTA
SETDB1	AGGAACTTCGGCATTTCATCG	TGTCCCGGTATTGTAGTCCCA
ZEB1	TTACACCTTTGCATACAGAACCC	TTTACGATTACACCCAGACTGC
EpCAM	TGATCCTGACTGCGATGAGAG	CTTGTCTGTTCTTCTGACCCC
CDH1	CGAGAGCTACACGTTCACGG	GGGTGTCGAGGGAAAAATAGG
SNAIL1	TCGGAAGCCTAACTACAGCGA	AGATGAGCATTGGCAGCGAG
SNAIL2	CGAACTGGACACACATACAGTG	CTGAGGATCTCTGGTTGTGGT

Table S2. ChIP-qPCR primers used in this study

Gene	Forward (5' - 3′)	Reverse (5' - 3′)
ZEB1 3	CCGGATAATGGGGCTTGGAT	TTGGCACAGCAGCACAAATC
ZEB1 5	TCTCCTGAACCAGGCAAAGT	CCCACTGGTAAAACTGGGGA
ZEB1 6	TCTCAACACATGAATCATCGCT	CGTGCTCATTCGAGAGGATTTC
ZNF180	TGCAGTCAATGTGGGAAGTC	TGATGCACAATAAGTCGAGCA
ZNF554	CGGGGAAAAGCCCTATAAAT	TCCACATTCACTGCATTCGT
ZNF555	CAATTGGCCCATATCTTTACG	CATGTTCTCGAAAGCAAGCA
ZNF556	CAATCTTGCGGGAAGACATT	CACACTGCCCACATTCGTAG
CDH1_promoter	GTGAACCCTCAGCCAATCAG	TCACAGGTGCTTTGCAGTTc
CDH1_3’exon	ACAGCCCCGCCTTATGATT	GCGATTGCCCCATTCGTTCA
EpCAM_promoter	ACCAAAGATCCCTAACGCCG	GGGAGTTGGGGGAGTGAGTA
EpCAM_3’exon	ACACTTAAATGTGTGTTTCCTTGC	TCACCCATCTCCTTTATCTGAAACA

CHAPTER 4:

This chapter is all unpublished work.

Title: Transcriptional inhibition induces loss of nucleolar integrity in basal PDA

Authors: Jessica E. Gianopulos[1,2], Ashely Tsue[3], David Micheal Shechner[3], Sita Kugel[1]

Affiliations:
[1]Human Biology Division, Fred Hutchinson Cancer Center, Seattle, WA, 98109
[2]Program in Molecular and Cellular Biology, University of Washington, Seattle, WA,98105
[3]Department of Pharmacology, University of Washington, Seattle, WA, 98109

ABSTRACT

The nucleolus is a small yet complex organelle. As an organelle without a membrane, its function quite directly determines its structure. The nucleolus is the main site of ribosome biogenesis and predominantly consist of protein and RNA. The nucleolus is apt at responding to cellular stress but not impervious to dysregulation. Nucleolar stress is most often visitable through changes in nucleolar morphology which can indicate changes in RNA Pol I transcription and ribosomal biogenesis. In this chapter, we will investigate nucleolar changes induced by a transcriptional inhibitor in pancreatic ductal adenocarcinoma (PDA) cell lines. We will assess dysregulation of nucleolar proteins and ribosomal RNA following transcriptional inhibition. Additionally, we will use a new technology called O-MAP to further interrogate the nucleolar changes observed in basal but not classical PDA cell lines upon treatment with transcriptional inhibition. This work will elucidate new therapeutic vulnerabilities by better understanding how nucleolar integrity is maintained or lost in basal and classical PDA subtypes in the context of transcriptional inhibition.

INTRODUCTION

The nucleolus is a membraneless organelle within the nucleus and is the major site of ribosome biogenesis[1]. Since the nucleolus has no membrane, it maintains its structure through phase-separation as the nucleolus is predominantly made up of RNA and protein[2],[3]. The nucleolus has three subcompartments that each play a specific role in the process of ribosome biogenesis. The inner most compartment is the fibrillar center (FC) which is the site of ribosomal DNA transcription. Next is the dense fibrillar component (DFC) which surrounds the FC and is the site of ribosomal RNA (rRNA) processing. Last, is the granular component (GC) which fills all other space of the nucleolus and is the site of ribosome assembly. Ribosomal proteins from the nucleoplasm enter the nucleolus and complexes with the processed rRNA from DFC to build ribonucleoprotiens (RNPs). Mature ribosomes are made up of the 40S RNP and the 80S RNP, which are then exported to the cytoplasm where they can start translating proteins[4,5].

rRNA processing is a very specific process by which the precursor 47S rRNA is processed and spliced to create the three mature rRNAs, 28S, 18S and 5.8S. The 47S rRNA contains internal transcribed spacers 1 (ITS1) and 2 (ITS2) as well as 5′ and 3′ external transcribed spacers (5′-ETS and 3′-ETS). Processing of the 47S rRNA can occur through a few different pathways in which the ITS and ETS regions are cleaved and removed in different orders that can produce different rRNA intermediate products but eventually all lead to production of the same three mature rRNAs [6,7].

Not only is the nucleolus the site of ribosome biogenesis but it is also an organizational hub for heterochromatin. The nucleolus is surrounded by a dense layer of compacted chromatin which is visible as a thick open circle when nuclei are stained with DAPI[8]. This layer of compact chromatin is made up of many small regions from a variety of different chromosomes; these

regions are called NADs or nucleolar-associated domains. Studies have identified that NADs are enriched for repetitive element genes, inactive regions of the X chromosome, and some RNA polymerase III-transcribed genes[9]. These regions cluster near the nucleolus and some even flank the ribosomal DNA repeats which belong to the core nucleolar genome. Disputations to NADs along with other nucleolar changes have been identified in human diseases and cancer. A variety of different stressors have been associated with changes in nucleolar morphology such as hypoxia, hydrogen peroxide, and heat just to name a few[10]. In cancer, nucleolar changes such as an increase in size and number have been observed. An increase in nucleolar size can be associated with an increase in RNA POL I transcription leading to increased production of rRNA[11]. As a result, many studies are assessing the therapeutic potential of RNA POL I inhibitors for cancer treatment. Additionally, dysregulation of ribosomal biogenesis has been found to contribute to cellular transformation thereby identify the nucleolus as a promising target for new cancer therapies[12]. Current cancer therapies have also been shown to induce nucleolar stress and nuclear morphology changes. One study assessed a variety of chemotherapy drugs and saw that many of these drugs also inhibit different stages of rDNA transcription and rRNA processing leading to dramatic changes in nucleolar morphology[13].

Current approaches used to better understand changes in nucleolar biology isolate intact nucleoli by biochemical fractionation and then analyze components by mass spectrometry or deep sequencing[14–16]. Unfortunately, these methods are not standard across cell types, nor would they work for clinical samples that may have fragile, therapeutically disrupted nucleoli. Even though nucleolar structure and protein make up may be different, all nucleoli share the common architectural scaffold the 47S pre-ribosomal RNA[4,6,17]. To enable multi-omic analysis of the nucleolus, the Shechner lab has developed O-MAP, an oligonucleotide-directed biotinylation

method to map structures surrounding an RNA scaffold such as the 47S rRNA of the nucleolus[18]. O-MAP comprehensively identifies the proteins, RNAs, and genomic loci near any target RNA within its native cellular context, bypassing the need for any biochemical fractionation. O-MAP uses DNA oligonucleotides linked to horseradish peroxidase (HRP), a promiscuous biotinylating enzyme, which tags nearby molecules with biotin. The DNA oligonucleotides hybridize to a target RNA in fixed cells and thereby facilitate biotinylation of molecules surrounding the target RNA. A streptavidin pulldown will isolate all biotin labeled molecules enabling assessment of them by proteomics, RNA-sequencing, or DNA-sequencing[18]. This technique will be instrumental in better understanding changes in nucleolar biology and other RNA centered processes.

RESULTS

We have previously shown that the basal PDA subtype is more sensitive to transcriptional inhibition by THZ1 than classical PDA[19]. THZ1 induces apoptosis in basal cells following treatment with 100nM-500nM of THZ1 for 16 hours. Interestingly, THZ1 treatment also induces a dramatic reduction in protein translation solely in basal PDA cells which have higher baseline translation rate than classical PDA cells[19]. To investigate if this change in translation upon THZ1 treatment results from alterations to ribosomal biogenesis, we first assessed the nucleolus for any morphological changes that could indicate disruption in ribosomal biogenesis. We treated basal PDA cells with low dose THZ1 (100nM) for a short amount of time to assess changes that occur prior to THZ1 induced apoptosis. Immunofluorescence on THZ1 treated PDA cell lines stained for nucleolar marker, nucleolin, showed a clear loss of nucleolar integrity in basal PDA cell lines (in red) with increasing treatment time following the initial dose of 100nM THZ1 (Figure 1A). Classical PDA cell lines (in black) showed no loss of nucleolar integrity and maintained defined

nucleolar borders even upon the longest treatment time with 100nM THZ1 (Figure 1A). We observed the same loss of nucleolar integrity in a basal PDA cell line treated with THZ1 and then stained for a different nucleolar marker, nucleophosminutes(Figure 1B), validating that this change in nucleolar morphology is not specific to just nucleolin proteins but is characteristic of nucleolar integrity as a whole. This change in nucleolar morphology provides the first indications that the nucleolus might be involved in the translation changes induced upon THZ1 treatment.

To further investigate this change in nucleolar morphology, we assessed if changes in rRNA expression occurred upon THZ1 treatment. We would expect a decrease in rRNA expression as that would correspond with the decrease in protein translation. Mature rRNA is too abundant in cells to measure any changes in expression therefore a decrease in rRNA transcription would be evident by a decrease in expression of the precursor 47S/45S rRNA. Additionally, inhibition of rRNA transcription has also been shown to lead to changes in nucleolar morphology[13], therefore we performed qPCR on the 45S precursor rRNA following THZ1 treatment of a basal and classical PDA cell line. We observed no clear decrease in 45S rRNA expression with increasing treatment time of THZ1 in either basal or classical PDA (Figure 1C). To determine if this change in morphology is due to baseline difference in mature rRNAs between PDA subtypes, we performed a normal RNA extraction and then ran total RNA on a 3% agarose gel. We observed no difference in baseline mature rRNA (28S, 18S, and 5.8S) expression between untreated basal and classical PDA cell lines (Figure 1D). Together, this data identifies no changes in rRNA expression that could explain the nucleolar morphological changes or translation changes induced by THZ1 treatment.

To further investigate this change in nucleolar morphology upon THZ1 treatment, we compared baseline nucleolar morphology of basal and classical PDA cell lines. Nucleolar

staining of basal and classical PDA cell lines showed that basal PDA cells have clear, round, and intact nucleoli as stained by the nucleolin marker. In contrast, classical PDA cell lines have a wide variety of nucleolar morphologies. Some classical PDA cell lines have more intact nucleoli like the basal PDA cell lines, while others have more dispersed nucleoli that seem to lack clear and defined edges. Lastly some classical PDA cell lines have very high number of smaller nucleoli and thereby fill more of the nucleus with nucleoli (Figure 2A). This difference in baseline nucleolar morphology could explain why only basal PDA exhibits a nucleolar morphology change upon THZ1 treatment. Classical PDA cell lines may be less sensitive to nucleolar stressors since their morphology is not as stringent as basal PDA cell lines. Basal PDA cell lines may rely on super intact nucleoli to function properly and thereby enable higher rates of cellular translation but as a result are more susceptible to stressors disrupting that structure. Classical PDA cell lines don't seem to need well defined nucleolar structures in order to function as they are not reliant on high translation levels and can therefore recover from the stress of THZ1 treatment better.

To understand these differences better, we collaborated with the Shechner lab to start the processes of using their new technology to further characterize these nucleolar morphology changes in PDA and hopefully identity how these changes connect to our translational changes. We set out to optimize O-MAP in 2 basal and 2 classical PDA cell lines. From O-MAP followed by imaging, we were able to identify nucleolar specific biotin labeling in our basal and classical PDA cell lines (Figure 2B). Next, we took one basal PDA cell line treated with 100nM THZ1 for 2 and 6 hours and then subjected those cells to the O-MAP protocol. We followed O-MAP with imaging and saw clear biotin labeling of the nucleolus in the DMSO treated cells and then saw an increase in dispersion of the biotin signal with increased treatment of THZ1. By the 6 hours

THZ1 treatment timepoint, the biotin labeling no longer resembled a nucleolus but instead seemed to label an area surrounding where the nucleolus has been previously (Figure 2C). This data matched what we had seen previously with THZ1 treatment of basal cells leading to a change in nucleolar organization and integrity. Pervious literature has indicated that the nucleolus is also involved in the DNA Damage response[20]. This presents as an additional explanation for the nucleolar morphology changes as western blot for yH2A.x, a marker of DNA damage, have shown a striking increase in yH2A.x signal upon lower doses of THZ1 treatment in basal but not classical PDA cell lines (Figure 2D). Further investigation of the DNA damage response will be needed to confirm the role of this pathway in our THZ1 induced nucleolar morphology change in basal PDA. This project was placed on hold while the downstream proteomics of the O-MAP technique were being optimized.

DISCUSSION

Completion of O-MAP followed by proteomic analysis of the nucleolus would provide new insight into the biological changes occurring in the nucleoli of basal PDA cell lines treated with low dose THZ1. We have hypothesized that the DNA damage pathway may be involved in how the basal PDA nucleoli is responding to THZ1 induced stress driving the loss of nucleolar integrity and resulting in altered translation levels. O-MAP will help validate this hypothesis by identifying changes in how DNA damage proteins interact with the nucleolus before and after treatment with THZ1 as well as identify changes in ribosomal proteins that could impact translation. Finally, O-MAP could identify changes in other nucleolar proteins upon THZ1 treatment that could shed light on how nucleolar integrity is lost when basal PDA cells are treated with this drug. A comparison of O-MAP in basal vs classical PDA cell lines treated with

THZ1 would also elucidate differences in how the nucleoli of classical PDA cells respond and recover from the drug treatment that enables it to maintain its normal nucleolar morphology.

Changes in nucleolar morphology have long been known to results from disruptions in ribosomal biogenesis which can lead to altered protein translation. In most cases these kinds of disruptions occur in combination with human diseases, including viral infection or cancer. For example, in premature aging disorders, such as progeria, research has found that nucleolar expansion can occur which enhances ribosomal biogenesis and elevates protein translation[21]. A similar phenomenon has been seen in cancer where enlarged nucleoli and increased ribosomal biogenesis drive more aggressive tumor progression while smaller nucleoli and reduced nucleolar activity can led to prolonged survival[22]. Nucleolar size is a highly studied area of nucleolar morphology changes from which we can elucidate the importance of maintaining nucleolar integrity to promote nucleolar function. Therefore, in our model system, basal PDA cells seem to rely on an intact and functional nucleolus to maintain its high levels of translation and this is imperative for the continued progression of the PDA tumor.

Further investigation could lead to broader insights into how basal PDA cells attempts to cope with the stress of transcriptional inhibition before being eventually driven to apoptosis. This insight could facilitate more research into preventing resistance to transcriptional inhibitors like THZ1 that will be used to treat PDA patients. By understanding how a basal PDA cell responds and attempts to cope with a drug, we could preemptively block the ways in which a basal PDA cell may acquire resistance to that drug and thereby make it more effective in the clinic. For classical PDA cells, we could identify new mechanisms that could be targeted to sensitize classical PDA cells to transcriptional inhibitors like THZ1, thereby broadening the application of these drugs in the clinic.

MATERIALS AND METHODS

Immunofluorescence. Immunofluorescence was performed as previously described[19]. Antibodies used were: Nucleolin (NCL, abcam # ab136649) and Nuclophosmin (NPM1, abcam # ab10530).

Real-time quantitative PCR (q-PCR). Total RNA extraction, cDNA synthesis and real-time quantitative PCR were performed as previously described[19]. Data were expressed as relative mRNA abundance normalized to the β-ACTIN expression level in each sample or as fold change over control and error bars are represented as mean ± s.e.m. between two independent experiments unless otherwise indicated in the figure legend. 45S primer sequences are forward (5'-3'): GAACGGTGGTGTGTCGTT and reverse (5'-3'): GCGTCTCGTCTCGTCTCACT.

O-MAP. O-MAP followed by imaging was performed as described in the O-MAP methods paper[18].

Protein isolation and Western blot. Protein lysates were prepared by resuspending the cell pellets in RIPA lysis buffer supplemented with a protease inhibitor cocktail (Complete EDTA-free, Roche Applied Science), 5μM TSA, 5mM sodium butyrate, 1mM DTT, and phosphatase inhibitors (Phosphatase Inhibitor Cocktail Sets I, II, and III Calbiochem) and incubated on ice for 20 minutes. The lysate was then centrifuged at 14,000 rpm for 10 minutes at 4°C and the supernatant was harvested. Protein concentration was measured by using a BCA protein assay kit (Pierce). 20μg of the cell lysate (from lysis with buffer) electrophoresed on a 4-20% gradient polyacrylamide gel with SDS (Genscript) and electroblotted onto polyvinylidene difluoride

membranes (PVDF) (Millipore). Membranes were blocked in TBS with 5% non-fat milk and 0.1% Tween and probed with antibodies. Bound proteins were detected with horseradish-peroxidase-conjugated secondary antibodies (Vector Biolaboratories) and Clarity Max Western ECL Blotting Substrate (Biorad). Antibodies used were anti-Cleaved Caspase-3 (CST #9664), anti-PARP (CST #9542), anti-yH2A.x (Millipore Sigma # 05-636) and anti-betaACTIN (Sigma A5316) as a loading control.

FIGURES

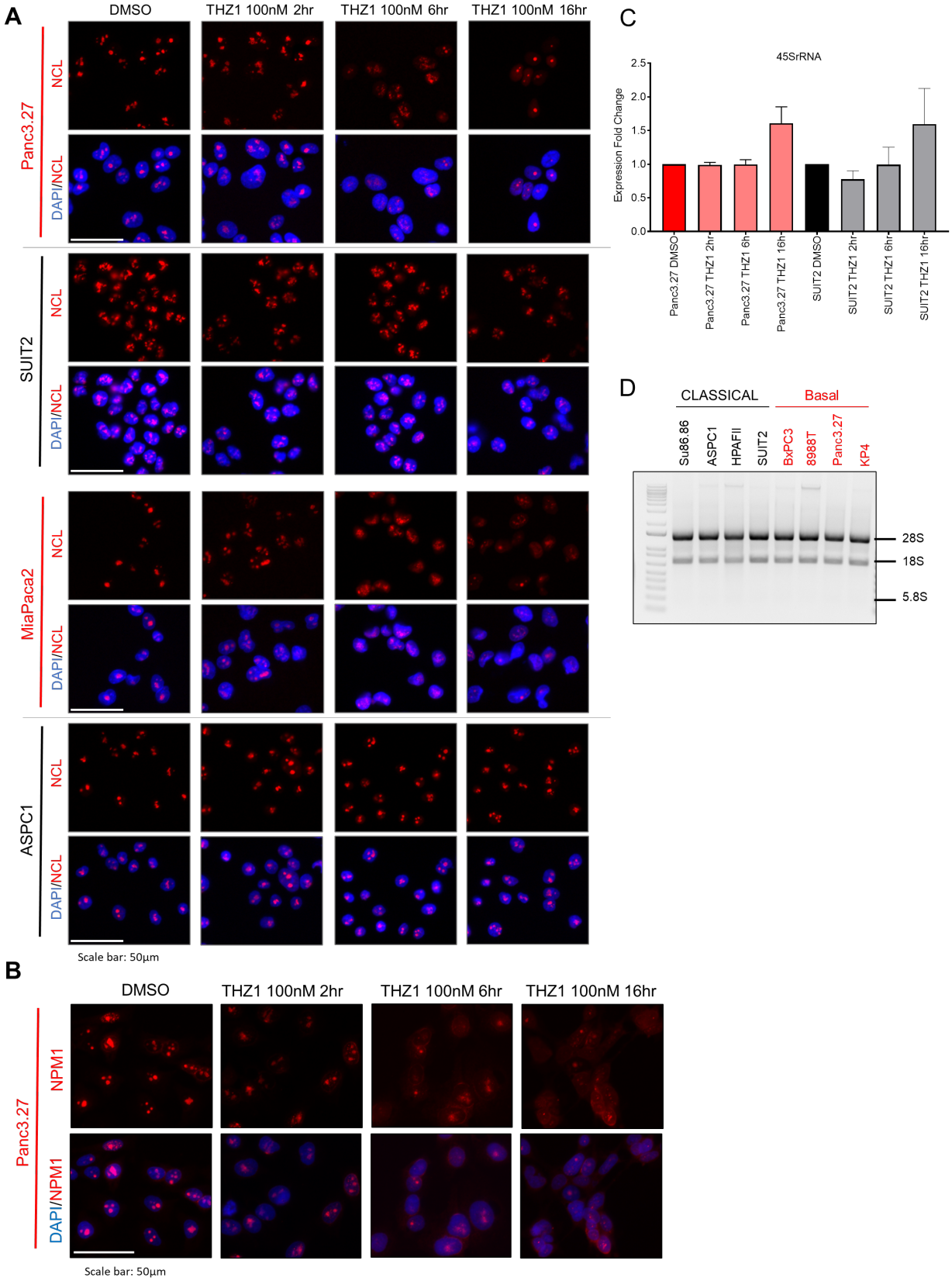
A
DMSO
THZ1 100nM 2hr
THZ1 100nM 6hr
THZ1 100nM 16hr
Panc3.27
SUIT2
MiaPaca2
ASPC1
NCL
DAPI/NCL
Scale bar: 50µm
B
DMSO
THZ1 100nM 2hr
THZ1 100nM 6hr
THZ1 100nM 16hr
Panc3.27
NPM1
DAPI/NPM1
Scale bar: 50µm
C
45SrRNA
Expression Fold Change
2.5
2.0
1.5
1.0
0.5
0.0
Panc3.27 DMSO
Panc3.27 THZ1 2hr
Panc3.27 THZ1 6hr
Panc3.27 THZ1 16hr
SUIT2 DMSO
SUIT2 THZ1 2hr
SUIT2 THZ1 6hr
SUIT2 THZ1 16hr
D
CLASSICAL
Basal
Su86.86
ASPC1
HPAFII
SUIT2
BxPC3
8988T
Panc3.27
KP4
28S
18S
5.8S

Figure 1: THZ1 treatment reduces nucleolar integrity in basal PDA. A, Immunofluorescence for basal (red) and classical (black) PDA cell lines treated with 100nM THZ1 for 2, 6, and 16 hours and then stained with the marker Nucleolin (NCL) and DAPI. **B,** Immunofluorescence for a basal (red) PDA cell line treated with 100nM THZ1 for 2, 6, and 16 hours and then stained with the marker Nuclophosmin (NPM1) and DAPI. **C,** qPCR for 45SrRNA (precursor rRNA) in basal (red), compared with classical (black) PDA cell lines treated with 100nM THZ1 for 2, 6, and 16hrs expressed as fold change normalized to DMSO. **D,** Agarose gel for total RNA from basal (red) and classical (black) PDA cell lines comparing expression of the mature rRNAs (28S, 18S, and 5.8S).

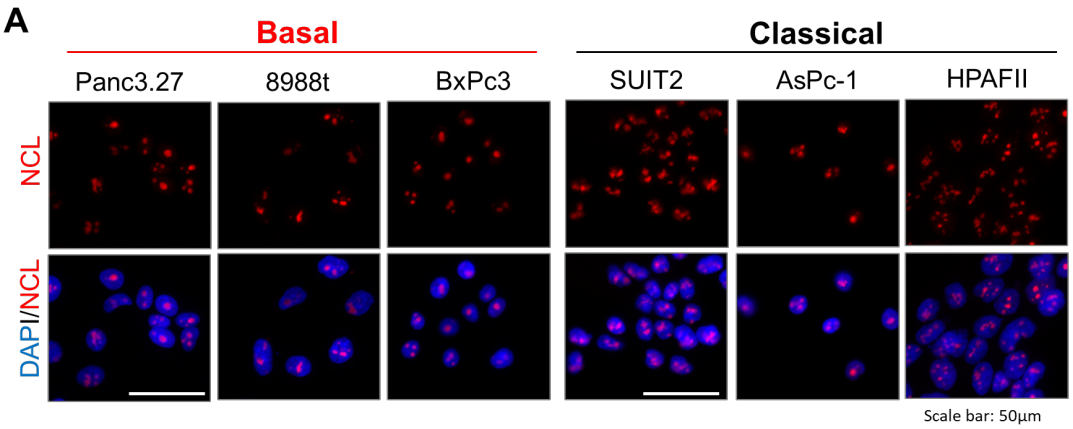
A
Basal
Classical
Panc3.27
8988t
BxPc3
SUIT2
AsPc-1
HPAFII
NCL
DAPI/NCL
Scale bar: 50μm

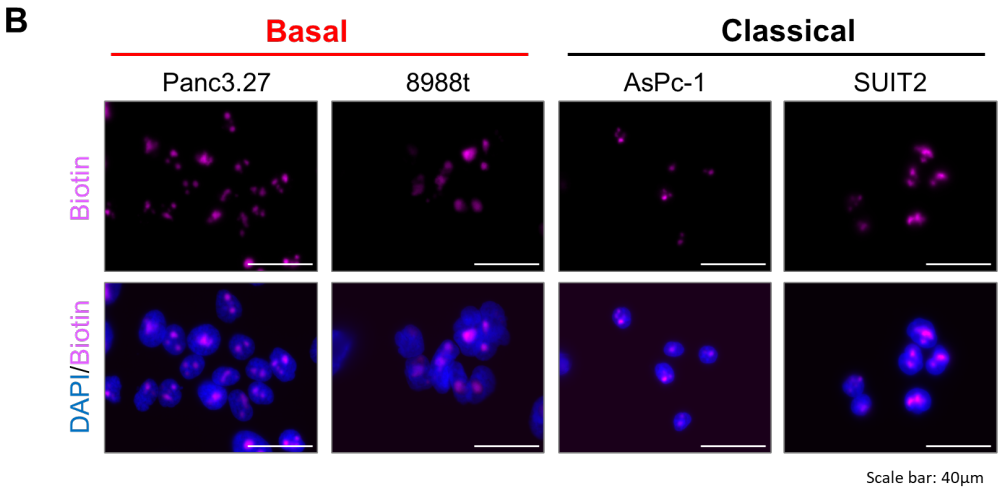
B
Basal
Classical
Panc3.27
8988t
AsPc-1
SUIT2
Biotin
DAPI/Biotin
Scale bar: 40μm

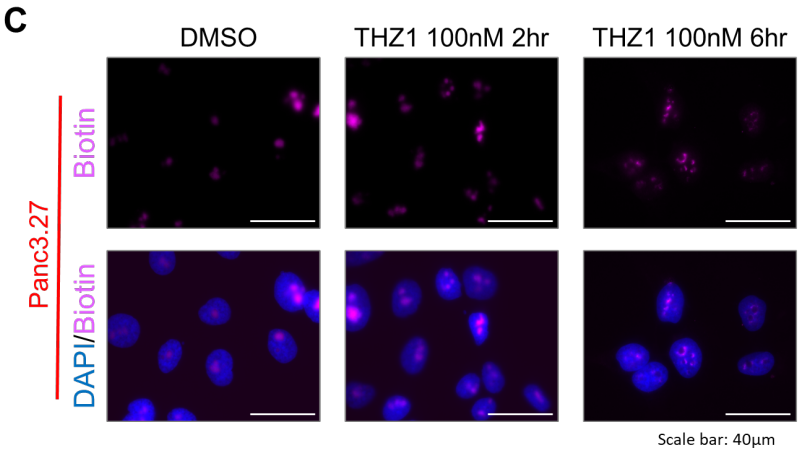
C
DMSO
THZ1 100nM 2hr
THZ1 100nM 6hr
Panc3.27
Biotin
DAPI/Biotin
Scale bar: 40μm

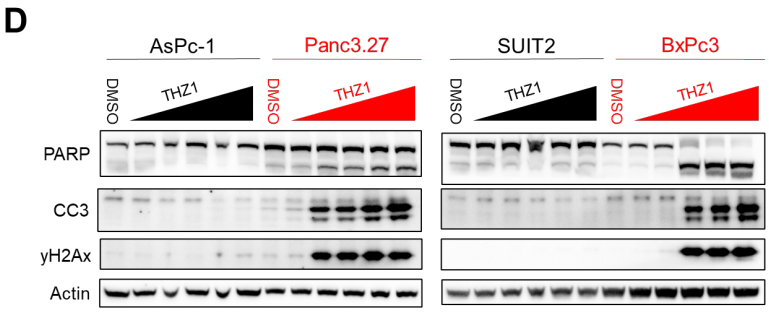
D
AsPc-1
Panc3.27
SUIT2
BxPc3
DMSO
THZ1
PARP
CC3
yH2Ax
Actin

Figure 2 O-MAP to characterize alterations to nucleolar morphology. A, Immunofluorescence for basal (red) and classical (black) PDA cell lines stained with the marker Nucleolin (NCL) and DAPI. **B,** O-MAP for basal (red) and classical (black) PDA cell lines labeled with biotin directed by 47S (rRNA precursor) specific probes. **C,** O-MAP for a basal PDA cell line treated with 100nM THZ1 for 2 and 6 hours labeled with biotin directed by 47S (rRNA precursor) specific probes. **D,** Western blot for PARP, CC3, yH2Ax and β-actin in basal (red), compared with classical (black) PDA cell lines treated with increasing doses of THZ1 (20nM – 5uM).

CHAPTER 4: REFERENCES

1. Pederson, T. The Nucleolus. *Cold Spring Harb. Perspect. Biol.* **3**, a000638 (2011).
2. Yoneda, M., Nakagawa, T., Hattori, N. & Ito, T. The nucleolus from a liquid droplet perspective. *J. Biochem. (Tokyo)* **170**, 153–162 (2021).
3. Feric, M. *et al.* Coexisting Liquid Phases Underlie Nucleolar Subcompartments. *Cell* **165**, 1686–1697 (2016).
4. Weipoltshammer, K. & Schöfer, C. Morphology of nuclear transcription. *Histochem. Cell Biol.* **145**, 343–358 (2016).
5. Aitchison, J. D. & Rout, M. P. The Road to Ribosomes. *J. Cell Biol.* **151**, 23–26 (2000).
6. Henras, A. K., Plisson-Chastang, C., O'Donohue, M.-F., Chakraborty, A. & Gleizes, P.-E. An overview of pre-ribosomal RNA processing in eukaryotes. *WIREs RNA* **6**, 225–242 (2015).
7. Tafforeau, L. *et al.* The Complexity of Human Ribosome Biogenesis Revealed by Systematic Nucleolar Screening of Pre-rRNA Processing Factors. *Mol. Cell* **51**, 539–551 (2013).
8. Németh, A. & Längst, G. Genome organization in and around the nucleolus. *Trends Genet.* **27**, 149–156 (2011).
9. Matheson, T. D. & Kaufman, P. D. Grabbing the genome by the NADs. *Chromosoma* **125**, 361–371 (2016).
10. Yang, K., Yang, J. & Yi, J. Nucleolar Stress: hallmarks, sensing mechanism and diseases. *Cell Stress* **2**, 125–140.
11. Quin, J. E. *et al.* Targeting the nucleolus for cancer intervention. *Biochim. Biophys. Acta BBA - Mol. Basis Dis.* **1842**, 802–816 (2014).
12. Hein, N., Hannan, K. M., George, A. J., Sanij, E. & Hannan, R. D. The nucleolus: an emerging target for cancer therapy. *Trends Mol. Med.* **19**, 643–654 (2013).
13. Burger, K. *et al.* Chemotherapeutic Drugs Inhibit Ribosome Biogenesis at Various Levels. *J. Biol. Chem.* **285**, 12416–12425 (2010).
14. Andersen, J. S. *et al.* Nucleolar proteome dynamics. *Nature* **433**, 77–83 (2005).
15. van Koningsbruggen, S. *et al.* High-resolution whole-genome sequencing reveals that specific chromatin domains from most human chromosomes associate with nucleoli. *Mol. Biol. Cell* **21**, 3735–3748 (2010).
16. Bai, B. & Laiho, M. Deep Sequencing Analysis of Nucleolar Small RNAs: Bioinformatics. *Methods Mol. Biol. Clifton NJ* **1455**, 243–248 (2016).
17. Farley, K. I., Surovtseva, Y., Merkel, J. & Baserga, S. J. Determinants of mammalian nucleolar architecture. *Chromosoma* **124**, 323–331 (2015).
18. Tsue, A. F. *et al.* Oligonucleotide-directed proximity-interactome mapping (O-MAP): A unified method for discovering RNA-interacting proteins, transcripts and genomic loci in situ. *BioRxiv Prepr. Serv. Biol.* 2023.01.19.524825 (2023) doi:10.1101/2023.01.19.524825.
19. Kartha, N., Gianopulos, J., Schrank,Z. *et al.* Sirtuin 6 is required for the integrated stress response and resistance to inhibition of transcriptional cyclin-dependent kinases. *Sci. Transl. Med.* **15**, eabn9674 (2023).
20. Lindström, M. S. *et al.* Nucleolus as an emerging hub in maintenance of genome stability and cancer pathogenesis. *Oncogene* **37**, 2351–2366 (2018).
21. Buchwalter, A. & Hetzer, M. W. Nucleolar expansion and elevated protein translation in premature aging. *Nat. Commun.* **8**, 1–13 (2017).
22. Corman, A., Sirozh, O., Lafarga, V. & Fernandez-Capetillo, O. Targeting the nucleolus as a therapeutic strategy in human disease. *Trends Biochem. Sci.* **48**, 274–287 (2023).

Acknowledgments: We thank past and present members of the Kugel Laboratory and Shechner Laboratory for helpful discussions.

Funding: This work was supported by a Brotman Baty Institute Catalytic Collaborations Pilot Grant to S.K and D.M.S. This research was supported by the Cellular Imaging Core in Shared Resource of the Fred Hutch/University of Washington Cancer Consortium (P30 CA015704).

Author contributions: JEG and AT collected data. JEG, DMS and SK analyzed the data. JEG, DMS and SK contributed to the experimental design. JEG wrote this chapter.

CHAPTER 5: Conclusion and Future direction

My dissertation research has aimed to address the questions of (1) how PDA tumors respond to inhibitors of transcriptional CDKs from a therapeutic and mechanistic perspective, (2) how chromatin regulators define PDA cell state and control sensitivity to these inhibitors, and (3) what PDA cell state weaknesses can be exploited for future therapeutic development. These questions can be addressed from many angles meaning there is no one answer to each question. My research has uncovered that basal PDA is uniquely more sensitive to inhibitors of CDK7 and 9 than inhibitors of CDK12 and 13, while classical PDA is resistant to all these transcriptional CDK inhibitors. Additionally, classical PDA is regulated by a complex chromatin landscape, and we found that disrupting specific chromatin modifying proteins that help regulate this landscape can lead to cellular changes including altered sensitivity to CDK7 inhibitors. Lastly, we identified nucleolar integrity as a potential weakness that could be further exploited for new therapeutic development in PDA. In this chapter, I will address how this research has furthered our understanding of transcriptional CDK inhibitors in PDA and their ability to be used in a clinical setting. I will also touch on multiple different future directions that have developed out of the work in this thesis and how these further investigations will inform the field.

5.1 Covalent versus non-covalent transcriptional CDK inhibitors

Covalent CDK inhibitors, THZ1 and YKL-5-124, are very potent in vitro inhibitors of CDK7. They strongly inhibit phosphorylation of the CTD of RNA POL II at low doses inducing swift apoptosis in cell lines sensitive to the drugs. Non-covalent CDK inhibitors such as flavopiridol and samuraciclib are less potent in vitro requiring higher dose of drug to have a similar impact (Chapter 2 Figure 3B and Appendix 1 Figure A2E). As previously described in

chapter 1, non-covalent inhibitors are often ATP competitive inhibitors which bind in place of ATP with the intention of flooding the system with more drug than ATP so that the drug out-competes binding of ATP to the ATP binding pocket[1]. The issue with these types of inhibitors is that the drug will eventually unbind from the ATP binding pocket enabling ATP to replace it, therefore explaining why higher doses of non-covalent inhibitor drugs can be needed to induce the full effect of the drug.

Potency of these inhibitors' in vivo highlights why non-covalent inhibitors are approved in the clinic more often than covalent inhibitors. THZ1, which has a very short half-life in vivo and must be given twice a day, was very toxic to the mice and is hardly ever used for pre-clinical in vivo efficacy studies as a result. YKL-5-124 was much less toxic than THZ1 *in vivo*, it required only once a day injections in the mice which was tolerated very well enabling a thorough pre-clinical efficacy study in nude mice with PDA PDX tumors (Appendix Figure A2A). From our studies as well as others, YKL-5-124 seemed like a very promising candidate for a clinical CDK7 inhibitor. Unfortunately, attempts to modify YKL-5-124 into a clinical version proved that the covalent nature of YKL-5-124 binding to CDK7 was too potent and thereby too toxic for use in humans. This led to all clinically approved CDK7 inhibitors reverting to a non-covalent inhibition of CDK7's ATP binding pocket[2]. Even though non-covalent CDK inhibitors are less potent in vitro, they can still be quite potent in vivo. Both flavopiridol and SY5609 significantly inhibited tumor growth of basal PDA PDX tumors in nude mice (Chapter 2 Figure 7D and Chapter 3 Figure 5). SY5609 did show increased potency over flavopiridol given it only required a dose of 0.5 mg/kg while flavopiridol required doses of 5mg/kg. This differential only further confirms that in PDA, CDK7 inhibition leads to more effective inhibition of tumor growth than CDK9 inhibition. The does not renounce that CDK9 inhibition

would still present as a much better therapeutic option for PDA patients than current standard of care. This data only claims that if CDK7 inhibition can be tolerated by patients than it may provide a slightly better anti-tumor effect than CDK9 inhibition.

5.2 Current and Future Clinical trials with CDK7/9 inhibitors for pancreas cancer

Our work has identified CDK7 and CDK9 as potent therapeutic targets for treating PDA tumors. A clinical trial with a CDK9/2 inhibitor is expanding to include Fred Hutch as a recruiting institution. Based on our data, we believe this is an invaluable opportunity for patients with PDA and are working on adding them to the pool of patients to be recruited. This inhibitor is slightly different than flavopiridol as it targets both CDK9 and CDK2 so the Kugel lab is also characterizing this drug in PDA in vitro and in vivo to validate its potential therapeutic benefit to PDA patients who could be enrolled in this clinical trial.

In addition, Dr. Sita Kugel was awarded a large V foundation grant to start our own clinical trial with a CDK7 inhibitor for PDA patients who undergo FOLFIRINOX chemotherapy. FOLFIRINOX chemotherapy treatment in PDA patients has been shown to shrink PDA tumors in order to improve surgical resection outcome but has also shown that this chemotherapy kills off mostly classical PDA tumor cells therefore skewing the tumor to a more basal like state. This presents a perfect opportunity to administer a CDK7 inhibitor since the patient's tumor will be more basal and we have shown that basal PDA tumors are extremely sensitive to CDK7 inhibitors. All in vitro and in vivo characterizations of the clinical CDK7 inhibitors in PDA tumor samples are complete and shown in this thesis (Appendix Figure A2B-E and Chapter 3 Figure 5). The clinical trial logistics are being finalized and the trial is expected to start recruiting patients by the end of 2024. We are very excited to see what started as initial characterization of

CDK7 and CDK9 inhibitors to determine potential therapeutic benefit in PDA patients become a real clinical trial in which these therapeutic drugs can actually become accessible to PDA patients who would benefit from their treatment.

5.3 Future Directions

With the broad scope of this work, there are many avenues to explore further and a plethora of future directions to take. Therefore, the future directions described here are only a subset of the possibilities to be explored. In general, all projects derived from the work in this thesis will still focus on better understanding PDA tumor biology, weaknesses in cellular mechanisms that can be exploited for new therapies, as well as how these therapies impact different intra- and extra-cellular processes. All of this research will inform development of new combination and single target therapies to increase the therapeutic options for patients with this devastating disease.

As described in the introduction, most PDA patient tumors acquire some kind of drug resistance to treatment therapies. Therefore, a necessary next step is to uncover possible mechanisms of resistance that PDA tumors would develop in response to CDK7 inhibitor treatment. A number of studies have investigated THZ1 resistance predominantly in breast cancer cell lines. These studies elucidated that the ABC multidrug transporters are often upregulated in THZ1 resistant cells enabling the resistant cells to expel the drug at a faster rate and evade CDK7 inhibition[3–5]. One particular study investigated acquired drug resistance to THZ1 and ICEC0942 (Samuraciclib). They found that ICEC0942 resistant cells upregulated the ABC transporter ABCB1 and that these cells were also resistant to THZ1. In contrast, THZ1 resistant cells showed upregulation of ABCB2 but were still sensitive to ICEC0942[4]. Additionally, we have

preliminary data that these ABC multidrug transports are also associated with THZ1 resistance in PDA tumor cells, however tumor cells can acquire drug resistance through multiple altered mechanism beyond solely changes in efflux pump expression and inhibitors of the same target can also lead to different mechanisms of acquired resistance. Therefore, we plan to continue investigating different mechanism of drug resistance to inhibitors of CDK7 in PDA model systems and eventually discover modes of preventing or treating CDK7 inhibitor drug resistance in patients.

Another avenue for continued investigation dives deeper into regulation of ATF4 degradation. Specifically, how β-TRCP may differ between basal and classical PDA subtypes adding another level of ATF4 degradation regulation. In chapter 2, we identified that β-TRCP is an E3 ligase that can recruit ATF4 to the proteasome for degradation by showing that double knockdown of SIRT6 and β-TRCP lead to rescue of ATF4 expression which typically decreases in the absence of SIRT6. If β-TRCP expression is higher or if the protein is more active in the basal subtype of PDA this would further explain the rapid degradation of ATF4 in basal PDA cell lines. Therefore, β-TRCP presents as an important candidate for further exploration of its role in PDA tumor cells response to inducers of cellular stress.

Additionally, ATF4 degradation is also regulated by its localization to nuclear speckles. Previous literature had shown that p300, a HAT, could stabilize and localize ATF4 to nuclear speckles thereby increasing its transcriptional activity[6]. In chapter 2, we identified that SIRT6, a HDAC, can bind and recruit ATF4 to nuclear speckles, which enables activation of ATF4 target genes and protection of ATF4 from proteasomal degradation in PDA tumor cells. Together, this data supports a model in which epigenetic modifier can control ATF4 through regulation of its localization to nuclear speckles. We speculate that this model may hold true for other HATs and

HDACs in PDA as well as in other cancers. We plan to continue exploring this important connection between chromatin regulators and ATF4 stress response in PDA and other cancers.

Another avenue of continued investigation is further exploring regulation of EMT independent of ZNF274 in PDA. Specifically, SETDB1 regulation of epithelial genes more in depth as in chapter 3 we showed that SETDB1 binds with ZNF274 to regulate ZEB1 but that SETDB1 also controls EpCAM and E-cadherin expression independent of ZNF274 binding in classical PDA. Additionally, ZNF274 OE altered ZEB1 expression but did not change epithelial gene expression and SETDB1 KD did change epithelial gene expression with no impact on ZEB1. Together, this confirmed that SETDB1 functions both independent and dependent of ZNF274 in classical PDA. So, we would like to further investigate how SETDB1 regulates gene expression independent of ZNF274. Does SETDB1 use a different ZNF DNA binding partner, or does it bind to DNA directly? Does SETDB1 function in a complex or recruit any other proteins to alter chromatin accessibility such as DNMT1? What role does SETDB1 play in regulating epithelial genes in basal PDA? Would SETDB1 KD have a different impact on EMT in basal PDA than in classical PDA? Since all the literature on SETDB1 regulation of EMT has led to the conclusion that SETDB1 control of EMT is very context specific, all of these questions would have to be investigate in our PDA model systems to parse out all the different ways SETDB1 can regulate EMT in PDA.

Lastly, we will continue investigating of how maintenance of chromatin states in basal and classical PDA is vital to continued tumor progression and how perturbation to these chromatin states drives such intense cellular disruption that it increases the susceptibility of the tumor cells to more stress inducing drugs. In this thesis, we have shown that multiple chromatin regulators can control PDA subtype specific drug sensitivity, even though the mechanism of

action is different, it is still important to understand the tumor biology as it can inform future therapeutic development.

5.4 Concluding Remarks:

My research demonstrates the importance of chromatin regulating proteins in characterizing PDA subtypes as well as regulating chromatin states and stress pathways within the basal and classical PDA subtypes. Identification of this regulation elucidated multiple mechanisms that regulate basal and classical PDA sensitivity to inhibitors of transcriptional CDKs and uncovered the strong therapeutic potential of clinically approved CDK9 and CDK7 inhibitors for the treatment of aggressive, chemoresistant PDA. Finally, this work has culminated in a Phase 1b clinical trial for PDA patients at Fred Hutchinson Cancer Center who will receive treatment with a clinically approved CDK7 inhibitor following FOLFIRINOX treatment with the goal of reducing tumor size such that surgical resection can be performed. We are hopeful that this dissertation work and the clinical trial will lead to more therapeutic options and improve PDA patient survival.

CHAPTER 5: REFERENCES

1. Olivieri, C. *et al.* ATP-competitive inhibitors modulate the substrate binding cooperativity of a kinase by altering its conformational entropy. *Sci. Adv.* **8**, eabo0696 (2022).
2. Marineau, J. J. *et al.* Discovery of SY-5609: A Selective, Noncovalent Inhibitor of CDK7. *J. Med. Chem.* **65**, 1458–1480 (2022).
3. Sava, G. P. *et al.* ABC-transporter upregulation mediates resistance to the CDK7 inhibitors THZ1 and ICEC0942. *Oncogene* **39**, 651–663 (2020).
4. Gao, Y. *et al.* Overcoming Resistance to the THZ Series of Covalent Transcriptional CDK Inhibitors. *Cell Chem. Biol.* **25**, 135-142.e5 (2018).
5. Webb, B. M. *et al.* TGF-β/activin signaling promotes CDK7 inhibitor resistance in triple-negative breast cancer cells through upregulation of multidrug transporters. *J. Biol. Chem.* **297**, 101162 (2021).
6. Lassot, I. *et al.* p300 Modulates ATF4 Stability and Transcriptional Activity Independently of Its Acetyltransferase Domain*. *J. Biol. Chem.* **280**, 41537–41545 (2005).